Automated Derivation of Glacial and Glacier-Proximal Parameters from Spaceborne SAR Data

Dissertation
zur
Erlangung der naturwissenschaftlichen Doktorwürde
(Dr. sc. nat.)
vorgelegt der
Mathematisch-naturwissenschaftlichen Fakultät
der
Universität Zürich

von
Christoph Rohner
von
Schaffhausen SH

Promotionskommission
Prof. Dr. Andreas Vieli (Vorsitz der Dissertation)
Prof. Dr. Alexander Damm
Dr. David Small (Leitung der Dissertation)
Dr. Martin P. Lüthi

Zürich, 2023

Summary

Due to atmospheric warming, the Greenland Ice Sheet is losing mass at an increasing rate, making it one of the main contributors to global sea level rise. Two components significantly influence the mass loss: increased surface melt on the one hand, and dynamic mass loss due to tidal outlet glaciers on the other. Both components together account for about 85% of the observed mass loss since 2009. At the same time, observations indicate a trend toward increasing runoff, thinning, and glacier tongue retreat across the vast majority of Greenland's outlet glaciers. In order to accurately predict these changes and thus future trends in global sea level rise, a deeper understanding of the interactions between glacier dynamics and oceanic, atmospheric, and topographic forcing factors is needed. Such a deeper understanding not only requires suitable models, but also long-term measurement series in order to improve, validate and calibrate these models.

Due to Greenland's remoteness and climatic challenges, *in situ* measurements are not only logistically but also financially challenging, causing measurement series to be interrupted during the winter season. As a result, seasonal aspects of glacier dynamics can be challenging to capture. Long-term time series from optical satellites also have gaps through the winter due to the polar night as well as year-round due to cloud cover, limiting the availability of retrievals based on those sensors.

To circumvent these drawbacks, the use of active radar satellite systems such as Synthetic Aperture Radars, which provide their own source of illumination and thus can acquire data independent of daylight and weather, is a viable option. Thanks to the free availability of satellite data with both high spatial and temporal resolution from the Sentinel-1 constellation, year-round measurements of various parameters are possible. The constellation has been in orbit since 2014 (Sentinel-1A) and 2016 (Sentinel-1B). In order to be able to evaluate the accumulating data volumes, automated and widely applicable algorithms are required to derive many desired parameters at a high spatio-temporal resolutions from an input data set without requiring substantial additional information. For long-term investigations of thematic effects, such as the detection of melting processes in snow or ice, there is simultaneously a need for products offering a normalized backscattering behavior with consistent local resolution (i.e. no exceptions for layover/foreshortening). This combination of features cannot be achieved working directly from datasets that have had only standard geometric or radiometric terrain-correction applied.

While existing algorithms can derive single parameters from satellite imagery, this PhD thesis works toward further closing this gap. It shows how different glacial and glacier-proximal parameters can be efficiently derived from single images for three outlet glaciers, each with its unique movement behavior. The glaciers considered in this thesis, *Eqip Sermia*, *Kangilerngata Sermia*, and *Sermeq Kujalleq*, are located north of *Ilulissat* in West Greenland. *Eqip Sermia* was surveyed using GPS, an Unmanned Aerial Vehicle, a Terrestrial Radar Interferometer, and weather stations to validate the measurements.

The algorithms developed in this PhD thesis allow automated extraction of Glacier Flow Dynamics, the location of the glacier front, the glacier area affected by surface melt, and the composition of the ice in front of the glacier tongue with only minimal, freely available additional information at high spatial and temporal resolutions. The resulting continuous time series allows us to see seasonal or multi-

year dynamics at the transition between the glacier tongue and fjord, and to study the interactions between the individual parameters in depth. This dissertation shows how SAR products from different satellites can be combined by weighing each acquisition's individual sample with its local resolution. Thus, continuous and radiometrically consistent products can be calculated over a wide area while simultaneously densifying the time series. These products allow measurement of, e.g., melting processes in sea ice and snow at unprecedented spatial and temporal resolution.

Zusammenfassung

Aufgrund der atmosphärischen Erwärmung verliert der grönländische Eisschild gegenwärtig in zunehmendem Mass an Masse und ist dadurch einer der Hauptverursacher des globalen Meeresspiegelanstieges. Dabei haben zwei Komponenten einen grossen Einfluss auf den Massenverlust: verstärkte Oberflächenschmelze einerseits und dynamischer Massenverlust durch Gezeitenauslassgletscher andererseits. Beide Komponenten zusammen machen dabei etwa 85% der beobachteten Zunahme des Massenverlustes seit 2009 aus. Gleichzeitig wird bei der grossen Mehrheit der grönländischen Auslassgletscher eine Tendenz zur Beschleunigung des Abflusses, zur Abnahme der Mächtigkeit und zum Rückzug der Gletscherzunge beobachtet. Um diese Veränderungen und somit auch die zukünftigen Entwicklungen des globalen Meeresspiegelanstieges präzise voraussagen zu können, ist ein vertieftes Verständnis der Interaktionen zwischen der Gletscherdynamik und den ozeanischen, atmosphärischen und topographischen Einflussfaktoren von grosser Wichtigkeit. Dazu werden neben geeigneten Modellen auch langjährige Messreihen benötigt, um diese Modelle zu verbessern, validieren und kalibrieren zu können.

Aufgrund der Abgeschiedenheit und der klimatischen Herausforderungen Grönlands sind Messungen vor Ort nicht nur logistisch, sondern auch finanziell eine Herausforderung, weshalb Messreihen über die Wintersaison oftmals unterbrochen und dadurch saisonale Aspekte der Gletscherdynamik nur schwer zu erfassen sind. Auch langjährige Zeitreihen optischer Satelliten weisen während des Winters aufgrund der Polarnacht sowie ganzjährig aufgrund von Wolkenbedeckung Lücken auf, was deren Nutzbarkeit einschränkt.

Um diese Nachteile zu umgehen, bietet sich die Nutzung aktiver Radarsatellitensysteme wie Synthetic Aperture Radar an, welche ihre eigene Beleuchtungsquelle sind und somit unabhängig von Tageslicht und Wetter Daten erfassen können. Dank der frei verfügbaren und raumzeitlich hochaufgelösten Satellitendaten der Sentinel-1-Konstellation, welche seit 2014 (Sentinel-1A) und 2016 (Sentinel-1B) im Orbit sind, ist somit eine ganzjährige Erfassung verschiedener Messgrössen möglich. Damit die anfallenden Datenmengen ausgewertet werden können, sind automatisierte und generell anwendbare Algorithmen nötig, welche aus den Eingabedaten mit minimalen Zusatzinformationen möglichst viele relevante Parameter in einer hohen raumzeitlichen Auflösung ableiten können.

Während bestehende Algorithmen einzelne Parameter aus einem Satellitenbild ableiten können, schliesst diese Doktorarbeit diese Lücke und zeigt auf, wie verschiedene glaziale und gletscherumgebende Parameter effizient aus Einzelbildern für drei Auslassgletscher mit unterschiedlichen Bewegungsverhalten abgeleitet werden können. Die im Rahmen dieser Arbeit betrachteten Gletscher *Eqip Sermia*, *Kangilerngata Sermia* und *Sermeq Kujalleq* befinden sich nördlich von *Ilulissat* in Westgrönland. Zur Validierung der Messungen wurde der Gletscher *Eqip Sermia* zusätzlich mittels GPS, Drohnen, einem terrestrischen Radarinterferometer und Wetterstationen vermessen.

Die im Rahmen dieser Doktorarbeit entwickelten Algorithmen erlauben eine automatisierte Extraktion der Gletscherfliessdynamik, der Lage der Gletscherfront, der von Oberflächenschmelze betroffenen Gletscherfläche und des Zustandes des Meereises vor der Gletscherzunge mit nur minimalen, frei verfügbaren Zusatzinformationen in hoher raumzeitlicher Auflösung. Die daraus entstandene kontinuierliche Zeitserie erlaubt es, saisonale respektive mehrjährige Dynamiken am Übergang

zwischen Gletscherzunge und Fjord zu erkennen und dabei die Interaktionen zwischen den einzelnen Parametern vertieft untersuchen zu können.

Structure and Contents

This dissertation contains four research publications reproduced in Chapters 2 to 5. For each publication, a short summary, the main findings and the author contribution are first provided. Overall, the thesis is divided into 7 different chapters as follows:

Chapter 1 introduces the scientific background and the related research questions of this thesis.

Chapter 2 analyzes the validity of glacier flow velocities derived from intensity tracking using spaceborne SAR data (Publication 1).

Chapter 3 presents a methodology to produce wide-area Analysis Ready Data (ARD) composite backscatter images (Publication 2).

Chapter 4 investigates the usability of the ARD composite backscatter images presented in the previous chapter to estimate melt onset over Arctic sea ice in 2016 and 2017 (Publication 3).

Chapter 5 demonstrates the methodology to automatically derive multiple glacial and glacier-proximal parameters from spaceborne SAR data (Publication 4).

Chapter 6 presents the main findings in view of the research questions formulated in Chapter 1.

Chapter 7 provides concluding remarks and an outlook on potential future research applications.

Table of Contents

Abbreviations

ARD Analysis Ready Data. vii, 4, 10, 11, 50, 61, 126, 127
ASCAT Advanced Scatterometer. 76, 79, 87–93, 127
AVHRR Advanced Very High Resolution Radiometer. 79

CQM Composite Quality Map. 58, 59, 61
CSA Canadian Space Agency. 68, 78, 82, 84, 90

DEM Digital Elevation Model. 16, 17, 29, 49, 50, 55, 57, 61, 80, 81
dGPS Differential Global Positioning System. 4, 14, 16, 131
DSM Digital Surface Model. 21, 25, 26, 52, 53

ESA European Space Agency. 15, 29, 32, 50, 68, 77
EW Extra Wide Swath. 60–62, 67, 78, 79

FYI First-Year Ice. 5, 77–79, 83–89, 91–93, 126

GCP Ground Control Points. 21
GFD Glacier Flow Dynamics. iii, v, 2–4, 8–12, 26, 125–129, 131–133
GIMP Greenland Ice Mapping Project. 16, 29
GPS Global Positioning System. 13–15, 17, 19, 20, 22–26, 29, 31, 33, 34, 38
GRDH Ground Range Detected High-resolution. 50, 52, 53, 55, 60, 65, 79
GRDM Ground Range Detected Medium resolution. 60, 79
GrIS Greenland Ice Sheet. iii, 1, 2, 5, 8, 14, 126
GSD Ground Sampling Distance. 20, 21
GTC Geometrically Terrain Corrected. 11, 49–51, 53–55

IMU Intertial Measurement Unit. 20
InSAR Interferometric SAR. 10, 15, 17
IW Interferometric Wide-swath. 16, 18, 50, 52, 53, 55, 60, 61, 67, 78, 79

LOS Line-of-Sight. 21, 25, 27, 28
LRW Local Resolution Weighting. 4, 11, 47, 49, 54–61, 64–66, 75, 76, 85, 92, 126, 127, 132

MODIS Moderate Resolution Imaging Spectroradiometer. 48, 49
MYI Multi-Year Ice. 5, 77, 78, 86–93, 126

PMW Passive Microwave. 79, 87, 88, 90–93, 126, 127, 132

RCM RADARSAT Constellation Mission. 2, 11, 61, 67, 76, 77, 93, 126, 133
RMSE Root Mean Square Error. 23
RS1 RADARSAT-1. 77
RS2 RADARSAT-2. 11, 13, 14, 16–19, 22, 24, 47, 61, 62, 67, 68, 75–80, 82, 84–87, 89, 90, 93, 125, 126, 131
RTC Radiometrically Terrain Corrected. 11, 50, 51, 53–57, 59, 61, 65, 80, 126

S1 Sentinel-1. iii, x, 3, 4, 9–13, 15, 16, 24, 26, 30, 32, 47, 49–56, 60, 61, 64, 67, 68, 75, 76, 79, 80, 99–101, 103–107, 110–112, 115, 117–119, 125–128, 131, 132
S1A Sentinel-1A. iii, v, 2, 14–22, 24, 26, 29, 31, 36–39, 57, 61–63, 65, 77, 78, 80–82, 85–87, 89, 93, 103
S1B Sentinel-1B. iii, v, 2, 14–16, 29, 61, 77, 78, 80–82, 85–87, 89, 93, 103
S2 Sentinel-2. 24, 109–114, 116–118, 128

SAR Synthetic Aperture Radar. iii, v, vii, ix, x, 2–4, 6, 9–27, 29–32, 39, 49, 56, 58, 60, 61, 67, 76–81, 83, 85, 86, 89, 93, 99–101, 103, 105, 107, 108, 125–129, 131–133
SAT Surface Air Temperature. 76, 79, 87, 88, 92, 93
SCWA ScanSAR Wide. 78
SLC Single Look Complex. 16, 18, 60
SMA Surface Melt Area. iii, v, 2–4, 12, 103, 115, 127–129, 132, 133
SNR Signal-to-Noise Ratio. 17–20, 22, 23, 27, 129
SRTM Shuttle Radar Topography Mission. 52, 53, 57, 63, 64

TRI Terrestrial Radar Interferometer. iii, v, 4, 13, 14, 16, 17, 21, 25–29, 33, 131

UAV Unmanned Aerial Vehicle. iii, 4, 13, 14, 16, 17, 20, 21, 23–26, 28, 29, 31–33, 36, 37, 39, 131
UF-W Ultra-Fine Wide. 16, 18

Chapter

1

Introduction

1.1 Context and Motivation

As the second largest ice mass on Earth, the Greenland Ice Sheet (GrIS) has a total sea level potential of 7.42 ± 0.05 m (Morlighem et al., 2017) and with its current ice mass losses of 260–380 $Gt \cdot a^{-1}$ represents a major component of the current global sea level rise (Enderlin et al., 2014; Shepherd et al., 2012). However, the projected range of global sea level rise over the next centuries diverges considerably between different climate scenarios (Aschwanden et al., 2019; Clark et al., 2016; Mengel et al., 2016). Regarding the current ice mass losses in Greenland, 30–50% can be attributed to runoff from *ocean-terminating (tidewater) outlet glaciers* (Cowton et al., 2018; Enderlin et al., 2014; Moon et al., 2015). This term refers to narrow, fast-flowing major drainage channels of ice sheets and polar ice caps that terminate in ocean fjords, calving off the ice as icebergs (Vieli & Nick, 2011). These glaciers have shown considerable changes within the last decades regarding thinning, acceleration, and rapid retreat in many parts of the world (Benn et al., 2007; Enderlin et al., 2014; Moon et al., 2012). In addition to their ice discharge through calving, losses through *in situ* melt, a process mainly influenced by atmospheric temperatures, also accounts for a large part of current ice mass losses (Cowton et al., 2018; Enderlin et al., 2014; Moon et al., 2015). Together, both mechanisms account for almost all (84%) of the increase in the rate of mass loss since 2009 (Enderlin et al., 2014). This increase can be attributed to the general warming trend in Greenland (the Arctic's atmospheric warming is projected to reach 2.2–8.3 °C until the end of the 21st century; IPCC, 2013) and the migration of subtropical water currents toward Greenland's coast (Straneo et al., 2013). Changes in the calving rate and routing also lead to changes in latent and sensible heat exchange, thereby influencing the oceanic climate system (Benn et al., 2007; Kenneally & Hughes, 2006).

Despite numerous studies, understanding of ocean-terminating glaciers' dynamics and their interactions with, e.g., oceanic, atmospheric, and topographic influences

remains limited (Catania et al., 2020; Straneo et al., 2013; Vieli & Nick, 2011). This lack of understanding continues to lead to significant uncertainties in the projected mass loss of the GrIS (IPCC, 2013; Nick et al., 2013; Straneo et al., 2013). Furthermore, differences between outlet glaciers concerning these interactions, including inter-annual variations, are likely to result in even more significant challenges (Moon et al., 2015).

According to Moon et al. (2015), the following mechanisms have been identified that may control changes in the near-terminus behavior of outlet glaciers:

1. Rigid sea ice and ice mélange (a mixture of sea ice and icebergs, also known as *sikkusak*; Jennings & Weiner, 1996) appear to suppress calving at the glacier terminus, allowing for terminus advance (Amundson et al., 2010; Howat et al., 2010; Joughin et al., 2008),
2. Terminus advance, retreat, and/or thinning influence velocity by changing the resistive stress caused by contact with the fjord walls and/or glacier bed (Howat et al., 2008, 2005; Pfeffer, 2007),
3. Warming subsurface ocean water and/or increased subglacial runoff may increase below-surface ice melt at the terminus, affecting terminus stability (Holland et al., 2008; Motyka et al., 2011; Rignot et al., 2010; Sciascia et al., 2013),
4. The position of the terminus relative to basal topography (e.g., overdeepening or sills) influences rates of retreat for a given forcing (e.g., Enderlin et al., 2013a,b; Joughin et al., 2012b; Oerlemans & Nick, 2005).

While direct measurements of resistive forces from the glacier bed and/or the surrounding topography (cf. items 2 and 4) as well as changes in below-surface melt (cf. item 3) are difficult to acquire, other parameters such as Glacier Flow Dynamics (GFD), the ice conditions in the proglacial fjord, Surface Melt Area (SMA) or the front position *can* be measured. However, due to Greenland's remoteness, continuous *in situ* measurements of such glacial and glacier-proximal parameters are not only logistically difficult but also expensive, resulting in data gaps, predominantly in the winter. Remote sensing data can be and are used to overcome these challenges. As optical sensors (e.g., Landsat, ASTER, MODIS) depend passively on the availability of sunlight, the long polar winter and cloud cover are frequent causes of data gaps similar to those from *in situ* measurements. By supplying their own illumination, active satellite systems (e.g., Synthetic Aperture Radar; SAR) do not rely on the availability of sunlight and are not affected by cloud cover. Therefore, they offer a temporally significantly more reliable series of measurements.

With the launch of Sentinel-1A (S1A) in 2014 and Sentinel-1B (S1B) in 2016, the availability of openly and freely available data sets increased significantly, resulting in a coverage of Europe once every six days and 12 days nearly globally with the two-satellite constellation. Coverage is more frequent at polar latitudes such as Greenland, ranging from 4 to 2 days per satellite (Torres et al., 2012). In combination with additional data sets, e.g., from SAR constellations such as the RADARSAT Constellation Mission (RCM), the temporal resolution of acquisitions could increase even further (Dabboor et al., 2018), allowing for high spatial and temporal resolutions and continual measurement time series.

While publications and data sets exist, which are investigating *individual* glacial and glacier-proximal parameters of outlet glaciers in Greenland over longer time periods, these studies offer insights into the state of parameters on a regional or

ice-sheet level, thereby focusing on a lower spatial or temporal resolution. Examples of such studies are:

- GFD: Fried et al., 2018; Howat et al., 2010; Joughin, 2021; Moon et al., 2015,
- Sea-ice/mélange condition: Carr et al., 2017; Fried et al., 2018; Howat et al., 2010; Moon et al., 2015,
- Runoff: Cowton et al., 2018; Fried et al., 2018; Moon et al., 2015,
- Terminus position: Carr et al., 2017; Catania et al., 2018; Cheng et al., 2021; Cowton et al., 2018; Fried et al., 2018; Lea et al., 2014; Moon & Joughin, 2008; Moon et al., 2015.

The lower resolution of these ice-sheet wide products means that they are not easily suited for analyzing the immediate *interaction* of the glacier's terminus with the proglacial fjord. Furthermore, integrative, long-term studies investigating the interaction between multiple parameters and over varying time scales are lacking (Moon et al., 2015).

To improve our understanding of ocean-terminating glaciers' dynamics and to better constrain current calving models, long-term studies focusing on *interactions* between different forcings are needed. This thesis closes this gap by demonstrating how multiple glacial and glacier-proximal parameters can be derived efficiently from individual or series of SAR data sets for three medium-sized outlet glaciers that exhibit differing movement behaviors. The algorithms developed allow an automated, temporally quasi-continuous extraction of GFD, the location of the glacier front, the glacier area affected by surface melt (SMA), and the composition of the ice in front of the glacier tongue with only minimal, freely available additional information, all at high spatial and temporal resolutions.

1.2 Objectives and Research Questions

This thesis aims to improve the understanding of calving glacier dynamics by providing new approaches to derive year-round measurements of multiple glacial and glacier-proximal parameters at the high spatial and temporal resolutions needed to further constrain current calving models. Therefore, we present methodologies to facilitate and automate the extraction of four parameters from Sentinel-1 (S1) SAR data sets and link their observed patterns with external forcings throughout a multi-year time series. The results enable new constraints to improve current calving models and thereby help to reduce uncertainties regarding the projected range of global sea level rise.

In this dissertation, three research questions are asked addressing the motivation and research gaps, which resulted in two first-author and two co-author publications.

> *1) How can we improve the resolution of steep velocity gradients in the area of a glacier's terminus using SAR intensity tracking, and how can these derived products be used to give better estimates of ice fluxes and the mass budget?*

This question is essential for improving the estimate of ice fluxes and the mass budget. Ice fluxes are commonly calculated using the flux-gate approach, whereby

fluxes are estimated using surface velocity observations to approximate horizontal, depth-averaged ice velocity (Osmanoğlu et al., 2013). Given that operational GFD products such as MEaSUREs (Joughin, 2021) or the Greenland Ice Sheet CCI Ice Velocity (Nagler et al., 2015) focus on GFD on an ice sheet scale, they operate at a lower spatial resolution and are therefore unable to capture the steep velocity gradients present in the area of a glacier's terminus. To validate the iterative offset tracking approach adjusted to capture these steep velocity gradients, we used *in situ* measurements from Differential Global Positioning System (dGPS) stations, a Terrestrial Radar Interferometer (TRI) and repeated Unmanned Aerial Vehicle (UAV) surveys. We assessed the agreement of our derived SAR velocity fields with the *in situ* data and compared it with existing operational GFD products. This research has been published in Rohner et al. (2019) and is presented in chapter 2.

> *2) How can SAR data sets from different sensors and orbital tracks be integrated into a single backscatter composite, and how can a time-series of these composites be used to estimate the timing of melt onset over Arctic (sea) ice?*

This question focuses on the ability to analyze wide-area thematic effects such as the presence of liquid water in snow and surface melt in ice. Therefore, the availability of normalized data sets at high spatial and temporal resolutions is a prerequisite. Despite improvements in the availability of freely and openly available SAR data sets, thematic investigations of large areas continue to be impaired due to terrain-induced distortions and local resolution effects in the SAR data, even when using so-called terrain corrected Level 1 backscatter data. In chapter 3 (Small et al., 2022) we demonstrate the possibility of seamlessly integrating SAR data sets from different sensors and multiple orbits into a single, wide-area Level 3 Analysis Ready Data (ARD) composite product. Further, in chapter 4 (Howell et al., 2019) we assess these Local Resolution Weighting (LRW) composites to estimate melt onset over arctic sea ice and compare their retrievals against lower-resolution scatterometer and passive microwave data.

> *3) How can we continuously, automatically, and efficiently derive multiple glacial and glacier-proximal variables from S1 SAR time series, and how do these parameters interact?*

This research question builds on research questions one and two, and implements methodologies to facilitate and automate the extraction of several glacial and glacier-proximal parameters (GFD, SMA, presence and development of ice mélange, and terminus position) from individual SAR amplitude data sets, thereby circumventing the drawbacks of optical platforms. Looking at the three outlet glaciers, we demonstrate the feasibility of the methodologies providing quasi-continuous time series at high spatial and temporal resolutions in chapter 5 (Rohner et al., 2022).

1.3 Study Areas

In order to answer these questions, our research focused on two locations. Research questions 1 and 3 were investigated based on multiple glaciers in Western Greenland, namely *Eqip Sermia* (69° 48′ N, 50° 14′ W), *Kangilerngata Sermia* (69° 54′ N, 50° 20′ W) and *Sermeq Kujalleq* (70° 00′ N, 50° 14′ W), located north of *Ilulissat* (cf.

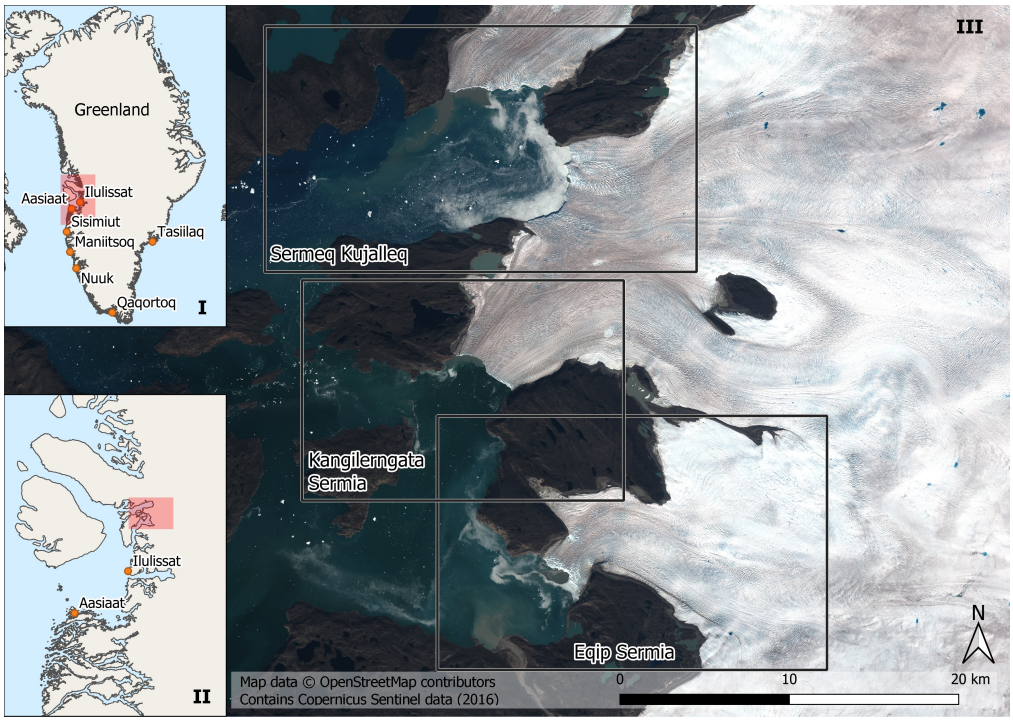

Fig. 1.1: Overview of *Eqip Sermia*, *Kangilerngata Sermia*, and *Sermeq Kujalleq*

Fig. 1.1). These three medium-sized ocean terminating outlet glaciers are located within 30 km, thus exhibiting little differences in the prevailing climatic conditions. Geometrically, *Kangilerngata Sermia* and *Sermeq Kujalleq* are similar, exhibiting near vertical calving fronts of around 100 m freeboard. *Eqip Sermia* differs partially, with the grounded northern lobe exhibiting a 200 m high inclined calving face with slope angles exceeding 45° and a southern lobe featuring a vertical ice cliff of about 50 m freeboard (Mercenier et al., 2018).

Research question 2 was investigated in the region of Ellesmere Island, Nunavut, located in the Northern Canadian Arctic (cf. Fig. 1.2). As a result of its location between 76° N and 83° N, Ellesmere Island features landfast First-Year Ice (FYI) and Multi-Year Ice (MYI) as well as drifting MYI in the Arctic Ocean (Howell et al., 2019). Furthermore, its heavily fjorded coast is perfectly suited to investigating the sensitivity of different products of varying resolutions to change (Howell et al., 2019).

1.4 Scientific Background

As laid out in section 1.1, calving and *in situ* melt together account for the majority of current ice mass losses in Greenland, which contribute substantially to the current global sea level rise (Cowton et al., 2018; Enderlin et al., 2014; Moon et al., 2015). To better understand and predict the changes for the whole GrIS, the influencing factors for dynamic mass loss (i.e., mass lost through ice discharge into bodies of water; Bollen et al., 2022) and surface processes and thus the complex interactions between different forcings on an individual glacier level first need to be better constrained (Joughin et al., 2012a; Straneo et al., 2013). This chapter presents these fundamental influencing factors of dynamic mass loss, surface processes,

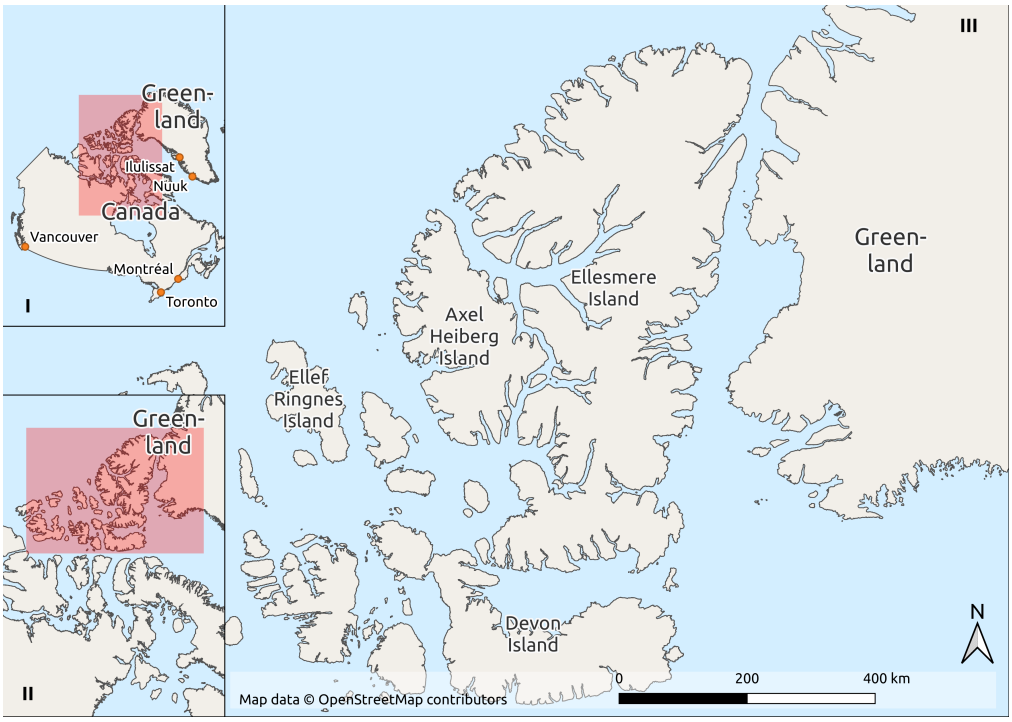

Fig. 1.2: Overview of Ellesmere Island, Canada

and current observational methods using SAR satellite data to quantify glacial and glacier-proximal parameters and the limitations in estimating them from SAR.

1.4.1 Influencing Factors for Dynamic Mass Loss

Calving is a phenomenon that can be observed in various climatic environments. It occurs when a floating or grounded glacier terminus releases blocks of ice into a proglacial body of water, either fresh- or tidewater (Benn et al., 2007; van der Veen, 2013). As a result of the variety of possible environments, the calving processes differ significantly between individual glaciers (Benn et al., 2007; van der Veen, 2013). Despite the variation between individual calving glaciers, four principal processes can be identified that allow fracture propagation at the glacier terminus and thus can trigger calving events (Benn et al., 2007). In general, stretching in response to large-scale velocity gradients (cf. section 1.4.1a) is the first-order mechanism, with force imbalances and undercutting by subaqueous melting (cf. sections 1.4.1b and 1.4.1c) second-order influences, while subaqueous calving (cf. section 1.4.1d) is a third-order mechanism (Benn et al., 2007; Krug et al., 2014). However, the order of these mechanisms can differ between glaciers and is strongly influenced by the velocity gradients at the grounding line, and their control of the calving rate or terminus position is a subject of debate (Benn et al., 2007; van der Veen, 2013).

In the following, the four mechanisms listed above, as discussed in Benn et al. (2007), are briefly presented.

1.4.1a Stretching in response to large-scale velocity gradients

As a result of high velocity gradients on the glacier, crevasses form, penetrating through the glacier (cf. Fig. 1.3 (a)). These velocity-gradient induced crevasses are typical for glaciers with grounded calving margins (Benn et al., 2007; Vieli

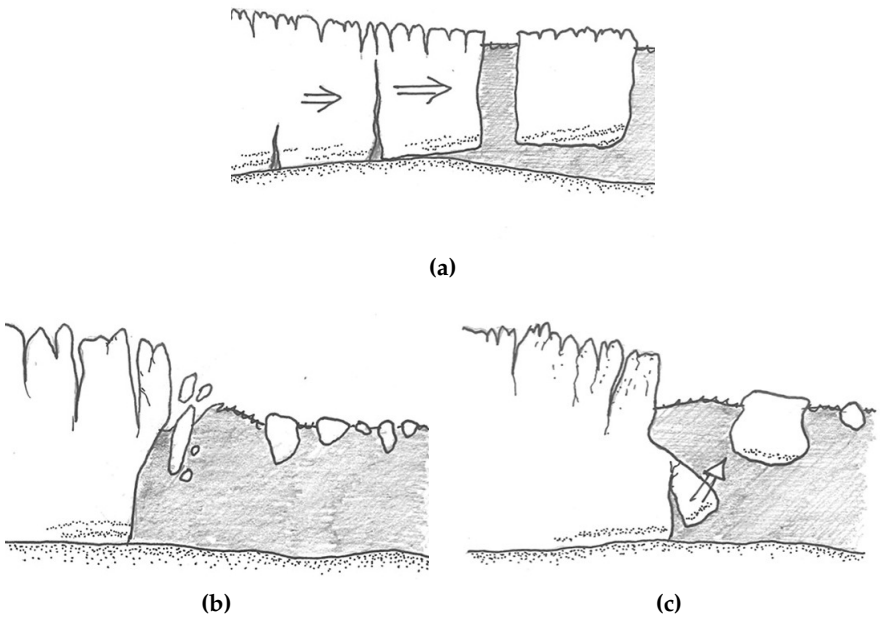

Fig. 1.3: Selection of calving mechanisms: (a) crevasse formation due to large-scale velocity gradients, (b) undercutting by subaqueous melting, resulting in an oversteepened ice cliff, (c) calving due to buoyant forces. Adapted from Benn & Åström (2018)

et al., 2000), and result in a weakening of the ice close to the glacier terminus, thus influencing the position and geometry of the calving front (Powell, 1983). Furthermore, the presence of liquid water (from e.g. surface melt) strongly influences the crevasse depth by opposing the cryostatic pressure, enabling crevasses to propagate downward as far as the glacier bed (Benn et al., 2007; van der Veen, 1998, 2013).

1.4.1b Force imbalances at unsupported ice cliffs

In the contact zone between the calving front and the proglacial water body, calving is governed by the opposing forces of water/air pressure and the cryostatic pressure of the calving front (Benn et al., 2007; Reeh, 1968). As a result of the significant differences between the air pressure acting against the cryostatic pressure of the calving front above the waterline and the respective water pressure at the parts of the calving front below the waterline, the outward acting force of the calving front is maximal at the waterline (Benn & Åström, 2018; Benn et al., 2007). As a consequence, the forward and downward acting rotation of the ice causes tensile and shear stresses, resulting in surface fractures of the glacier's terminus, thus facilitating calving (Benn et al., 2007; Reeh, 1968).

1.4.1c Undercutting by subaqueous melting

As a result of differences in the magnitude of the melt rates above (subaerial) and at or below the waterline (subaqueous), the calving front can be undercut, leading to increased calving. In case of enhanced melting at the waterline, the subaerial ice cliff will be overhanging a notch at the waterline; in the case of increased subaqueous melting, the calving front will overhang an oversteepened subaqueous ice cliff (cf. Fig. 1.3 (b); Benn et al., 2007). These overhangs lead to stresses within the ice, thereby encouraging calving (Benn et al., 2017, 2007; Vieli & Nick, 2011). As a result, the temperature and density structure of the water as well as the circulation patterns at the water-ice interface influence the rate of calving, especially so due

to the buoyant ascent of meltwater discharged from subglacial drainage systems (Benn & Åström, 2018; Benn et al., 2017, 2007; Jenkins, 2011; Slater et al., 2016).

1.4.1d Torque arising from buoyant forces

While calving in the mechanisms presented in sections 1.4.1a to 1.4.1c are a result of gravity, it can also be caused by buoyant forces acting on ice below the waterline (cf. Fig. 1.3 (c); Benn & Åström, 2018; Benn et al., 2017, 2007). A prerequisite for this type of calving is ice, in which the gravitational forces acting on it are smaller than the buoyant forces of the water surrounding the ice, thereby causing fracture propagation and, finally, calving failure. Benn et al. (2007) lists two principal causes for this force imbalance:

- Development of an ice foot due to enhanced subaerial melt,
- Basal/surface melt or longitudinal/transverse extension, leading to a thinning and thus buoyancy of previously grounded glacier termini.

1.4.2 Glacier Flow Dynamics

Given the mechanisms presented in section 1.4.1, the interconnection between ice flow velocity and calving is apparent. Nevertheless, there is a debate concerning whether or not changes in calving intensity are a cause or consequence of changes in the ice flow velocity (Benn et al., 2007; Vieli et al., 2001). Two schools of thought exist on the subject: while one perceives calving as the "driver" (calving causing dynamic changes upstream, including an acceleration of ice flow velocity; Benn et al., 2007; Hughes, 1986; Meier & Post, 1987), the other looks at it as the "response", whereby dynamic and geometrical changes of a glacier result in an acceleration of ice flow and thinning, causing increased calving activity (Benn et al., 2007; van der Veen, 2013). Independent of this discourse, knowledge of GFD is a crucial parameter for estimating the calving rate, a major factor in mass loss (Howat et al., 2007; van der Veen, 2002). In this context, the calving rate is defined as the ice velocity at the terminus minus the rate of change of the terminus position (Vieli et al., 2001).

The GFD accounts for roughly half of GrIS's mass loss, mainly through a rapid speedup, retreat, and thinning of outlet glaciers (Moon et al., 2012; Straneo et al., 2013). Despite a generally accelerating trend for ice loss from Greenland's fast-flowing marine-terminating glaciers, glaciers appear to be affected by a wide range of local factors (Howat et al., 2005; Moon et al., 2012; Nick et al., 2012), sometimes resulting in an asynchronous behavior between neighboring glaciers (Moon et al., 2012). These often interlinked influencing factors can be grouped into topographic (fjord, glacier, and bed geometry), climatological, and oceanographic factors (small-scale ocean water flow and terminus sea ice conditions; Moon et al., 2012; Vieli, 2015; Vieli et al., 2001).

1.4.2a Topographical influencing factors

The topography surrounding a glacier, such as the fjord, glacier, and glacier bed, is the most obvious factor influencing the GFD (Benn et al., 2007; Moon et al., 2012; Vieli et al., 2001). Firstly, for grounded glaciers, GFD is strongly influenced by the relation between water depth and height above freeboard of the calving front, with the water depth being dependent on the basal topography (Mercenier et al., 2018). Further, basal drag is influenced by resistive stresses due to subglacial undulations

(form drag; van der Veen, 2013) as well as the forces of friction between the moving ice and the bed (skin drag; van der Veen, 2013), with the latter being controlled by basal water pressure (Iken, 1981; Vieli et al., 2001). Unlike basal drag, lateral drag, i.e., the drag originating at a glacier's margin, has an upper limit, as most glaciers are much wider than they are deep, limiting the (relative) area over which lateral drag acts (van der Veen, 2013). Finally, the presence of a submarine frontal moraine (Vieli et al., 2001) not only exerts back pressure, but, in the case of a glacier's recession into a basal overdeepening, may also cause a rapid retreat instigated by a retreat instability, the process of increased mass loss through calving and thus an unstable retreat (Vieli, 2015).

1.4.2b Climatological influencing factors

In their paper, Meier & Post (1987) assumed an indirect relationship between climate fluctuations and cyclic advances and retreats of a glacier (Vieli, 2015). With increased air temperatures due to climate change, larger amounts of surface meltwater can penetrate the glacier through crevasses and reach the glacier bed, resulting in an evacuation of this water through the glacier's drainage system. Despite the persistent lack of a complete theory of the flow of water beneath a glacier (van der Veen, 2013; Weertman, 1972), a subglacial drainage system's efficiency is assumed to strongly control the basal water pressure (van der Veen, 2013). In cases of inefficient drainage or increasing amounts of meltwater, basal water pressure builds up, reducing the basal friction and increasing basal flow speeds (cf. section 1.4.2a; Iken, 1981; van der Veen, 2013).

1.4.2c Oceanographic influencing factors

In addition to the effects described in section 1.4.2b, increasing air temperatures cause secondary effects as well, which in turn influence the GFD. First, higher air temperatures increase the temperature of the proglacial body of water, elevating the calving rate through the mechanisms presented in section 1.4.1c. Second, higher water and air temperatures also influence the presence and persistence of ice mélange in the proglacial body of water. As pointed out by, among others, Joughin et al. (2008), Amundson et al. (2010), and Howat et al. (2010), ice mélange as a nearly rigid mass can almost entirely suppress calving and enables the advance of a glacier's terminus while ice mélange is present. By extension, higher air and water temperatures and a resulting shortening of the duration of ice mélange presence might allow a higher calving rate, influencing a glacier's GFD during the winter season.

1.4.3 SAR for Glaciological Research

The increase in availability of freely and openly available SAR data following the launch of the S1 constellation enables scientists to measure glacial and glacier-proximal parameters at high spatial and temporal resolutions. In combination with the dependable, systematic, pre-programmed and conflict-free SAR image data flow of the S1 constellation (Torres et al., 2012), a quasi-continuous derivation of glacial and glacier-proximal parameters at high spatial and temporal resolutions became possible. In addition to the dependability of SAR systems due to their independence from weather and reflected sunlight, unique characteristics of SAR systems allow the derivation of data sets that would be not be possible with optical satellites. One of these characteristics is the ability of SAR to penetrate into a

terrain surface. The penetration depth of microwave radiation is a function of the wavelength used, the polarization, the incidence angle of the radiation, and the object properties, especially liquid water content. Furthermore, SAR sensors not only measure the intensity (*amplitude*), but also the *phase* of the signal scattered back to the sensor from the landscape (Richards, 2009). Both of these measurements can be used for glaciological research, either by using image statistics with the amplitude information or by combining the phase information of image pairs for interferometric analyses. In the following, the derivation of glacial and glacier-proximal parameters relevant for GFD is presented.

1.4.3a GFD from SAR for Fast Flowing Calving Glaciers

With the aforementioned increase in freely available SAR data sets that can be used for interferometry (Interferometric SAR; short: InSAR), the measurement of GFD in polar regions using well-established InSAR methodologies is performed at accuracies of a few $m \cdot a^{-1}$ at high spatial and temporal resolutions (Rohner et al., 2019). However, measuring the GFD by means of InSAR is limited to slow-moving glaciers with a reported upper limit for satellites e.g. at a 24 day repeat cycle of 200 $m \cdot a^{-1}$ (Gray et al., 1998; Joughin, 2002). This upper limit is caused by phase decorrelation due to a lack of coherence and/or rapid flow, or changes in meteorological conditions (Gray et al., 2001; Strozzi et al., 2002). In view of the interconnection between the near-terminus GFD and calving intensity (cf. sections 1.4.1a and 1.4.2), the focus is on the fast-moving part of the glacier close to the calving terminus, where ice velocities of multiple $m \cdot d^{-1}$ can be expected, severely reducing the usability of InSAR, even given a 6 day repeat-orbit of the S1 constellation. As an alternative approach to derive the GFD from SAR amplitude data, the offset tracking methodology was introduced to SAR by Fahnestock et al. (1993), Gray et al. (1998), Michel & Rignot (1999) and Joughin (2002). Using the speckle pattern of an image pair and cross-correlating it, offset tracking is not as sensitive to decorrelation as InSAR (Joughin, 2002; Luckman & Murray, 2005). By using offset tracking and adapting the parameters to the expected high velocities of the glacier's terminus, the GFD can be reliably derived in these fast-flowing parts of the glacier based on SAR amplitude image pairs (Joughin, 2002; Luckman & Murray, 2005; Rohner et al., 2019).

1.4.3b SAR ARD Products for Melt Onset Estimation

As presented in section 1.4, the presence and extent of ongoing melt processes in polar regions are highly relevant for understanding and predicting changes in response to a changing climate. Previously, passive microwave and scatterometer data have been used to retrieve melt onset dates in the arctic region. Traditionally, the high temporal resolution of 1 day in the case of passive microwave sensors (Belchansky et al., 2004; Drobot & Anderson, 2001), and 1-2 days in the case of scatterometer data was leveraged (Mortin et al., 2014). However, these data sets have a low spatial resolution of multiple kilometers, making small-scale analyses of the melt extent's spatial distribution impossible. With SAR, a technology capable of detecting changes in the presence of liquid water in snow or ice at high spatial resolution is available and has been used for such investigations (Bernier, 1991; Kwok et al., 2003; Livingstone et al., 1987; Mätzler, 1987). Unfortunately, the nature of SAR data makes its use challenging because of, among other reasons, the poorer temporal resolution in comparison to the aforementioned passive microwave and scatterometer data as well as inconsistencies regarding the imaging geometry

caused by the off-nadir viewing direction, resulting in terrain-induced effects like foreshortening, shadowing and layover (Howell et al., 2019; Small, 2011). These challenges have meant that thematic investigations of large areas was impaired, even when using terrain corrected Level 1 (NASA, 1986) SAR backscatter data.

In contrast to optical sensors, composited ARD (Level 3; NASA, 1986) SAR products are not widely available. For thematic investigations, a Radiometrically Terrain Corrected (RTC) product often needs to be calculated first (Small, 2011; Small et al., 2022), based on a terrain model rather than an ellipsoidal Earth model as used in Geometrically Terrain Corrected (GTC) SAR products (Small, 2011). By applying the RTC normalization, changes in the recorded brightness values as a result of differences in viewing geometries and scattering mechanisms as well as scattering effects from adjacent raster cells can be addressed. This RTC normalization enables time-series investigations for thematic questions (Small, 2011). In order to mitigate terrain-induced effects such as foreshortening, layover, and shadowing in rugged terrain and address coverage issues, a combination of SAR data from multiple imaging geometries is necessary. Using the LRW methodology presented in chapter 3, a combination of these different imaging geometries, even acquired from multiple platforms (e.g. S1 and RADARSAT-2 (RS2)) becomes possible (Howell et al., 2019). Using these ARD data sets and leveraging the differences in dielectric values between liquid water (high dielectric values) and ice (low dielectric values), a wide-area estimation of melt-onset at a high spatial and temporal resolutions becomes possible (Howell et al., 2019; Small et al., 2022; Woodhouse, 2006).

1.4.3c Automated Extraction of Glacial and Glacier-proximal Parameters from SAR Amplitude Data

As shown in section 1.4.2, in addition to knowledge of the GFD and surface melt, changes in (a) the terminus position or (b) the presence and development of ice mélange at intra- and inter-annual time-scales are of relevance to better constrain current calving models (Amundson et al., 2010; Howat et al., 2010; Moon et al., 2015).

As mentioned in section 1.1, many publications have used remote sensing data to derive glacial and glacier-proximal parameters. Due to the inherent limitations of optical data, data sets derived from such sensors usually exhibit large data gaps, especially during winter. Automated derivation of parameters like terminus position and the presence and development of ice mélange from SAR data sets is presently uncommon and usually achieved by manually digitizing the parameters of interest. In the case of estimation of the terminus position, a few automated derivation algorithms have been published, often using computationally demanding deep-learning algorithms (e.g. Cheng et al., 2021). Operational products exist but are limited in either temporal resolution, coverage, or both (e.g. Andersen et al., 2019; ENVEO, 2017; Joughin et al., 2015).

Regarding the presence and development of ice mélange in the proglacial fjord, most publications rely on manually categorizing and digitizing the ice (e.g. Fried et al., 2018; Howat et al., 2010). Moon et al. (2015) applied a hybrid approach, using the coherent movement of the ice mélange detectable through offset tracking and a manual approach in case of incoherent movement. In their paper, Carr et al. (2017) used ice concentration from the U.S. National Ice Center, that originate from a variety of remote and *in situ* measurements, but lack the temporal resolution that SAR constellations such as S1 or RCM can provide.

As a result of the lack of operational, automatically derived, and quasi-continuous time series of retrievals of the terminus position and the presence and development of ice mélange in the proglacial fjord and given that we already use S1 SAR data to derive the GFD and SMA, we developed methodologies to derive these two parameters in an automated manner based on image statistics. These methodologies result in an efficient derivation with only a minimal need for freely and openly available *a priori* data such as temperature data and outlines of the lateral proglacial moraine (cf. chapter 5).

Chapter

2

Paper 1: Multisensor validation of tidewater glacier flow fields derived from synthetic aperture radar (SAR) intensity tracking

Rohner, C., Small, D., Beutel, J., Henke, D., Lüthi, M.P., & Vieli, A.

This chapter is based on the peer-reviewed article:
Multisensor validation of tidewater glacier flow fields derived from synthetic aperture radar (SAR) intensity tracking.
The Cryosphere, 2019, 13(11), 2953–2975.
doi: 10.5194/tc-13-2953-2019.
and is reprinted as the final submitted manuscript.
It has been modified to fit into the layout of this thesis.

C.R. designed the paper with support of D.S., D.H., and A.V.. **C.R.** generated the flow fields, processed the UAV data and performed all analysis. D.S. prepared the processing of the Sentinel-1 and RADARSAT-2 data. M.P.L. performed TRI measurements and processing. J.B. prepared the GPS devices and processed the GPS data. **C.R.** wrote the draft of the paper. **All authors** contributed to the final version of the paper.

Abstract

Following the general warming trend in Greenland, an increase in calving rates, retreat and ice flow has been observed at ocean-terminating outlet glaciers. These changes contribute substantially to the current mass loss of the Greenland Ice Sheet. In order to constrain models of ice dynamics as well as estimates of mass change, detailed knowledge of geometry and ice-flow are needed, in particular on the rapidly changing tongues of ocean-terminating outlet glaciers. In this study, we validate velocity estimates and spatial patterns close to the calving terminus of such an outlet derived from an iterative offset tracking method based on SAR intensity data with a collection of three independent reference measurements of glacier flow. These reference data sets are comprised of measurements from dGPS, a TRI and repeated UAV surveys. Our approach for the SAR-velocity processing aims at achieving a relatively fine grid spacing and a high temporal resolution in order to best resolve the steep velocity gradients in the terminus area and to exploit the 12 day repeat interval of the single-satellite S1A sensor. Results from images of the medium-sized ocean terminating outlet glacier *Eqip Sermia* acquired by S1A and RS2 exhibit a mean difference of 11.5% when compared to the corresponding Global Positioning System (GPS) measurements. An areal comparison of our SAR velocity-fields with independently generated velocity maps from TRI and UAV showed a good agreement in magnitude and spatial patterns, with mean differences smaller than 0.7 md^{-1}. In comparison with existing operational velocity products, our SAR-derived velocities showed an improved spatial velocity pattern near the margins and calving front. There 8% to 30% higher surface ice velocities are produced, which has implications on ice fluxes and on mass budget estimates of similar sized outlet glaciers. Further, we showed that offset tracking from SAR intensity data at relatively low spatio-temporal sampling intervals is a valid method to derive glacier flow fields for fast-flowing glacier termini of outlet glaciers and, given the repeat period of 12 days of the S1A sensor (6 days with S1B), has the potential to be applied operationally in a quasi-continuous mode.

2.1 Introduction

As a result of the general warming trend in Greenland and the migration of subtropical water currents toward Greenland's coast, ice loss by submarine melt and iceberg calving – a process neither well understood nor well represented in the current generation of ice-sheet models – is increasing (Straneo et al., 2013). The related dynamic mass loss is expected to further intensify in the future, thereby strongly contributing to global sea level rise (IPCC, 2013; Nick et al., 2013). The increase in calving activity is related to substantial terminus retreat, thinning and speed-up. Over the past two decades, such flow acceleration has exceeded 30% for many of the GrIS outlet glaciers in the northeast and southwest (Moon et al., 2012; Rignot et al., 2008; Wood et al., 2018). Regarding the future of the GrIS in context of climate change, detailed and repeated observations of flow velocities of tidewater outlet glaciers are crucial for assessing the mass budget of the GrIS, for better understanding the mechanisms behind dynamic mass loss and for developing and constraining predictive flow models (Vieli & Nick, 2011).

Due to the remoteness of the Arctic region, *in situ* measurements are not only expensive and logistically difficult, but also limited in spatial and temporal coverage (Euillades et al., 2016; Joughin, 2002). In addition, the operational use of optical remote sensing to measure flow dynamics is limited by the availability of sunlight during the long polar winter as well as cloud cover. The launch of S1A by the European Space Agency (ESA) in 2014 and S1B in 2016 drastically increased the availability of active remote sensing data (i.e. SAR). Independent of the availability of sunlight and unaffected by cloud cover, SAR systems are able to circumvent the aforementioned drawbacks of passive (optical) systems, allowing for spatially and temporally quasi-continuous measurements of the ice sheets' flow dynamics as well as many other cryospheric parameters (Dowdeswell et al., 1999; Joughin et al., 2016). Our velocity processing is therefore focused on SAR imagery and specifically on the S1 sensor, as a 12 day repeat image acquisition of relatively high spatial resolution (2.3×14.1 m) is already operational (6 days with S1B; cf. section 2.2.1).

Using SAR systems, flow velocities can be estimated using either repeat-pass interferometry (InSAR) or offset tracking approaches. As reported by Michel & Rignot (1999) and Joughin (2002), fast moving glaciers in combination with relatively long repeat cycles can cause difficulties concerning the maintenance of coherence, limiting the InSAR-based velocity estimation to slow-moving areas, reducing the use of this approach close to the glaciers' termini. Furthermore, the presence of surface melt and high strain rates near the glacier's terminus reduces the usability of InSAR for velocity estimation. The offset-tracking methodology laid out by Scambos et al. (1992) and Frezzotti et al. (1998) for optical data and by Fahnestock et al. (1993), Gray et al. (1998), Michel & Rignot (1999) and Joughin (2002) using SAR imagery offers an alternative approach for velocity estimation. Relying on cross-correlating the speckle patterns of an image pair, offset-tracking is not as sensitive to decorrelation as InSAR and therefore allows derivation of flow dynamic parameters even in faster moving parts of the glacier (Joughin, 2002; Luckman & Murray, 2005). Despite the widespread use of SAR datasets for derivation of flow velocities (e.g. Gray et al., 2001; Lemos et al., 2018), fewer studies have been devoted to analysing the accuracy in magnitude and spatial patterns of the derived flow velocity products compared to in-situ measurements, in particular close to the calving terminus (e.g. Joughin et al., 2018a; Nagler et al., 2015). In view of the use of such SAR-derived velocities for mass change assessments, calving-process studies or as model constraints, a comprehensive evaluation of the performance, uncertainties and drawbacks of this spaceborne method is crucial.

Of the number of articles analysing the validity of velocity products derived from SAR sensors, almost all focus on results using the interferometric approach (e.g. Goldstein et al., 1993; Gray et al., 1998; Rignot et al., 1995), therefore limited to slow-moving areas. With respect to the use of intensity tracking to derive flow velocities, only a small number of articles validated the results against *in situ* measurements (e.g. Fallourd et al., 2011; Schellenberger et al., 2015; Schubert et al., 2013), all focusing on glaciers reaching a maximum of $<3\,\mathrm{md}^{-1}$. The works of Ahlstrøm et al. (2013, ALOS/PALSAR, TerraSAR-X/Tandem-X data) and Boncori et al. (2018, ALOS/PALSAR, ASAR, and ERS-1/-2 data) looked at both, interferometric and offset tracking approaches in combination with GPS measurements.

In this paper, we are investigating the limits of offset tracking methods and demonstrate that accurate estimates are possible even close to the calving front when choosing appropriate template sizes. As validation datasets, for the derived flow velocity information (magnitude and spatial pattern) we use field measurements

based on three independent methods, namely dGPS, a TRI, and high resolution imagery from an UAV. The glacier studied is *Eqip Sermia*, a medium sized marine-terminating outlet glacier in the southwest of Greenland (cf. Fig. 2.1). We demonstrate that flow velocity estimates generated at a relatively fine ground sampling distance are more accurate close to the glacier's terminus compared to operational, ice-sheet wide ice velocity products which tend to underestimate the glacier's dynamics and thus also the calving flux.

2.1.1 Study Area

For this study, the medium-sized ocean terminating outlet glacier of *Eqip Sermia* (69°48′ N, 50°13′ W), located in Western Greenland, was observed by multiple sensors. Given the available historical geometry and flow velocity survey data, dating back to 1912 (e.g., de Quervain & Mercanton, 1925), *Eqip Sermia* offers ideal preconditions. *Eqip Sermia* has a calving front roughly 3.5 km wide and 30–200 m high. The long-term flow speed at the terminus was stable for almost a century at about 3 md^{-1} (Bauer, 1968), followed by an acceleration towards the end of the 20^{th} century. Between 2000 and 2005, *Eqip Sermia* accelerated by 30% as well, doubling the discharge (Kadded & Moreau, 2013; Lüthi et al., 2016; Rignot & Kanagaratnam, 2006). More detailed velocity fields from the recent decade (Joughin et al., 2008, 2010) indicate strong spatial variations in flow in the terminus area and a strong acceleration towards the calving front (Catania et al., 2018; Lüthi et al., 2016).

2.2 Data and Methods

2.2.1 SAR Data

The increasing availability of freely and openly available SAR data over the ice sheets at high spatial and temporal resolutions allows circumvention of acquisition issues intrinsic to optical systems that have been available for several decades. Making use of the all-weather, day/night imaging capabilities of SAR sensors, cloud cover or illumination effects do not interfere with the acquisition schedule. The source data consists of a dual-pol (HH/HV) Sentinel-1A/B Single Look Complex (SLC) C-band (5.405 GHz) time series starting in October 2014, accessed through the Copernicus Open Access Hub (Torres et al., 2012). Out of these more than 200 acquisitions, 5 scenes complement ground measurement data acquired during a field campaign that took place in August 2016. These S1A satellite products have a 12-day repeat cycle and all interferometric wide swath (IW-mode) SLC products used were acquired from the same ascending relative orbit (cf. table 2.1). After this validation campaign, the S1B satellite was commissioned, lowering the S1 repeat interval to 6 days. In addition to the S1A data sets, a total of 20 RS2 acquisitions were made available through the Science and Operational Applications Research Program (Project CSA-SOAR-EU-16821). Based on this allowance, two SLC scenes were acquired using RS2's Ultra-Fine Wide (UF-W) mode operating also at the frequency of 5.405 GHz with a temporal baseline of 24 days (cf. table 2.1). The detected HH polarized SAR images from both sensors were geometrically terrain corrected using Range-Doppler geocoding (Meier et al., 1993) based on the Greenland Ice Mapping Project (GIMP) Digital Elevation Model (DEM). The GIMP DEM has a grid spacing of 30×30 m (Version 2.1; Howat et al., 2014), which was

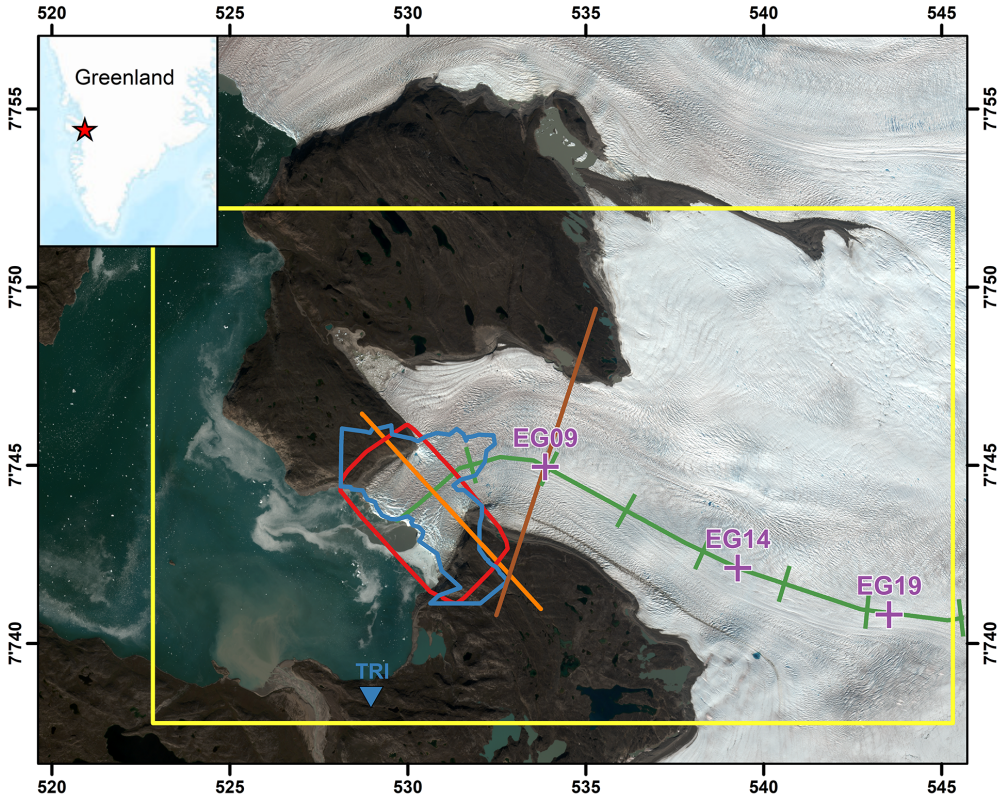

Fig. 2.1: Eqip Sermia Glacier in West Greenland. The yellow area indicates the region evaluated in this study using spaceborne SAR images (S1A and RS2), with the red line showing the extent of the mosaic built up using airborne UAV and the blue polygon depicting the area with mean ground-based backscatter coherence >0.7 acquired from the TRI (its position is indicated with the blue triangle). The purple crosses mark the GPS tracker positions. In orange and brown the flowlines across the tongue are depicted (cf. Figs. 2.14 and 2.15). The green line depicts the central flowline with distance markers every 2500 m, starting at the glacier's terminus (cf. Fig. 2.13). Background: Sentinel-2A scene from 3 August 2016 (UTM 22N projection). Contains Copernicus Sentinel data (2016).

oversampled to 2.5×2.5 m. As we operated in the DEM geometry, no separate co-registration was performed. No tiepoints were employed during geocoding, as the geolocation accuracy was sufficient (Schubert et al., 2017). The HH polarization was chosen due to its higher Signal-to-Noise Ratio (SNR).

2.2.2 SAR Intensity Tracking

With the increasing availability of space-borne interferometric data and using well-established methodologies, measurements of ice-velocities at high spatio-temporal resolutions and accuracies of a few meters per year are performed on a regular basis for the polar regions. Glacier flow speeds as low as 200 ma^{-1} have been reported as a practical upper limit for phase interferometry with a 24 day repeat-cycle duration (Gray et al., 1998; Joughin, 2002). As this study focuses on the glacier's flow dynamics at the fast-moving glacier terminus area, interferometric methods were not expected to be viable with a temporal baseline of 12 days. In addition to the temporal decorrelation, InSAR is limited to observing the line of sight. By evaluating both ascending and descending tracks (Joughin et al., 1998) and making an assumption of surface-parallel flow of the surface ice one can

Tab. 2.1: S1A/RS2 acquisitions of *Eqip Sermia* investigated in this study

Acq. Date	Platform	Mode	Prod. Type	Orbit #	Pass Dir.	Px Spacing
2016/07/08	S1A	IW	SLC	12062	Asc.	2.3×14.1 m
2016/07/20	S1A	IW	SLC	12237	Asc.	2.3×14.1 m
2016/08/01	S1A	IW	SLC	12412	Asc.	2.3×14.1 m
2016/08/06	RS2	UF-W	SLC	311	Asc.	1.3×2.1 m
2016/08/13	S1A	IW	SLC	12587	Asc.	2.3×14.1 m
2016/08/25	S1A	IW	SLC	12762	Asc.	2.3×14.1 m
2016/08/30	RS2	UF-W	SLC	311	Asc.	1.3×2.1 m

retrieve a full 3D displacement using two different tracks. As only ascending geometries were available in this instance for *Eqip Sermia*, we used a speckle tracking approach to derive the glacier's movements. This method makes use of the backscattered speckle pattern within image patches from subsequent, co-registered image acquisitions to derive two-dimensional offset values by calculating the normalized cross-correlation between the image patches (Gray et al., 2001; Joughin, 2002; Strozzi et al., 2002). As this approach does not rely on phase information, using instead the detected SAR image, phase decorrelation caused by meteorological conditions or incoherent and/or rapid flow does not influence the velocity estimation and therefore allows retrievals at higher ice speeds and longer orbit repeat intervals (Gray et al., 2001; Strozzi et al., 2002). Nevertheless, strong changes in the amplitude of the backscattered signal (e.g. due to substantial changes in the presence of surface melt water) may result in a deterioration of the velocity estimates.

Following Strozzi et al. (2002), the methodology outlined in Fig. 2.2 was implemented in MATLAB, resulting in pixel-wise X- and Y-offsets. A patch size of 101×101 pixels was chosen for the template image, corresponding to about 250×250 m. Given the glacier's flow velocity of up to 15 md^{-1} at the glacier front (Lüthi et al., 2016) and the temporal baseline of 12 days between repeat-pass S1A acquisitions (24 days for RS2), the search region was set to 181×181 pixels for S1A IW product pairs and 261×261 pixels for RS2. Each of the resulting correlation matrices was oversampled by a factor of 9 in both dimensions to locate the sub-pixel position of the correlation peak. This procedure was repeated for every second pixel in both dimensions, resulting in a sample interval of the initial velocity map (V_{map}) of 5×5 m. Choosing a smaller sample step size is beneficial for capturing of strong velocity gradients (e.g. close to the glacier's terminus), but at an increased computational cost and a known correlation between adjacent pixels due to overlap of subsequent image patches.

2.2.2a Outlier Detection and Process Iteration

To cull out bad matches, the two-step approach outlined in Fig. 2.3 was implemented, using a long-term flow velocity average product (V_{med}) and a correlation value threshold. For this V_{med}, offsets in X- and Y-direction were calculated using a 101×101 pixel (252.5×252.5 m) template patch size and search window sizes based on the temporal baseline of each of the 256 image pairs available between 2014/10/11 and 2018/03/18 (cf. table 2.2). Subsequently, a median flow velocity (V_{med}) and median flow angle map ($\measuredangle_{med}$) were computed based on these 256 flow fields. The correlation SNR was calculated by dividing the maximum height of the

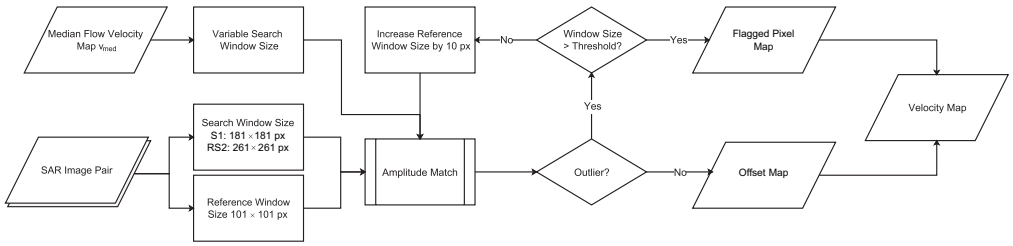

Fig. 2.2: Amplitude Match Methodology for 12-day S1A SAR products. The same methodology was used for RS2 image pairs, but with an increased search window size of 261×261 pixels to accommodate the 24-day repeat orbit.

Tab. 2.2: Overview of search window sizes used to calculate offsets for the long-term flow velocity average product (V_{med}). Image pairs with a temporal baseline >24 days (in rare cases of extended missing acquisitions) were not used.

Temporal baseline	Search Window Size (pixels)	Search Window Size (m)
6 days	141×141	352.5×352.5
12 days	181×181	452.5×452.5
24 days	261×261	652.5×652.5

correlation peak (C_{max}) by the mean level of the correlation function (C_{mean}) for every pixel (Strozzi et al., 2002).

An outlier mask was calculated following Eq. (2.1).

$$(V_{map} > 2 \cdot V_{med}) \vee (SNR < 2 \wedge C_{max} < 0.5) \vee \angle_{diff} > 45^{\circ}, \tag{2.1}$$

where $\angle_{diff} = |\angle_{med} - \angle_{map}|$ and $\angle_{map}$ representing the mapped flow angle from the image pair. For every pixel flagged as an outlier, the intensity tracking was reiterated with the reference patch size increased by 10 pixels in each dimension. The patch size of the search region was defined for every outlier pixel as a function of V_{med}, limiting the search region to three times the expected displacement, thus decreasing the chance of missing the peak correlation. Following the outlier detection, iterative intensity tracking for outlier pixels was repeated for a maximum of five times or until no further outlier pixels were detected. The application of the iteration procedure drastically reduced the number of void pixels, while enabling reasonably small patch sizes and therefore meaningful results even close to the lateral glacier margin and in particular at the calving front.

Following the outlier detection and process iteration step, V_{map} was downscaled to a pixel spacing of 100×100 m by applying a median filter to account for the spatial correlation of adjacent pixels caused by overlapping template patches in the initial V_{map} (cf. section 2.2.2).

2.2.3 GPS Velocity Data

For validation purposes, seven low-cost single-frequency continuous GPS receivers (Buchli et al., 2012; Wirz et al., 2013) were deployed on the glacier using a photovoltaic system in combination with a battery (cf. Fig. 2.1). In addition to the receivers on the glacier, a base station was deployed on bedrock. The devices were installed on June 29, 2016: five were recovered by August 25, 2016, a sixth one was

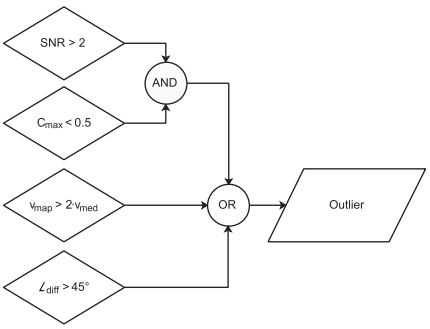

Fig. 2.3: Two-step outlier detection approach, with C_{max} being the maximum, C_{mean} the absolute mean value for each correlation function. The SNR is calculated by dividing C_{max}/C_{mean}. V_{map} describes the calculated flow velocity for an image pair, V_{med} the long-time median.

Tab. 2.3: Overview of acquisitions using the UAV during the 2016 field campaign. Date of acquisition is listed together with the average Ground Sampling Distance (GSD), number of images acquired (N_{img}) and the area covered.
* Acquisition aborted due to high winds

Name	Date	GSD	N_{img}	Area covered	Weather
eBee1	2016/08/21	17.21 cm	628	12.87 km²	Clear Skies
eBee2*	2016/08/23	17.93 cm	214	7.06 km²	Overcast
eBee3	2016/08/25	17.3 cm	616	12.53 km²	Overcast

recovered in Summer 2017 and GPS solutions at 24 h intervals were calculated at the Geodesy and Geodynamics Lab of ETH Zurich (Wirz et al., 2013). To derive robust average velocities over the relevant image-pair periods, the 24 h GPS solutions were further processed using a three-step approach that begins with the culling of outliers, followed by temporally averaging both, the latitudinal and longitudinal positions as well as the resulting velocities, in the manner described by Ahlstrøm et al. (2013). The velocities of the three sensors located in parts of the glacier with flow velocities higher than 1 md^{-1} (GPS sensors EG09, EG14 and EG19) were chosen for accuracy assessment, as lower flow velocities exhibit relatively low SNR when intensity tracking was applied to two immediately successive S1A SAR acquisitions.

2.2.4 UAV survey

To acquire additional ground-truth data, an UAV was flown over *Eqip Sermia* on three occasions in August 2016 (cf. table 2.3). The UAV surveys were carried out using a SenseFly eBee system, a light, fixed-wing UAV with a wingspan of 96 cm (senseFly SA, 2016a). The images were acquired using a modified Sony Cyber-shot DSC-WX220 with 18.2 MP and a sensor size of 6.17×4.55 mm. For every image, the approximate 3D position as well as the UAV's orientation (i.e. roll, pitch, and yaw) were annotated based on information from the on-board GPS and Intertial Measurement Unit (IMU) (senseFly SA, 2016a,b). A total of 6 flights per mission were carried out in parallel strips within 3 h, resulting in an average of more than 5 overlapping images (i.e. 70% longitudinal/lateral overlap per image), with reduced redundancy near the outer limits of the acquisition areas.

For each flight, the images acquired by the eBee UAV were processed by applying the structure from motion technique using Pix4Dmapper Pro (Eltner & Schneider, 2015), resulting in an optical mosaic (RGB) and a Digital Surface Model (DSM) of the area with a GSD of ∼0.17 m (cf. table 2.3). The resulting datasets were georeferenced using 5 manually surveyed Ground Control Points (GCP). As it was not possible to reach the northern lateral bedrock due to heavy crevassing, these GCPs were restricted to one side of the glacier, resulting in small residual differences between the geolocation accuracy of some mosaics. To reduce differences between the mosaics, an affine transformation based on a total of 40 manually selected GCPs was performed with acquisition eBee1 (cf. table 2.3) as a primary reference and the other two acquisitions as secondaries.

Due to differences in illumination between the acquisitions eBee1 and eBee3 (cf. table 2.3), image matching using the different optical bands was not feasible. We therefore used the DSMs to derive shaded reliefs and input these to the image matching algorithm, to minimize matching errors caused by illumination differences between the data sets. Flow velocity and direction were estimated by applying the approach described in section 2.2.2. Mosaics eBee1 and eBee3 with a temporal baseline of 4 days (cf. table 2.3) were chosen, as only those two included the tongue's full extent. Despite the difference in pixel spacing between the SAR images and the UAV's mosaics, the reference window size remained the same (101×101 pixels, ∼17×17 m), together with a larger search window size of 501×501 pixels (∼85×85 m) to accommodate the glacier's movement during the 4 days between the acquisitions.

2.2.5 Terrestrial Radar Interferometer Data

In order to reference flow velocity and geometry information with high spatial and temporal resolution at the calving front, a terrestrial radar interferometer (TRI; Caduff et al., 2015) was set up on stable ground 5 km south of the calving front with an unobstructed view of the glacier. The TRI system used was a GAMMA Portable Radar Interferometer (GPRI; Werner et al., 2008), operating at Ku-band (17.2 GHz). The device operates as a real-aperture radar interferometer, having one transmitting and two receiving antennas. The glacier was scanned at 1 min intervals for 8 consecutive days. Occasional data gaps were caused by hard-drive issues. The resulting radar intensity and phase measurements were processed further by application of a standard workflow to determine the displacements in Line-of-Sight (LOS) (e.g. Caduff et al., 2015; Lüthi et al., 2016). According to Voytenko et al. (2015) the absolute velocity errors were <0.5 md^{-1} with averaging times of ∼1 hour even for distant points in a humid atmosphere, with a range resolution of 0.75 m and a linearly scaling azimuth resolution of 35 m at 5 km distance (Werner et al., 2008).

2.3 Results

A typical example of a velocity field derived from a 12 day S1A repeat acquisition in August 2016 is shown in Fig. 2.4. In the main upstream tributary trunk of the glacier flow speeds were in between 1 and 2.5 md^{-1}, decreasing to zero towards the lateral margins. Within the last 5 km towards the calving front, the flow in the center line strongly increases to maximum values reaching up to 7 md^{-1} but with a rapid decrease towards the lateral margins. Within the last few hundred meters of

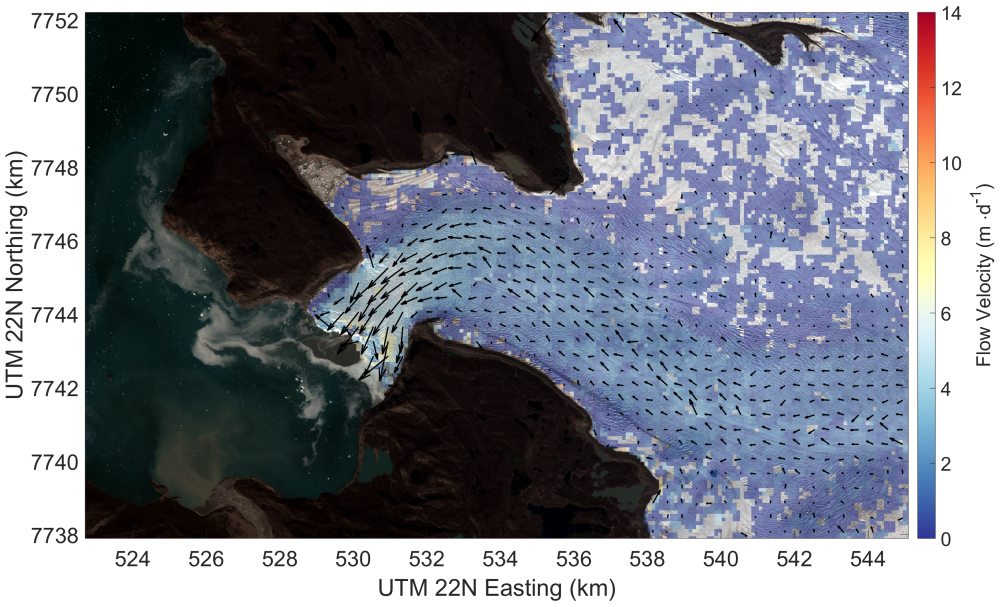

Fig. 2.4: Flow velocity field (magnitude and direction) from Intensity Tracking based on subsequent S1A acquisitions with a time difference of 12 days (2016/08/13 and 2016/08/25) from Intensity Tracking. Note that the low values close to the calving margin are due to image templates containing mixed information from the glacier and the sea, leading to erroneous values. Transparent areas on the glacier depict pixels flagged as outliers. Background: Sentinel-2A scene from 3 August 2016. Contains Copernicus Sentinel data (2016).

the calving front, velocities dropped again substantially due to image templates containing mixed information from the glacier and the sea (or ice-mélange in winter), leading to erroneous underestimations.

Note that the velocity field in Fig. 2.4 is from one single 12 day pair and was only filtered for outliers (magnitude and direction) and downscaled to 100×100 m but no further smoothing was applied, which explains the data voids and somewhat noisy appearance.

2.3.1 Comparison of GPS data to satellite-derived velocities

Using the GPS based flow velocity measurements as a first ground control dataset, we were able to assess the accuracy of the offset tracking approach applied to satellite products. In a first comparison, the flow velocities derived from spaceborne SAR satellites (cf. table 2.1, example in Fig. 2.4) were plotted against the mean GPS flow speeds of the corresponding periods, as shown in Fig. 2.5. A total of 13 SAR derived velocity estimates were compared with the GPS derived flow velocities, five periods for GPS tracker EG09 and four periods each for GPS trackers EG14 and EG19 (cf. table 2.4). To improve the SNR of the intensity tracking estimates, the integration time of the velocity estimates based on S1A was doubled to 24 days for the two GPS stations located in the upper part of the glacier (i.e. EG14 and EG19) where the velocities are relatively low (1-1.5 md^{-1}). In addition to the improvement in SNR and thus a decrease in pixels flagged as outliers (cf. Fig. 2.4), this allowed for direct comparisons with results from RS2 which also had a 24 day orbital repeat. The GPS velocities were averaged over the same periods as the satellite observation

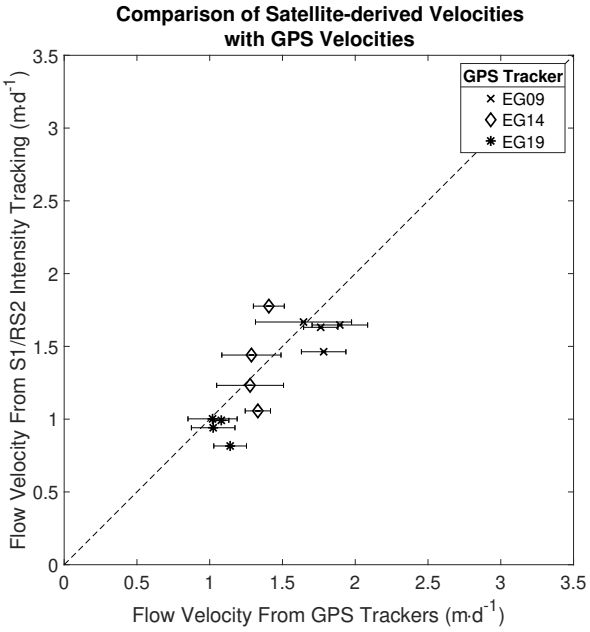

Fig. 2.5: Comparison of satellite-derived velocities with GPS velocities. To account for low SNR values in areas with flow velocities $\sim$1 md^{-1} (EG14/EG19), integration time was doubled to 24 days. Vertical bars depict the standard deviation of flow speeds based on Intensity Tracking, horizontal bars show the standard deviation of the GPS velocities.

interval. Comparing the flow velocities, they showed generally good agreement (R^2: 0.674), with a mean relative difference of 11.5% between the two methods and a Root Mean Square Error (RMSE) of 0.202 md^{-1}. When comparing the average of both, the GPS measurements and SAR derived flow velocities, for the whole campaign duration (about two months), the mean relative differences were reduced to 9.1% for EG09, 8.4% for EG14, and 5.4% for EG19.

2.3.2 Comparison of satellite-derived to UAV-derived velocities

The UAV-derived velocity field (2016/08/21 and 2016/08/25, table 2.3), shown in Fig. 2.6, covered the lower fast flowing 5 km of the glacier tongue and in general showed a very similar spatial pattern in flow speed to the SAR-derived velocities. The main differences were that the flow field was much smoother and that it was additionally able to significantly better resolve the acceleration towards the terminus where flow speeds of 12 md^{-1} are reached. These discrepancies can be attributed to the much higher spatial resolution and hence differences in patch size. This improved spatial resolution even allowed resolution of discontinuities in flow speed near the calving front related to deep crevasses and rifts. The UAV-derived flow field (Fig. 2.6) also confirms the decreased but non-zero flow along the orographic left margin on the tongue already indicated in the SAR data (Fig. 2.4).

In order to quantitatively (pixel by pixel) compare the flow speeds from the SAR with the UAV, the resolution differences between the radar and eBee datasets needed to be resolved. Therefore, the flow velocity map based on the UAV data was downscaled to match the 100 m grid size of the SAR based result. A mask was then applied for the areas outside of the glacier tongue to exclude stationary (e.g. moraine) and incoherently moving areas (e.g. open water) from the statistics (cf.

Tab. 2.4: Comparison of Flow Velocities derived by Intensity Tracking from S1/RS2 radar imagery and from GPS measurements. Ice velocities are given in md^{-1}, UTM 22N coordinates in m.

Tracker	Platform	Start Date	End Date	Mean UTM 22N Coord.	
EG09	RS2	2016/08/06	2016/08/30	533758.34	7744997.41
EG09	S1A	2016/07/08	2016/07/20	533813.03	7744977.74
EG09	S1A	2016/07/20	2016/08/01	533792.29	7744985.37
EG09	S1A	2016/08/01	2016/08/13	533772.48	7744992.40
EG09	S1A	2016/08/13	2016/08/25	533752.48	7744999.50
EG14	RS2	2016/08/06	2016/08/30	539286.31	7742106.13
EG14	S1A	2016/07/08	2016/08/01	539317.98	7742089.59
EG14	S1A	2016/07/20	2016/08/13	539303.35	7742097.21
EG14	S1A	2016/08/01	2016/08/25	539289.24	7742104.61
EG19	RS2	2016/08/06	2016/08/30	543547.47	7740771.73
EG19	S1A	2016/07/08	2016/08/01	543576.17	7740773.70
EG19	S1A	2016/07/20	2016/08/13	543562.81	7740772.75
EG19	S1A	2016/08/01	2016/08/25	543550.13	7740771.90

Tracker	vGPS	Std GPS	vSAR	vGPS-vSAR
EG09	1.70	0.28	1.68	0.02
EG09	1.89	0.19	1.65	0.24
EG09	1.78	0.15	1.46	0.32
EG09	1.76	0.12	1.63	0.13
EG09	1.64	0.33	1.67	-0.03
EG14	1.28	0.23	1.23	0.05
EG14	1.41	0.11	1.78	-0.37
EG14	1.33	0.09	1.06	0.27
EG14	1.29	0.20	1.44	-0.15
EG19	1.02	0.17	1.00	0.02
EG19	1.14	0.11	0.82	0.32
EG19	1.08	0.05	0.99	0.09
EG19	1.02	0.15	0.94	0.08

black outline in Fig. 2.7). The mask was manually traced using a Sentinel-2 (S2) scene acquired on 2016/08/03 as a reference.

The comparison between the two methods showed generally good agreement in most parts of the glacier tongue with differences between $\pm 1\,md^{-1}$. However, a discrepancy was observed near the calving front as well as at the side of the glacier, where differences exceeded $\pm 2\,md^{-1}$. Due to these larger differences, the standard deviation was $1.915\,md^{-1}$ with a mean difference of -0.689 and a median of -0.281, showing a shift towards higher flow velocities based on the UAV data. These differences were expected, as the initial 101×101 pixels (i.e. 252.5×252.5 m) template size crossed the glacier's boundaries at the calving front as well as at the sides, resulting in miscorrelations and therefore incorrect flow speeds from the SAR data, in particular close to the calving front. When possible border regions were excluded using a 250 m buffer around the glacier mask, the statistical values improved marginally (cf. red line in Fig. 2.7), resulting in a standard deviation of $1.576\,md^{-1}$ and mean and median values of -0.626 and $-0.317\,md^{-1}$ respectively.

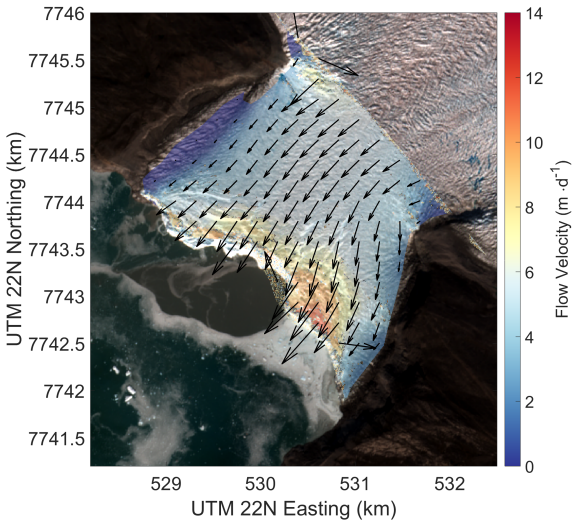

Fig. 2.6: Flow velocity field derived from Intensity Tracking using subsequent UAV acquisitions with a time difference of 4 days (2016/08/21 and 2016/08/25). Due to illumination differences between the acquisitions, shaded surface reliefs derived from structure from motion were used for the image matching procedure. Note the jumps in glacier flow speed close to the calving front that can be attributed to the presence of rifts. Erroneous values close to the calving margin can be caused by image templates containing mixed information from the glacier and the sea. Background: Sentinel-2A scene from 3 August 2016. Contains Copernicus Sentinel data (2016).

One should note that the time-periods of data acquisition were not identical (4 days UAV vs. 12 days SAR), but temporal variations within these time-scales reached their minimum at upstream GPS EG09 and were only substatial within 500 m of the terminus in the continuous TRI data (personal communication Andrea Walter, 26 Oct 2018).

2.3.3 Comparison of UAV-derived to interferometrically measured velocities

The TRI derived velocity map of the lower tongue was not continuous due to shadows from topography with respect to the TRI LOS. The general spatial patterns were very similar to the UAV data, confirming the spatial gradients towards the lateral margins as well as the strong rapid step-wise acceleration within the last 1 km towards the front. The flow at the calving front is now also very well resolved and there maximum speeds in LOS of 14 md^{-1} are reached.

Again for a detailed quantitative comparison of velocity measurements from the TRI measured interferometrically with those derived from the UAV's hillshaded DSMs, the UAV-derived velocity field was first projected into the LOS direction relative to the TRI's position, resampling the data onto the same grid. The comparison of these projected estimates and the interferometrically derived TRI flow velocities (cf. Fig. 2.9) show a close correspondence of the data for all areas aside from the very front and the lateral edges of the UAV's acquired area. The frontal differences can be explained by the differences in the measurement techniques, measurement times and spatial resolutions used. The image matching algorithm used with the UAV data relies on features visible in both the reference and search scenes. Due to calving events, features at the glacier front may no longer exist in

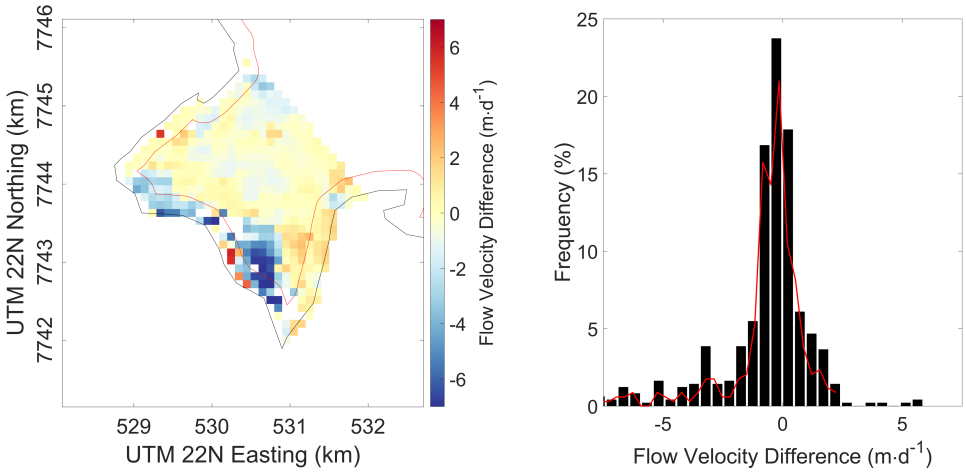

Fig. 2.7: Distribution of flow velocity differences between S1A satellite based and UAV based calculations. Negative values denote higher flow velocities from the UAV data set, positive values higher values based on the SAR data. The red line in the histogram shows the distribution of values when a 250 m buffer zone at the glacier's margins was excluded.

subsequent acquisitions, causing phantom image correlations. As the TRI relies on direct interferometric measurements at 1 minute intervals, it is less susceptible to errors caused by calving. As mentioned above, the point density of the drone's DSM was reduced at the margins of the acquired area, resulting in error-prone image matching results in those areas. Note that the non-zero ice flow at the orographic left lateral margin (in contrast to the right margin) was again very well reproduced by both acquisition methods.

Inspecting the overlapping areas between the two sensors within the glacier's marginal boundary (black line in Fig. 2.9), eBee showed a mean velocity of 1.982 md^{-1} vs. 2.62 md^{-1} for the TRI. The mean difference between the two datasets was 0.633 md^{-1}; the median difference was -0.007 md^{-1} (cf. Fig. 2.9). The standard deviation was 2.9 md^{-1}. After applying a 250 m buffer around the glacier's margin (cf. red line in Fig. 2.9), the statistical values changed to a standard deviation of 1.844 md^{-1} and mean and median differences of 0.372 and 0.129 md^{-1} respectively.

2.4 Discussion

The results and comparisons to other data presented here show the feasibility but also the limitations of operational offset tracking using S1 intensity data to estimate GFD at relatively high spatial (100×100 m) and temporal sample intervals (12 to 24 days). While the applicability of interferometric approaches has been demonstrated in the past, its applicability is limited by temporal decorrelation in cases of fast movements which is particularly the case on tongues of tidewater outlet glaciers. The S1/GPS comparison highlights the validity of the feature tracking approach with a mean velocity difference of 11.5% between the datasets, agreeing with the reported differences of 9.7% by Ahlstrøm et al. (2013). Further, in comparison to the UAV-derived velocities (which agrees with TRI), our approach is able to represent the spatial pattern of ice flow towards the fast-flowing calving front well.

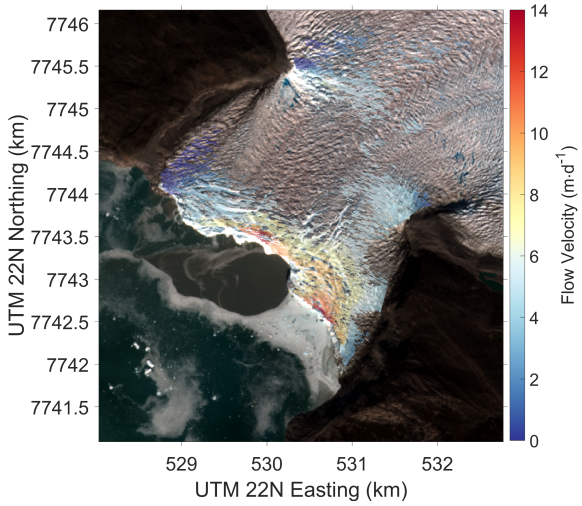

Fig. 2.8: Flow speed map based on 4 day integrated TRI acquisitions between 2016/08/21 and 2016/08/25. The shown flow speeds represent the flow magnitude in LOS direction towards the TRI sensor (cf. Fig. 2.1). No velocities could be derived for areas shadowed by the glacier's topography. Values with a coherence <0.6 or outside the glacier tongue were masked out. Clearly visible are the rifts close to the glacier's tongue, showing jumps in the glacier flow speed. Background: Sentinel-2A scene from 3 August 2016. Contains Copernicus Sentinel data (2016).

Specifically, the main acceleration in flow towards the front as well as gradients to the margins are well reproduced. However, some edge effects mostly at the calving front remain, due to overlaps of the templates used in the cross-correlation with non-glaciated areas, but this effect is limited to a narrow zone determined by the chosen template dimension and is mostly filtered out when considering flow directions as well. The non-zero velocity at the orographic left side of the terminus is reproduced surprisingly well by our 12 day SAR estimates, indicating that the inability of deducing strong velocity gradients within template patches mentioned by Nagler et al. (2015) does not impact our velocity results substantially or is compensated enough by the chosen smaller patch sizes. The good representation of spatial velocity gradients implies that strain rate fields are also robust which is crucial for constraining ice flow or calving models or process studies.

However, strong changes in backscatter occurring between two acquisitions (e.g. due to changes in temperature causing surface melt or precipitation) can cause a deterioration of the results, resulting in data voids after the outlier detection. This was especially the case for the acquisition of 2016/08/25 that was within a warm period with temperatures never falling below freezing for a week, while the corresponding acquisition on 2016/08/13 occurred during a period of pronounced diurnal variations of the temperature. Detection of small flow velocities (<2 md^{-1}) using our offset tracking from SAR intensity data can be impaired by low SNR, resulting in unreliable and noisy velocity estimates. An increase of the time between acquisitions for slower parts of the glacier, for example doubling the period to 24 days, can alleviate these issues, at the cost of reduced temporal resolution.

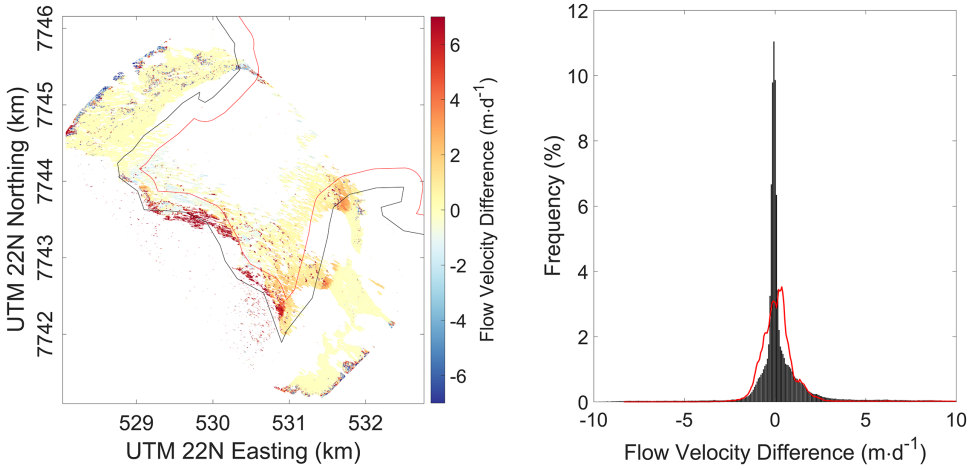

Fig. 2.9: Distribution of flow velocity differences derived from UAV image matching and TRI interferometry. Positive values (red colors) depict higher estimated flow velocities from UAV, negative (blue colors) higher derived velocities for the interferometric TRI measurements. Only values inside the glacier's marginal boundary (black line) were included in the histogram. The red line in the histogram shows the distribution of values when a 250 m buffer zone at the glacier's margins was excluded. Note the velocity differences are from the LOS components of the TRI.

2.4.1 Influence of sample interval

To improve the representation of the velocity gradients even close to the glacier's terminus, a short sample interval followed by a downsampling step to e.g. 100×100 m is beneficial, although at a higher computational cost. When choosing too large a sampling step size (e.g. 40×40 px, i.e. 100×100 m), large gradients in flow velocity (such as areas close to the calving margin) might not be resolved, whereas a fine sample interval increases the chance of calculating offsets right up to the calving front without the reference window overlapping into the fjord area (cf. Fig. A9). Given this paper's focus on *validation* of velocity estimates and spatial patterns using high-resolution reference data, the increased computational cost caused by a 2×2 pixel sample interval was acceptable. For processing at e.g. ice-sheet scale, choosing a coarser sample interval (e.g. 20×20 or 40×40 pixels) at the cost of some detail is advisable.

2.4.2 Uncertainties and sensitivities to patch size and acquisition period

As reported by Nagler et al. (2015) three main sources of error exist when using offset tracking for ice velocity estimation:

- Errors in the matching procedure,
- errors due to ionospheric disturbances,
- geocoding errors.

Errors in the matching procedure are not only influenced by the image pair's co-registration and the quality of the amplitude features, but also by the chosen size of the template (Nagler et al., 2015). This choice is not straightforward, as its

optimality depends on the presence and prominence of features within. A *smaller* patch size can produce better results in regions with strong velocity gradients, yet suffer from increased noisiness. In contrast, a patch size that is too *large* might cause a blurring of the velocities, resulting in a trend towards lower values. This issue is investigated along a center profile in Fig. 2.10, corresponding to spatial extents of about 150×150 m, 250×250 m, and 350×350 m. A larger template size substantially reduces the noise, but increases the area affected by edge effects such as the deceleration artifact at the calving front.

Furthermore, the temporal integration time of subsequent intensity trackings influences the results. While shorter integration times suffer from a higher noise level compared to products averaged over longer periods, they can be used to investigate short-term changes in flow dynamics of a glacier. This is illustrated in the sensitivity analysis of Fig. 2.11 showing SAR velocity results along the center flowline for different temporal averaging window sizes. Temporal averaging over several 12 day acquisitions substantially smooths the data and in particular reduces the artefact of velocity reduction at the calving front. Regarding the geocoding process, i.e. the transformation from slant range to map projection, the errors introduced are primarily caused by DEM inaccuracies, as the geolocation accuracy of the S1A/S1B products has been shown to be well within the 7 m absolute location accuracy requirements specified by the ESA (Miranda et al., 2018; Piantanida et al., 2018; Schubert et al., 2017). The DEM used for the project was the GIMP DEM generated from data nominally from around 2007 at an original resolution of 30×30 m. We oversampled to 2.5×2.5 m. Since then, the slope and shape of glaciers has changed due to rapid thinning over the last decade. Joughin et al. (2018a) report a horizontal location error of ∼1.25 m for every 1 m of elevation error. Based on a comparison between the GIMP DEM and the TanDEM-X 90 m DEM (acquisition date 2012/06; Rizzoli et al., 2017), the surface lowering rates were 6 ma^{-1} close to Eqip Sermia's calving front and 2 ma^{-1} at 17 km from the terminus, amounting to a maximum of ∼70 m of horizontal location error or less than one pixel in our product. Changes in slope and shape of the glacier need to be accounted for as well when comparing three-dimensional flow magnitudes or flow velocities assuming surface parallel flow, as they can introduce biases in the estimated magnitude of surface velocities (Nagler et al., 2015). Using the calculated lowering rates stated above, this results in a surface slope change of 0.15 degrees in 9 years. This value is almost identical to the one reported for Jakobshavn Glacier by Nagler et al. (2015), reporting a bias of 0.5% in the magnitude of surface velocity caused by surface lowering. Further, as *Eqip Sermia* is a fully grounded glacier, errors due to tidal influences can be neglected.

As we relied solely on the feature tracking methodology for the reasons explained in section 2.2.2, errors are expected to be larger compared to those derived from interferometric-based approaches alone (Short & Gray, 2014; Strozzi et al., 2002). When comparing the derived mean error of 11.5% between our GPS measurements and the velocities derived from intensity tracking, our findings agree with the 9.7% difference reported by Ahlstrøm et al. (2013) using intensity tracking. Similar errors were found when comparing the SAR derived velocities to the high-resolution UAV data over the glacier tongue, with a mean and median difference of 12.4% and 8.5%, respectively. The differing spatial resolutions of the ground truth data sets used (i.e. UAV, TRI, GPS) resulted in additional uncertainties introduced during the resampling of the data to match the spaceborne acquisitions.

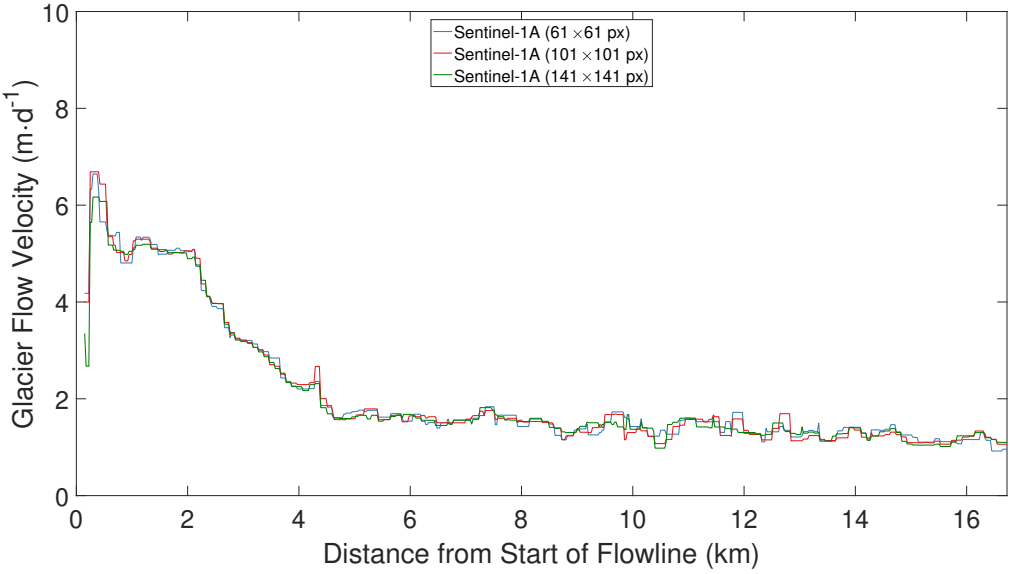

Fig. 2.10: Mean flow velocity along the central flowline (cf. Fig. 2.1) between 2016/07/08 and 2016/09/20 for different template sizes. Smaller templates are better in capturing the velocity gradients occurring towards the glacier front, resulting in slightly higher flow velocities. Furthermore, the area affected by overlaps with surrounding areas of the glacier is diminished, resulting in reliable values closer to the glacier front. Bigger template sizes tend to result in smoother results.

An analysis of the offsets in the easting and northing directions calculated over stable, non-moving terrain north and south of *Eqip Sermia* showed stable results with a mean velocity of <0.01 md^{-1} and a standard deviation of <0.3 md^{-1} in both the easting and northing directions over the 13 month period corresponding to the time span of the Greenland Ice Sheet CCI product (Nagler et al., 2015) (cf. Fig. 2.12).

2.4.3 Comparison to operational ice velocity products

Due to the large spatial coverage of currently available, operational ice flow velocity products such as products available from the Greenland Ice Sheet CCI (Nagler et al., 2015) and the National Snow & Ice Data Center's MEaSUREs Greenland Ice Sheet Velocity Map (Joughin et al., 2018b, 2010), these products are only available for specific glaciers and for specific times at a high temporal resolution and do not cover *Eqip Sermia*. For our observation period, the monthly MEaSUREs Ice Velocity products are available at a spatial resolution of 200×200 m, while the Greenland-wide ice velocity map from the Greenland Ice Sheet CCI is only available on a yearly basis with a grid spacing of 500×500 m. In order to avoid effects from differing time periods, we compiled time-averages over the Greenland Ice Sheet CCIs 13 months time period (2015/10/01 - 2016/10/31) (Nagler et al., 2015) based on the velocities from all available 40 S1 image pairs and 13 monthly MEaSUREs ice velocity products (Joughin et al., 2018b). Both operational products differ significantly from the flow velocities calculated in this study, both along the center flowline of the glacier (cf. Fig. 2.13) and along the two cross profiles (cf. Figs. 2.14 and 2.15). In addition to different processing methods, these differences are also likely a result of spatial smoothing in the operational products, and are most strongly pronounced towards the fast flowing frontal part of the glacier, where strong velocity gradients occur (cf. Fig. 2.13). There, and in contrast to our SAR-

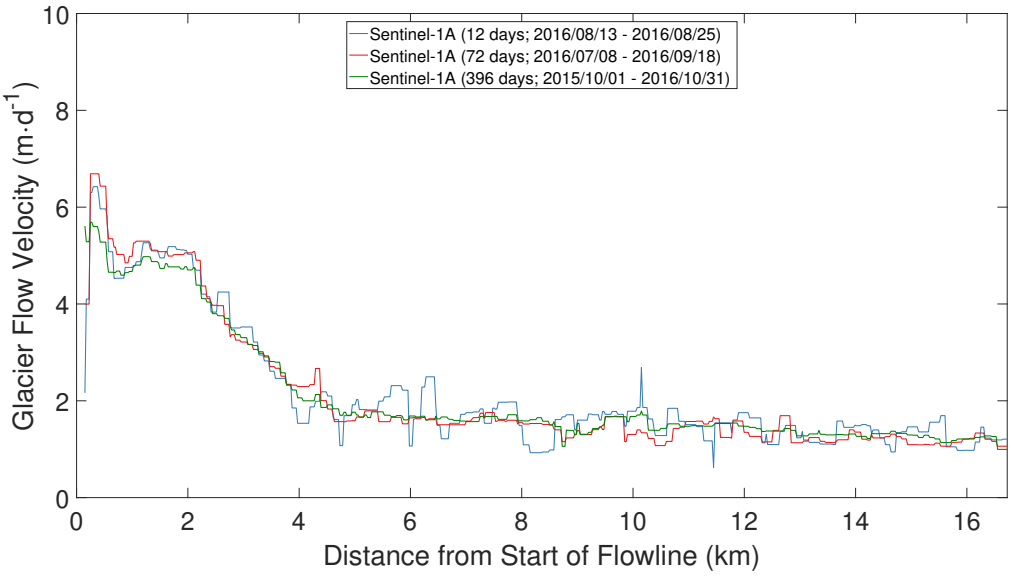

Fig. 2.11: Mean flow velocity along the central flowline (cf. Fig. 2.1) for different temporal integration periods. Shorter periods are more prone to noisy results, but offer higher temporal resolution, while an increase in temporal integration time smoothens the results.

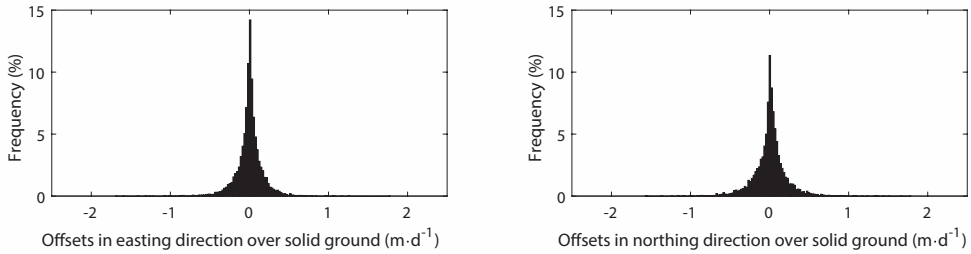

Fig. 2.12: Distribution of velocity offsets in easting and northing direction over solid ground from SAR Intensity Tracking between 2015/10/01 and 2016/10/31 (13 months). Mean easting offset is -0.002 md^{-1} with a standard deviation of 0.173 md^{-1}, mean northing offset is 0.003 md^{-1} with a standard deviation of 0.214 md^{-1}.

and UAV-derived velocities, the operational products indicate a slight or substantial deceleration in the vicinity of the terminus (cf. Fig. 2.13), likely an artefact from boundary effects and smoothing. The operational product appears to underestimate the velocities of the main tongue up to 3 km behind the front by about 10% to 20% as an effect that spans the whole width of the tongue (cf. Fig. 2.14). Our UAV-derived velocities confirm this underestimation over the tongue and are even slightly higher than our SAR-results which may be an effect of the different acquisition period over 4 days in the early Arctic summer. Further upstream, the discrepancies between SAR and the operational products generally decreases, but near the centerline our SAR estimates at the location of the lowest GPS (EG09, Fig. 2.15) were still significantly higher. These findings are also valid when comparing the monthly MEaSUREs product from August 2016 with time-averages based on our S1A image pairs (cf. Figs. A2 to A6). Despite the differences in flow velocities between our maps and the operational products, there is good agreement between the different products on direction along the flowline (calculated from the X- and Y-Offsets; cf. Fig. A8).

The above differences, calculated for the period between 2015/10/01 and 2016/10/31 (and similarly for the monthly MEaSUREs product), imply that using the available,

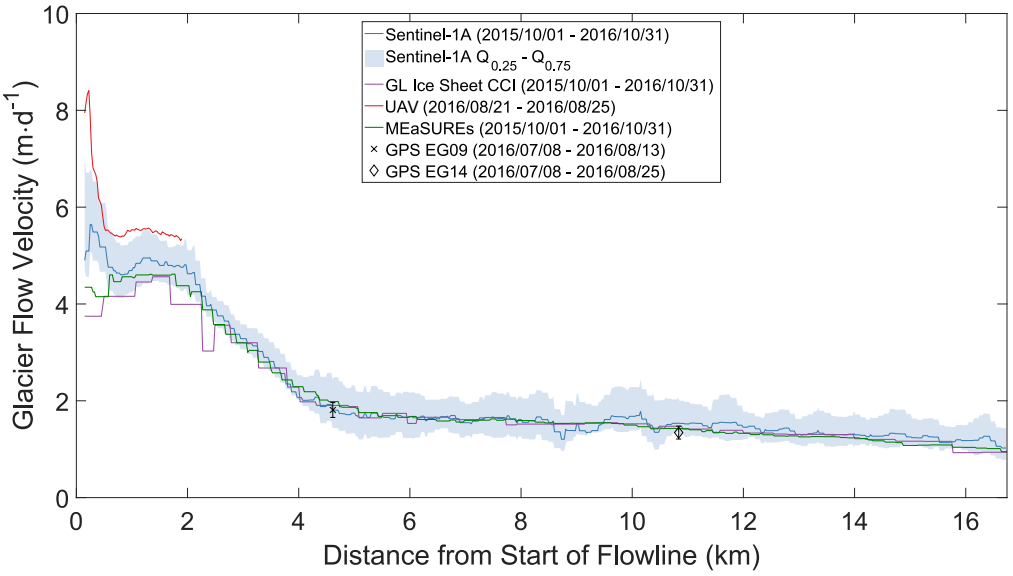

Fig. 2.13: Mean annual flow speed along the central flowline (cf. Fig. 2.1) between 2015/10/01 and 2016/10/31 (13 months) for different products, starting at the glacier's terminus. In red, the reference flow speed based on the 4-day UAV mosaics acquired on 2016/08/21 and 2016/08/25 is shown.

operational glacier flow velocity data sets for estimation of ice discharge with e.g. a flux-gate approach will result in an underestimation of ice flux (between 7% in comparison to MEaSUREs and 28% when compared to Greenland Ice Sheet CCI across the tongue, cf. Fig. 2.1), as such fluxes are calculated using surface velocity observations to approximate horizontal, depth-averaged ice velocity (Osmanoğlu et al., 2013). This underestimation cancels out if the focus is for example on changes in ice flux over time (Howat et al., 2011; Rignot et al., 2008). However, mass budget methods take the difference between the absolute discharge and the surface mass balance integrated over the upstream catchment and an underestimation in flow then systematically underestimates mass loss. Considering that the mass loss from the mass budget calculation is only a fraction (a few 10%) of the total discharge at the terminus (Enderlin et al., 2014; Rignot & Kanagaratnam, 2006), this 7% to 28% underestimation in near terminus ice flux would substantially affect mass loss estimates. Of course this issue is less pronounced if the flux gates are located in the slower flowing parts upstream, but then an extra estimation of mass changes downstream is still required. Given the parameter settings used to produce the operational products (i.e. template window size, sampling step size, ground sampling distance), this underestimation in ice flow near the terminus, may likely apply also to other similar medium-sized outlet glaciers and hence have an impact on mass loss estimates of the whole Greenland Ice Sheet.

Our near-terminus flow-fields will also imply higher frontal strain rates (compared to the operational products) which affects observational constraints for models of flow dynamics of calving and our understanding of terminus dynamics (Choi et al., 2018; King et al., 2018; Morlighem et al., 2017; Nick et al., 2013, 2009).

Data availability Data from this study can be made available from the authors upon request. The Sentinel-1 SAR data are available through the ESA Copernicus Science Hub: https://scihub.copernicus.eu/.

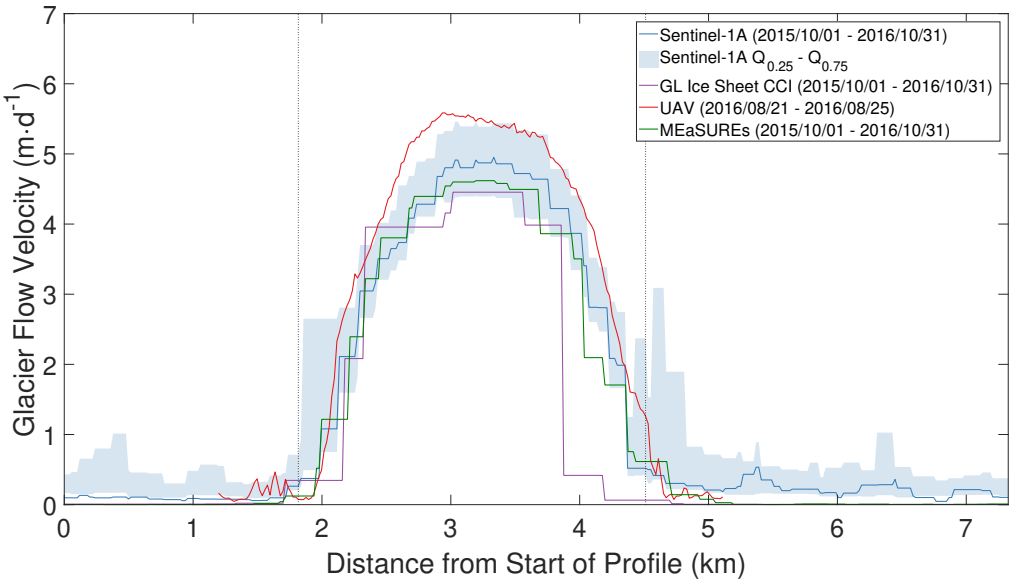

Fig. 2.14: Mean annual flow speed across the glacier tongue (cf. Fig. 2.1) between 2015/10/01 and 2016/10/31 (13 months) for different products, starting at the orographic left side of the glacier. In red, reference flow speed based on the 4-day UAV mosaics acquired on 2016/08/21 and 2016/08/25 is shown. The dashed lines depict the glacier's margins.

Author contributions C.R., D.S., D.H. and A.V. designed the paper. C.R. generated the flow fields, processed the UAV data and performed all analysis. D.S. prepared the processing of the Sentinel-1 and RADARSAT-2 data. M.P.L. performed TRI measurements and processing. J.B. prepared the GPS devices and processed the GPS data. C.R. wrote the draft of the paper. All authors contributed to the final version of the paper.

Competing interests The authors declare that they have no conflict of interest.

Acknowledgements This work was funded by the Swiss National Science Foundation Grant 200021_156098. RADARSAT-2 scenes were provided through the MDA/CSA SOAR Programme (Project #16821). We thank the European space agency (ESA) for providing the Sentinel-1 data. Lastly, we thank the reviewers for their valuable work, which led to significant improvements in the revised manuscript.

Financial support This research has been supported by the Swiss National Science Foundation (grant no. 200021_156098).

Review statement This paper was edited by Stef Lhermitte and reviewed by two anonymous referees.

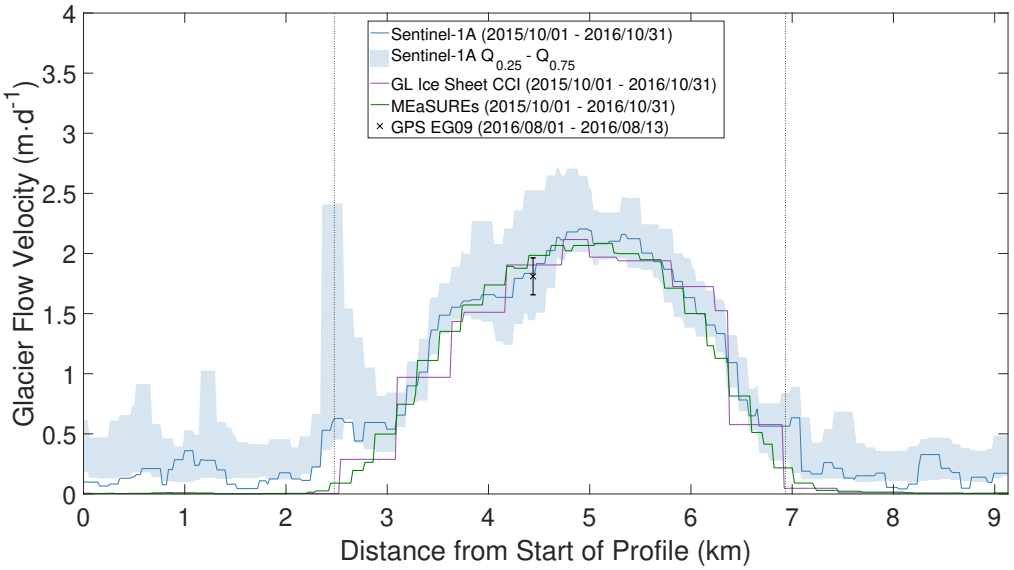

Fig. 2.15: Mean annual flow speed across the position of GPS tracker EG09 (cf. Fig. 2.1) between 2015/10/01 and 2016/10/31 (13 months) for different products, starting at the orographic left side of the glacier. The dashed lines depict the glacier's margins. Note: the peak at the orographic left margin emerges from a debris covered marginal moraine.

Appendix

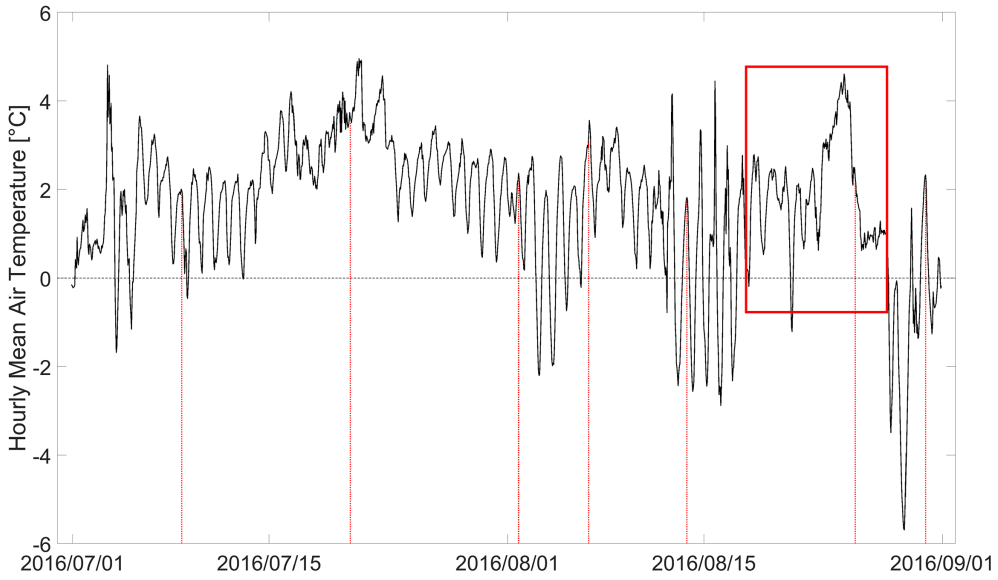

Fig. A1: Hourly Mean Temperatures in degrees Celsius for GCNet Station JAR1 (69°29′42″N, 49°42′14″W, 932 m a.s.l.; Steffen et al., 1996) in black, the satellite acquisition times shown in red. Highlighted by the red rectangle is the warm period starting on August 21st until August 28th.

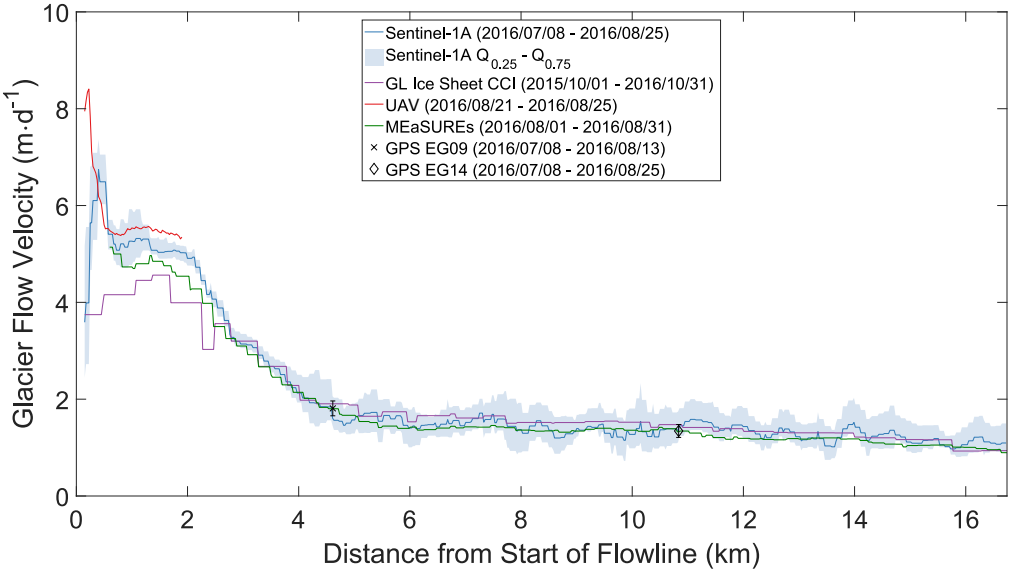

Fig. A2: Mean flow speed along the central flowline (cf. Fig. 2.1) derived from S1A scenes acquired between 2016/07/08 and 2016/08/25 (48 days), starting at the glacier's terminus. In red, reference flow speed based on the 4-day UAV mosaics acquired on 2016/08/21 and 2016/08/25, in green and purple flow velocities from MEaSUREs and Greenland Ice Sheet CCI products are shown.

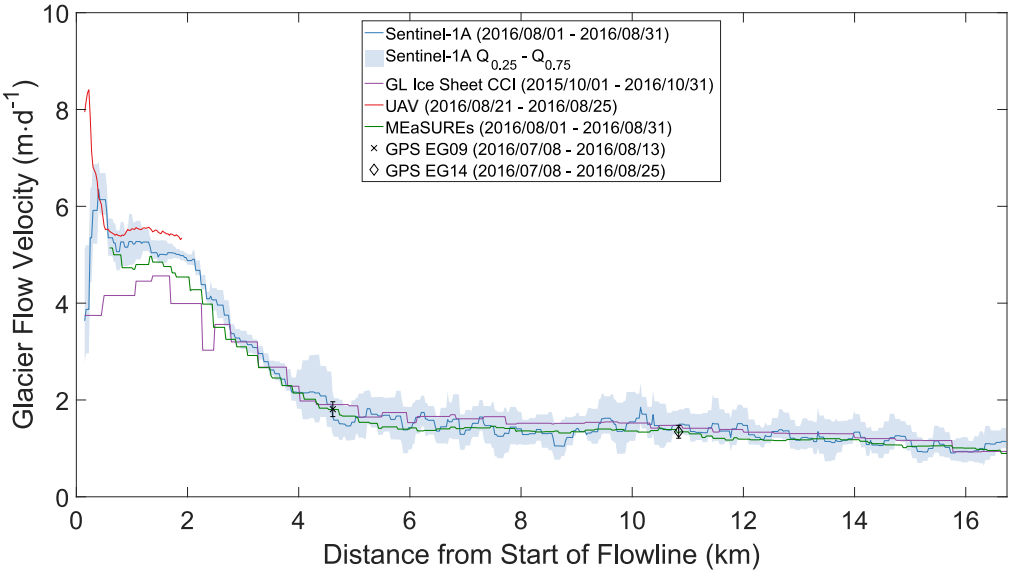

Fig. A3: Mean flow speed along the central flowline (cf. Fig. 2.1) derived from S1A scenes acquired between 2016/08/01 and 2016/08/31 (1 month), starting at the glacier's terminus. In red, reference flow speed based on the 4-day UAV mosaics acquired on 2016/08/21 and 2016/08/25, in green and purple flow velocities from MEaSUREs and Greenland Ice Sheet CCI products are shown.

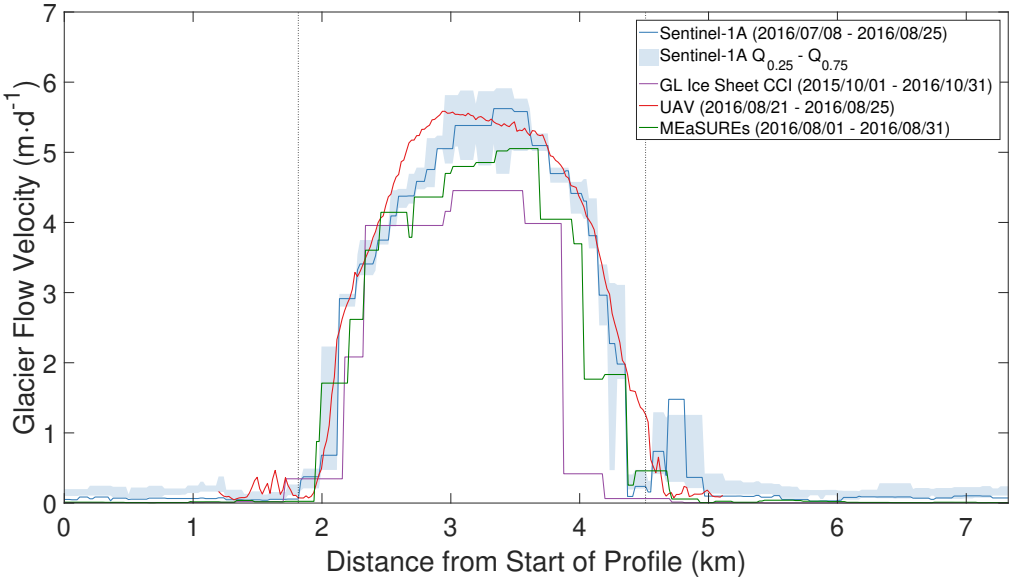

Fig. A4: Mean flow speed across the glacier tongue (cf. Fig. 2.1) derived from S1A scenes acquired between 2016/07/08 and 2016/08/25 (48 days), starting at the orographic left side of the glacier. In red, reference flow speed based on the 4-day UAV mosaics acquired on 2016/08/21 and 2016/08/25, in green and purple flow velocities from MEaSUREs and Greenland Ice Sheet CCI products are shown. The dashed lines depict the glacier's margins.

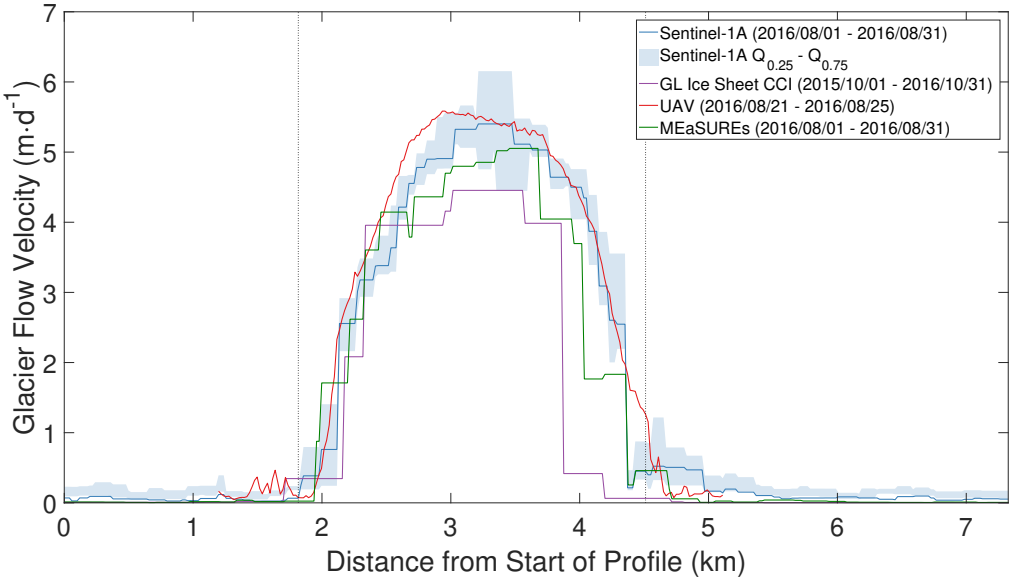

Fig. A5: Mean flow speed across the glacier tongue (cf. Fig. 2.1) derived from S1A scenes acquired between 2016/08/01 and 2016/08/31 (1 month), starting at the orographic left side of the glacier. In red, reference flow speed based on the 4-day UAV mosaics acquired on 2016/08/21 and 2016/08/25, in green and purple flow velocities from MEaSUREs and Greenland Ice Sheet CCI products are shown. The dashed lines depict the glacier's margins.

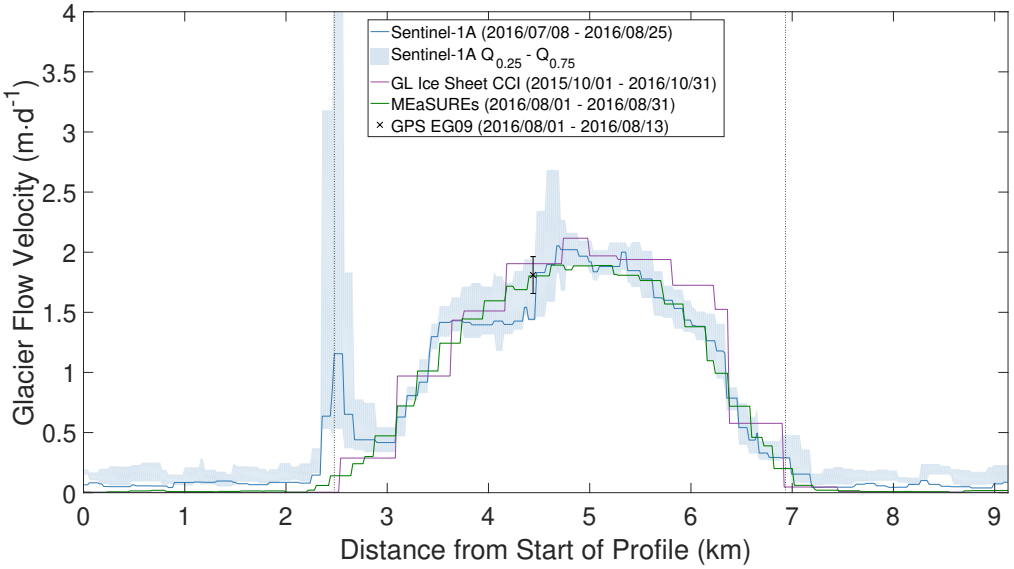

Fig. A6: Mean flow speed across the position of GPS tracker EG09 (cf. Fig. 2.1) derived from S1A scenes acquired between 2016/07/08 and 2016/08/25 (48 days), starting at the orographic left side of the glacier. In green and purple reference flow velocities from MEaSUREs and Greenland Ice Sheet CCI products are shown. The dashed lines depict the glacier's margins. Note: the peak at the orographic left margin emerges from a debris covered marginal moraine.

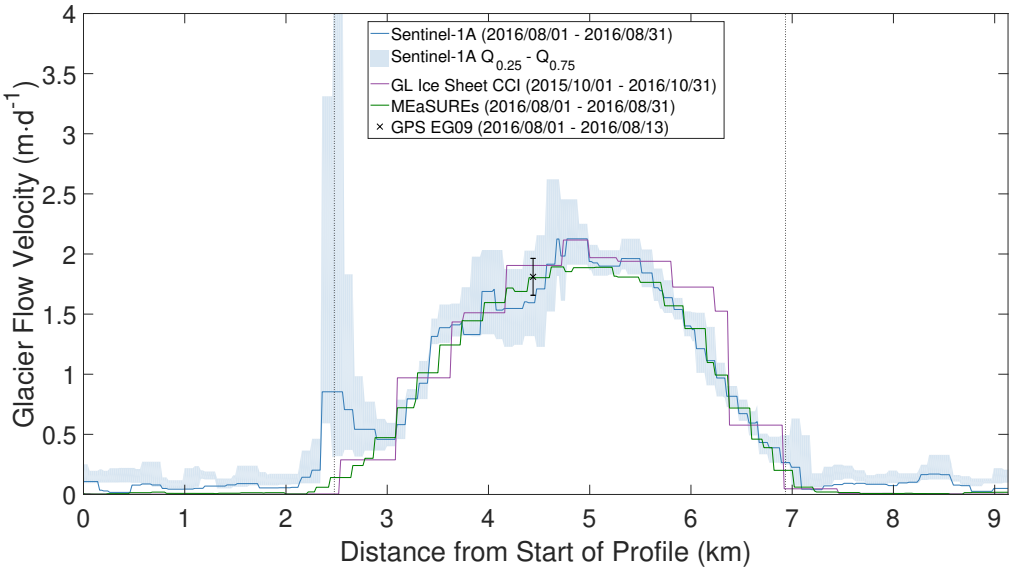

Fig. A7: Mean flow speed across the position of GPS tracker EG09 (cf. Fig. 2.1) derived from S1A scenes acquired between 2016/08/01 and 2016/08/31 (1 month), starting at the orographic left side of the glacier. In green and purple reference flow velocities from MEaSUREs and Greenland Ice Sheet CCI products are shown. The dashed lines depict the glacier's margins. Note: the peak at the orographic left margin emerges from a debris covered marginal moraine.

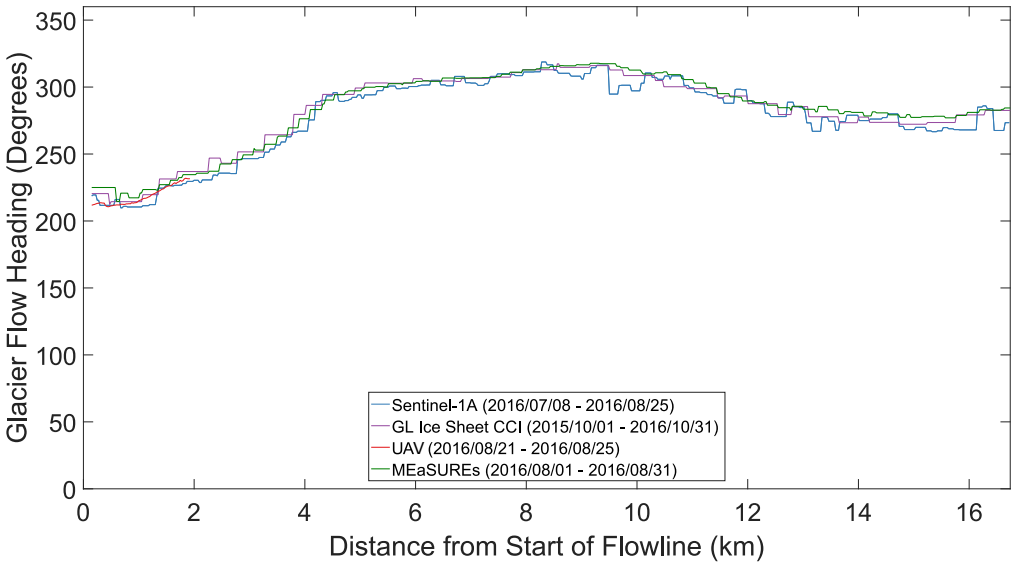

Fig. A8: Mean flow direction in degrees referenced to north along the central flowline (cf. Fig. 2.1) derived from S1A scenes acquired between 2016/07/08 and 2016/08/25 (48 days), starting at the glacier's terminus. In red, reference flow heading based on the 4-day UAV mosaics acquired on 2016/08/21 and 2016/08/25, in green and purple flow direction from MEaSUREs and Greenland Ice Sheet CCI products are shown. Mean absolute differences along the flowline are 5.8° between our SAR-based results and the Greenland Ice Sheet CCI product, and 6.1° when compared to the product from MEaSUREs.

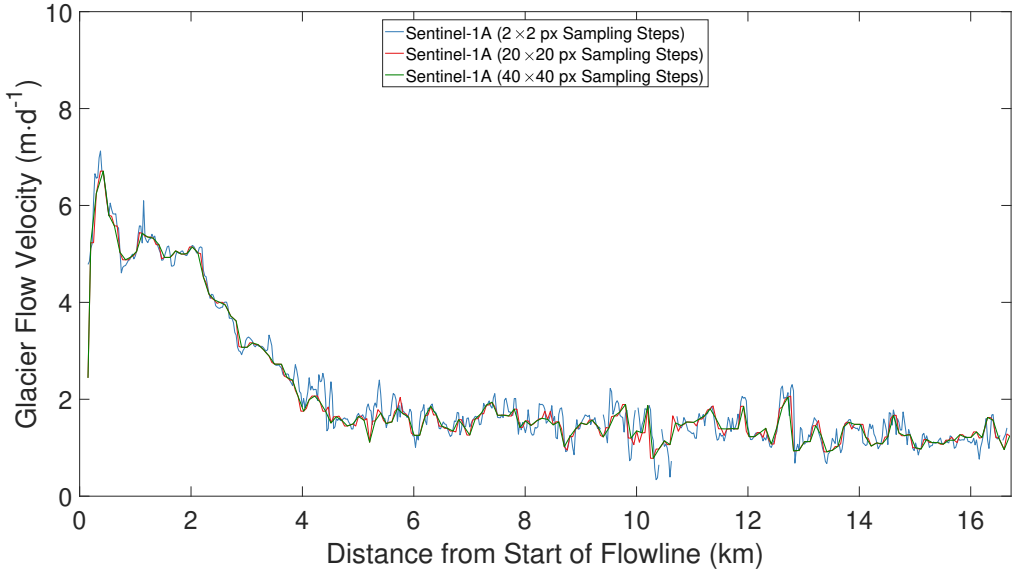

Fig. A9: Mean flow speed along the central flowline (cf. Fig. 2.1) for different sampling step sizes derived from S1A scenes acquired between 2016/07/08 and 2016/08/25 (48 days), starting at the glacier's terminus.

Bibliography

Ahlstrøm, A. P., Andersen, S. B., Andersen, M. L., Machguth, H., Nick, F. M., Joughin, I., Reijmer, C. H., van de Wal, R. S. W., Merryman Boncori, J. P., Box, J. E., Citterio, M., van As, D., Fausto, R. S., & Hubbard, A. (2013). Seasonal velocities of eight major marine-terminating outlet glaciers of the Greenland ice sheet from continuous in situ GPS instruments. *Earth System Science Data*, *5*(2), 277–287, doi: 10.5194/essd-5-277-2013.

Bauer, A. (1968). *Le glacier de l'Eqe (Eqip Sermia): Mouvement et variations du front (1959). Technical Report 2, Expédition glaciologique internationale au Groenland (EGIG)*. Copenhagen, Denmark: Meddelelser om Grønland.

Boncori, J. P. M., Andersen, M. L., Dall, J., Kusk, A., Kamstra, M., Andersen, S. B., Bechor, N., Bevan, S., Bignami, C., Gourmelen, N., Joughin, I., Jung, H.-S., Luckman, A., Mouginot, J., Neelmeijer, J., Rignot, E., Scharrer, K., Nagler, T., Scheuchl, B., & Strozzi, T. (2018). Intercomparison and Validation of SAR-Based Ice Velocity Measurement Techniques within the Greenland Ice Sheet CCI Project. *Remote Sensing*, *10*(6), 929, doi: 10.3390/rs10060929.

Buchli, B., Sutton, F., & Beutel, J. (2012). GPS-Equipped Wireless Sensor Network Node for High-Accuracy Positioning Applications. In G. P. Picco & W. Heinzelman (Eds.), *Wireless sensor networks*, volume 7158 of *Lecture Notes in Computer Science* (pp. 179–195). Berlin, Germany: Springer.

Caduff, R., Schlunegger, F., Kos, A., & Wiesmann, A. (2015). A review of terrestrial radar interferometry for measuring surface change in the geosciences. *Earth Surface Processes and Landforms*, *40*(2), 208–228, doi: 10.1002/esp.3656.

Catania, G. A., Stearns, L. A., Sutherland, D. A., Fried, M. J., Bartholomaus, T. C., Morlighem, M., Shroyer, E., & Nash, J. (2018). Geometric Controls on Tidewater Glacier Retreat in Central Western Greenland. *Journal of Geophysical Research: Earth Surface*, *29*(1), 2024–2038, doi: 10.1029/2017JF004499.

Choi, Y., Morlighem, M., Wood, M., & Bondzio, J. H. (2018). Comparison of four calving laws to model Greenland outlet glaciers. *The Cryosphere*, *12*(12), 3735–3746, doi: 10.5194/tc-12-3735-2018.

de Quervain, A. & Mercanton, P.-L. (1925). *Résultats scientifiques de l'expédition Suisse au Groenland 1912-1913*. Copenhagen, Denmark: Reitzel.

Dowdeswell, J. A., Unwin, B., Nuttall, A.-M., & Wingham, D. J. (1999). Velocity structure, flow instability and mass flux on a large Arctic ice cap from satellite radar interferometry. *Earth and Planetary Science Letters*, *167*(3-4), 131–140, doi: 10.1016/S0012-821X(99)00034-5.

Eltner, A. & Schneider, D. (2015). Analysis of Different Methods for 3D Reconstruction of Natural Surfaces from Parallel-Axes UAV Images. *The Photogrammetric Record*, *30*(151), 279–299, doi: 10.1111/phor.12115.

Enderlin, E. M., Howat, I. M., Jeong, S., Noh, M.-J., van Angelen, J. H., & van den Broeke, M. R. (2014). An improved mass budget for the Greenland ice sheet. *Geophysical Research Letters*, *41*(3), 866–872, doi: 10.1002/2013GL059010.

Euillades, L. D., Euillades, P. A., Riveros, N. C., Masiokas, M. H., Ruiz, L., Pitte, P., Elefante, S., Casu, F., & Balbarani, S. (2016). Detection of glaciers displacement time-series using SAR. *Remote Sensing of Environment*, *184*, 188–198, doi: 10.1016/j.rse.2016.07.003.

Fahnestock, M. A., Bindschadler, R. A., Kwok, R., & Jezek, K. C. (1993). Greenland Ice Sheet Surface Properties and Ice Dynamics from ERS-1 SAR Imagery. *Science*, *262*(5139), 1530–1534.

Fallourd, R., Harant, O., Trouvé, E., Nicolas, J.-M., Gay, M., Walpersdorf, A., Mugnier, J.-L., Serafini, J., Rosu, D., Bombrun, L., Vasile, G., Cotte, N., Vernier, F., Tupin, F., Moreau, L., & Bolon, P. (2011). Monitoring Temperate Glacier Displacement by Multi-Temporal TerraSAR-X Images and Continuous GPS Measurements. *IEEE Journal of Selected Topics in Applied Earth Observations and Remote Sensing*, *4*(2), 372–386, doi: 10.1109/JSTARS.2010.2096200.

Frezzotti, M., Capra, A., & Vittuari, L. (1998). Comparison between glacier ice velocities inferred from GPS and sequential satellite images. *Annals of Glaciology*, *27*, 54–60, doi: 10.3189/1998AoG27-1-54-60.

Goldstein, R. M., Engelhardt, H., Kamb, B., & Frolich, R. M. (1993). Satellite radar interferometry for monitoring ice sheet motion: Application to an antarctic ice stream. *Science*, *262*(5139), 1525–1530, doi: 10.1126/science.262.5139.1525.

Gray, A. L., Mattar, K. E., Vachon, P. W., Bindschadler, R. A., Jezek, K. C., Forster, R., & Crawford, J. P. (1998). InSAR results from the RADARSAT Antarctic Mapping Mission data: estimation of glacier motion using a simple registration procedure. In *IGARSS 1998* (pp. 1638–1640). Piscataway, USA: Institute of Electrical and Electronics.

Gray, A. L., Short, N. H., Mattar, K. E., & Jezek, K. C. (2001). Velocities and Flux of the Filchner Ice Shelf and its Tributaries Determined from Speckle Tracking Interferometry. *Canadian Journal of Remote Sensing*, *27*(3), 193–206, doi: 10.1080/07038992.2001.10854936.

Howat, I. M., Ahn, Y., Joughin, I., van den Broeke, M. R., Lenaerts, J. T. M., & Smith, B. E. (2011). Mass balance of Greenland's three largest outlet glaciers, 2000-2010. *Geophysical Research Letters*, *38*(12), doi: 10.1029/2011GL047565.

Howat, I. M., Negrete, A., & Smith, B. E. (2014). The Greenland Ice Mapping Project (GIMP) land classification and surface elevation data sets. *The Cryosphere*, *8*(4), 1509–1518, doi: 10.5194/tc-8-1509-2014.

IPCC (2013). *Climate Change 2013: The Physical Science Basis. Contribution of Working Group I to the Fifth Assessment Report of the Intergovernmental Panel on Climate Change*. Cambridge, United Kingdom and New York, USA: Cambridge University Press.

Joughin, I. (2002). Ice-sheet velocity mapping: a combined interferometric and speckle-tracking approach. *Annals of Glaciology*, *34*(1), 195–201, doi: 10.3189/172756402781817978.

Joughin, I., Howat, I. M., Fahnestock, M. A., Smith, B. E., Krabill, W., Alley, R. B., Stern, H., & Truffer, M. (2008). Continued evolution of Jakobshavn Isbrae following its rapid speedup. *Journal of Geophysical Research*, *113*(F4), 6487, doi: 10.1029/2008JF001023.

Joughin, I., Kwok, R., & Fahnestock, M. A. (1998). Interferometric estimation of three-dimensional ice-flow using ascending and descending passes. *IEEE Transactions on Geoscience and Remote Sensing*, *36*(1), 25–37, doi: 10.1109/36.655315.

Joughin, I., Smith, B. E., & Howat, I. M. (2018a). Greenland Ice Mapping Project: Ice Flow Velocity Variation at sub-monthly to decadal time scales. *The Cryosphere*, *12*(7), 2211–2227, doi: 10.5194/tc-12-2211-2018.

Joughin, I., Smith, B. E., Howat, I. M., Moon, T., & Scambos, T. A. (2016). A SAR record of early 21st century change in Greenland. *Journal of Glaciology*, *62*(231), 62–71, doi: 10.1017/jog.2016.10.

Joughin, I., Smith, B. E., Howat, I. M., & Scambos, T. A. (2018b). MEaSUREs Greenland Ice Sheet Velocity Map from InSAR Data, Version 2. Retrieved 2022-09-06, from https://dx.doi.org/10.5067/OC7B04ZM9G6Q.

Joughin, I., Smith, B. E., Howat, I. M., Scambos, T. A., & Moon, T. (2010). Greenland flow variability from ice-sheet-wide velocity mapping. *Journal of Glaciology*, *56*(197), 415–430, doi: 10.3189/002214310792447734.

Kadded, F. & Moreau, L. (2013). Sur les traces du Paul-Emile Victor, relevés topographiques 3D au Groenland. *Revue XYZ*, *137*(4), 47–56.

King, M. D., Howat, I. M., Jeong, S., Noh, M.-J., Wouters, B., Noël, B. P. Y., & van den Broeke, M. R. (2018). Seasonal to decadal variability in ice discharge from the Greenland Ice Sheet. *The Cryosphere*, *12*(12), 3813–3825, doi: 10.5194/tc-12-3813-2018.

Lemos, A., Shepherd, A. P., McMillan, M., Hogg, A. E., Hatton, E., & Joughin, I. (2018). Ice velocity of Jakobshavn Isbræ, Petermann Glacier, Nioghalvfjerdsfjorden, and Zachariæ Isstrøm, 2015–2017, from Sentinel 1-a/b SAR imagery. *The Cryosphere*, *12*(6), 2087–2097.

Luckman, A. & Murray, T. (2005). Seasonal variation in velocity before retreat of Jakobshavn Isbræ, Greenland. *Geophysical Research Letters*, *32*(8), doi: 10.1029/2005GL022519.

Lüthi, M. P., Vieli, A., Moreau, L., Joughin, I., Reisser, M., Small, D., & Stober, M. (2016). A century of geometry and velocity evolution at Eqip Sermia, West Greenland. *Journal of Glaciology*, *62*(234), 640–654, doi: 10.1017/jog.2016.38.

Meier, E., Frei, U., & Nüesch, D. (1993). Precise terrain corrected geocoded images. In G. Schreier (Ed.), *SAR geocoding: data and systems* (pp. 173–185). Karlsruhe, Germany: Wichmann.

Michel, R. & Rignot, E. (1999). Flow of Glaciar Moreno, Argentina, from repeat-pass Shuttle Imaging Radar images: Comparison of the phase correlation method with radar interferometry. *Journal of Glaciology*, *45*(149), 93–100, doi: 10.3189/s0022143000003075.

Miranda, N., Piantanida, R., Recchia, A., Franceschi, N., Small, D., Schubert, A., & Meadows, P. J. (2018). S-1 Instrument and Product Performance Status: 2018 Update. In *2018 IEEE International Geoscience and Remote Sensing Symposium* (pp. 1551–1554). Valencia, Spain: IEEE.

Moon, T., Joughin, I., Smith, B. E., & Howat, I. M. (2012). 21st-Century Evolution of Greenland Outlet Glacier Velocities. *Science*, *336*(6081), 576–578, doi: 10.1126/science.1219985.

Morlighem, M., Williams, C. N., Rignot, E., An, L., Arndt, J. E., Bamber, J. L., Catania, G. A., Chauché, N., Dowdeswell, J. A., Dorschel, B., Fenty, I., Hogan, K., Howat, I. M., Hubbard, A., Jakobsson, M., Jordan, T. M., Kjeldsen, K. K., Millan, R., Mayer, L., Mouginot, J., Noël, B. P. Y., O'Cofaigh, C., Palmer, S., Rysgaard, S., Seroussi, H., Siegert, M. J., Slabon, P., Straneo, F., van den Broeke, M. R., Weinrebe, W., Wood, M., & Zinglersen, K. B. (2017). BedMachine v3: Complete Bed Topography and Ocean Bathymetry Mapping of Greenland From Multibeam Echo Sounding Combined With Mass Conservation. *Geophysical Research Letters*, *44*(21), 11051–11061, doi: 10.1002/2017GL074954.

Nagler, T., Rott, H., Hetzenecker, M., Wuite, J., & Potin, P. (2015). The Sentinel-1 Mission: New Opportunities for Ice Sheet Observations. *Remote Sensing*, *7*(7), 9371–9389, doi: 10.3390/rs70709371.

Nick, F. M., Vieli, A., Andersen, M. L., Joughin, I., Payne, A. J., Edwards, T. L., Pattyn, F., & van de Wal, R. S. W. (2013). Future sea-level rise from Greenland's main outlet glaciers in a warming climate. *Nature*, *497*(7448), 235–238, doi: 10.1038/nature12068.

Nick, F. M., Vieli, A., Howat, I. M., & Joughin, I. (2009). Large-scale changes in Greenland outlet glacier dynamics triggered at the terminus. *Nature Geoscience*, *2*(2), 110–114, doi: 10.1038/NGEO394.

Osmanoğlu, B., Braun, M. H., Hock, R., & Navarro, F. J. (2013). Surface velocity and ice discharge of the ice cap on King George Island, Antarctica. *Annals of Glaciology*, *54*(63), 111–119, doi: 10.3189/2013AoG63A517.

Piantanida, R., Recchia, A., Franceschi, N., Valentino, A., Miranda, N., Schubert, A., & Small, D. (2018). Accurate Geometric Calibration of Sentinel-1 Data. In VDE Verlag GmbH (Ed.), *Proceedings of the European Conference on Synthetic Aperture Radar, EUSAR* (pp. 63–68). Berlin, Germany: VDE Verlag GmbH.

Rignot, E., Box, J. E., Burgess, E., & Hanna, E. (2008). Mass balance of the Greenland ice sheet from 1958 to 2007. *Geophysical Research Letters*, *35*(20), doi: 10.1029/2008GL035417.

Rignot, E., Jezek, K. C., & Sohn, H.-G. (1995). Ice flow dynamics of the Greenland Ice Sheet from SAR interferometry. *Geophysical Research Letters*, *22*(5), 575–578, doi: 10.1029/94GL03381.

Rignot, E. & Kanagaratnam, P. (2006). Changes in the velocity structure of the Greenland Ice Sheet. *Science*, *311*(5763), 986–990, doi: 10.1126/science.1121381.

Rizzoli, P., Martone, M., Gonzalez, C., Wecklich, C., Borla Tridon, D., Bräutigam, B., Bachmann, M., Schulze, D., Fritz, T., Huber, M., Wessel, B., Krieger, G., Zink, M., & Moreira, A. (2017). Generation and performance assessment of the global TanDEM-X digital elevation model. *ISPRS Journal of Photogrammetry and Remote Sensing*, *132*, 119–139, doi: 10.1016/j.isprsjprs.2017.08.008.

Scambos, T. A., Dutkiewicz, M. J., Wilson, J. C., & Bindschadler, R. A. (1992). Application of image cross-correlation to the measurement of glacier velocity using satellite image data. *Remote Sensing of Environment*, *42*(3), 177–186, doi: 10.1016/0034-4257(92)90101-O.

Schellenberger, T., Dunse, T., Kääb, A., Kohler, J., & Reijmer, C. H. (2015). Surface speed and frontal ablation of Kronebreen and Kongsbreen, NW Svalbard, from SAR offset tracking. *The Cryosphere*, *9*(6), 2339–2355, doi: 10.5194/tc-9-2339-2015.

Schubert, A., Faes, A., Kääb, A., & Meier, E. (2013). Glacier surface velocity estimation using repeat TerraSAR-X images: Wavelet- vs. correlation-based image matching. *ISPRS Journal of Photogrammetry and Remote Sensing*, *82*, 49–62, doi: 10.1016/j.isprsjprs.2013.04.010.

Schubert, A., Miranda, N., Geudtner, D., & Small, D. (2017). Sentinel-1A/B Combined Product Geolocation Accuracy. *Remote Sensing*, *9*(12), doi: 10.3390/rs9060607.

senseFly SA (2016a). eBee and eBee Ag with eMotion 2 Extended User Manual: Revision 19. Retrieved 2019-11-05, from http://www.sensefly.com.

senseFly SA (2016b). WX Camera User Manual: Revision 4. Retrieved 2017-05-12, from http://www.sensefly.com.

Short, N. H. & Gray, A. L. (2014). Glacier dynamics in the Canadian High Arctic from RADARSAT-1 speckle tracking. *Canadian Journal of Remote Sensing*, *31*(3), 225–239.

Steffen, K., Box, J. E., & Abdalati, W. (1996). Greenland Climate Network: GC-Net. In S. C. Colbeck (Ed.), *Glaciers, Ice Sheets and Volcanoes: A Tribute to Mark F. Meier* (pp. 98–103). Hanover, USA: Cold Regions Research and Engineering Laboratory (CRREL) Special Report 96-27.

Straneo, F., Heimbach, P., Sergienko, O., Hamilton, G., Catania, G. A., Griffies, S., Hallberg, R., Jenkins, A., Joughin, I., Motyka, R., Pfeffer, W. T., Price, S. F., Rignot, E., Scambos, T. A., Truffer, M., & Vieli, A. (2013). Challenges to Understanding the Dynamic Response of Greenland's Marine Terminating Glaciers to Oceanic and Atmospheric Forcing. *Bulletin of the American Meteorological Society*, *94*(8), 1131–1144, doi: 10.1175/BAMS-D-12-00100.1.

Strozzi, T., Luckman, A., Murray, T., Wegmuller, U., & Werner, C. L. (2002). Glacier motion estimation using SAR offset-tracking procedures. *IEEE Transactions on Geoscience and Remote Sensing*, *40*(11), 2384–2391, doi: 10.1109/TGRS.2002.805079.

Torres, R., Snoeij, P., Geudtner, D., Bibby, D., Davidson, M., Attema, E., Potin, P., Rommen, B., Floury, N., Brown, M., Traver, I. N., Deghaye, P., Duesmann, B., Rosich, B., Miranda, N., Bruno, C., L'Abbate, M., Croci, R., Pietropaolo, A., Huchler, M., & Rostan, F. (2012). GMES Sentinel-1 mission. *Remote Sensing of Environment*, *120*, 9–24, doi: 10.1016/j.rse.2011.05.028.

Vieli, A. & Nick, F. M. (2011). Understanding and Modelling Rapid Dynamic Changes of Tidewater Outlet Glaciers: Issues and Implications. *Surveys in Geophysics*, *32*(4-5), 437–458, doi: 10.1007/s10712-011-9132-4.

Voytenko, D., Dixon, T. H., Howat, I. M., Gourmelen, N., Lembke, C., Werner, C. L., de La Peña, S., & Oddsson, B. (2015). Multi-year observations of Breiðamerkurjökull, a marine-terminating glacier in southeastern Iceland, using terrestrial radar interferometry. *Journal of Glaciology*, *61*(225), 42–54, doi: 10.3189/2015JoG14J099.

Werner, C. L., Strozzi, T., Wiesmann, A., & Wegmuller, U. (2008). A Real-Aperture Radar for Ground-Based Differential Interferometry. In *IGARSS 2008* (pp. III – 210–III – 213). Piscataway, USA: IEEE.

Wirz, V., Beutel, J., Buchli, B., Gruber, S., & Limpach, P. (2013). Temporal Characteristics of Different Cryosphere-Related Slope Movements in High Mountains. In C. Margottini, P. Canuti, & K. Sassa (Eds.), *Landslide Science and Practice* (pp. 383–390). Dordrecht, Netherlands: Springer.

Wood, M., Rignot, E., Fenty, I., Menemenlis, D., Millan, R., Morlighem, M., Mouginot, J., & Seroussi, H. (2018). Ocean-Induced Melt Triggers Glacier Retreat in Northwest Greenland. *Geophysical Research Letters*, *57*(73), 8334–8342, doi: 10.1029/2018GL078024.

Chapter

3

Paper 2: Wide-Area Analysis-Ready Radar Backscatter Composites

Small, D., **Rohner, C.**, Miranda, N., Rüetschi, M., & Schaepman, M.E.

This chapter is based on the peer-reviewed article:
Wide-area analysis-ready radar backscatter composites.
IEEE Transactions on Geoscience and Remote Sensing, 2022, 60, 1–14.
doi: 10.1109/TGRS.2021.3055562.
and is reprinted as the final submitted manuscript.
It has been modified to fit into the layout of this thesis.

C.R. implemented the code for calculating the LRWs from Sentinel-1 and RADARSAT-2 data and performed the LRW calculation. **C.R.**, D.S., and M.R. performed the analysis. D.S. prepared the processing of the Sentinel-1 and RADARSAT-2 data. D.S. designed the paper. D.S. wrote the draft of the paper. **All authors** contributed to the final version of the paper.

Abstract

The benefits of composite products are well known to users of data from optical sensors: cloud-cleared composite reflectance or index products are commonly used as an analysis ready data layer. No analogous composite products are currently in widespread use that are based on spaceborne radar satellite backscatter signals. Here we present a methodology to produce wide-area analysis ready data composite backscatter images. They build on the existing heritage of geometrically and radiometrically terrain corrected level 1 products. By combining backscatter measurements of a single region seen from multiple satellite tracks (incl. ascending and descending), they are able to provide wide-area coverage with low latency. The analysis ready composite backscatter maps provide flattened backscatter estimates that are geometrically and radiometrically corrected for slope effects. A mask layer annotating the local quality of the composite resolution is introduced. Multiple tracks are combined by weighting each observation by its local resolution, generating seamless wide-area backscatter maps suitable for applications ranging from wet snow monitoring to land cover classification or short-term change detection.

3.1 Introduction

Composite products are well-known to users of optical sensors, as it is a commonplace to automatically generate cloud-cleared reflectance data. For example, in the case of the well-known Moderate Resolution Imaging Spectroradiometer (MODIS) sensor, if one browses through its product table (Justice et al., 2002; NASA, 2020), one notices that almost all entries are composite products.

Recall that remote sensing products are generally distinguished by processing levels, quoted from NASA (1986) (own emphasis):

- *L0*: Reconstructed unprocessed instrument data at full resolution
- *L1A*: Reconstructed unprocessed instrument data at full resolution, time referenced, and annotated with ancillary information, including radiometric and geometric calibration coefficients and georeferencing parameters (i.e. platform ephemeris) computed and appended but not applied to the L0 data.
- *L1B*: L1A data that has been processed to sensor units (i.e. radar backscatter cross section, brightness temperature, etc.). Not all instruments will have a L1B equivalent.
- *L2*: Derived environmental variables (e.g. ocean wave height, soil moisture, ice concentration) at the same resolution and location as the source data.
- *L3*: Variables mapped on *uniform space-time scales*, usually with some *completeness and consistency properties* (e.g. missing points interpolated, *complete regions mosaicked together from multiple orbits*).
- *L4*: Model output or results from analyses of lower-level data (i.e. variables that were not measured by the instruments but instead are derived from these measurements).

In comparison to the MODIS product table, no analogous standardised set of methodologies to generate L3 backscatter products from L1 radar data have been established to date.

ESA's S1 satellites are providing free and open data with unprecedentedly high geolocation quality (Gisinger et al., 2021; Schubert et al., 2012a, 2017) and wide spatial coverage at high temporal resolution.

In this paper, we introduce a new standardised approach for generation of L3 backscatter composites. This enables multi-track and multi-sensor integration, opening the door to the "daily" level of temporal resolution that has long been a goal (Alverson & Ryan, 2007).

We begin with a review of L1 terrain corrections in section 3.2. This is followed in section 3.3 with a description and demonstration of LRW applied to generate L3 backscatter composites. Applications of the backscatter composites are discussed at the end of Section 3.4. Conclusions and recommendations are then summarised.

3.2 Level 1 Terrain Corrections

We first review products based on conventional range-Doppler geocoding (i.e. *geometric* terrain correction), and illustrate the benefits of *radiometric* terrain correction (i.e. "RTC" product type; Small, 2011), whereby the influence of mountainous terrain on the retrieved radiometry is mitigated.

3.2.1 Geometric Terrain Correction (GTC)

In many "geocoding" analyses, each SAR input product is first individually translated to map geometry as "geometrically terrain corrected" (GTC) products. Range-Doppler geolocation (Meier et al., 1993; Small et al., 2007) is typically applied, whereby external precise orbital state vectors (OSVs) are interpolated at each azimuth line. The backscatter values are then resampled from the input products' slant or ground range geometry into the map geometry of the DEM being used. "Blind" geocoding with modern sensors is possible, whereby no "tie-points" need to be used (Schubert et al., 2015). One assumes that an accurate geometric calibration (Schubert et al., 2008) has been applied to the sensor, and that the L1 product annotations can be applied directly. For even higher accuracy (e.g. geodetic applications), further corrections for atmospheric path delay distortions, solid Earth tides, frame shift, and further SAR processor-specific artefacts can be considered during geolocation (Schubert et al., 2017). Depending on the desired resolution of the output product, these latter corrections may or may not provide added benefit. However good the geometric correction is, only the *positions* of the measurements are adjusted in GTC backscatter products: their backscatter values (σ^0_E or γ^0_E) themselves remain ellipsoid-based. Methods for radiometric corrections evolved over the years from relatively simple approaches that used the local angle of incidence (Bayer et al., 1991; Foody, 1986; Kellndorfer et al., 1998; Mladenova et al., 2013) to a trend in recent years of acknowledging that "heteromorphic" approaches are required (Frey et al., 2013; Löw & Mauser, 2007; Simard et al., 2016; Small, 2011). These approaches acknowledge the "heteromorphism" (Small et al., 2000) (i.e. lack of 1-to-1 correspondence) between the topologies inherent in radar vs. map (DEM) geometries.

3.2.2 Radiometric Terrain Correction (RTC)

Whereas in the case of GTC products, only the *location* of pixels is modified between the L1 input product and the output map geometry, in the case of RTC products *both the location and the brightness* (radiometry) of each pixel is corrected to account for terrain-induced modulations of the image radiometry.

First, an image simulation is performed by proceeding through the available DEM and projecting each DEM triangular facet into the plane perpendicular to the local slant range direction. The areas are summed at each image location (range and azimuth), with facets covered by radar shadow carefully excluded from the summation. The projection into the plane perpendicular to slant range follows the gamma nought convention, and ensures that the actual area seen by the sensor is replicated in the final image simulation (Small, 2011). The RTC backscatter (γ^0_T) is computed by sourcing the normalised radar cross section generated during the image simulation to provide the local area, rather than a simple ellipsoid-based incident angle model traditionally widely applied to backscatter (σ^0_E or γ^0_E) in the literature. Whereas the normalisation area $\underline{A}_\gamma(\theta_E)$ is a function of the ellipsoidal incident angle θ_E for γ^0_E (Small, 2011),

$$\gamma^0_E = \frac{A_\beta}{\underline{A}_\gamma(\theta_E)} \cdot \beta^0 = \beta^0 \cdot tan\theta_E, \tag{3.1}$$

in the case of γ^0_T, the normalisation area $A_\gamma(r, a)$ is individual to each range and azimuth coordinate (r, a) in the L1 product:

$$\gamma^0_T = \frac{A_\beta}{A_\gamma(r, a)} \cdot \beta^0. \tag{3.2}$$

Fig. 1 shows GTC and RTC products of the same dataset juxtaposed for comparison. In the top row, GTC VH backscatter (γ^0_E) is shown for a set of three S1 IW Ground Range Detected High-resolution (GRDH) products covering the central Alps acquired on May 4 and 5, 2016. In the lower row, the associated RTC images (γ^0_T) are shown for comparison. Note how the dark wet snow backscatter signals are mixed with terrain-induced brightness distortions in the GTC images in the top row, but are directly visible in the RTC image in the bottom row. Given that RTC backscatter retrievals show less contamination from the effects of terrain, they are a preferred product for higher level analysis, i.e. they are an "Analysis Ready Data" (ARD) product.

Fig. 2 shows a geocoded version of the ascending image simulation (in map geometry). One can understand the RTC product roughly as a β^0 GTC backscatter image divided by the area (seen in the image simulation). Note how the mountainous foreslopes are much brighter in the area image, while the back-slopes are darker. By dividing the β^0 backscatter by the local contributing area, the foreslopes are proportionally darkened while the back-slopes are lightened in comparison to flat regions.

The algorithm for producing standardised RTC terrain-flattened gamma nought (γ^0_T) was published in Small (2011), and is referenced within the "CARD4L" CEOS Analysis Ready Data for Land specifications (CEOS, 2020). The algorithm's pseudo-code was used as a template while implementing the terrain-flattening module within European Space Agency's (ESA) SNAP toolbox (ESA European Space

Agency, 2020). Some errors in SNAP's implementation remain (Truckenbrodt et al., 2019) and will hopefully be remedied. Further implementations (Frey et al., 2013; Simard et al., 2016) have been widely applied, e.g. at the Alaska Satellite Facility.

Issues surrounding standardised RTC production for integration in data cubes were reviewed in Truckenbrodt et al. (2019).

3.2.3 Added value of Radiometric Flattening

Gamma nought backscatter retrieved from three S1 tracks covering Switzerland is shown in Fig. 3. The green region was covered by one ascending track, while the yellow and purple regions were covered by one ascending track and one descending track each. The grey region was covered by all three tracks (one descending, two ascending). A further ascending track covering the western extreme and another descending track covering the eastern extreme are not shown, as red/green/blue (RGB) overlays can only unambiguously highlight three tracks. Fig. 3(a) shows the GTC gamma nought backscatter γ^0_E, while in Fig. 3(b), the RTC gamma nought γ^0_T is shown. Note how the mountainous regions produce wildly different backscatter values on the fore- vs. backslopes in the GTC overlay, and that the terrain-induced distortions clearly visible in the GTC overlay are strongly reduced in the RTC overlay.

It should be noted that thematic land cover change interpretation would be severely impaired by terrain-induced distortions when analysis is based on a GTC time series. However, the RTC products allow interpretations also within the mountainous terrain (Small et al., 2011).

3.2.4 Local resolution in GTC and RTC products

Although the improvement to the thematic backscatter estimation is much improved in RTC vs. GTC products, the *local resolution* within both product types is identical. The poor local resolution on *foreslopes* in GTC products is made visible by their bright return (see Fig. 1). Although the distortion in the local radar brightness is strongly mitigated in the RTC case, the poor local resolution remains on the foreslopes. Indeed, no further improvement is conceivable given only a single image acquisition, as in that case no better resolved backscatter values are available at those locations.

In the following, a novel further stage of processing is introduced that works to mitigate that remaining issue.

3.3 Backscatter Composites through Local Resolution Weighting

In this section, we introduce a second stage process whereby the highly variable local resolution of radar imagery in mountainous terrain is dealt with by combining multiple data acquisitions acquired from differing geometries. Mosaicking processes typically place backscatter values from a single date next to adjacent areas viewed on a different date, applying Boolean class membership to each input data set. Here we instead apply the concept of fuzzy class membership (Wang, 1990)

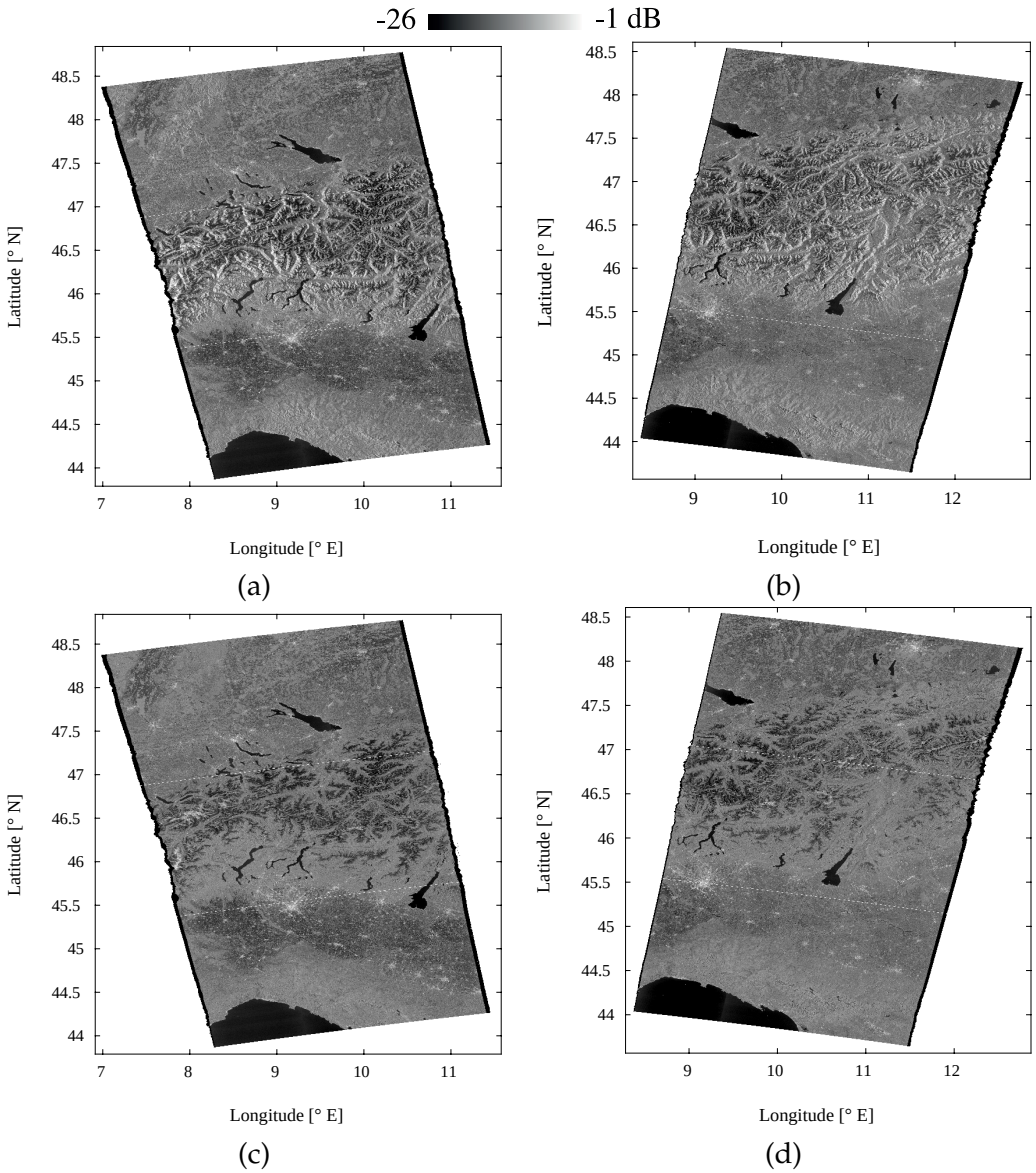

Fig. 1: S1 VH-pol. backscatter mosaics of central Alps in of three azimuth-adjacent IW GRDH products – geographic coordinates – Shuttle Radar Topography Mission (SRTM) DSM applied – (a) 2016.05.04 γ^0_E, (b) 2016.05.03 γ^0_E, (c) 2016.05.04 γ^0_T, (d) 2016.05.03 γ^0_T - Contains modified Copernicus Sentinel data (2016)

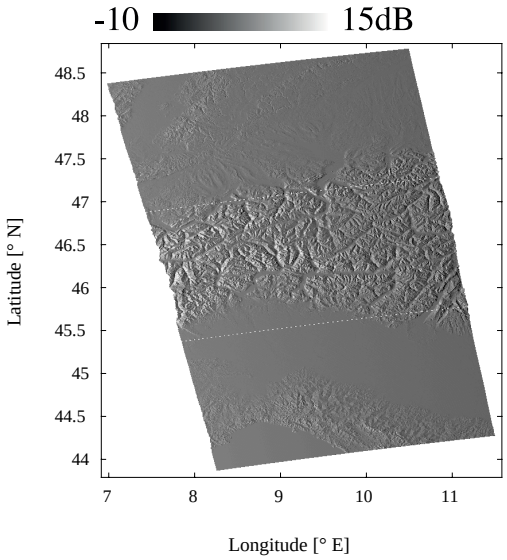

Fig. 2: Local contributing area of three azimuth-adjacent S1 IW GRDH products from 2016.05.04 - SRTM DSM applied - Central Alps

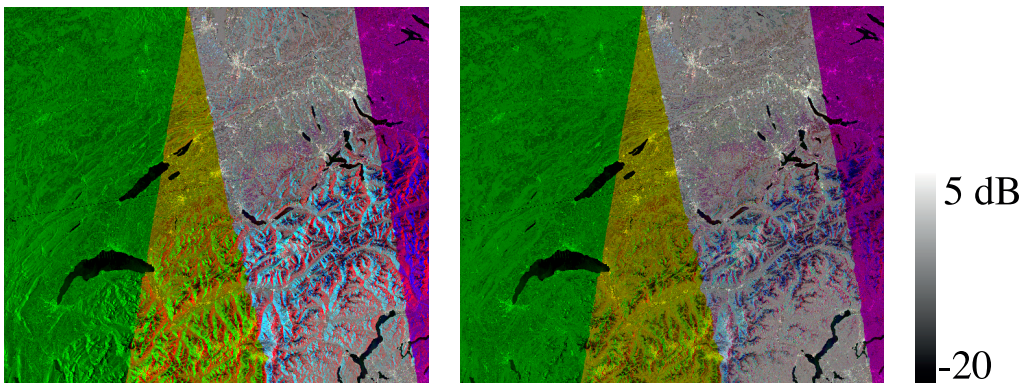

(a) GTC γ^0_E backscatter overlay (b) RTC γ^0_T backscatter overlay

Fig. 3: Comparison of temporal signature in S1 (a) GTC vs. (b) RTC VV-pol. backscatter overlays for IW acquisitions over Switzerland from 2017.04.27-29; Swiss map projection; Red=2017.04.27 05:33; Green=2017.04.28 17:21; Blue=2017.04.29 17:14 - Contains modified Copernicus Sentinel data (2017).

to each pixel, with variable (fractional) degrees of attribution from each input set based on the local resolution.

This method can be used to produce wide-area backscatter composites for a variety of applications that maintain validity also in mountainous regions. Unlike "one-off" SAR mosaicking approaches (de Grandi et al., 2011; Hoekman et al., 2010; Shimada et al., 2011; Soille et al., 2018; Syrris et al., 2019), LRW combines all available data into a local backscatter estimate based on a weighting appropriate for the local terrain distortions applicable within each individual contributing image product. This opens the door to seamless composites using data from multiple imaging modes and satellites. We demonstrate here how composites can be generated automatically over large regions. More generally, they have seen application as an *analysis ready* product (CEOS, 2016a,b) for a wider variety of users investigating land cover time series for applications such as forest classification (Rüetschi et al., 2018), storm-driven windthrow in forests (Rüetschi et al., 2019), or estimating melt onset (Howell et al., 2019).

3.3.1 Local Contributing Area

Recall how during RTC product generation, the local area was necessary in order to properly calculate the normalised radar cross section in the gamma nought convention under consideration of terrain. That local area can also be terrain geocoded for every acquisition, so after GTC and RTC processing one can have the GTC backscatter, RTC terrain-flattened gamma nought backscatter, and the local area – all in map geometry.

An example of two sets of GTC/Area/RTC product groups is illustrated in Fig. 4. The swissALTI3D height model (Federal Office of Topography swisstopo, 2019) was used for processing with 10 m postings. An ascending acquisition is shown in the top row, a descending acquisition in the bottom row. The dark regions are Lake *Thun* in the west and Lake *Brienz* in the east, with the city of *Interlaken* located directly between the lakes. Note how the foreslopes are clearly visible on one side of the hills in the GTC/Area images for the ascending case, and the opposite in the descending case. Similarly, the small black radar shadow regions are generally visible in one location in the ascending case, and a different one in the descending (see RTC and Area images). RTC images mark regions affected by radar shadow with a null-cell-value, as no backscatter estimate is possible there.

By combining RTC products generated from images acquired in different geometries, one is able to produce a composite backscatter image where such radar-shadow artefacts are strongly mitigated. Note that radar shadow is not common in S1 geometries: the example shown contains some of the steepest terrain in Europe, particularly the *Lauterbrunnen* valley south of Interlaken.

3.3.2 Local Resolution Weighting

Users of radar data should be aware that the local area observed is inversely proportional to the local image resolution (Small, 2012). So if one generates a composite with multiple co-registered inputs, whereby the inverse of the local area is used to weight the contribution of each input image, one has weighted each image by its local resolution. Given a local set of M non-shadowed input RTC image samples $\gamma^0_1 ... \gamma^0_M$, for each image i with a local area A_i, the sum of the available resolutions is:

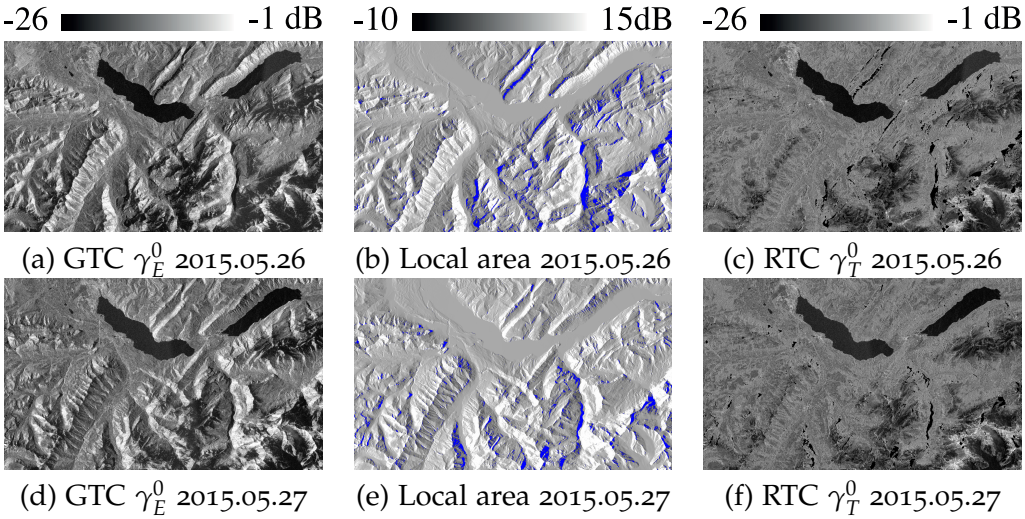

(a) GTC γ^0_E 2015.05.26 (b) Local area 2015.05.26 (c) RTC γ^0_T 2015.05.26

(d) GTC γ^0_E 2015.05.27 (e) Local area 2015.05.27 (f) RTC γ^0_T 2015.05.27

Fig. 4: GTC (left), Local Area with shadow marked blue (middle), RTC (right) for S1 IW GRDH descending (top, 2015.05.26) and ascending (bottom, 2015.05.267) acquisitions - Region surrounding Interlaken, Switzerland - Swiss oblique Mercator - VH-pol. swissALTI3D DEM applied - Contains modified Copernicus Sentinel data (2015).

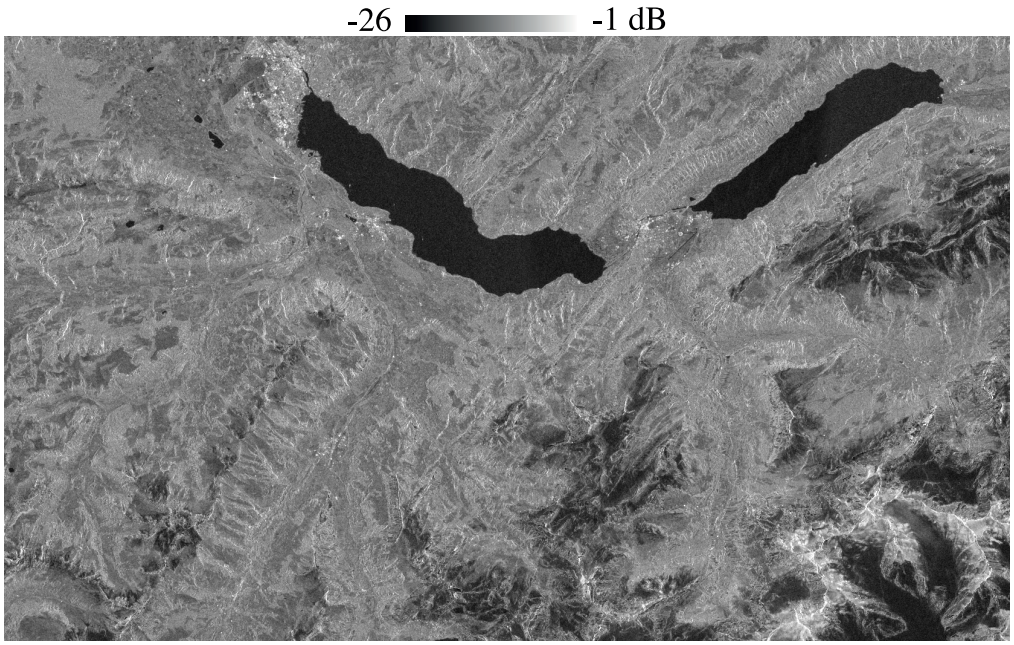

Fig. 5: LRW VH-pol. backscatter composite generated with ascending/descending combination of S1 IW acquisitions of 2015.05.26 and 2015.05.27 - Interlaken, Switzerland – Swiss map coordinates - swissALTI3D DEM applied - Contains modified Copernicus Sentinel data (2015).

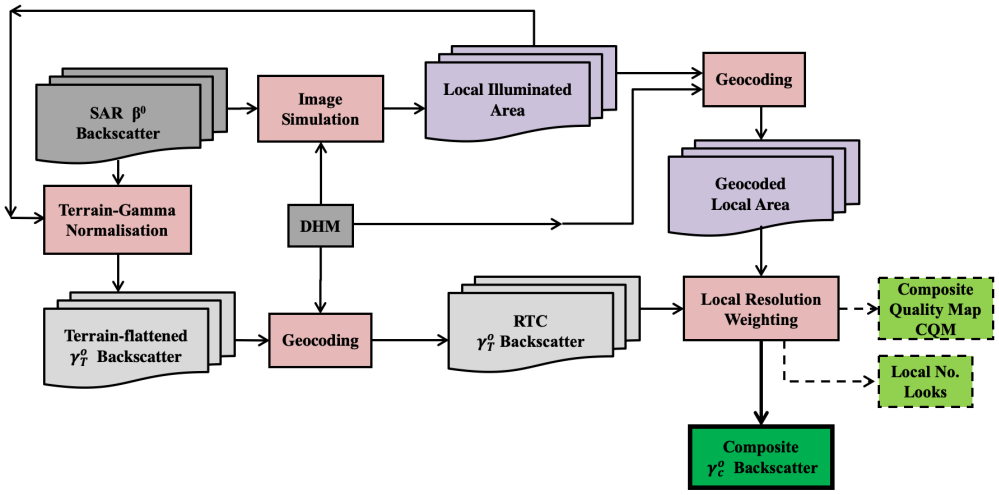

Fig. 6: Flowchart of LRW Backscatter Composite Processing starting with inputs DHM and SAR β^0 backscatter

$$S_r = \sum_{j=1}^{M} \frac{1}{A_j}. \tag{3.3}$$

The weight W_i to be applied to each image i is then:

$$W_i = \frac{\frac{1}{A_i}}{\sum_{j=1}^{M} \frac{1}{A_j}}. \tag{3.4}$$

Given that all weights $W_1 \dots W_M$ are now available, for any given map geometry sample location, the composite's backscatter estimate γ_c is the weighted sum of all M available input RTC backscatter values (Small, 2012; Small et al., 2004):

$$\gamma_c = \sum_{i=1}^{M} W_i \cdot \gamma_i^0. \tag{3.5}$$

Input images where the location in question is subject to radar shadow are *not included*, as they do not offer an observation. In those cases, the number of available images M is locally smaller and the weights account for that. A flowchart outlining the processing scheme is shown in Fig. 6. From the DHM and SAR backscatter inputs, image simulation is used to estimate the local illuminated area in radar geometry, then used to normalise the backscatter. Both the normalised backscatter and the area are terrain-geocoded. A set of areas and backscatter maps corresponding to a set time window are then integrated into a single backscatter map for a region of interest.

By applying the above equations given the two sets of S1 Area/RTC images shown in Fig. 4, one is able to generate the composite shown in Fig. 5. One can see that the radar shadow regions (black in the input RTC images) do not appear in the composite, as they only very rarely are co-located in multiple input images. This

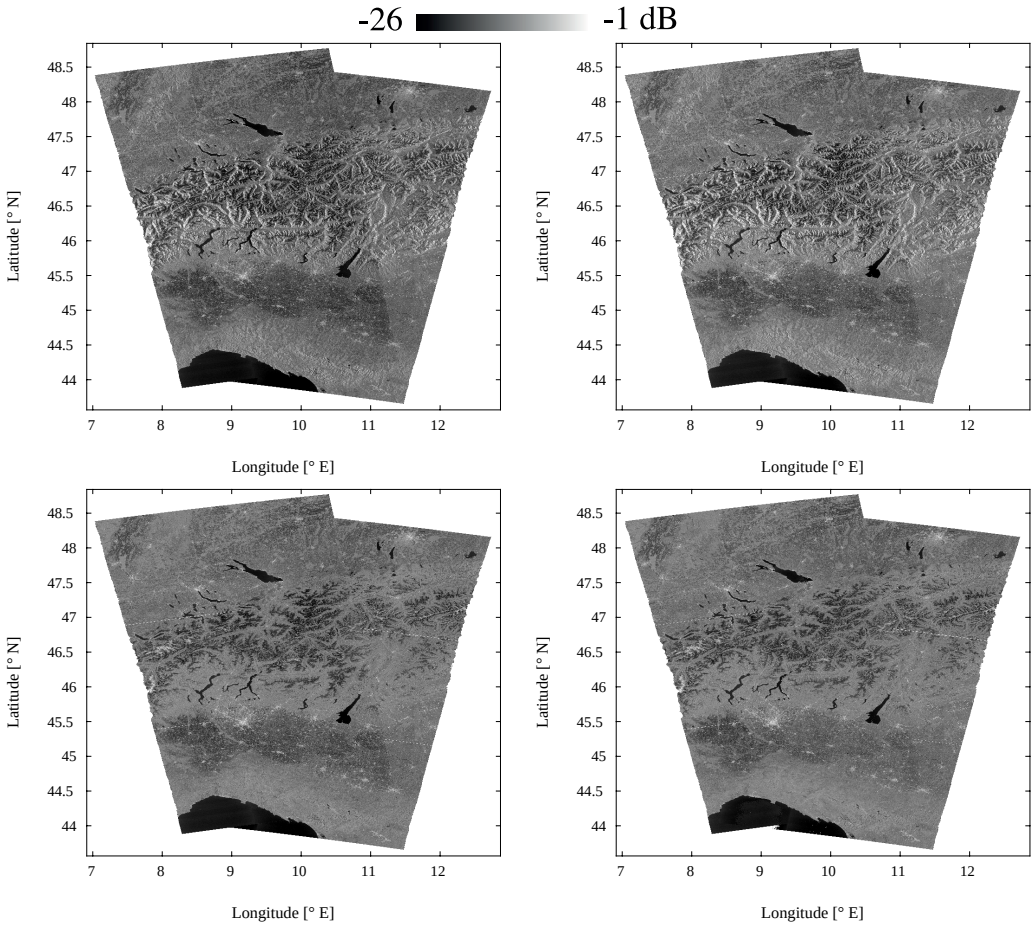

Fig. 7: Sigma nought vs. Gamma nought in the Alps - S1A Ascending/Descending 2016.05.03-04 - SRTM DEM applied – (top-left) σ^0_E mosaic, (top-right) γ^0_E mosaic, (bottom-left) γ^0_T mosaic, (bottom-right) γ^0_c composite - Contains modified Copernicus Sentinel data (2016)

leads to both sides of the hills and mountains being well resolved, as the effects of foreshortening and layover are strongly mitigated.

In this simple example, the number of input images was $M = 2$. But the technique can be applied with a larger number of input images: all available images that satisfy membership within the specified (a) spatial extent and (b) time window, can contribute to the local composite backscatter value. By increasing the number of images, one is able to extend full coverage and further lower the noise in the output composite. Lowering the noise is particularly important when working at the full resolution of the sensor. The composites are L3 products, expressed on a uniform spacetime grid scale (NASA, 1986; Wikipedia, 2020).

The top row of Fig. 7 juxtaposes simple mosaics following the σ^0_E and γ^0_E conventions, respectively. As radiometric terrain effects are not compensated, edge effects are prominent at the cutover between different sources. In Fig. 7 at bottom-left, one sees that an RTC has much improved behaviour in the mountains. Though not visible at this scale, variations in local resolution remain. In Fig. 7 at bottom right, the LRW backscatter is shown, whereby all available datasets were integrated to produce the composite. In the overlap region, the local resolution became more consistent, with fewer poor-quality outliers.

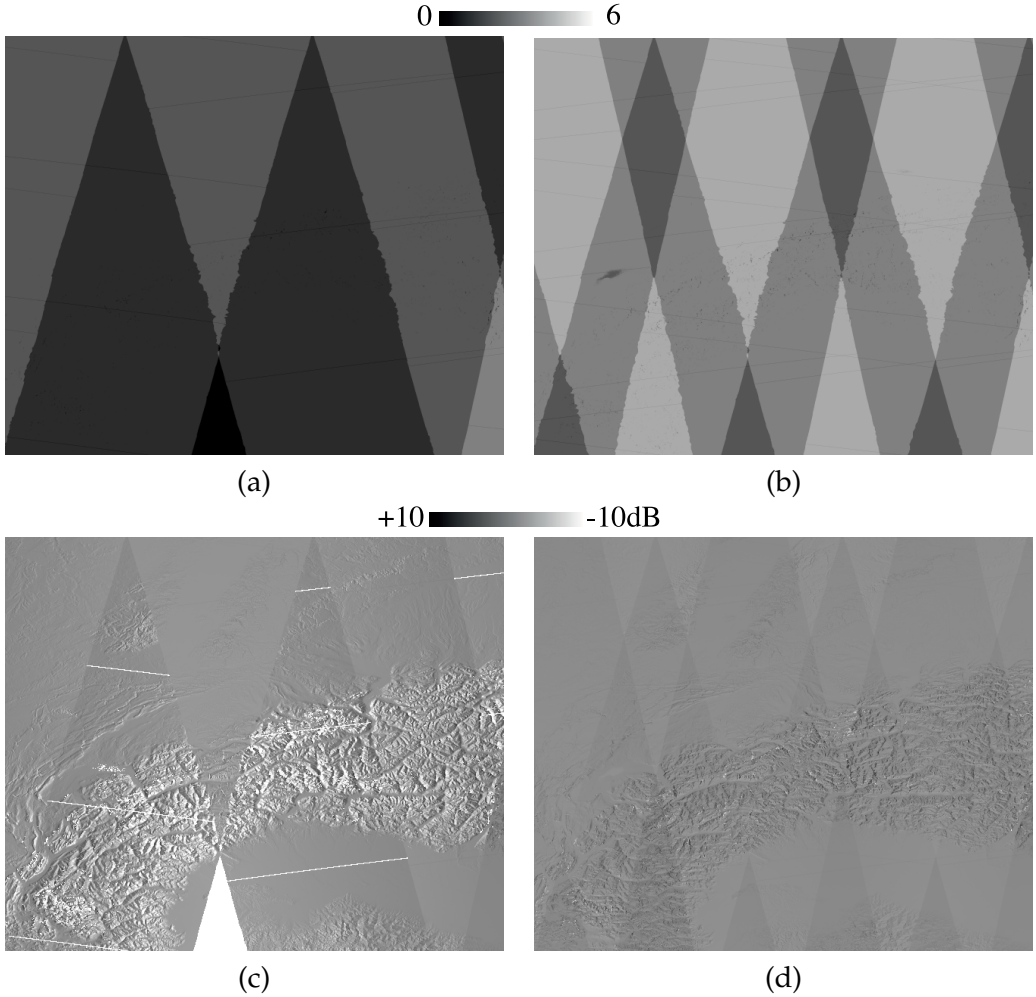

Fig. 8: Potential auxiliary products - Number of local observations vs. Composite Quality Map (CQM) - Western Alps: (a) No. of local observations in 4-day LRW, (b) No. of local observations in 6-day LRW, (c) CQM 4-day LRW, (d) CQM 6-day LRW

3.3.3 Local Quality: Number of Observations

Depending on the time window length and the number of tracks where a SAR sensor observes a specific region within the coverage area, the number of observations can vary significantly across a single LRW-backscatter map. Radar shadow can also reduce the number of local observations in areas affected by steep terrain. A map of the number of observations that were used to generate a backscatter composite can be useful as a potential auxiliary product to document variations in the quality of the composite generated. Examples of such auxiliary products are illustrated in Fig. 8. Fig. 8(a) shows the local number of observations in the case of a 4-day window, while Fig. 8(b) shows the same for a 6-day window. Note how widening the observation window by two days significantly increased the number of independent observations available for integration within the composite. Widening the temporal window improves the number of observations available, but also increases susceptibility to the introduction of uncertainties caused by natural variability within the time span of the window. That can potentially make interpretation of the composite backscatter value more difficult, so narrow time windows are preferred when possible.

These maps are useful as a qualitative map of possible variations in the quality of the composite, but they do not differentiate between ascending and descending observations, nor do they give a direct indication of the locally valid resolution within the composite. We propose a further auxiliary product to help map those variations.

3.3.4 Local Quality: Composite Local Resolution

A more quantitative auxiliary product that would be potentially useful to document variations in quality within an LRW-backscatter mosaic is illustrated in Fig. 8(c) and (d). These are Composite Quality Maps (CQM), calculated in a manner similar to the calculation of the backscatter composite itself. The map expressed in dB is calculated as:

$$CQM = -10 \cdot log_{10}(\sum_{i=1}^{M} W_i \cdot A_i). \tag{3.6}$$

Rather than applying the weights to each input RTC image, for these products, the weights are instead applied to the local contributing areas (originally used to generate the RTC products) to produce a map of the weighted relative area within the LRW-composite. High values indicate relatively high (good) resolution, low values indicate relatively coarse local resolution. CQM maps give a better indication of local quality, as they provide a finer account of the local availability (or not) of high quality observations. Note in Fig. 8(c) how the local resolution remains poor in mountainous regions when only ascending or only descending observations are available. When both ascending and descending observations are available for combination, then the local variations in resolution are reduced, and the composite's quality becomes more homogeneous. The types of variations seen in Fig. 8(c) would be cause for concern, and one might need to consult the auxiliary product to ensure that an analysis conducted on the composite would be valid in the region of interest. However, once relative homogeneity is achieved such as that seen in Fig. 8(d), then the auxiliary product can serve as a "green light" indicating that 2D analysis across the wide region covered by the whole composite can be applied without significant reservation. Fig. 9 shows the distribution of CQM for elevations above 1000 m in the western alps given acquisitions over (a) 4 days, and (b) 6 days vs. the local slope. Note that the 4-day case includes many points lower than -3dB, while after 6-days most of those poor quality points were improved to above that level. As expected, steep slopes exhibit even higher quality than flatter regions, as the back-slope acquisitions dominate there locally, with high local resolution. In the steepest slopes, the low number of such observations made the calculation of the median erratic. A log scale was applied here; the actual improvement in *linear* backscatter is even more pronounced.

3.4 Discussion

3.4.1 Input SAR product resolution

The LRW-approach can be used to integrate products from different sensors and modes into a single 2D backscatter map. Different L1 processing schemes can

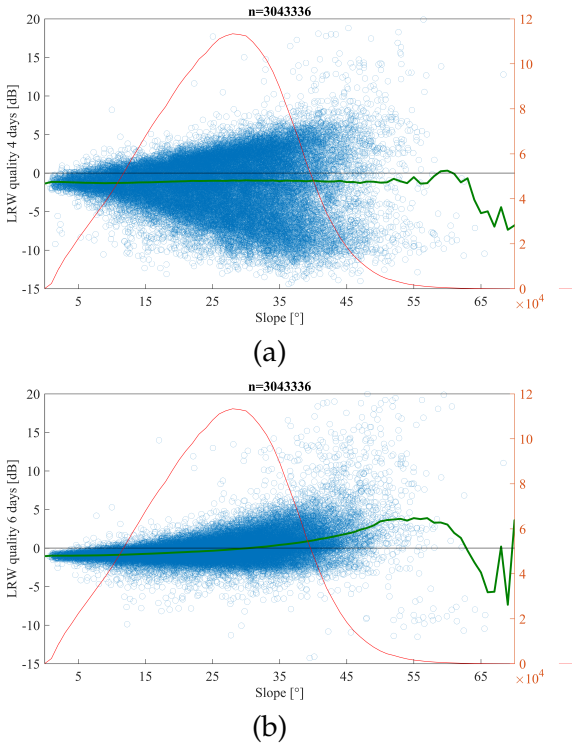

Fig. 9: Composite Quality vs. slope for (a) 4-day and (b) 6-day composites over Western Alps at elevations above 1000 m – Green line is median, red shows number of occurrences with given slope in data set

also be accommodated: e.g. if users prefer detected L1 SLC products presented in slant range as input, they can be used instead, or even "mixed" with ground range detected (GRD) products. Cases can arise where a set of contributing modes have different inherent resolutions. For example, one might wish to mix S1 IW GRDH (10 m samples) and Extra Wide Swath (EW) Ground Range Detected Medium resolution (GRDM) (40 m samples) into a single composite product. Then the user must decide how to treat the uneven input image resolutions. One can (a) undersample the IW-GRDH data to the same sample rate as GRDM and proceed with a uniform input sample interval, or (b) oversample the GRDM data into the higher sampling rate available in GRDH data. In the following, we chose the former option in order to reduce the data volume. Other use cases might favour other options.

3.4.2 Composite backscatter resolution

It is important to recall that the backscatter composite has a better mean spatial resolution than any one of the input SAR images used to generate it. This is the case because the LRW prefers to use information from the back-slopes (with high local resolution) in comparison to fore-slopes (with very poor local resolution due to foreshortening/layover). As a bonus, back-slopes provide more looks (more independent observations). The noise characteristics of the composite backscatter product are therefore superior to those of the individual input products due to (a) more looks per image, and (b) integration of information from more images. The composites can be based on backscatter values with or without denoising applied (Park et al., 2018; Piantanida, 2017) at the L1 input stage. In a manner similar to

the CQM, composite "noise maps" generated using the same weights applied to make the backscatter composite could provide guidance on local noise levels.

3.4.3 Multi-sensor Integration

The LRW compositing approach enables the integration of observations from multiple radar modes (e.g. S1 IW and EW or RS2 ScanSAR Wide (SCWA)) but also from different sensors. In cases where the sensors observe at the same wavelength (e.g. S1 and RS2 or RCM), then given that all sensors meet consistently high standards of geometric and radiometric calibration, the LRW-backscatter composites can benefit from an increased diversity of viewing geometries rather than suffering from it, as is the case in single-track analyses or InSAR combinations that require repeat passes. For example, S1 data crossed with RS2 or RCM will not likely be able to offer systematic InSAR pairs, but their L1 backscatter products can be combined into hybrid backscatter maps using the LRW approach.

An example of the differences between evaluations of a region given data only from a single sensor, or by integrated calibrated "hybrid" multisensor retrievals is shown in Fig. 10. A DEM based on the Canadian DEM (CDED) data set (Santoro & Strozzi, 2012) was used during LRW product generation. For the period of Aug. 2–3, 2016, in Fig. 10(a), an LRW-backscatter composite of Ellesmere island is shown that was based on RS2 data only. In Fig. 10(b), an LRW-backscatter composite is shown for the same region and time period that was based on S1A data alone. S1B had not yet been commissioned when these data were acquired. S1A mainly covered only the southern part of the region, and RS2 mainly the eastern central portion.

In Fig. 10(c) an integrated LRW taking data from both S1A and RS2 is shown. This is the first known instance of a composite based on calibrated *multi-sensor SAR* input. Each sensor's tracks have individual terrain-induced distortions that were first corrected (RTC product generation) and then used to locally weight each sensor's contribution to the composite (LRW ARD product generation). The coverage is much wider than either in isolation. Note that no obvious "edge" effects are visible at the boundary between S1A and RS2 acquisitions. LRW products from our processor were recently used to demonstrate that single-day temporal resolution is becoming possible with SAR sensors (Howell et al., 2019), becoming competitive with the coverage and revisit of passive microwave and scatterometer sensors while providing orders of magnitude of improvement in spatial resolution. Multiple sensors can be combined at appropriate "Application Readiness Levels" (ARL), as introduced in Wulder et al. (2015). ARL-1 through ARL-3 categorise sensors according to their compatibility. Seamless ARL-3 backscatter coverages of the types shown here are well suited to direct integration of multiple virtual constellations for regional or global terrestrial monitoring.

3.4.4 Seamless Wide-area Composites

Users of a radar composite need not always know the ultimate origin of each backscatter observation used to build up the 2D maps they analyse. These composites are not simple "mosaics" of independent images, but actual merged composite outputs, where in overlapping regions the quality of the composite improves upon the individual inputs. Note that no "feathering" was applied at the edges between individual acquisitions: a hard cutover was always applied. The guarantor for the lack of edge effects between individual acquisitions is that both data sources meet

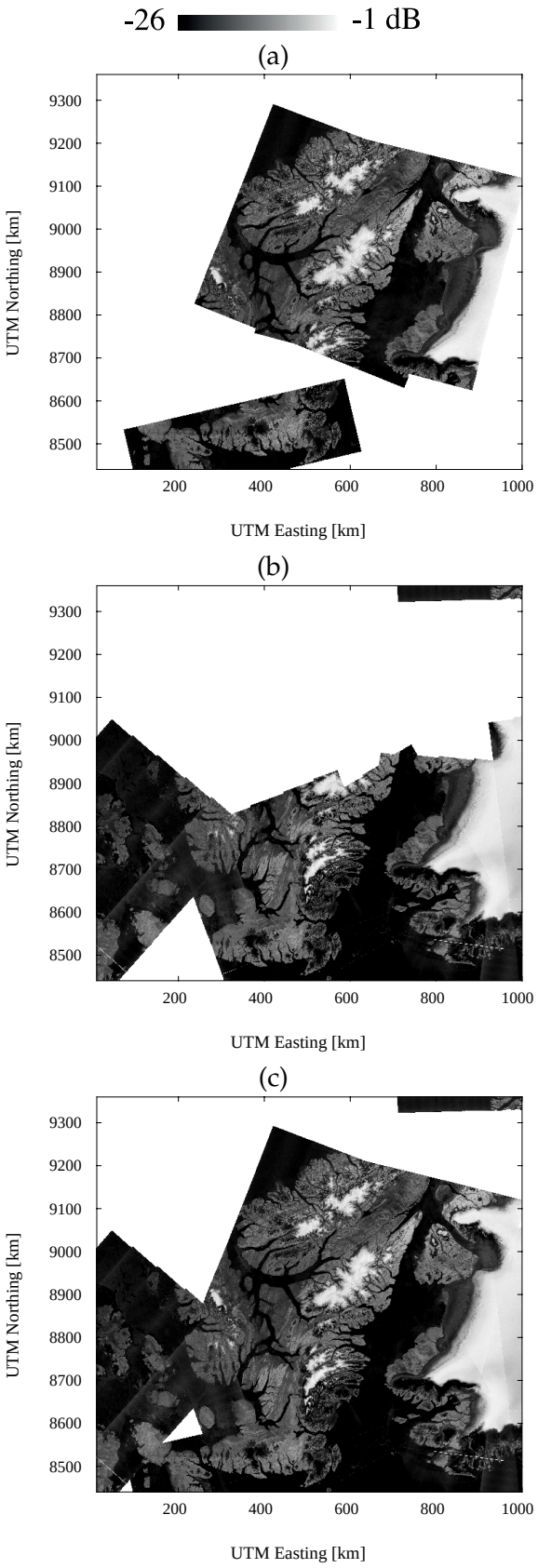

Fig. 10: Single vs. multisensor HV-pol. backscatter composites - (unobserved voids white) - Aug. 2-3, 2016 - Ellesmere Island, Nunavut, Canada - (a) RS2 only (SCWA), (b) S1A only (EW), (c) S1A combined with RS2 - UTM zone 22 map projection - Contains modified Copernicus Sentinel data (2016) - RADARSAT-2 Data and Products ©MacDonald Dettwiler and Associates Ltd. (2016) - All Rights Reserved. RADARSAT is an official trademark of the Canadian Space Agency.

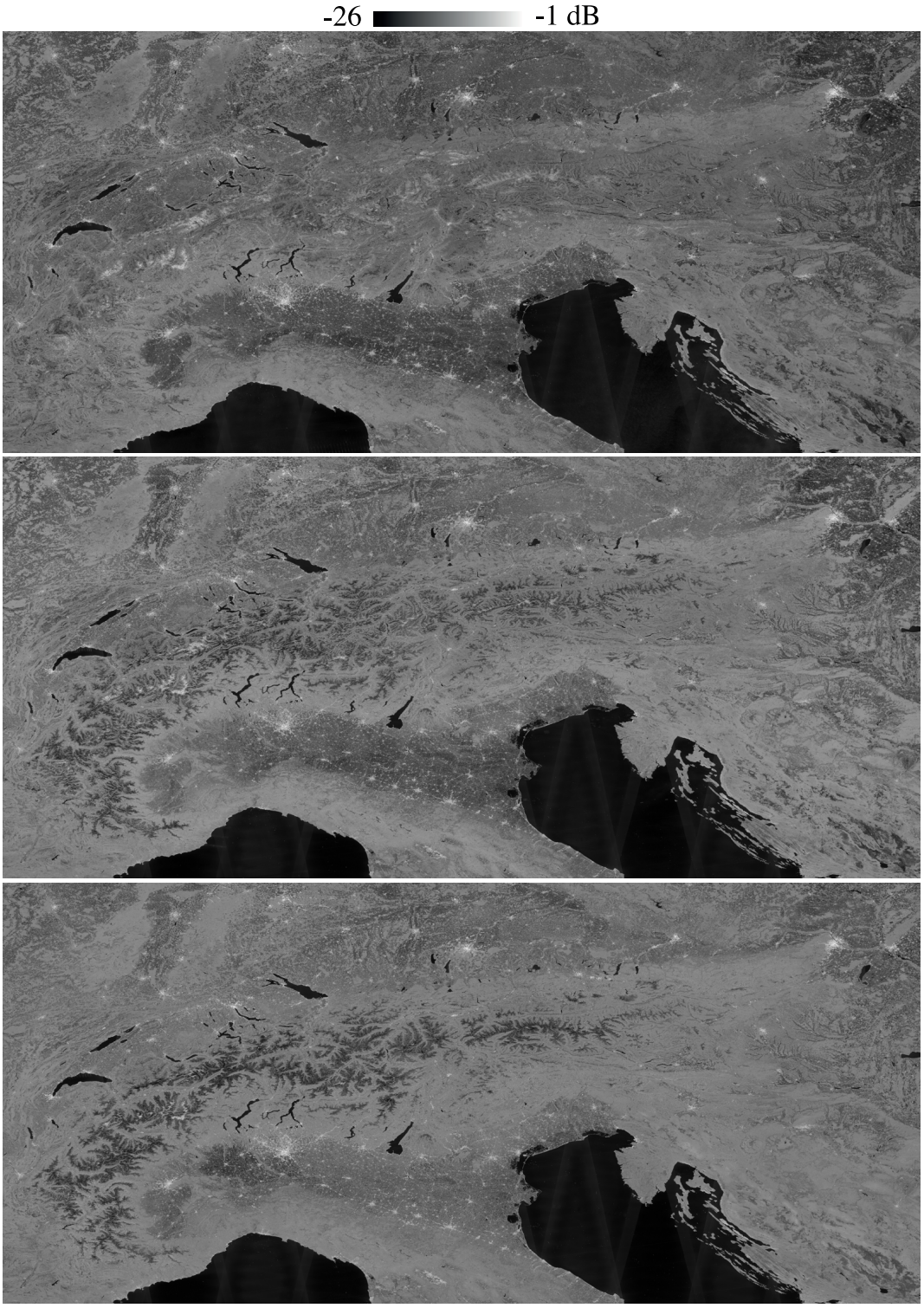

Fig. 11: Time series of wide-area S1A VH-pol. backscatter composites with 12 day time windows in 2017 covering the Alps – (a) 2017.01.01-12, (b) 2017.03.26-04.06, (c) 2017.05.13-24 – Lat/Lon 43.5-49°N; 5.5-17.5°E – SRTM applied – Contains modified Copernicus Sentinel data (2017).

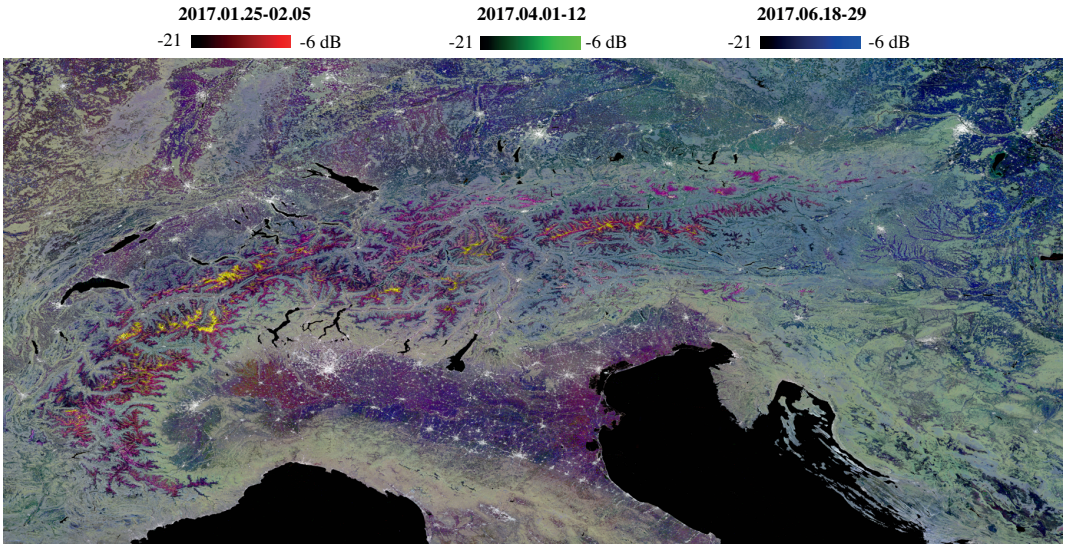

Fig. 12: Alpine snow melt visualised in RGB overlay of three LRW S1 VH-pol. backscatter composites; each colour channel corresponds to the following date ranges – Red: 2017.01.25-02.05, Green: 2017.04.01-12, Blue: 2017.06.18-29 – Lat/Lon 43.5-49°N; 5.5-17.5°E – SRTM applied – Contains modified Copernicus Sentinel data (2017).

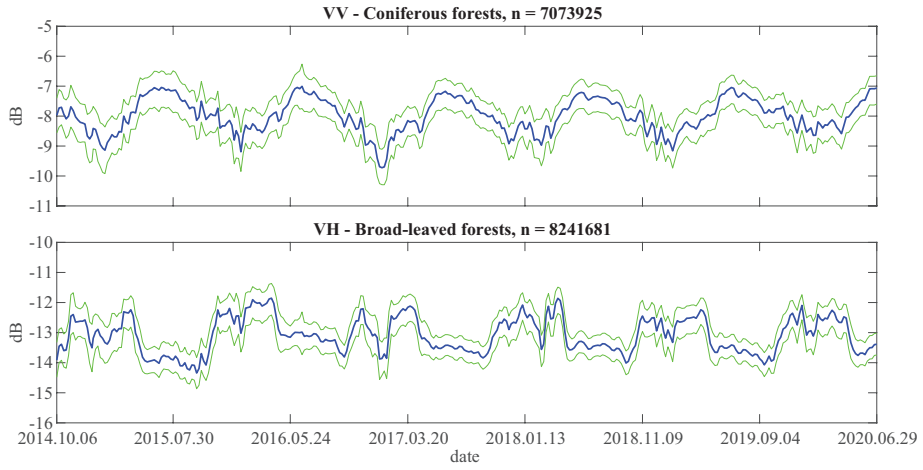

Fig. 13: Alpine Forest time series: (top) LRW VV-pol. backscatter from coniferous forests, (bottom) VH-pol. backscatter from broad-leaved forests. The number of investigated pixels (n) was comparable for both forest types – Medians in blue, quartiles in green - Lat/Lon 43.5-49°N; 5.5-17.5°E – Contains modified Copernicus Sentinel data (2014-2020).

strict geometric and radiometric calibration requirements (Schubert et al., 2012b; Small et al., 2011). The method is applicable to single, dual- or quad-pol datasets, and not dependent on the availability of the full scattering matrix (Antropov et al., 2012).

Proper terrain-corrections ensure that no significant beam-edge artefacts are visible. Being able to combine data from multiple radar sensors could offer 1-2 day temporal resolution over wide regions, opening up research questions and applications that base their analysis on 2D change detection to wide-area coverage. It is also more cost-effective to cooperate among space agencies, as services built on their satellite constellation become less sensitive to a single point of failure.

Examples of wide-area composites covering the whole of the European Alps are shown in Fig. 11. Alpine wide-area mosaics have been generated since the first release of S1A data in Oct. 2014. In the following, we show three sample images illustrating the seasonal progression of snow melting in the Alps from Jan. through May 2017. In these cases, first 10x10 multi-looking was applied to the input GRDH products, RTC processing was performed, and local resolution weighting was applied. This was performed for a set of (overlapping) time windows. In the first example, a time-window of 12 days was used. Fig. 11 shows a series of three wide-area backscatter composites calculated using the LRW approach. The backscatter range was set identically for all 3 RGB channels (-21 to -6dB). A 12-day window length was applied. Note how relatively high backscatter is seen during the winter in Fig. 11(a), with melting (lower backscatter) evident in the March image seen in Fig. 11(b). The melting is seen to be more intense and extends also to higher elevations by May, as seen in Fig. 11(c). The progression of melting from lower elevations to higher is made even clearer in the RGB-overlay of three 12-day composites shown in Fig. 12. The highest peaks appear yellow, as their backscatter remained high (from the dry snow present locally) in the first two time-windows (bright red and green channels), only reducing in the final composite (dark blue channel). Short time windows can increase the probability of parts of the composite having a "single source", which can increase the likelihood of having a visible edge within a composite.

3.4.5 Wet snow and ice mapping

Optical sensors see snow clearly in the absence of clouds, but they are not able to differentiate well between dry and wet snow. C-band radar sensors provide an extra layer of information: the backscatter they receive is modulated strongly by wet snow (Linlor, 1980), while dry snow is often nearly transparent.

Mapping wet snow is important for hydrology (Bavay et al., 2009) and run-off models (He et al., 2014). Mapping wet snow particularly in the *mountains* is important, as (a) that is where snow lies for extended periods, and (b) snow-laden mountains provide a water source to many people for many months when alternative sources are not easily accessible (Viviroli & Weingartner, 2004). LRW backscatter composites provide wide area coverage with an otherwise unknown combination of high geometric accuracy, radiometric calibration, and consistent local resolution.

Wet snow has traditionally been mapped by comparing new incoming "candidate" images with a dry cold reference backscatter image, and delineating image regions where the backscatter is significantly lower than the reference (Nagler & Rott, 2000; Nagler et al., 2016). This relies on a stream of strictly single-track acquisitions,

with dry cold reference images pre-calculated for each track (Baghdadi et al., 1997; Haefner & Piesbergen, 1997). The temporal resolution is tied to the repeat-pass interval.

Studies of requirements for snow products in the past (Alverson & Ryan, 2007; Malenovský et al., 2012) have requested *daily* temporal resolution – however, this has never been achieved over wide areas: neither with optical sensors (due to cloud cover) nor radar (due to longer revisit intervals). Using LRW wide-area composites, one is able to provide maps with large spatial coverage with temporal resolution not directly tied to the orbital repeat interval, while simultaneously ensuring use of a consistent dry cold reference and more homogeneous local resolution, especially in mountainous regions (Jäger, 2016; Rohner, 2014).

3.4.6 Land cover monitoring

Fig. 13 illustrates a longitudinal time series of backscatter signatures retrieved from LRW composites covering the Alps from 2014 to 2020. Backscatter from CORINE land cover 2018 (Copernicus, 2019) forest class regions were extracted after 3x3 erosion to reduce edge contamination. The backscatter statistics for each forest type were then evaluated through time. As seen in Fig. 13(top) the conifer VV-pol. backscatter regularly rises in the summer and falls in the winter, possibly due to needle growth (Rüetschi et al., 2018). A seasonal trend with opposite phase is seen in VH-pol. within broad-leaved forests in Fig. 13(bottom). This may be caused by stronger backscatter from branches and/or a stronger ground scattering component in the leaf-off state (Rüetschi et al., 2018). Thaw events occasionally introduce ambiguity in mid-winter, esp. in VH-pol. Quartile backscatter intervals are marked in green above and below the blue median. Similar backscatter trends were reported in local Alpine test sites in Rüetschi et al. (2018) and Dostálová et al. (2018).

Backscatter composites generated via this LRW method have been successfully used to monitor the phenology and classify different types of forest (Rüetschi et al., 2018) and for change detection on short time scales, e.g. to detect windthrow in forests after a storm (Rüetschi et al., 2019). Achieving a seasonal overview of Alpine conifer backscatter would be more challenging using single-track approaches based on L1 products (NASA, 1986), but it becomes a relatively quick task given the availability of L3 (NASA, 1986) backscatter composites. Single-track approaches do not integrate information from other viewpoints and are hence subject to higher noise levels.

3.5 Conclusions and Recommendations

We demonstrated backscatter composites that fulfil the definition of L3 products (NASA, 1986). LRW composites are generated on *uniform space-time scales*, have *completeness and consistency properties* (seamless wide-area coverage with robust radiometric terrain correction), and cover *complete regions mosaicked together from multiple orbits*. To our knowledge, no previously proposed backscatter mosaicking methodology has fulfilled these criteria, often lacking radiometric terrain correction and always exhibiting inconsistent geometric resolution over areas with steep terrain. Our methodology is also the first to demonstrate seamless multi-sensor integration.

Space agencies have until now developed constellations that included a maximum of a few radar imaging platforms. With "new space", we are entering an era with possibly larger constellations (Filippazzo & Dinand, 2017; Plourde et al., 2018; Seguin & Geudtner, 2018) (e.g. ICEYE (Antropov et al., 2018; Laurila et al., 2016), Capella Space (Farquharson et al., 2018)) and this may enable the attainment of daily coverage (at X-band) by combining data acquired in different geometries. Only limited spatial coverage will be possible in cases where solely spotlight or stripmap *narrow*-swath acquisitions are available - it will be possible to extend the size of the region covered at high temporal resolution if instead predominantly *wide*-swath acquisitions are available (e.g. ScanSAR or TOPSAR). Using wide-swath modes, operators are encouraged to exploit a nominal incident angle range that endeavours to stay within a consistent backscatter regime (e.g. as S1 IW). In the future, there will likely be a trend to naturally introduce this data into the mix of existing institutional data streams. These trends underline again the need for powerful techniques for constructing composites.

Comparing the two major methods of wet snow detection, one may note the following. Ensuring that ascending/descending acquisitions are acquired close in time allows composites generated from their data to maintain a narrow time-tag (Small, 2014).

Single-track/mode methodologies are tied to a single sensor setting and best suited to "data poor" environments.

Backscatter composite methodologies are open to combining inputs from multiple SAR sensors and modes, whether that be e.g. IW+EW in the S1 case, or S1 IW+EW + RS2 SCNB+SCWA. They are best suited to "data rich" environments. Multiple beam modes may even be acquired in different tracks/relative orbits. Diversity in the details of the acquisition modes being integrated is not a hindrance. On the contrary, it can provide extra information, e.g. by providing measurements in mountain valleys in perpetual radar shadow given only a different sensor's set of available geometries. Although backscatter composites from local resolution weighting show their largest benefits in mountainous regions where the high resolution on backslopes is harnessed, they do not lose applicability also in comparative flatlands. In flat smooth terrain, differences caused by individual viewing geometries may remain apparent (e.g. co-pol. Bragg scattering on water). Depending on their relative strength, without further corrections, these may hinder interpretation of local backscatter behaviour in the composite, detracting from the "analysis readiness" of the L3 dataset.

The following recommendations are made:

- Over mountainous regions, radar satellite acquisition plans should stress ascending/descending tracks to be planned with as little delay as possible to ensure temporal coherency (these requirements can vary with application - e.g. for wet snow: daily).
- Consideration should be given to adding level 3 (NASA, 1986) analysis ready wide-area backscatter composites to the standard product families of radar satellites.
- Space agencies may consider consulting with each other to define a possible test region with a harmonised acquisition pattern (Small, 2014) for study of improvements to composite backscatter temporal resolution. For example, were the full complement of S1 and RCM satellites to participate in monitoring

a springtime melt process over a mountainous region, the temporal resolution would be significantly improved. Improving the temporal resolution will be advantageous in capturing leaf emergence, monitoring leaf fall, and generally in change detection (e.g. mapping wet snow or windthrow).

By adding wide-area calibrated geocoded backscatter products to their standard offerings, space agencies would make their data much more accessible to a wide spectrum of users, encouraging the development of new applications.

3.6 Acknowledgments

The authors wish to thank the European Space Agency (ESA) and the Copernicus Programme for the Sentinel-1 data, as well as the Canadian Space Agency (CSA) and MDA for the use of the RADARSAT-2 data. Thanks in particular are due to Stephen Howell and Mike Brady of Environment and Climate Change Canada and Yves Crevier of CSA for arranging access to the RADARSAT-2 Data and Products ©MacDonald Dettwiler and Associates Ltd. (2016) - All Rights Reserved. RADARSAT is an official trademark of the Canadian Space Agency. Figures contain modified Copernicus Sentinel data (2014-2020). Support from the ESA-funded Telespazio/Vega IDEAS+ VEGA/AG/15/01757 project is gratefully acknowledged. Thanks to the reviewers for their highly constructive comments.

Bibliography

Alverson, K. & Ryan, B. (2007). Cryosphere Theme Report. Retrieved 2022-08-28, from http://igos-cryosphere.org/docs/cryos_theme_report.pdf.

Antropov, O., Praks, J., Kauppinen, M., Laurila, P., Ignatenko, V., & Modrzewski, R. (2018). Assessment of Operational Microsatellite Based SAR for Earth Observation Applications. In *2018 2nd URSI Atlantic Radio Science Meeting (AT-RASC)* (pp.ĩ).: IEEE.

Antropov, O., Rauste, Y., Lonnqvist, A., & Hame, T. (2012). PolSAR Mosaic Normalization for Improved Land-Cover Mapping. *IEEE Geosci. Remote Sens. Lett.*, *9*(6), 1074–1078, doi: 10.1109/LGRS.2012.2190263.

Baghdadi, N., Gauthier, Y., & Bernier, M. (1997). Capability of Multitemporal ERS-1 SAR Data for Wet-Snow Mapping. *Remote Sensing of Environment*, *60*(2), 174–186, doi: 10.1016/S0034-4257(96)00180-0.

Bavay, M., Lehning, M., Jonas, T., & Löwe, H. (2009). Simulations of future snow cover and discharge in Alpine headwater catchments. *Hydrol. Process.*, *23*(1), 95–108, doi: 10.1002/hyp.7195.

Bayer, T., Winter, R., & Schreier, G. (1991). Terrain influences in SAR backscatter and attempts to their correction. *IEEE Transactions on Geoscience and Remote Sensing*, *29*(3), 451–462, doi: 10.1109/36.79436.

CEOS (2016a). The CEOS Data Cube: Three-year work plan 2016-2018. Retrieved 2022-08-11, from http://ceos.org/document_management/Meetings/Plenary/30/Documents/5.3_Killough_Cube-3-Year-Work-Plan_v1.1.pdf.

CEOS (2016b). CEOS Future data access and analysis architectures study. Retrieved 2022-08-11, from http://ceos.org/document_management/Meetings/Plenary/30/Documents/5.2_Future-Data-Architectures-Interim-Report_v.1.pdf.

CEOS (2020). Analysis Ready Data for Land (CARD4L) - Product Family Specification, Normalised Radar Backscatter. Retrieved 2022-08-11, from http://ceos.org/ard/files/PFS/NRB/v5.0/CARD4L-PFS_Normalised_Radar_Backscatter-v5.0.pdf.

Copernicus (2019). Copernicus Data Product CLC2018. Retrieved 2022-08-28, from https://land.copernicus.eu/pan-european/corine-land-cover/clc2018.

de Grandi, G. D., Bouvet, A., Lucas, R. M., Shimada, M., Monaco, S., & Rosenqvist, A. (2011). The K&C PALSAR Mosaic of the African Continent: Processing Issues and First Thematic Results. *IEEE Transactions on Geoscience and Remote Sensing*, *49*(10), 3593–3610, doi: 10.1109/TGRS.2011.2165288.

Dostálová, A., Wagner, W., Milenković, M., & Hollaus, M. (2018). Annual seasonality in Sentinel-1 signal for forest mapping and forest type classification. *International Journal of Remote Sensing*, *39*(21), 7738–7760, doi: 10.1080/01431161.2018.1479788.

ESA European Space Agency (2020). SNAP https://earth.esa.int/eogateway/tools/snap.

Farquharson, G., Woods, W., Stringham, C., Sankarambadi, N., & Riggi, L. (2018). The Capella Synthetic Aperture Radar Constellation. In *EUSAR 2018* (pp. 1245–1249). Berlin, Germany.

Federal Office of Topography swisstopo (2019). swissALTI3D. Retrieved 2019-09-04, from https://www.swisstopo.admin.ch/content/swisstopo-internet/de/geodata/height/alti3d/_jcr_content/contentPar/tabs_copy/items/dokumente/tabPar/downloadlist/downloadItems/846_1464690554132.download/swissALTI3D_detaillierte%20Produktinfo_DE_bf.pdf.

Filippazzo, G. & Dinand, S. (2017). The Potential Impact Of Small Satellite Radar Constellations On Traditional Space Systems. In *Federated and Fractionated Satellite Systems Workshop*, volume 5 (pp. 1–12). Toulouse, France: ISAE SUP AERO.

Foody, G. M. (1986). An Assessment of the Topographic Effects on SAR Image Tone. *Canadian Journal of Remote Sensing*, *12*(2), 124–131, doi: 10.1080/07038992.1986.10855104.

Frey, O., Santoro, M., Werner, C. L., & Wegmüller, U. (2013). DEM-Based SAR Pixel-Area Estimation for Enhanced Geocoding Refinement and Radiometric Normalization. *IEEE Geosci. Remote Sens. Lett.*, *10*(1), 48–52, doi: 10.1109/L-GRS.2012.2192093.

Gisinger, C., Schubert, A., Breit, H., Garthwaite, M., Balss, U., Willberg, M., Small, D., Eineder, M., & Miranda, N. (2021). In-Depth Verification of Sentinel-1 and TerraSAR-X Geolocation Accuracy Using the Australian Corner Reflector Array. *IEEE Transactions on Geoscience and Remote Sensing*, *59*(2), 1154–1181, doi: 10.1109/TGRS.2019.2961248.

Haefner, H. & Piesbergen, J. (1997). High Alpine snow cover monitoring using ERS-1 SAR and Landsat TM data. *IAHS Remote Sens. Hydrol.*, (242), 113–118.

He, Z. H., Parajka, J., Tian, F. Q., & Blöschl, G. (2014). Estimating degree-day factors from MODIS for snowmelt runoff modeling. *Hydrol. Earth Syst. Sci.*, *18*(12), 4773–4789, doi: 10.5194/hess-18-4773-2014.

Hoekman, D. H., Vissers, M. A. M., & Wielaard, N. (2010). PALSAR Wide-Area Mapping of Borneo: Methodology and Map Validation. *IEEE Journal of Selected Topics in Applied Earth Observations and Remote Sensing*, *3*(4), 605–617, doi: 10.1109/JSTARS.2010.2070059.

Howell, S. E., Small, D., Rohner, C., Mahmud, M. S., Yackel, J. J., & Brady, M. (2019). Estimating melt onset over Arctic sea ice from time series multi-sensor Sentinel-1 and RADARSAT-2 backscatter. *Remote Sensing of Environment*, *229*, 48–59, doi: 10.1016/J.RSE.2019.04.031.

Jäger, D. (2016). *Wide-area wet snow mapping of the Alps based on Sentinel-1 multi-track radar backscatter composites*. Master's thesis, University of Zurich, Zurich, Switzerland.

Justice, C. O., Townshend, J. R. G., Vermote, E. F., Masuoka, E., Wolfe, R. E., Saleous, N., Roy, D., & Morisette, J. T. (2002). An overview of MODIS Land data processing and product status. *Remote Sensing of Environment*, *83*(1-2), 3–15, doi: 10.1016/S0034-4257(02)00084-6.

Kellndorfer, J. M., Pierce, L. E., Dobson, M. C., & Ulaby, F. T. (1998). Toward consistent regional-to-global-scale vegetation characterization using orbital SAR systems. *IEEE Transactions on Geoscience and Remote Sensing*, *36*(5), 1396–1411, doi: 10.1109/36.718844.

Laurila, P., Modrzewski, R., Cheng, T., Campbell, B., & Yanni, V. G. (2016). Validation of ICEYE Small Satellite SAR Design for Ice Detection and Imaging. In *Arctic Technology Conference* (pp. 1–10). St. John's, Canada: Offshore Technology Conference.

Linlor, W. I. (1980). Permittivity and attenuation of wet snow between 4 and 12 GHz. *J. Appl. Phys.*, *51*(5), 2811–2816, doi: 10.1063/1.327947.

Löw, A. & Mauser, W. (2007). Generation of geometrically and radiometrically terrain corrected SAR image products. *Remote Sensing of Environment*, *106*(3), 337–349, doi: 10.1016/j.rse.2006.09.002.

Malenovský, Z., Rott, H., Cihlar, J., Schaepman, M. E., García-Santos, G., Fernandes, R., & Berger, M. (2012). Sentinels for science: Potential of Sentinel-1, -2, and -3 missions for scientific observations of ocean, cryosphere, and land. *Remote Sensing of Environment*, *120*, 91–101, doi: 10.1016/j.rse.2011.09.026.

Meier, E., Frei, U., & Nüesch, D. (1993). Precise terrain corrected geocoded images. In *SAR Geocoding: Data and Systems* (pp. 173–186). Karlsruhe, Germany: Wichmann Verlag.

Mladenova, I. E., Jackson, T. J., Bindlish, R., & Hensley, S. (2013). Incidence Angle Normalization of Radar Backscatter Data. *IEEE Transactions on Geoscience and Remote Sensing*, *51*(3), 1791–1804, doi: 10.1109/TGRS.2012.2205264.

Nagler, T. & Rott, H. (2000). Retrieval of wet snow by means of multitemporal SAR data. *IEEE Transactions on Geoscience and Remote Sensing*, *38*(2), 754–765, doi: 10.1109/36.842004.

Nagler, T., Rott, H., Ripper, E., Bippus, G., & Hetzenecker, M. (2016). Advancements for Snowmelt Monitoring by Means of Sentinel-1 SAR. *Remote Sensing*, *8*(4), 348, doi: 10.3390/rs8040348.

NASA (1986). Report of the EOS Data Panel. Retrieved 2022-08-19, from http://hdl.handle.net/2060/19860021622.

NASA (2020). MODIS Data Products. Retrieved 2022-08-11, from https://modis.gsfc.nasa.gov/data/dataprod/.

Park, J., Korosov, A. A., Babiker, M., Sandven, S., & Won, J. (2018). Efficient Thermal Noise Removal for Sentinel-1 TOPSAR Cross-Polarization Channel. *IEEE Transactions on Geoscience and Remote Sensing*, *56*(3), 1555–1565, doi: 10.1109/TGRS.2017.2765248.

Piantanida, R. (2017). Thermal denoising of products generated by the Sentinel-1 IPF. Retrieved 2022-08-11, from https://sentinel.esa.int/documents/247904/0/Thermal-Denoising-of-Products-Generated-by-Sentinel-1-IPF/11d3bd86-5d6a-4e07-b8bb-912c1093bf91.

Plourde, P., Thompson, A., Jochum, M., Geudtner, D., Seguin, G., Beckett, K., Brisco, B., van der Kooij, M., & Vachon, P. W. (2018). EO Summit 2017: Challenges for Next Generation SAR. *Canadian Journal of Remote Sensing*, *44*(3), 243–246, doi: 10.1080/07038992.2018.1498740.

Rohner, C. (2014). *Relating Snow Wetness Information Gained from the Intercantonal Measurement and Information System Stations in Switzerland to Envisat ASAR Backscatter*. Master's thesis, University of Zurich, Zurich, Switzerland.

Rüetschi, M., Schaepman, M. E., & Small, D. (2018). Using Multitemporal Sentinel-1 C-band Backscatter to Monitor Phenology and Classify Deciduous and Coniferous Forests in Northern Switzerland. *Remote Sensing*, *10*(55), 30, doi: 10.3390/RS10010055.

Rüetschi, M., Small, D., & Waser, L. T. (2019). Rapid Detection of Windthrows Using Sentinel-1 C-Band SAR Data. *Remote Sensing*, *11*(2), 23, doi: 10.3390/rs11020115.

Santoro, M. & Strozzi, T. (2012). Circumpolar digital elevation models > 55° N with links to geotiff images.

Schubert, A., Jehle, M., Small, D., & Meier, E. (2008). Geometric validation of TerraSAR-X high-resolution products. In *TerraSAR-X Science Team Meeting* (pp.6̃). Oberpfaffenhofen, Germany: DLR.

Schubert, A., Jehle, M., Small, D., & Meier, E. (2012a). Mitigation of atmospheric perturbations and solid Earth movements in a TerraSAR-X time-series. *J. Geod.*, *86*(4), 257–270, doi: 10.1007/s00190-011-0515-6.

Schubert, A., Miranda, N., Geudtner, D., & Small, D. (2017). Sentinel-1A/B Combined Product Geolocation Accuracy. *Remote Sensing*, *9*(607), doi: 10.3390/rs9060607.

Schubert, A., Small, D., Jehle, M., & Meier, E. (2012b). COSMO-skymed, TerraSAR-X, and RADARSAT-2 geolocation accuracy after compensation for earth-system effects. In *International Geoscience and Remote Sensing Symposium* (pp. 3301–3304). Munich, Germany: IEEE.

Schubert, A., Small, D., Miranda, N., Geudtner, D., & Meier, E. (2015). Sentinel-1A Product Geolocation Accuracy: Commissioning Phase Results. *Remote Sensing*, *7*(7), 9431–9449, doi: 10.3390/rs70709431.

Seguin, G. & Geudtner, D. (2018). Challenges for Next Generation SAR. In *EUSAR 2018* (pp. 1350–1353). Berlin, Germany.

Shimada, M., Watanabe, M., Motooka, T., Isoguchi, O., Mukaida, A., Okumura, H., Otaki, T., & Itoh, T. (2011). Generation of 10m resolution PALSAR and JERS-1 SAR MOSAIC and Forest/Non-Forest Maps for Forest carbon Tracking. In *International Asia-Pacific Conference on SAR* (pp. 1–4).: IEEE.

Simard, M., Riel, B. V., Denbina, M., & Hensley, S. (2016). Radiometric Correction of Airborne Radar Images Over Forested Terrain With Topography. *IEEE Transactions on Geoscience and Remote Sensing*, *54*(8), 4488–4500, doi: 10.1109/TGRS.2016.2543142.

Small, D. (2011). Flattening Gamma: Radiometric Terrain Correction for SAR Imagery. *IEEE Transactions on Geoscience and Remote Sensing*, *49*(8), 3081–3093, doi: 10.1109/TGRS.2011.2120616.

Small, D. (2012). SAR backscatter multitemporal compositing via local resolution weighting. In *International Geoscience and Remote Sensing Symposium* (pp. 4521–4524). Munich, Germany: IEEE.

Small, D. (2014). Coordinated SAR Acquisition Planning for Terrestrial Snow Monitoring. Retrieved 2022-08-11, from https://globalcryospherewatch.org/satellites/docs/PSTG-4_Doc_08-01_UserReq-Snow-SARCWG-v0-9.pdf.

Small, D., Biegger, S., & Nüesch, D. (2000). The Topology of SAR Imagery in Rough Topography. In *EUSAR* (pp. 501–504). Berlin, Germany: VDE Verlag GmbH.

Small, D., Jehle, M., Meier, E., & Nüesch, D. (2004). Radiometric Terrain Correction Incorporating Local Antenna Gain. In *EUSAR* (pp. 929–932). Berlin, Germany: VDE Verlag GmbH.

Small, D., Schubert, A., Rosich, B., Meier, E., & Rosich, B. (2007). Geometric and Radiometric Correction of ESA SAR Products. In *ESA Envisat Symposium 2007* (pp. 1–6). Montreux, Switzerland: ESA.

Small, D., Zuberbühler, L., Schubert, A., & Meier, E. (2011). Terrain-flattened gamma nought Radarsat-2 backscatter. *Canadian Journal of Remote Sensing*, *37*(5), 493–499, doi: 10.5589/m11-059.

Soille, P., Burger, A., de Marchi, D., Kempeneers, P., Rodriguez, D., Syrris, V., & Vasilev, V. (2018). A versatile data-intensive computing platform for information retrieval from big geospatial data. *Future Generation Computer Systems*, *81*, 30–40, doi: 10.1016/J.FUTURE.2017.11.007.

Syrris, V., Corbane, C., Pesaresi, M., & Soille, P. (2019). Mosaicking Copernicus Sentinel-1 Data at Global Scale. *IEEE Transactions on Big Data*, (pp.1̃1)., doi: 10.1109/TBDATA.2018.2846265.

Truckenbrodt, J., Freemantle, T., Williams, C., Jones, T., Small, D., Dubois, C., Thiel, C., Rossi, C., Syriou, A., & Giuliani, G. (2019). Towards Sentinel-1 SAR Analysis-Ready Data: A Best Practices Assessment on Preparing Backscatter Data for the Cube. *Data*, *4*(3), 93, doi: 10.3390/data4030093.

Viviroli, D. & Weingartner, R. (2004). The hydrological significance of mountains: from regional to global scale. *Hydrol. Earth Syst. Sci.*, *8*(6), 1017–1030, doi: 10.5194/hess-8-1017-2004.

Wang, F. (1990). Fuzzy classification of remote sensing images. *IEEE Transactions on Geoscience and Remote Sensing*, *28*(2), 194–201, doi: 10.1109/36.46698.

Wikipedia (2020). Remote Sensing Data Product Levels. Retrieved 2022-08-11, from https://en.wikipedia.org/wiki/Remote_sensing.

Wulder, M. A., Hilker, T., White, J. C., Coops, N. C., Masek, J. G., Pflugmacher, D., & Crevier, Y. (2015). Virtual constellations for global terrestrial monitoring. *Remote Sensing of Environment*, *170*, 62–76, doi: 10.1016/j.rse.2015.09.001.

Chapter

4

Paper 3: Estimating melt onset over Arctic sea ice from time series multi-sensor Sentinel-1 and RADARSAT-2 backscatter

Howell, S.E.L., Small, D., **Rohner, C.**, Mahmud, M.S., Yackel, J.J., & Brady, M.

This chapter is based on the peer-reviewed article:
Estimating melt onset over Arctic sea ice from time series multi-sensor Sentinel-1 and RADARSAT-2 backscatter.
Remote Sensing of Environment, 2019, 229, 48–59.
doi: 10.1016/j.rse.2019.04.031.
and is reprinted as the final submitted manuscript.
It has been modified to fit into the layout of this thesis.

C.R. implemented the code for calculating the LRWs from 5710 Sentinel-1 and RADARSAT-2 image products and performed the LRW calculation. **C.R.**, S.E.L.H., and D.S. performed the analysis. D.S. prepared the processing of the Sentinel-1 and RADARSAT-2 data. S.E.L.H. and D.S. designed the paper. S.E.L.H. and D.S. wrote the draft of the paper. **All authors** contributed to the final version of the paper.

Abstract

Information on the timing of melt onset over sea ice is important for understanding the Arctic's changing climate. The daily temporal resolution of passive microwave brightness temperatures provides the most widely utilized observations to detect melt onset but are limited to a spatial resolution of 25 km. Wide-swath SAR imagery provides a much higher spatial resolution (20–100 m) but melt onset detection remains challenging because of i) insufficient temporal resolution to facilitate accurate melt onset detection, ii) inconsistent viewing geometries and iii) limited image availability across the Arctic. Here, we construct high temporal resolution composite gamma nought backscatter products (1 day, 1–2 day and 2–4 day) using S1 and RS2 over a close-to-seamless revisit region located in northern Canadian Arctic and Greenland for estimating melt onset over Arctic sea ice in 2016 and 2017. We employ the necessary radiometric terrain flattening and local resolution weighting techniques to generate normalised backscatter over the entire study region, removing restrictions limiting analysis to a single sensor or track's swath width by integrating both ascending and descending passes into the composite products. Results indicate that higher temporal resolution multi-sensor composite gamma nought products (1 day) that make use of the most imagery provide a robust temporal evolution of the backscatter. This allows for more representative estimates of melt onset as it is easier to separate the melt onset threshold from winter variability that is otherwise a considerable challenge for SAR based melt onset algorithms because of inconsistent temporal resolution. Multi-sensor composite gamma naught melt onset detection is in good agreement with melt onset estimates derived from the Advanced Scatterometer (ASCAT) backscatter values and passive microwave brightness temperatures over homogenous sea ice regions but very noticeable improvement was found within narrow channels and regions with more heterogeneous sea ice. In anticipation of the availability of data from even more SAR satellites with the launch of the RCM, the multi-sensor composite gamma nought approach presented here may offer the most robust approach to estimate the timing of melt onset over sea ice across the Arctic using high spatiotemporal resolution SAR.

4.1 Introduction

Recent Surface Air Temperature (SAT) increases in the Arctic have been attributed to anthropogenic influence (Fyfe et al., 2013). Advection of warm and humid air over the Arctic sea ice resulting in downwelling longwave radiation increases is the dominant process that initializes melt onset (Mortin et al., 2016). Information on the timing of melt onset over sea ice is therefore important for understanding the response of the Arctic climate system to anthropogenic influence. An earlier melt onset facilitates the absorption of more solar radiation into the sea ice, leading to larger decreases in sea ice extent during the melt season (Perovich et al., 2007). Melt onset over Arctic sea ice has shifted to an earlier timing at a rate of -5.69 days per decade over the entire period from 1979 to 2017 (Bliss & Anderson, 2018) which is associated with decreasing trends in the Arctic's sea ice extent (Comiso, 2012; Stroeve et al., 2012).

Time series microwave remote sensing can be utilized for estimating the timing of melt onset over the Arctic sea ice because changes in microwave emission and scattering are reflective of the physical melt onset process. The most widely utilized techniques are those based on high temporal resolution (1 day) passive microwave brightness temperatures time series values that use change thresholds to identify the transition from dry winter sea ice conditions to melt onset (e.g. Belchansky et al., 2004; Bliss & Anderson, 2014; Drobot & Anderson, 2001; Markus et al., 2009). Passive microwave brightness temperatures also allow for long term estimates of melt onset (1979 to present) but only at a spatial resolution of 25 km. There are also several techniques that use high temporal resolution (1–2 day) scatterometer backscatter observations which provide a higher spatial resolution (2–5 km) but they are only available over a shorter time period (2000 to present) (e.g. Howell et al., 2006; Mortin et al., 2014, 2012; Wang et al., 2011). C-band SAR imagery provides the highest wide swath spatial resolution (20–100 m) and techniques have been developed to detect melt onset of Arctic sea ice (e.g. Kwok et al., 2003; Livingstone et al., 1987; Mahmud et al., 2016; Onstott et al., 1987; Winebrenner et al., 1994; Yackel et al., 2007) but it still remains challenging because of i) insufficient temporal resolution to facilitate accurate melt onset detection, ii) inconsistent viewing geometries and iii) limited image availability across the Arctic domain. Mahmud et al. (2016) successfully utilized RADARSAT-1 (RS1) and RS2 for melt onset detection in the northern Canadian Arctic Archipelago but noted that the temporal resolution of the imagery was a limitation with respect to representative spatiotemporal melt onset estimates.

With the recent launch of the ESA S1A (2014) and S1B (2016) the potential for high resolution pan-Arctic melt onset detection from C-band SAR has increased. However, despite the considerable spatial coverage provided by S1A and S1B, there are still gaps across the Arctic and construction of high temporal resolution time series SAR datasets (i.e. 1–2 day) is still problematic. The upcoming launch of the RCM adds yet more C-band SAR sensors to the existing satellite image pool. Combining the RCM with S1A and S1B provides a unique opportunity to construct high temporal resolution datasets across the Arctic, analogous to what is possible from passive microwave brightness temperatures but at very high spatial resolution. In anticipation of the multiple C-band SAR satellites from S1A, S1B and the RCM, we suggest that a multi-sensor backscatter approach may offer the most robust approach to estimate the timing of melt onset over Arctic sea ice from C-band SAR. In this analysis, we construct composite normalised gamma naught (γ_c^0; Small, 2011, 2012) backscatter products at high temporal resolution from S1A, S1B and RS2 SAR imagery and evaluate their utility for melt onset detection over Arctic sea ice.

4.2 Study area

The study area for this analysis is located in the northern Canadian Arctic and Greenland during the years of 2016 and 2017 (Fig. 1). This is a close-to-seamless revisit region imaged by S1A, S1B and RS2 that contained a considerable number of overlapping images in 2016 and even more in 2017 (Fig. 2). Sea ice within the study region for 2016 and 2017 contains both landfast seasonal FYI and MYI as well as the mobile MYI found in Arctic Ocean. The narrow channels and mix of ice types make it an ideal region to illustrate the benefits of high spatial resolution

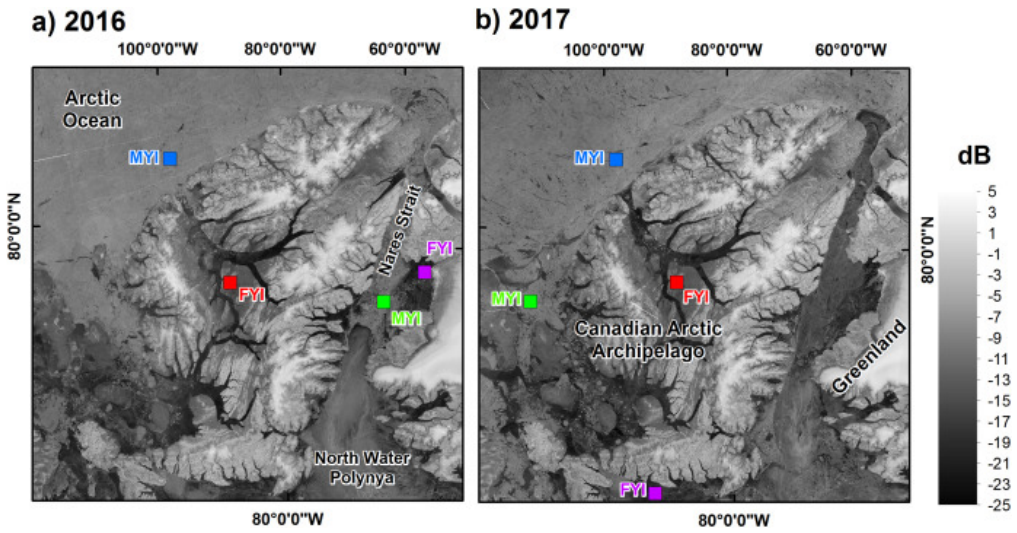

Fig. 1: Multi-sensor γ^0_c backscatter (dB) map of study region on (a) March 19, 2016 using data from S1A and RS2 and on (b) March 24, 2017 using data from S1A, S1B and RS2. The FYI and MYI sample sites locations color code corresponds to the time series plots in Figs. 6, 10, 12 and 13. (a) and (b) contain modified Copernicus Sentinel data (2017). RS2 Data and Products ©MacDonald, Dettwiler and Associates Ltd. (2016; 2017) - All Rights Reserved. RADARSAT is an official trademark of the Canadian Space Agency. (For interpretation of the references to color in this figure, the reader is referred to the web version of this article.)

SAR for melt onset detection. Time series sample locations for FYI and MYI types were identified in both years to represent the aforementioned conditions and are indicated in Fig. 1.

4.3 Data

The primary datasets used in this analysis were C-band (wavelength, $\lambda = 5.5$ cm) SAR imagery from S1A and S1B EW, S1A and S1B IW and RS2 ScanSAR Wide (SCWA) acquired at dual polarization (HH + HV) from March to August over the northern Canadian Arctic Archipelago and Greenland (Fig. 1) in 2016 and 2017 (table 4.1). The S1A and S1B imagery is freely available at the Copernicus Open

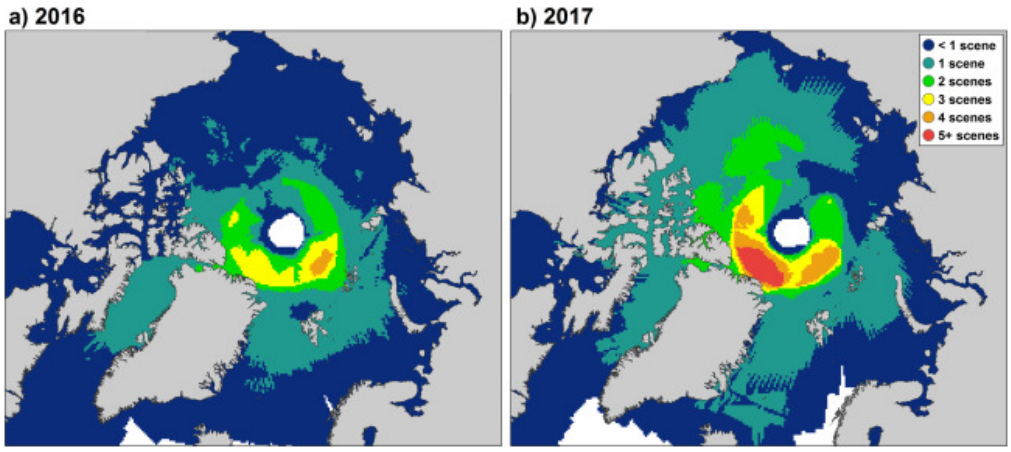

Fig. 2: Spatial distribution of available imagery (scenes per day) from S1A, S1B and RS2 for (a) April 2016 and (b) April 2017.

Tab. 4.1: SAR image products and counts used in this analysis for 2016 and 2017.

Image product	Spati. res. (m)	Inc. angle	Swath (km)	# 2016	# 2017
RS2 SCWA-SGF	100	20.0°–49.3°	500	280	321
S1 EW-GRDM	90	18.0°–47.0°	400	1699	2428
S1 IW-GRDH	20	31.0°–46.0°	250	301	681

Access Hub (https://scihub.copernicus.eu/dhus/#/home) and RS2 imagery is available online for a fee at Natural Resources Canada's Earth Observation Data Management System (https://www.eodms-sgdot.nrcan-rncan.gc.ca).

To evaluate the representativeness of the γ_c^0 products for 2016 and 2017, we used additional data from: i) the ASCAT single polarization (VV) Scatterometer Image Reconstruction (SIR; Early & Long, 2001) 4.45 km spatial resolution dataset available online from Brigham Young University at http://www.scp.byu.edu/data/Ascat/SIR/Ascat_sir.html; daily SAT from the extended Advanced Very High Resolution Radiometer (AVHRR) Polar Pathfinder dataset (APP-x; Key et al., 2016) available online from the NOAA National Centers for Environmental Information at https://www.ncdc.noaa.gov/cdr/atmospheric/extended-avhrr-polar-pathfinder-app-x; weekly in situ snow thickness values over FYI at Eureka, Nunavut (Fig. 1, red box) available online from the Canadian Ice Service (http://www.ec.gc.ca/glaces-ice/, see Archive followed by Ice Thickness Data); and finally 25 km spatial resolution estimates of the first date of melt onset from the Passive Microwave algorithm (PMW; Markus et al., 2009) available online from the NASA Cryosphere Science Research Portal at https://neptune.gsfc.nasa.gov/csb/ (see section 4.3).

4.4 Construction of normalised composite gamma naught (γ_c^0) backscatter products

The ratio between the scattered and transmitted power of microwave energy is referred to as radar backscatter and the backscatter coefficient is this ratio expressed over a reference ground area (Ulaby et al., 1986). Depending on which reference area chosen, the scattering coefficient is different. Complete details with respect to scattering coefficient differences are provided in Small (2011) but briefly, the most common scattering coefficient is sigma naught (σ^0) and is the result when the reference area is the ground area projected on an ellipsoid. Beta naught (β^0) which is also referred to as radar brightness (see also Raney et al., 1994) is the simplest definition, least encumbered by an Earth model, placing the reference area is in the sensor's slant range plane, with no requirement for an ellipsoidal or terrain Earth model. Finally, gamma naught (γ^0) is the result when the reference area is in the plane perpendicular to the local look direction, representing the local area that the radar system actually sees.

Terrain-induced radiometric distortions are present in SAR backscatter maps unless they are properly compensated. Knowledge of modern radar satellite state vectors and timing annotations has improved to the point where tie-point free geolocation of each point in a radar image is now routinely possible at better than 1 m accuracy.

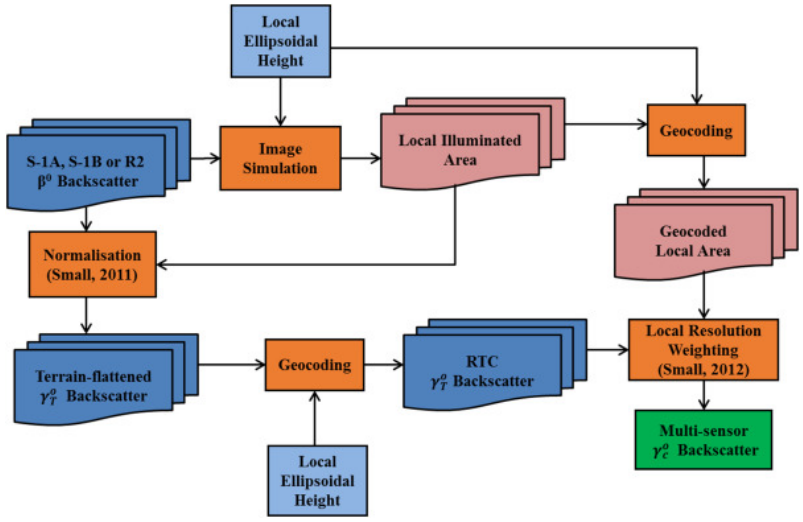

Fig. 3: Processing chain for construction of the composite γ_c^0 backscatter products.

Accuracies achieved with multiple radar sensors were reported in Schubert et al. (2012) and sub-meter accuracy for the two S1 satellites was reported in Schubert et al. (2017). Use of high quality SAR sensor geometric calibration enables routine automatic connection of each SAR pixel with a corresponding DEM location on the Earth's surface. Correction of the position of each measurement is called geocoding, and is a standard step available in many software packages, whereby the applicable Doppler (azimuth) and range equations are solved. Although the geometry was corrected in the geocoding step, unless further steps are taken, the effect of terrain on the local radar brightness (radiometry) will remain tied to a simple ellipsoidal Earth model and not the local terrain and the variable resolution within a single acquisition will also remain (Small, 2011).

The approach we use to generate the multi-sensor γ_c^0 image products accounts for the aforementioned problems and is universal in that it is applicable to both marine and terrestrial regions across the SAR image. Although the focus of this study is Arctic sea ice, for which terrain correction using a DEM is not possible but it is still required to obtain the local ellipsoidal height, a complete description of the approach is provided because terrain correction is only one component of the overall processing chain illustrated in Fig. 3. The S1A, S1B and RS2 images are first converted to beta naught (β^0). Then, following Small (2011), radiometric terrain distortions are modeled by summing up all DEM-facet contributions to each SAR image pixel. DEM locations blocked from observation by radar shadow are accounted for in the image simulation by not including such DEM-facets in the sum. Once the map of local contributing area is complete, the original β^0 image is normalised using that map. This newly normalised backscatter is initially in radar geometry but can then be easily geocoded in a further step to produce an RTC (γ_T^0) backscatter image in map geometry.

These RTC images are properly normalised radiometrically for terrain distortions, but the variable resolution within a single acquisition can remain quite considerable. To lower the noise and ensure that the image and backscatter properties become even more uniform, a second stage of processing is used that combines data from multiple tracks into a single wide-area backscatter composite image. A set of N_i available RTC images acquired within a time window i are combined by applying their local resolution (i.e. the reciprocal of the local illuminated area used to

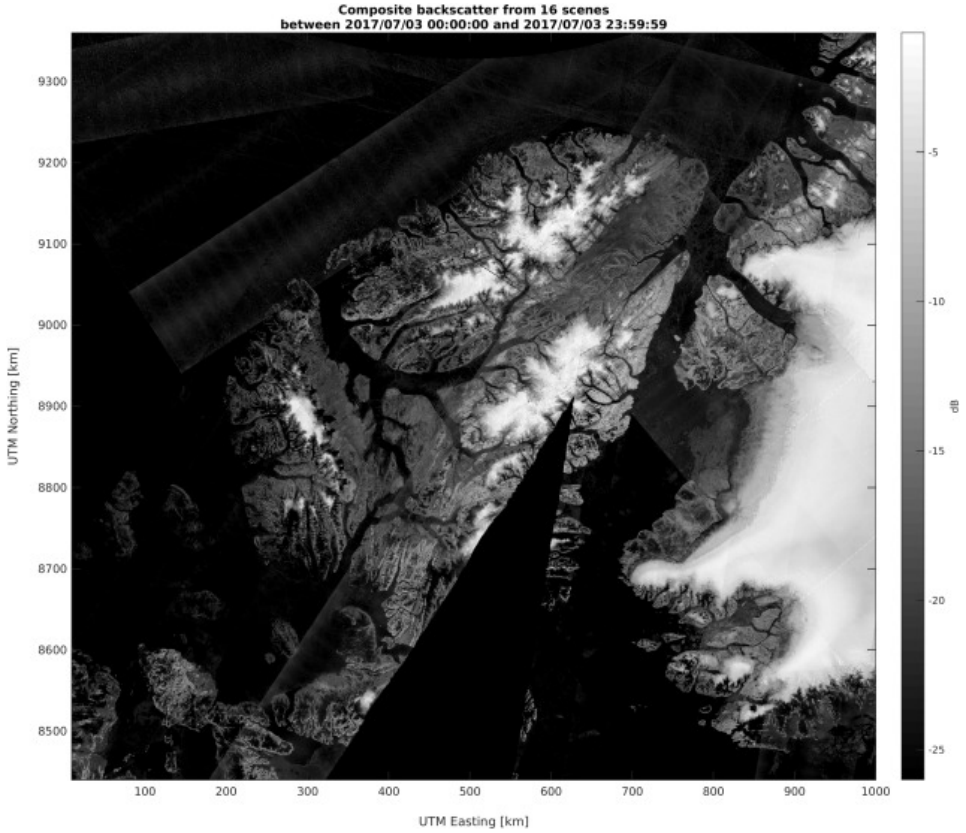

Fig. 4: Multi-sensor γ^0_c backscatter (dB) for (a) July 3, 2017 using 16 images from S1A and S1B. Contains modified Copernicus Sentinel data (2017).

normalise them) as a weighting function. The methodology behind this step is discussed in detail by Small (2012) which results in a single backscatter composite per defined time window i (e.g. 1 day, 1–2 day and 2–4 day). An example of these final multi-sourced γ^0_c products for 1 day time window using 16 and 20 SAR images is shown in Figs. 4 and 5, respectively. These final multi-sourced γ^0_c products have a spatial resolution of 400 m with relatively spatially homogenous image properties with lower noise than a single acquisition, making them a useful "analysis ready data" level 3 product for higher level application studies. They have for example been previously applied to normalising terrain distortions to successfully map forest-type using seasonal backscatter signatures over the whole of the Alps (Rüetschi et al., 2018). This is the first known application to a relatively flat landscape. The DEM utilized in this study (Santoro & Strozzi, 2012) was deemed to be sufficient for product generation at 400 m spatial resolution, but given sufficient DEM resolution and quality, achieving 100 m spatial resolution or higher would only be a matter of computational and storage resources. Finally, it should be noted that although, this processing chain was applied to both HH and HV polarizations, the higher noise floor associated with the HV channel resulted in numerous temporal gaps in the γ^0_c time series and therefore, we restricted this analysis to only the γ^0_c products at HH polarization.

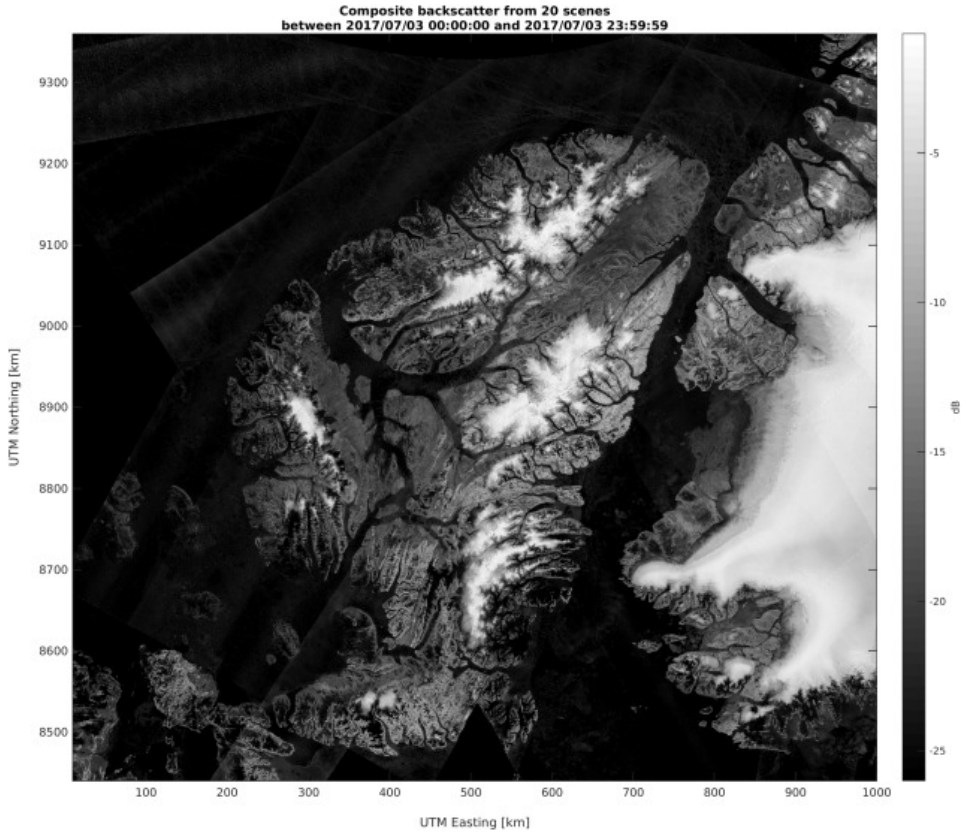

Fig. 5: Multi-sensor γ_c^0 backscatter for July 3, 2017 using 20 images from S1A, S1B, and RS2. Contains modified Copernicus Sentinel data (2017). RS2 Data and Products ©MacDonald, Dettwiler and Associates Ltd. (2017) - All Rights Reserved. RADARSAT is an official trademark of the Canadian Space Agency.

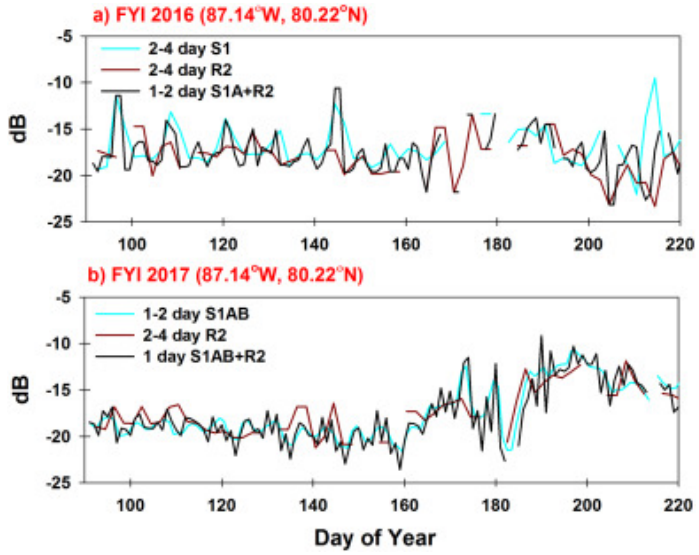

Fig. 6: Time series of γ_c^0 backscatter (dB) products over seasonal FYI for (a) 2016 and (b) 2017.

4.5 Temporal evolution of γ_c^0 products from winter to melt onset

Remotely sensed techniques using time series sigma nought (σ^0) values have a long history for detecting melt onset over Arctic sea ice (e.g. Kwok et al., 2003; Livingstone et al., 1987; Mahmud et al., 2016; Mortin et al., 2014; Onstott et al., 1987; Winebrenner et al., 1994; Yackel et al., 2001). To our knowledge, γ^0 or γ_c^0 has not been previously utilized for time series melt onset detection over Arctic sea ice. Moreover, γ^0 is less sensitive to incidence angle effects (Small, 2011) making it potentially more robust than σ^0 for melt onset detection.

4.5.1 First-Year Ice (FYI)

Over the FYI sample site in 2016 and 2017, γ_c^0 backscatter values for all constructed SAR products were relatively low during the pre-melt winter period from day of year (DOY) 90–150 because the near snow-ice interface is cold resulting in low basal layer snow brine volume, a relatively small dielectric permittivity and low volume scattering (Fig. 6). Surface scattering largely controls C-band backscatter at these cold temperatures. The variability in the winter backscatter time series is known to be influenced by atmospheric forcing as a function of snow thickness causing changes in brine volumes in the snow and at the snow-sea ice interface that are reflected in the backscatter coefficient (Barber & Nghiem, 1999; Barber et al., 1995). Changing incidence angles also contribute to backscatter variability over FYI during the winter (Mahmud et al., 2018; Mäkynen & Karvonen, 2017). The higher γ_c^0 values in 2016 versus 2017 are likely the result of a rougher sea ice surface surrounding the sample site in 2016, as evident from Fig. 7, and not atmospheric forcing. Moreover, the rougher surface in 2016 was also associated with thicker snow on sea ice (Fig. 8) which would likely buffer against the influence of atmospheric forcing on the γ_c^0 backscatter.

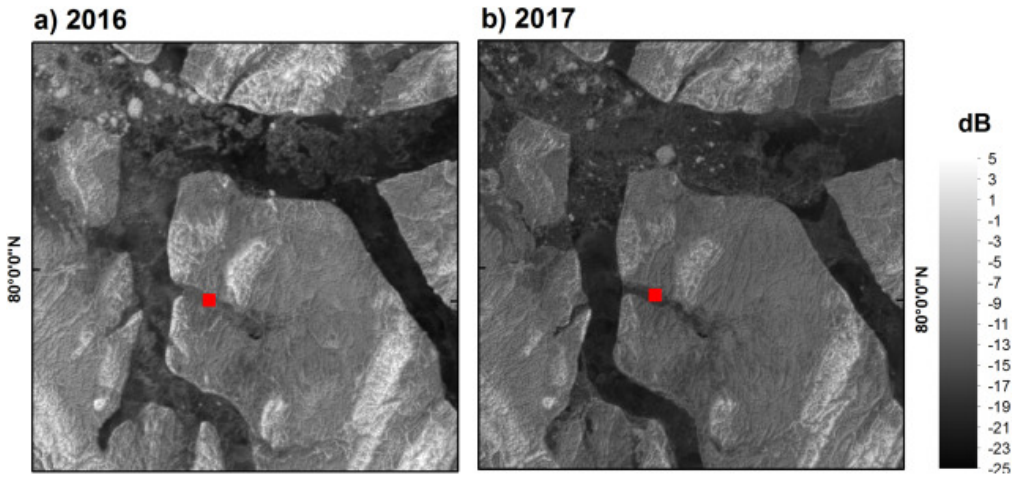

Fig. 7: Multi-sourced γ_c^0 backscatter (dB) image on (a) March 19, 2016 and (b) March 24, 2017. The red square corresponds to the location of the snow depth on sea ice measurements and the seasonal FYI γ_c^0 time series shown in Fig. 6. (a) and (b) contain modified Copernicus Sentinel data (2017). RS2 Data and Products ©MacDonald, Dettwiler and Associates Ltd. (2016; 2017) - All Rights Reserved. RADARSAT is an official trademark of the Canadian Space Agency. (For interpretation of the references to color in this figure legend, the reader is referred to the web version of this article.)

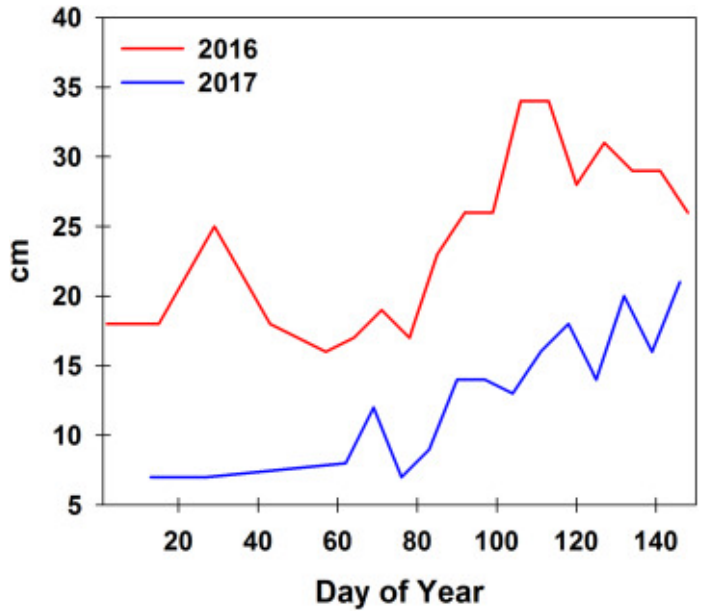

Fig. 8: Time series of snow depth on sea ice (cm) at Eureka, Nunavut for 2016 and 2017.

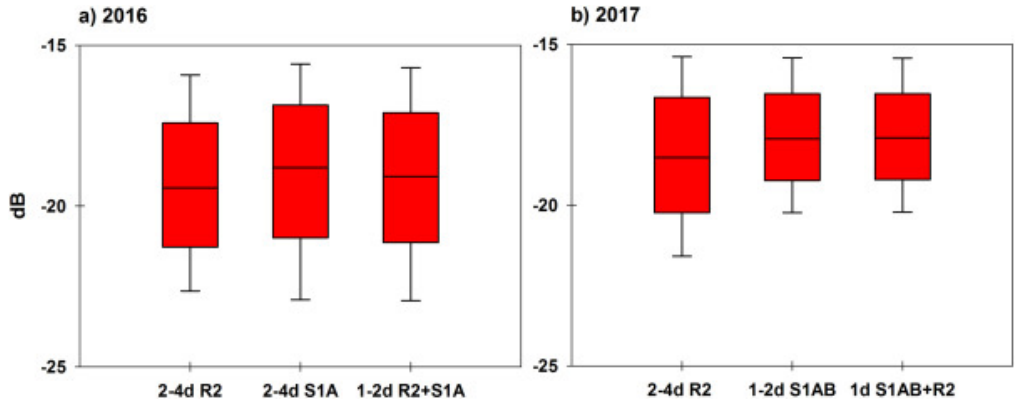

Fig. 9: Boxplots of the mean γ_c^0 backscatter (dB) for each constructed product (x-axis) calculated over landfast FYI during the winter period from day of year 90–120 for (a) 2016 and (b) 2017.

The major difficulty with using a threshold backscatter change for melt onset detection over FYI from SAR is separating winter backscatter variability from the first major upturn in backscatter that denotes melt onset, especially when temporal gaps are present in the time series. Warming first causes an increase in the brine volume at the snow-sea ice interface, increasing volume scattering that facilitates the major backscatter upturn (Barber et al., 1995; Drinkwater, 1989). For the sample site in 2016, the melt onset upturn was indeed difficult to pinpoint (∼DOY170) because of high γ_c^0 variability during the winter, combined with some temporal gaps in the time series for all products (Fig. 6a). In 2017, the upturn in γ_c^0 was also difficult to identify using the 2–4 day RS2 product given the presence of temporal gaps however, the γ_c^0 upturn was clearly apparent after DOY160 for the 1-day S1AB + RS2 and 1–2 day S1AB products (Fig. 6b).

To explore the utility of these products beyond surface roughness conditions surrounding the local time series scale at Eureka, we calculated the April (DOY90–120) mean γ_c^0 of all FYI landfast pixels (∼500,000) in the study region for all constructed SAR products in both years. For each product, FYI pixels were identified using the Kwok (2004) threshold as having a γ_c^0 value less than -14.5 dB. The variability in mean April γ_c^0 for all products, for both years is illustrated by boxplots in Fig. 9. In 2016, γ_c^0 winter variability was similar for all products and suggests additional imagery in the multi-sensor product does not appreciably impact its winter variability (Fig. 9a). However, higher temporal resolution multi-sourced 1–2 day S1A + RS2 product certainly provided a γ_c^0 temporal evolution with less temporal gaps compared to the 2–4 day products (Fig. 6a). There was more imagery utilized for the γ_c^0 products in 2017 compared to 2016 (table 4.1) and winter γ_c^0 variability was subsequently lower in 2017 (Fig. 9). Moreover, the largest amount of imagery was utilized for the 1–2 day S1AB and 1 day S1AB + RS2 products in 2017 that in turn experienced the lowest winter γ_c^0 variability (Fig. 9b).

Image availability from SAR typically results in a trade-off between image homogeneity and temporal blurring using LRW (Small, 2012) but with the considerable amount of imagery available over the study region in 2017, it is evident that both image homogeneity and temporal resolution can be maintained. Specifically, Figs. 6b and 9b illustrate that the mean weighted backscatter for the higher temporal resolution SAR products that take into account all available imagery (i.e. increased number of looks) contributes to less variable γ_c^0 values and in turn a more robust temporal evolution of γ_c^0 over FYI during the winter period. This suggests that

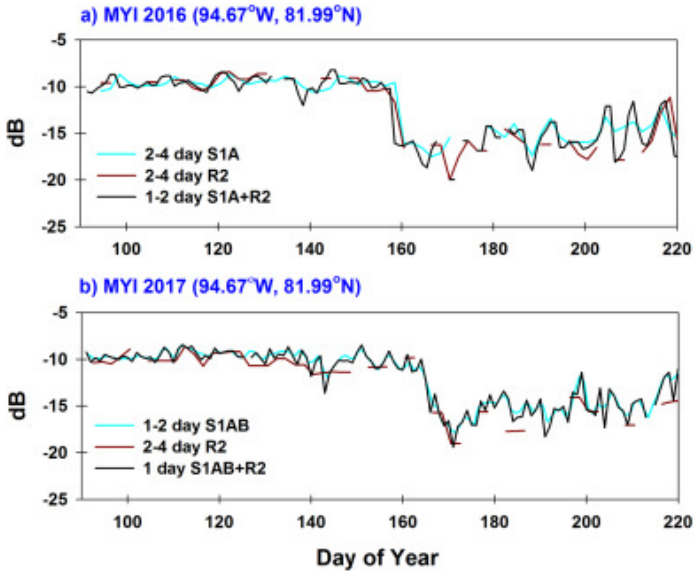

Fig. 10: Time series of γ_c^0 backscatter (dB) products over seasonal MYI for (a) 2016 and (b) 2017.

for multi-sourced γ_c^0 products with higher temporal resolution and more included imagery, separating the melt onset upturn from winter γ_c^0 variability over FYI is less problematic.

4.5.2 Multi-Year Ice (MYI)

Over the MYI sample site in 2016 and 2017, γ_c^0 for all products was high and stable during the pre-melt winter period (DOY90–150) (Fig. 10) because air bubbles cause volume scattering to occur within the ice. Over MYI which is brine free, the first major downturn in backscatter is identified as melt onset because ice volume scattering is masked by increases in liquid water content within the snowpack (Winebrenner et al., 1994). The differences in temporal evolution were close to negligible between the γ_c^0 products, although more temporal gaps were apparent in 2016 than 2017 (Fig. 10). With the exception of the 2–4 day RS2 product in 2017 that contained considerable temporal gaps, all the downturn in γ_c^0 was easily distinguishable on DOY158 and DOY165 for 2016 and 2017, respectively in all products (Fig. 10). The winter stability of γ_c^0 resulting from an absence of brine induced changes on γ_c^0 allows identifying the melt onset downturn over MYI less problematic than FYI. Moreover, the winter backscatter over MYI is less sensitive to incidence angle variations (Mahmud et al., 2018).

Analogous to FYI, we also calculated the mean April (DOY90–120) γ_c^0 of all MYI landfast pixels (~250,000) in the study region for all constructed SAR products. MYI pixels were identified using the Kwok (2004) threshold as having a γ_c^0 value greater than -14.5 dB. Boxplots of the mean April γ_c^0 over landfast MYI during the winter for all constructed SAR products are shown in Fig. 11 and confirm that γ_c^0 variability is less than over FYI. Fig. 11 also indicates that the mean weighted backscatter for the highest temporal resolution multi-sensor SAR products (i.e. 1–2 day S1AB and 1 day S1AB + RS2) has less of an impact on γ_c^0 winter variability over MYI compared to FYI since it is already quite stable (i.e. absence of brine). Despite this, the highest temporal resolution SAR products that utilized the most

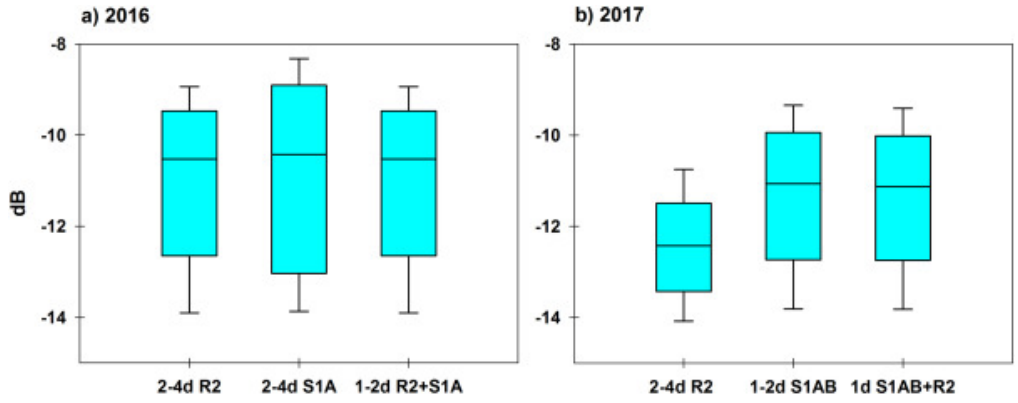

Fig. 11: Boxplots of the mean γ_c^0 backscatter (dB) values for each constructed product (x-axis) calculated over landfast MYI during the winter period from day of year 90–120 for (a) 2016 and (b) 2017.

imagery certainly facilitated an improved and more robust γ_c^0 temporal evolution over MYI compared to lower temporal resolution product (Fig. 10).

4.5.3 Comparison with ASCAT β^0, passive microwave estimates of melt onset and surface air temperature

The high temporal resolution of satellite-based passive microwave brightness temperatures and scatterometer backscatter has contributed to these sensors being widely utilized for melt onset detection, with the trade-off being moderate to coarse spatial resolution. Considering that the multi-sensor γ_c^0 S1A + RS2 product in 2016 and S1AB + RS2 product in 2017 provided the highest achievable temporal resolution in our study region, we now compare these products to ASCAT σ^0, melt onset from the passive microwave algorithm and SAT.

At the sample sites for 2016 and 2017, variability from the multi-sensor γ_c^0 products was larger than ASCAT σ^0 at the daily time scale, but the overall temporal evolution was remarkably similar (Fig. 12). Correlations (r) between ASCAT σ^0 and multi-sensor γ_c^0 ranged from $r = 0.81 - 0.93$. The multi-sensor γ_c^0 also correlated reasonably well with SAT ranging between $r = 0.48 - 0.71$ denoting changes in dielectrics are responding to changes in SAT that are in turn reflected in γ_c^0. The strength of relationship is similar to Yackel et al. (2001) who found SAT explained between 30 and 55% of the variation in the backscatter.

For all test sites, the first major upturn (FYI) or downturn (MYI) of the multi-sensor γ_c^0 generally corresponded with SAT approaching or rising slightly above 0 °C (Figs. 12 and 13). This correspondence has been widely reported by previous studies identifying factors that are associated with melt onset detected by microwave remote sensing (e.g. Belchansky et al., 2004; Mahmud et al., 2016; Mortin et al., 2014; Yackel et al., 2001). For the first date of melt onset from the PMW algorithm, only the landfast MYI site in 2016 (Fig. 12b) and the mobile MYI site in 2017 (Fig. 13a) were in good agreement with the multi-sensor γ_c^0 melt onset transition. The PMW algorithm detected melt onset too early for the remaining samples sites (Figs. 12a, c, 13b, c). Very early melt detection was apparent at the 2017 landfast MYI test site when both ASCAT and multi-sensor γ_c^0 showed that the first major downturn was much later (Fig. 13b). Possible explanations for the early PMW algorithm melt detection as well as a spatial inter-comparison are presented in the following section. Overall, with temporal evolution of the multi-sensor γ_c^0 being similar to

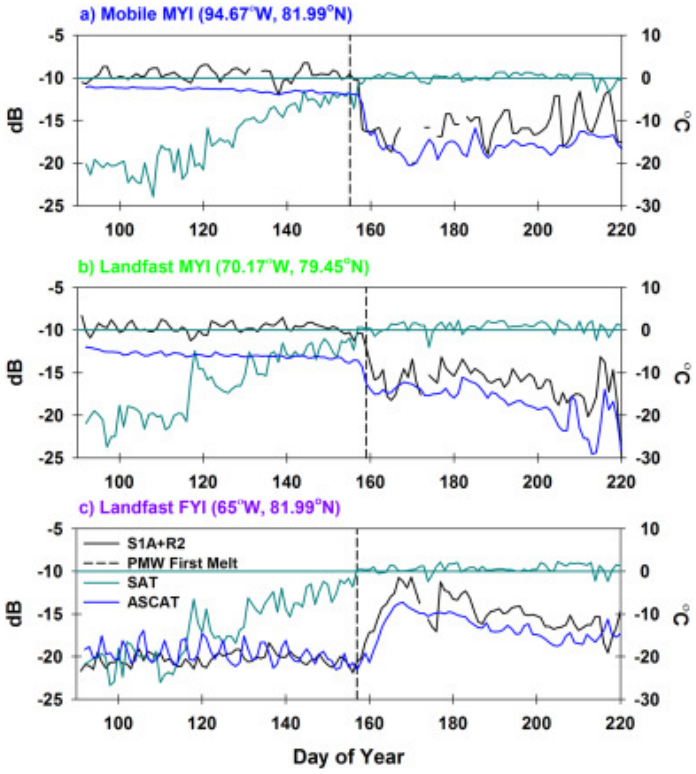

Fig. 12: Time series of γ_c^0 backscatter (dB), the ASCAT sigma naught (σ^0) backscatter, SAT and the first date of melt onset detected by the PMW algorithm in 2016 over (a) mobile MYI, (b) landfast MYI and (c) landfast seasonal FYI.

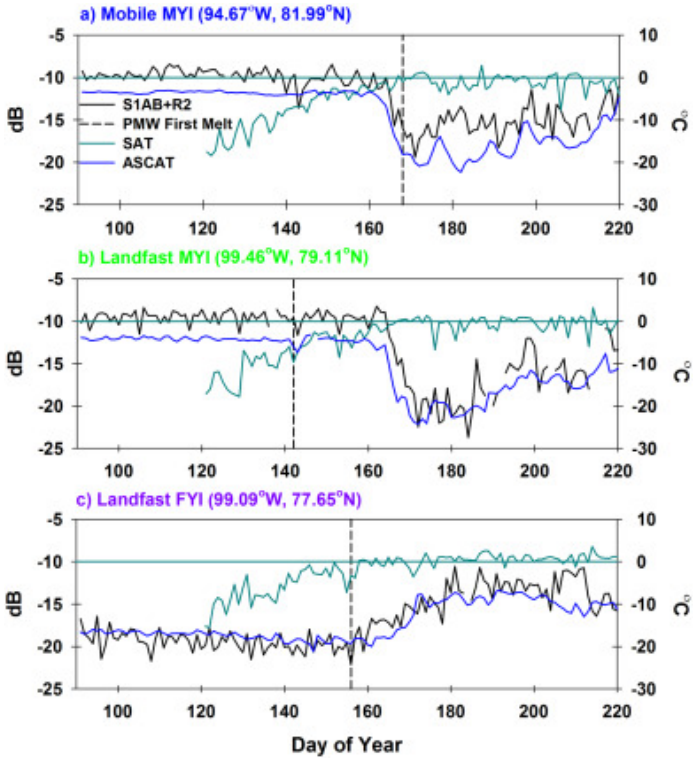

Fig. 13: Time series of γ_c^0 backscatter (dB), the ASCAT sigma naught (σ^0) backscatter, SAT and the first date of melt onset detected by the PMW algorithm in 2017 over (a) mobile MYI, (b) landfast MYI and (c) landfast seasonal FYI.

ASCAT σ^0, the melt onset transitions were relatively easy to detect, which is a considerable improvement compared to previous studies using time series SAR for melt detection (e.g. Mahmud et al., 2016; Yackel et al., 2007) where the datasets suffered from irregular temporal resolution inconsistency.

4.6 Spatially mapping multi-sensor γ_c^0 detected melt onset

4.6.1 Melt onset transition retrieval

We now make use of γ_c^0 at its highest available temporal resolution (S1A + RS2 product in 2016 and S1AB + RS2 in 2017) to develop a melt onset threshold retrieval approach for spatial application and evaluation. Given that such a multi-sensor γ_c^0 time series has never been utilized for melt onset detection over sea ice, a different strategy with different thresholds was required compared to previous algorithms based on σ^0 values. Our intent in this study is to provide a simple, yet robust approach for comparison purposes, as the focus of this paper is not melt onset algorithm development. Accordingly, we also develop an approach to map melt onset in our study region from ASCAT σ^0 to best compare against multi-sensor γ_c^0. We acknowledge that application of these algorithms beyond this study region may require modifications.

For multi-sensor γ_c^0 melt onset detection, we first calculate the winter mean γ_c^0 during April for each pixel. We use the winter mean γ_c^0 as a baseline from which to flag melt onset for a pixel if γ_c^0 departs at a certain absolute value threshold from it. Next, we separate FYI and MYI using a value of -14.5 dB (Kwok, 2004) because the magnitude of the γ_c^0 upturn (FYI) is different than the magnitude of the γ_c^0 downturn (MYI) as shown in both Figs. 12 and 13. In order to determine a melt onset γ_c^0 absolute value threshold, we iterated through numerous values in 0.25 dB increments starting with at 3 dB for each ice type, arriving at 8 dB for MYI and 5 dB for FYI. The 5 dB threshold for FYI was sufficient to avoid most early melt onset detection from time series winter γ_c^0 variability and still capture the first major upturn (not shown). When the 5 dB threshold was also applied to MYI, melt onset detection was too early, especially over mobile MYI in the presence of leads (not shown). Using the 8 dB threshold for MYI best reduced early melt onset detection in these mobile MYI regions however, this threshold was too aggressive over FYI as it resulted in very late melt onset (not shown). Overall, in this study region, using the aforementioned thresholds for FYI and MYI best ensured the γ_c^0 detected melt onset fell within the first significant upturn or downturn of the γ_c^0 time series and was representative of each ice type.

For ASCAT, we also calculated the winter mean backscatter during April for each pixel and used it as a baseline from which to flag melt onset. However, unlike γ_c^0, there was no improvement in using separate thresholds for FYI and MYI (not shown) and as a result, we selected a threshold of 5 dB to denote melt onset with ASCAT σ^0 in our study region. Based on the time series plots in Figs. 12 and 13, the 5 dB threshold was sufficient to avoid early melt onset detection from winter variability while at the same time not being overly aggressive to result in very late melt onset as would be the case with higher threshold values over MYI. Divergent sea ice motion resulting in leads was not an appreciable problem for early melt onset detection with ASCAT because unless there is a sustainable amount of open

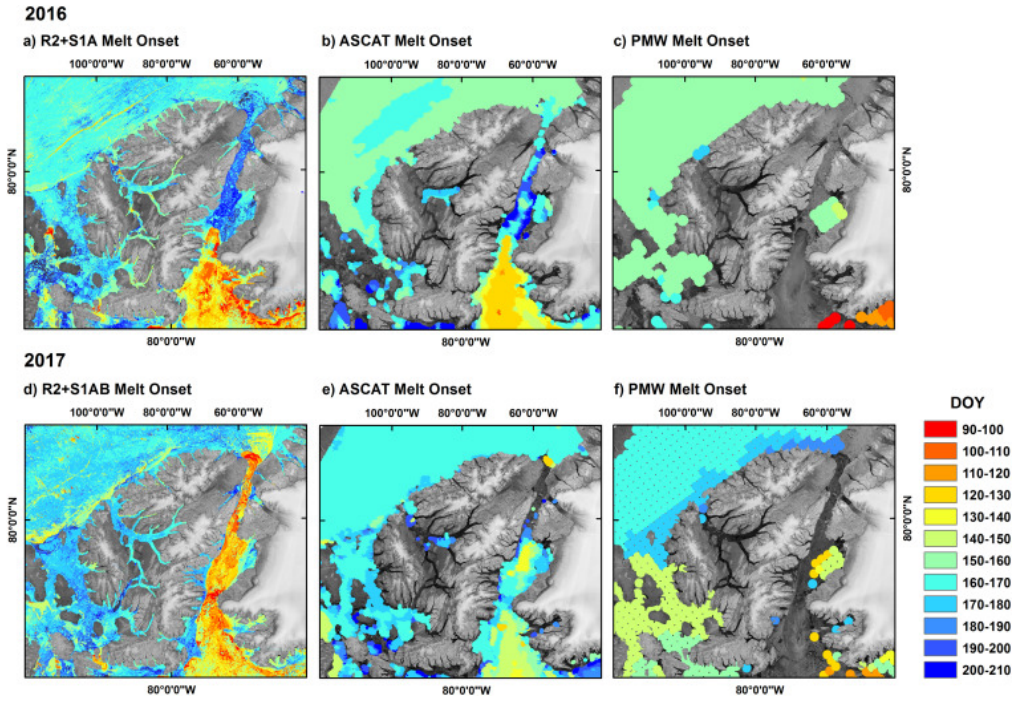

Fig. 14: Melt onset spatial distribution as detected by multi-sensor γ_c^0 (a and d), ASCAT sigma naught (σ^0) (b and e) and the PMW algorithm (e and f) for 2016 and 2017. (a-f) contain modified Copernicus Sentinel data (2016–2017). RS2 Data and Products ©MacDonald, Dettwiler and Associates Ltd. (2016; 2017) - All Rights Reserved. RADARSAT is an official trademark of the Canadian Space Agency.

water, ice will still be the dominant scattering mechanism given ASCAT's moderate spatial resolution.

4.6.2 Spatial distribution of melt onset

Fig. 14 illustrates melt onset timing spatially for the multi-sensor γ_c^0, ASCAT σ^0 and the PMW algorithm for 2016 and 2017. It is important to note that the 2017 melt onset map is more representative because it was based on a 1 day γ_c^0 time series with fewer spatiotemporal gaps than 2016. The most striking feature in Fig. 14 is the level of spatial detail captured by the multi-sensor γ_c^0 products in both years. Early melt onset was expected within the surrounding region of North Water Polynya and south of the ice arch in Nares Strait. Early melt onset was also expected in the south west region of the study area as it is known to be a location for recurring polynyas (Smith & Rigby, 1981). Coarse PMW algorithm retrievals were unable to detect melt onset in Nares Strait and the narrow channels located in the Canadian Arctic Archipelago. ASCAT performed slightly better in the aforementioned regions but spatial gaps were still apparent.

While the multi-sensor γ_c^0 certainly provides unprecedented spatial detail, leads caused by divergent sea ice motion are better resolved. As a result, in both 2016 and 2017 the multi-sensor γ_c^0 algorithm detected these leads as earlier melt onset within the Arctic Ocean MYI pack as well as along the shear zone between the Arctic Ocean and northern Canadian Arctic Archipelago (Figs. 14a, d). These dynamic sea ice features are less of a concern for the lower resolution ASCAT and PMW satellite sensors as the open water does not exert sufficient influence on their larger pixels to be classified as melt onset (Figs. 14b, c, e, f).

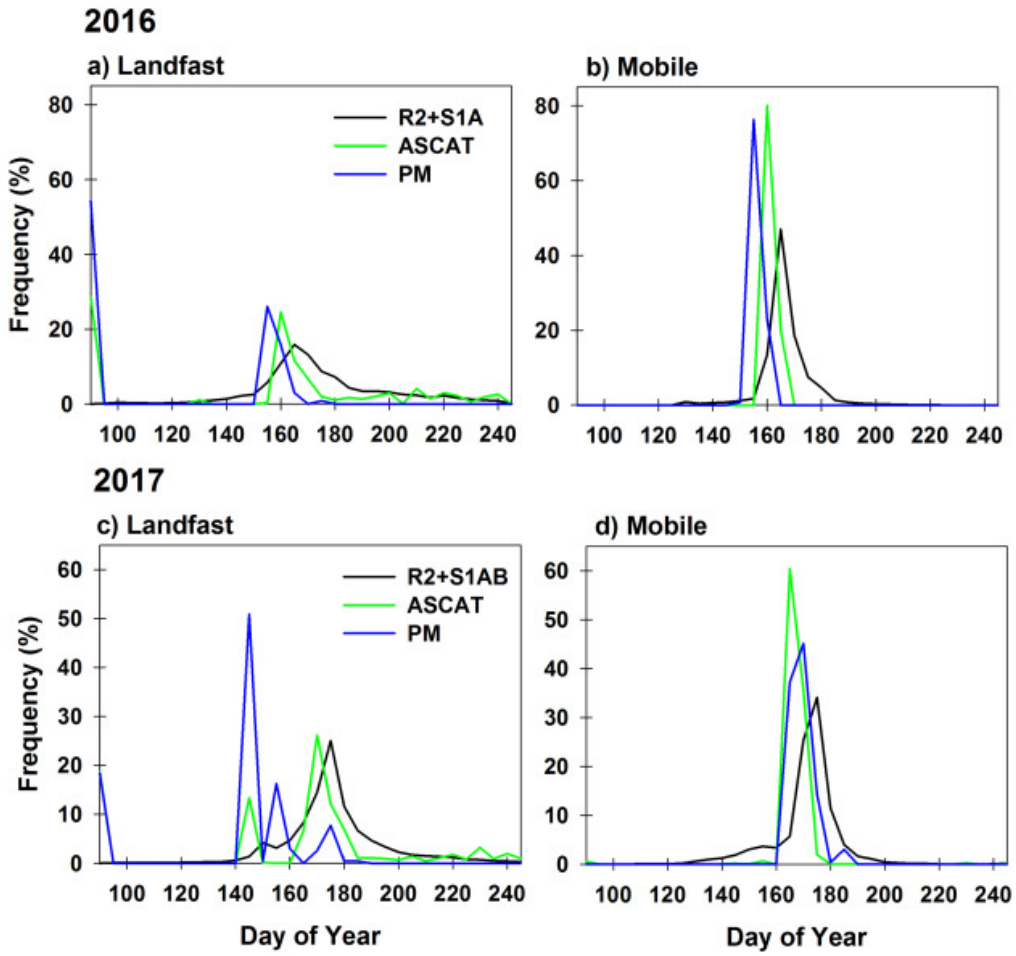

Fig. 15: Frequency distribution (%) of melt onset date (day of year) estimated from multi-sensor γ_c^0, ASCAT sigma naught (σ^0) the PMW algorithm for landfast ice (a and c) and mobile ice in the Arctic Ocean (b and d).

The highest frequency range of multi-sensor γ_c^0 melt onset detection was observed between DOY155–165 in 2016 and between DOY145–175 in 2017 (Fig. 15). For both 2016 and 2017, these date ranges were in good agreement with the spatial distribution of SAT between -5 °C and 5 °C (Fig. 16) when melt onset is expected to be detected from microwave sensors (Barber et al., 1995; Yackel et al., 2007). Melt onset was detected first by the PMW algorithm, ASCAT and then multi-sensor γ_c^0 (table 4.2 and Fig. 15). The standard deviation was high for the multi-sensor γ_c^0 approach (table 4.2) as a result of leads on the Arctic Ocean MYI pack, but more so from early melt detection in Nares Strait and the North Water Polynya (Figs. 14a,d).

The multi-sensor γ_c^0 approach likely detects slightly later melt onset dates than ASCAT because MYI regions are better isolated in the multi-sensor γ_c^0 product. When MYI is "sampled" in the ASCAT pixel it almost always captures some FYI since MYI floes are found at sub-resolution of 4.45 km ASCAT. Therefore, the brine effect with FYI that contributes to earlier melt onset detection is likely picked up in MYI samples for ASCAT. The PMW algorithm likely detects melt onset earlier than ASCAT and multi-sensor γ_c^0 because the shorter wavelengths used in the PMW algorithm are more sensitive to changes in liquid water content at the surface. It has been shown that small increases in liquid water will cause the scattering to be dominated by water instead of dry snow (Hallikainen et al., 1986; Linlor, 1980). The process is enhanced within FYI compared to MYI because of the strong

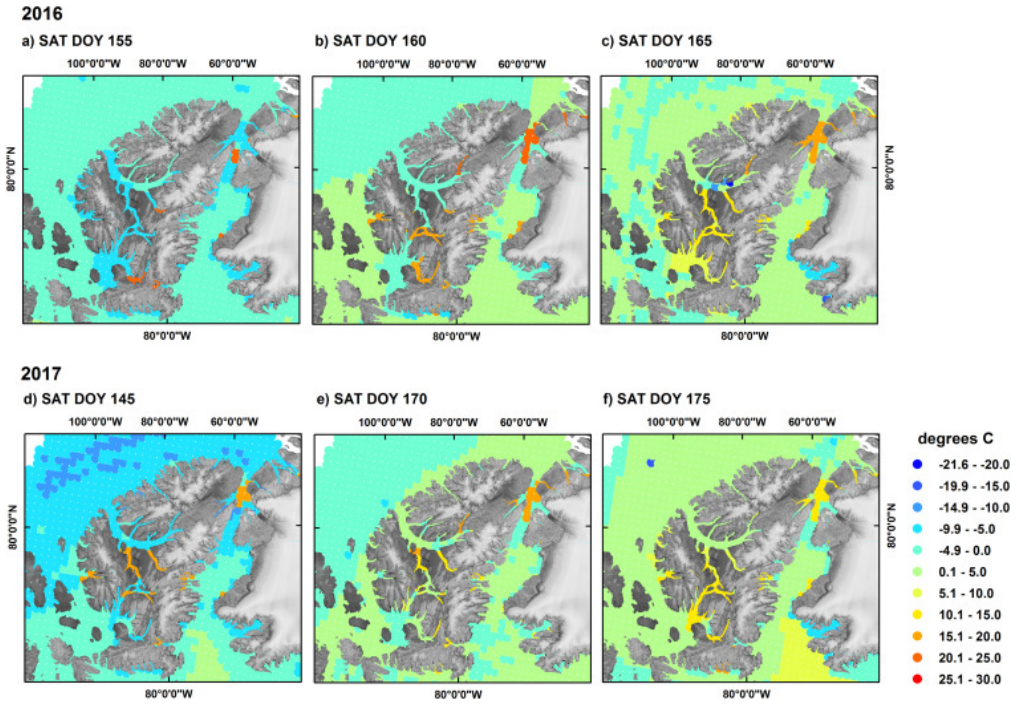

Fig. 16: SAT spatial distribution in the study region on day of year (DOY) (a) 155, (b) 160 and (c) 165 for 2016 and DOY (d) 155, (e) 170 and (f) 175 for 2017.

Tab. 4.2: Mean melt onset timing dates for each sensor with standard deviation in brackets.

Approach	2017	2016
Multi-sensor γ_c^0	167 (44.2)	168 (43.9)
ASCAT σ^0	166 (17.7)	161 (20.5)
PMW algorithm	155 (14.8)	152 (14.28)

influence of temperature on brine volume and dielectric permittivity and in turn the backscatter (Barber & Thomas, 1998). This is particularly apparent in our study for 2017 as the PMW algorithm detected the majority of very early melt onset over heterogeneous MYI and FYI landfast regions on DOY145 whereas ASCAT and multi-sensor γ_c^0 did not (Figs. 14d–f, 15c). This very early melt detected by the PMW algorithm on DOY145 for 2017 was coincident with SAT in the range of -5 °C to 0 °C which is sufficient to be detected at lower PMW frequencies (Fig. 16d). One of our temporal evolution time series sample sites was within this region and confirmed that SAT increases circa DOY145 were indeed sufficient to detect melt onset using the PMW (Fig. 13b). The SAT increases circa DOY145 did contribute to change in the backscatter of both the multi-sensor γ_c^0 and ASCAT σ^0 values but not of sufficient magnitude to detect melt onset (Fig. 13b).

4.7 Conclusions

In this analysis, we employed radiometric terrain flattening and LRW techniques described by Small (2011, 2012) to construct high temporal resolution γ_c^0 products

(1 day, 1–2 day and 2–4 day) from S1A, S1B and RS2 SAR imagery. We then evaluated the γ_c^0 products for melt onset detection over Arctic sea ice as compared to ASCAT and the PMW algorithm in 2016 and 2017 for a study region located in the Canadian Arctic and Greenland.

The weighted γ_c^0 mean for the higher temporal resolution multi-sourced SAR products that take into account the most imagery facilitates more homogenous (less variable) γ_c^0 values and enhances the temporal stability of γ_c^0. This was particularly apparent with the 2017 multi-sensor γ_c^0 product that used more imagery than the 2016 multi-sensor γ_c^0. The temporal evolution from the multi-sensor γ_c^0 was found to be consistent with temporal evolution of ASCAT σ^0. This was found to be particularly useful over FYI and provided improved separability between dry winter conditions and melt onset which have been a significant challenge for SAR-based melt onset algorithms. Estimating melt onset over sea ice the study region using highest temporal resolution the multi-sensor γ_c^0 products in both years resulted in an unprecedented level of detail with respect to the spatial distribution of melt onset in both years. Melt onset was found to be coincident in its spatial distribution with SAT approaching 0 °C associated with earlier melt in 2016 and later melt in 2017. Multi-sensor γ_c^0 melt onset detection was also found to be in good agreement with ASCAT and the PMW algorithm over homogenous sea ice regions but very noticeable improvement was found within narrow channels and regions with more heterogeneous sea ice. However, the high spatial resolution from multi-sensor γ_c^0 products detected erroneous melt onset in leads within the Arctic Ocean MYI pack as well as along the shear zone between the Arctic Ocean and northern Canadian Arctic Archipelago. Localised sea ice dynamics will therefore need to be taken into consideration for future melt onset algorithm development from multi-sensor γ_c^0 SAR products. However, the ability of the multi-sensor γ_c^0 SAR products to identify leads suggests these products could be utilized for lead detection studies.

Given that the timing of melt onset influences the end of summer sea ice extent in the Arctic (Perovich et al., 2007) and that positive trends in downwelling longwave radiation are linked to positive melt onset trends across the Arctic (Mortin et al., 2016), continuing to provide melt onset estimates is important for understanding the response of sea ice to a warming Arctic. Indeed, the PMW algorithm provides the best long-term measure of melt onset but SAR imagery can provide more robust estimates, especially as the spatiotemporal constraints of its application are dwindling with the current generation of C-band SAR satellites (i.e. S1A, S1B and RS2). Efforts to implement retrieved sea ice geophysical variables from SAR in data assimilation systems are currently underway and eventually SAR imagery will find utility in seasonal forecasting systems (e.g. Komarov & Buehner, 2017). In this study, we have shown excellent potential for the use of multi-sensor backscatter from SAR to provide high quality melt onset information over Arctic sea ice which would be of significant value to data assimilation systems. In anticipation of the availability of data from even more SAR satellites with the launch of the RCM, the multi-sensor γ_c^0 approach presented here may offer the most robust approach to estimate the timing of melt onset over sea ice across the Arctic.

Acknowledgements The authors wish to thank the Polar Space Task Group who coordinated the SAR acquisitions that made this work possible.

Bibliography

Barber, D. G. & Nghiem, S. V. (1999). The role of snow on the thermal dependence of microwave backscatter over sea ice. *Journal of Geophysical Research: Oceans*, *104*(C11), 25789–25803, doi: 10.1029/1999JC900181.

Barber, D. G., Papakyriakou, T. N., LeDrew, E. F., & Shokr, M. E. (1995). An examination of the relation between the spring period evolution of the scattering coefficient (σ) and radiative fluxes over landfast sea-ice. *International Journal of Remote Sensing*, *16*(17), 3343–3363, doi: 10.1080/01431169508954634.

Barber, D. G. & Thomas, A. (1998). The influence of cloud cover on the radiation budget, physical properties, and microwave scattering coefficient (σ^0) of first-year and multiyear sea ice. *IEEE Transactions on Geoscience and Remote Sensing*, *36*(1), 38–50, doi: 10.1109/36.655316.

Belchansky, G. I., Douglas, D. C., Mordvintsev, I. N., & Platonova, N. G. (2004). Estimating the time of melt onset and freeze onset over Arctic sea-ice area using active and passive microwave data. *Remote Sensing of Environment*, *92*(1), 21–39, doi: 10.1016/j.rse.2004.05.001.

Bliss, A. C. & Anderson, M. R. (2014). Snowmelt onset over Arctic sea ice from passive microwave satellite data: 1979–2012. *The Cryosphere*, *8*(6), 2089–2100, doi: 10.5194/tc-8-2089-2014.

Bliss, A. C. & Anderson, M. R. (2018). Arctic Sea Ice Melt Onset Timing From Passive Microwave–Based and Surface Air Temperature–Based Methods. *Journal of Geophysical Research: Atmospheres*, *123*(17), 9063–9080, doi: 10.1029/2018JD028676.

Comiso, J. C. (2012). Large Decadal Decline of the Arctic Multiyear Ice Cover. *Journal of Climate*, *25*(4), 1176–1193, doi: 10.1175/JCLI-D-11-00113.1.

Drinkwater, M. R. (1989). LIMEX '87 ice surface characteristics: implications for C-band SAR backscatter signatures. *IEEE Transactions on Geoscience and Remote Sensing*, *27*(5), 501–513, doi: 10.1109/TGRS.1989.35933.

Drobot, S. D. & Anderson, M. R. (2001). An improved method for determining snowmelt onset dates over Arctic sea ice using scanning multichannel microwave radiometer and Special Sensor Microwave/Imager data. *Journal of Geophysical Research: Atmospheres*, *106*(D20), 24033–24049, doi: 10.1029/2000JD000171.

Early, D. S. & Long, D. G. (2001). Image reconstruction and enhanced resolution imaging from irregular samples. *IEEE Transactions on Geoscience and Remote Sensing*, *39*(2), 291–302, doi: 10.1109/36.905237.

Fyfe, J. C., von Salzen, K., Gillett, N. P., Arora, V. K., Flato, G. M., & McConnell, J. R. (2013). One hundred years of Arctic surface temperature variation due to anthropogenic influence. *Scientific reports*, *3*, doi: 10.1038/srep02645.

Hallikainen, M., Ulaby, F. T., & Abdelrazik, M. (1986). Dielectric properties of snow in the 3 to 37 GHz range. *IEEE Transactions on Antennas and Propagation*, *34*(11), 1329–1340, doi: 10.1109/TAP.1986.1143757.

Howell, S. E. L., Tivy, A., Yackel, J. J., & Scharien, R. K. (2006). Application of a SeaWinds/QuikSCAT sea ice melt algorithm for assessing melt dynamics in the Canadian Arctic Archipelago. *Journal of Geophysical Research*, *111*(C7), doi: 10.1029/2005JC003193.

Key, J., Wang, X., & Liu, Y. (2016). NOAA Climate Data Record (CDR) of AVHRR Polar Pathfinder Extended (APP-X) Cryosphere.

Komarov, A. S. & Buehner, M. (2017). Automated Detection of Ice and Open Water From Dual-Polarization RADARSAT-2 Images for Data Assimilation. *IEEE Transactions on Geoscience and Remote Sensing*, *55*(10), 5755–5769, doi: 10.1109/TGRS.2017.2713987.

Kwok, R. (2004). Annual cycles of multiyear sea ice coverage of the Arctic Ocean: 1999–2003. *Journal of Geophysical Research*, *109*(C11), doi: 10.1029/2003JC002238.

Kwok, R., Cunningham, G. F., & Nghiem, S. V. (2003). A study of the onset of melt over the Arctic Ocean in RADARSAT synthetic aperture radar data. *Journal of Geophysical Research*, *108*(C11), doi: 10.1029/2002JC001363.

Linlor, W. I. (1980). Permittivity and attenuation of wet snow between 4 and 12 GHz. *Journal of Applied Physics*, *51*(5), 2811–2816, doi: 10.1063/1.327947.

Livingstone, C. E., Singh, K. P., & Gray, A. L. (1987). Seasonal and Regional Variations of Active/Passive Microwave Signatures of Sea Ice. *IEEE Transactions on Geoscience and Remote Sensing*, *GE-25*(2), 159–173, doi: 10.1109/TGRS.1987.289815.

Mahmud, M. S., Geldsetzer, T., Howell, S. E. L., Yackel, J. J., Nandan, V., & Scharien, R. K. (2018). Incidence Angle Dependence of HH-Polarized C- and L-Band Wintertime Backscatter Over Arctic Sea Ice. *IEEE Transactions on Geoscience and Remote Sensing*, *56*(11), 6686–6698, doi: 10.1109/TGRS.2018.2841343.

Mahmud, M. S., Howell, S. E. L., Geldsetzer, T., & Yackel, J. J. (2016). Detection of melt onset over the northern Canadian Arctic Archipelago sea ice from RADARSAT, 1997–2014. *Remote Sensing of Environment*, *178*, 59–69, doi: 10.1016/j.rse.2016.03.003.

Mäkynen, M. & Karvonen, J. (2017). Incidence Angle Dependence of First-Year Sea Ice Backscattering Coefficient in Sentinel-1 SAR Imagery Over the Kara Sea. *IEEE Transactions on Geoscience and Remote Sensing*, *55*(11), 6170–6181, doi: 10.1109/TGRS.2017.2721981.

Markus, T., Stroeve, J. C., & Miller, J. (2009). Recent changes in Arctic sea ice melt onset, freezeup, and melt season length. *Journal of Geophysical Research*, *114*(C12), doi: 10.1029/2009JC005436.

Mortin, J., Howell, S. E. L., Wang, L., Derksen, C., Svensson, G., Graversen, R. G., & Schrøder, T. M. (2014). Extending the QuikSCAT record of seasonal melt–freeze transitions over Arctic sea ice using ASCAT. *Remote Sensing of Environment*, *141*, 214–230, doi: 10.1016/j.rse.2013.11.004.

Mortin, J., Schrøder, T. M., Walløe Hansen, A., Holt, B., & McDonald, K. C. (2012). Mapping of seasonal freeze-thaw transitions across the pan-Arctic land and sea ice domains with satellite radar. *Journal of Geophysical Research: Oceans*, *117*(C8), doi: 10.1029/2012JC008001.

Mortin, J., Svensson, G., Graversen, R. G., Kapsch, M.-L., Stroeve, J. C., & Boisvert, L. N. (2016). Melt onset over Arctic sea ice controlled by atmospheric moisture transport. *Geophysical Research Letters*, *43*(12), 6636–6642, doi: 10.1002/2016GL069330.

Onstott, R. G., Grenfell, T. C., Matzler, C., Luther, C. A., & Svendsen, E. A. (1987). Evolution of microwave sea ice signatures during early summer and midsummer in the marginal ice zone. *Journal of Geophysical Research*, *92*(C7), 6825–6835, doi: 10.1029/JC092iC07p06825.

Perovich, D. K., Nghiem, S. V., Markus, T., & Schweiger, A. (2007). Seasonal evolution and interannual variability of the local solar energy absorbed by the Arctic sea ice–ocean system. *Journal of Geophysical Research*, *112*(C3), doi: 10.1029/2006JC003558.

Raney, R. K., Freeman, T., Hawkins, R. W., & Bamler, R. (1994). A plea for radar brightness. In *International Geoscience and Remote Sensing 1994* (pp. 1090–1092). Pasadena, USA: IEEE.

Rüetschi, M., Schaepman, M., & Small, D. (2018). Using Multitemporal Sentinel-1 C-band Backscatter to Monitor Phenology and Classify Deciduous and Coniferous Forests in Northern Switzerland. *Remote Sensing*, *10*(1), 1–30, doi: 10.3390/rs10010055.

Santoro, M. & Strozzi, T. (2012). Circumpolar digital elevation models > 55° N with links to geotiff images.

Schubert, A., Miranda, N., Geudtner, D., & Small, D. (2017). Sentinel-1A/B Combined Product Geolocation Accuracy. *Remote Sensing*, *9*(6), doi: 10.3390/rs9060607.

Schubert, A., Small, D., Jehle, M., & Meier, E. (2012). COSMO-skymed, TerraSAR-X, and RADARSAT-2 geolocation accuracy after compensation for earth-system effects. In *International Geoscience and Remote Sensing Symposium* (pp. 3301–3304). Munich, Germany: IEEE.

Small, D. (2011). Flattening Gamma: Radiometric Terrain Correction for SAR Imagery. *IEEE Transactions on Geoscience and Remote Sensing*, *49*(8), 3081–3093, doi: 10.1109/TGRS.2011.2120616.

Small, D. (2012). SAR backscatter multitemporal compositing via local resolution weighting. In *International Geoscience and Remote Sensing Symposium* (pp. 4521–4524). Munich, Germany: IEEE.

Smith, M. & Rigby, B. (1981). Distribution of Polynyas in the Canadian Arctic, Polynyas in the Canadian Arctic, Occasional Paper 45.

Stroeve, J. C., Serreze, M. C., Holland, M. M., Kay, J. E., Malanik, J., & Barrett, A. P. (2012). The Arctic's rapidly shrinking sea ice cover: a research synthesis. *Climatic Change*, *110*(3-4), 1005–1027, doi: 10.1007/s10584-011-0101-1.

Ulaby, F. T., Moore, R. K., & Fung, A. K. (1986). *Microwave remote sensing: Active and Passive*, volume 1-3 of *Remote Sensing*. Reading, USA: Addison-Wesley.

Wang, L., Wolken, G. J., Sharp, M. J., Howell, S. E. L., Derksen, C., Brown, R. D., Markus, T., & Cole, J. (2011). Integrated pan-Arctic melt onset detection from satellite active and passive microwave measurements, 2000-2009. *Journal of Geophysical Research: Atmospheres*, *116*(D22), doi: 10.1029/2011JD016256.

Winebrenner, D. P., Nelson, E. D., Colony, R., & West, R. D. (1994). Observation of melt onset on multiyear Arctic sea ice using the ERS 1 synthetic aperture radar. *Journal of Geophysical Research*, *99*(C11), 22425–22441, doi: 10.1029/94JC01268.

Yackel, J. J., Barber, D. G., & Papakyriakou, T. N. (2001). On the estimation of spring melt in the North Water polynya using RADARSAT–1. *Atmosphere-Ocean*, *39*(3), 195–208, doi: 10.1080/07055900.2001.9649676.

Yackel, J. J., Barber, D. G., Papakyriakou, T. N., & Breneman, C. (2007). First-year sea ice spring melt transitions in the Canadian Arctic Archipelago from time-series synthetic aperture radar data, 1992–2002. *Hydrological Processes*, *21*(2), 253–265, doi: 10.1002/hyp.6240.

Chapter

5

Paper 4: Automated derivation of continuous glacial and glacier-proximal variables from Sentinel-1 SAR time series for investigating seasonal variations in tidewater glacier dynamics

Rohner, C., Small, D., Henke, D., Lüthi, M.P., & Vieli, A.

This chapter is based on the submitted article:
Automated derivation of continuous glacial and glacier-proximal variables from Sentinel-1 SAR time series for investigating seasonal variations in tidewater glacier dynamics.
Remote Sensing, in review
and is reprinted as the final submitted manuscript.
It has been modified to fit into the layout of this thesis.

C.R. designed the paper with support of D.S. and A.V.. **C.R.**, D.H., D.S., and A.V. defined the methodology. **C.R.**, M.P.L., and D.S. processed the data. **C.R.** implemented the software for and performed the analysis. **C.R.** wrote the draft of the paper. **All authors** contributed to the final version of the paper.

Abstract

Glacier ice discharge through calving represents a major component of current ice mass losses in Greenland. Despite numerous studies, understanding the dynamics and interactions involved remains limited and leads to substantial uncertainties in the projected future mass loss of the Greenland Ice Sheet. Focusing on three western Greenland glaciers with differing movement behaviors, we present new methodologies for deriving quasi-continuous measurements of *glacier flow dynamics*, *surface melt area*, *terminus position*, and *ice composition in the proglacial fjord* from Sentinel-1 SAR amplitude data at a high spatiotemporal resolution and with a minimal need for *a priori* data. By application of these methodologies, the prevalent gap in winter measurements using optical or *in situ* measurements can be closed, allowing analyses of intra- and inter-annual dynamics and interactions between these parameters. The derived time-series between 2017–2021 show a strong linkage between seasonal proglacial ice mélange conditions and terminus changes, despite differences in the seasonal velocity patterns between the glaciers.

5.1 Introduction

The Arctic's atmospheric warming is projected to reach 2.2–8.3°C until 2100 (IPCC, 2013), thereby contributing to ice mass loss in the Greenland Ice Sheet (GrIS). With current ice mass losses of 260–380 Gt a^{-1} (Enderlin et al., 2014; Shepherd et al., 2012), loss of ice from the GrIS represents a major component of global sea level rise. In this context, runoff from ocean-terminating outlet glaciers plays a major role, accounting for about 30-50% of Ice mass loss in Greenland (Cowton et al., 2018; Enderlin et al., 2014; Moon et al., 2015), well ahead of loss from *in situ* surface melt. Together, both mechanisms account for almost all (84%) of the increase in the rate of mass loss since 2009 (Enderlin et al., 2014) and are increasing as a result of, among others, the general warming trend in Greenland, and the migration of subtropical ocean currents toward Greenland's coast (Straneo et al., 2013). The ability to accurately estimate and project future development regarding these mechanisms is essential for predictions about global sea level rise. Due to a lack of understanding of the interactions of glacier dynamics with, e.g., oceanic, atmospheric, and topographic influences, such a projection has remained very challenging (Straneo et al., 2013) leading to large uncertainties in the projected mass loss of the Greenland Ice Sheet (GrIS) (IPCC, 2013; Nick et al., 2013; Straneo et al., 2013). Furthermore, variations between outlet glaciers concerning these interactions, including inter-annual variations, are likely to result in even greater challenges (Moon et al., 2015).
Among the mechanisms suspected to control changes in the near-terminus behavior of outlet glaciers are (Moon et al., 2015):

1. release from the buttressing effect of rigid sea ice and ice mélange, causing further retreat of the glacier terminus,

2. volumetric changes of the glacier by advance, retreat, or thinning, changing the resistive forces from the glacier bed and/or the surrounding topography, and influencing the glacier's flow velocity,

3. changes in terminus stability due to increased below-surface oceanic melt of ice at the terminus,

4. the relative position of the terminus with respect to basal topography, affecting the rates of retreat for a given forcing.

Due to Greenland's remoteness, continuous *in situ* measurements of such glacial and related environmental forcing parameters are not only logistically difficult but also expensive, resulting in data gaps, predominantly in winter. Remote sensing data can be and are used to overcome logistical challenges, with optical sensors (e.g. Landsat, ASTER, MODIS) but are influenced by the lack of availability of sunlight during the long polar winter as well as cloud cover, therefore exhibiting data gaps during winter seasons similar to those from *in situ* measurements.
Previous publications on the long-term temporal behavior of outlet glaciers in Greenland utilizing remote sensing data, focused on various parameters, such as glacier velocity (Fried et al., 2018; Howat et al., 2010; Joughin, 2021; Moon et al., 2015), terminus position (Carr et al., 2017; Catania et al., 2018; Cheng et al., 2021; Cowton et al., 2018; Fried et al., 2018; Lea et al., 2014; Moon & Joughin, 2008; Moon et al., 2015), sea-ice/mélange conditions (Carr et al., 2017; Fried et al., 2018; Howat et al., 2010; Moon et al., 2015), runoff (Cowton et al., 2018; Fried et al., 2018; Moon et al., 2015), and ocean temperatures (Carr et al., 2017; Cowton et al., 2018; Fried et al., 2018; Lea et al., 2014). Some operational products exist for several of the parameters (e.g., Joughin (2021); Nagler et al. (2015) for glacier flow velocity, Kim et al. (2017); Mote (2014) for surface melt). While offering insights into the state of the parameters on a regional or ice-sheet level and thus focusing on a lower resolution, they are not easily suited for researching the immediate interaction of the glacier's terminus with the proglacial fjord. Despite the availability of data sets for individual parameters, integrative, long-term studies investigating the interaction between multiple parameters and over varying time scales are lacking (Moon et al., 2015).
Our primary objective is to present methodologies to derive continuous glacial variables from S1 SAR time series in an automated fashion. To achieve this, we minimize or eliminate the need for *a priori* data such that the approaches are applicable independent of the chosen location and across various scenarios, with a focus on the interaction of the glacier's terminus with the proglacial fjord. In this glacier terminus region strong velocity gradients are expected, and the methodologies, especially regarding glacier flow dynamics, are adapted to reflect this. Nevertheless, our chosen methodologies depend on image statistics only, and are thus easy to implement.
In the following sections, we describe first the input data sets used for this paper and the algorithms to derive the parameters which are *flow velocity*, *surface melt*, *glacier front position*, and *ice cover and mélange*. Following that, the results of the application of these algorithms are presented for each of the three glaciers investigated. In the discussion, we analyze the strengths and weaknesses of each algorithm. Finally, we present the potential of the automated extraction of multiple glacial parameters from a single SAR satellite constellation to support integrative, long-term studies investigating interactions between these parameters.

5.1.1 Study Area

For this study, we focused on the three medium-sized ocean terminating outlet glaciers of *Eqip Sermia* (69° 48′ N, 50° 14′ W), *Kangilerngata Sermia* (69° 54′ N,

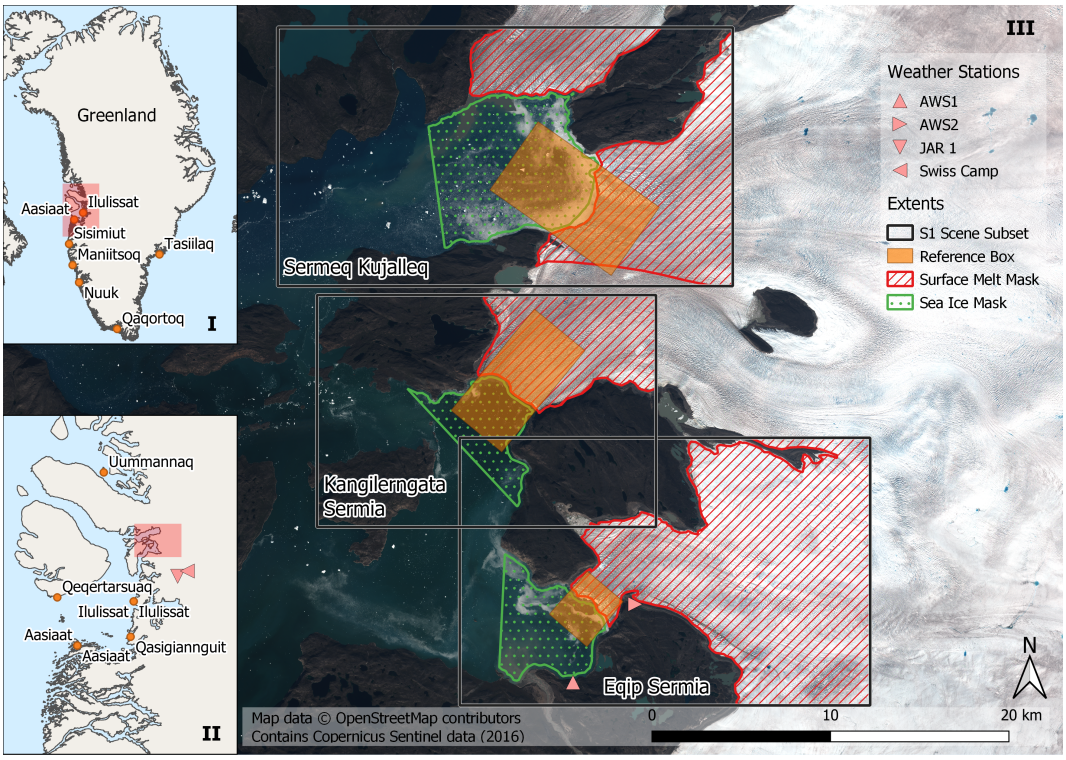

Fig. 1: Detailed overview over the three glaciers investigated for this study. From the North, Sermeq Kujalleq, Kangilerngata Sermia, and Eqip Sermia. In orange, the reference boxes used for the calculation of the glacier front position are shown. The red and green polygons depict the masks used for the glacier melt area estimation and ice mélange calculations, respectively. The red triangles in maps II and III show the locations of the automated weather stations.

50° 20′ W) and *Sermeq Kujalleq* (70° 00′ N, 50° 14′ W), located north of *Ilulissat* in Western Greenland. Despite being located in close proximity (within 30 km of each other) and therefore nearly identical meteorological conditions, the glaciers exhibit different behaviors, especially regarding advance/retreat and glacier flow dynamics. This makes the region an ideal subset to test our retrieval methodologies. The availability of historical geometry and flow velocity survey data for *Eqip Sermia*, dating back to 1912 (e.g., de Quervain & Mercanton, 1925) allows for comparisons regarding the past and present behavior of the glacier. With its roughly 3.5 km wide and 30-50 m high calving front, *Eqip Sermia* showed a long-term flow speed at the terminus of 3 $m \cdot d^{-1}$ (Bauer, 1968). This flow speed was stable for almost a century before accelerating towards the end of the 20th century, with a 30% acceleration between 2000 and 2005 and a doubling of the discharge (Kadded & Moreau, 2013; Rignot & Kanagaratnam, 2006).

5.2 Materials and Methods

5.2.1 SAR Data

Despite the availability of optical satellite data published under an open-data policy, polar night and frequent cloud cover hinders continuous observation of glacial and glacier-proximal parameters in polar regions at a high temporal resolution. Active

satellites (e.g. Synthetic Aperture Radars; SAR) supply their own illumination, not needing sunlight and are unaffected by cloud cover. They therefore offer a temporally more reliable stream of measurements. While earth observing SAR satellites have been in orbit for almost 30 years, the launch of S1A in 2014 and S1B in 2016 drastically increased the availability of openly and freely available data sets. The high duty cycle of 25 minutes per orbit results in a potential global coverage of all relevant land surfaces at least once every 12 days per satellite and 6 days for the constellation. At polar latitudes, coverage is more frequent, ranging from 4 to 2 days per satellite (Torres et al., 2012). In combination with further data sets, e.g. from SAR constellations such as the RADARSAT Constellation Mission (RCM), the temporal resolution of acquisitions can increase even further (Dabboor et al., 2018). For our analysis, we relied on HH polarized Single Look Complex (SLC) C-band (5.405 GHz) data sets acquired in the interferometric wide swath (IW) mode, accessed through the Copernicus Open Access Hub (Torres et al., 2012). The nominal pixel spacing of the data sets in slant range is 2.3 m in range and 14.1 m in azimuth (Nagler et al., 2015). The detected SAR images were geometrically terrain corrected using range-Doppler geocoding (Meier et al., 1993) using the TanDEM-X 90m DEM (Rizzoli et al., 2017). The TanDEM-X 90m DEM has a pixel spacing of 3 arcsec in the latitude dimension, and 6 arcsec in the longitude dimension for our region of interest ($\approx$ 93 m $\times$ 64 m), which was oversampled to 15 m $\times$ 15 m. As our operations take place in the DEM geometry, no separate co-registration was performed. The geolocation accuracy was sufficient to alleviate the need for tie points during geocoding (Schubert et al., 2017).
We chose a time period from when high temporal resolution as well as multiple relative orbits (namely 17, 25, 90, 98, and 127) were available: our study focuses on the period between 2017/01/01 and 2020/12/31, beginning after the successful commissioning of S1B. A total of 675 SAR acquisitions from the aforementioned five relative orbits were used that cover all of the three targeted outlet glaciers (see Table 1). Out of these 675 acquisitions, 220 were taken from an ascending orbit (relative orbits 17 and 90) and 455 from a descending orbit (relative orbits 25, 98, and 127). As the IW mode was used, the incident angles were between 30° to 45° for all acquisitions.

Tab. 5.1: Number of S1 acquisitions used per parameter and glacier.

Glacier	Flow Velocity	SMA	Ice Mélange	Glacier Front Pos.
Eqip Sermia	674	674	675	424
Kangil. Sermia	673	672	675	426
Sermeq Kujalleq	673	672	675	428

5.2.2 Meteo Data

Daily maximum temperatures were compiled from four automatic weather stations (AWS) whereby two were operated by the University of Zurich (AWS1 and AWS2; Kneib-Walter et al., 2019), and two by the Greenland Climate Network (JAR 1 and SwissCamp (SC); Steffen, 2020; Steffen et al., 1996). Based on their hourly measurements, daily maximum air temperatures were retrieved for each of the locations. When available, data from station AWS2 (cf. Table 5.2) were used, representing the meteorological conditions at the land ice margin of *Eqip Sermia* (Kneib-Walter et al., 2019) about 2 km from the calving front (362 m a.s.l.). Gaps

Tab. 5.2: Greenland *in situ* automatic weather stations used

Station	Operator	Lat. (°)	Lon. (°)	Elev. (m)	Meas. Interval
AWS1	UZH	69.75556	-50.25301	60	Hourly
AWS2	UZH	69.79442	-50.16115	362	Hourly
JAR 1	GC-Net	69.49836	-49.68156	962	Hourly
SC	EnviDat	69.55556	-49.36472	1138	Hourly

Station	Characteristics	Source
AWS1	On land (coast)	(Kneib-Walter et al., 2019)
AWS2	On land (ice margin)	(Kneib-Walter et al., 2019)
JAR 1	On ice sheet	(Steffen et al., 1996)
SC	On ice sheet	(Steffen, 2020)

occurring in this data set were filled with data from station AWS1 when necessary or from stations JAR 1 and SC. Differences due to the stations' elevations were corrected relative to AWS2 using the intercept of a time constant linear regression between the stations' measurements (i.e. -1.8655 °C for AWS1, +5.4029 °C for JAR 1, +6.4896 °C for SC). Station JAR1 melted out summer 2019 and was subsequently decommissioned (J. Box, personal communication, 2021/02/24), therefore it was not used thereafter.

5.2.3 Flow Velocity

Making use of the high spatiotemporal resolution of the S-1 constellation, flow dynamics for three outlet glaciers in the northern Disco Bay area were calculated based on S1 A/B SAR backscatter. The iterative offset-tracking approach described in Rohner et al. (2019) was employed. This approach compares the backscatter pattern within image patches between sequential, co-registered image acquisitions from a single track and mode to derive two-dimensional offset values. The method utilises the normalised cross-correlation between the image patches (Gray et al., 2001; Joughin, 2002; Strozzi et al., 2002). By relying solely on the SAR backscatter information and ignoring the phase, the velocity estimates are not influenced by meteorological conditions or incoherent and/or rapid flow of the glacier. To get reliable measurements close to the calving front of the glaciers, an iterative intensity tracking algorithm described in Rohner et al. (2019) was used. A reference window size of 25×25 pixels (375×375 m) and an initial search window size of 45×45 pixels (675×675 m) for a six day time delta between subsequent acquisitions was chosen, with a pixel step size of 1 pixel (Rohner et al., 2019). In case of a longer duration between subsequent acquisitions, the search window size increases by 20 pixels (300 m) in x and y direction for every additional six days, allowing for the detection of a maximum flow velocity of 25 m/d. In order to remove outlier pixels, as identified on the metrics laid out in Rohner et al. (2019), an additional iterative step was applied, that increased the window's dimension by 5 pixels in both x and y direction while additionally adjusting the search window size based on a long-time flow velocity average (Rohner et al., 2019). These iterations were repeated for a maximum of 5 times or until no more outliers pixels were detected. The resulting flow velocity maps were downscaled to a pixel spacing of 105×105 m (i.e. 7×7 pixels). The above velocity-tracking method was validated with independent velocity observations

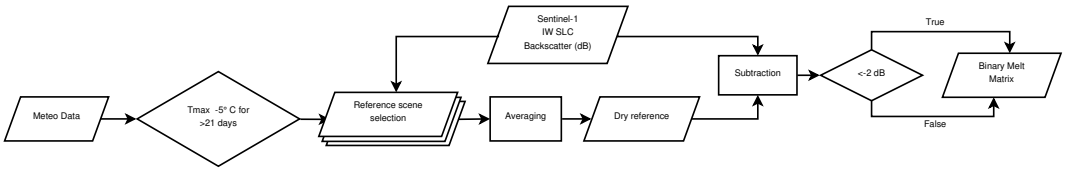

Fig. 2: Methodology for *surface melt detection*, relying solely on calibrated Sentinel-1 SAR backscatter and meteorological data. The areal percentage was calculated using a glacier mask.

from *in situ* dGPS measurements, terrestrial radar interferometry and repeat UAV. The mean differences in velocity magnitude is estimated to be 11.5%, 12.4% and 14.2% when comparing the offset-tracking approach with dGPS, repeat UAV and radar interferometry measurements, respectively (Rohner et al., 2019).

5.2.4 Surface Melt Detection

Radar-based discrimination of the surface melt area is typically based on the difference between the dielectric properties of frozen vs. liquid water, e.g. as described in Linlor (1980). By calculating backscatter differences between (a) candidate images and (b) a dry cold reference, one can map regions of wet snow and ice. This was originally demonstrated with the C-band European ERS-1 and Canadian Radarsat satellites (Linlor, 1980; Piesbergen et al., 1995) and has since been shown to be feasible also using S1 data (Nagler et al., 2016). Greenland-wide annual sigma nought backscatter mosaics were showcased in Joughin et al. (2016) to highlight different melt-extents. As a first step, dry reference images need to be selected for each of the relative orbits. Reference images are composed from multiple SAR images of either snow-free surfaces and/or covered by dry snow in order to minimize the presence of liquid water in the reference scenes. As the focus of this paper is on glaciated areas, we chose long cold periods during the winter as reference periods. Scenes within a period of ≥ 21 days with daily maximum temperatures over all of the weather stations of $\leq -5°C$ were used to calculate a reference image (see Table 5.2). Due to a lack of scenes acquired in winter, no reference scene could be calculated for relative orbit (track) 17, which we therefore omitted for this analysis. The reference scenes of tracks 25, 90, 98, and 127 were based on 28, 34, 9, and 27 scenes respectively.
After converting the SAR intensity to dB, we calculated the γ^0-difference on a pixel-by-pixel basis for each SAR acquisition versus the track's reference image. The presence of liquid water was defined based on a γ^0-ratio $< -2dB$, resulting in a binary melt matrix (see Fig. 2). As we focused on the detection of melt on the glacier's surface, non-glaciated areas were masked out and the percentage of glacial area affected by melt was calculated for both orbit configurations. Note, that the proposed methodology above aims first of all to mark the timing of onset and termination of the summer melt period. Further, be aware that the percentage in melt extent serves only as a proxy for melt intensity on the outlet glacier but not as an absolute measure for the melt-rate or surface runoff.

5.2.5 Glacier Front Position

Changes in terminus position are not only important for estimating dynamic mass loss (IPCC, 2013; Nick et al., 2013), but they also seem to be interrelated with variations in flow speed and elevation changes (Catania et al., 2018; Fried et al.,

2018; King et al., 2018). In contrast to most of the glacial and glacier-proximal parameters, the glacier *front position* can be mapped directly from using openly available remote sensing imagery from either active or passive sensors. Due to limitations intrinsic to optical systems such as cloud cover and - more important for polar applications - availability of daylight, use of such imagery is limited and existing front variation records are therefore often patchy (Catania et al., 2018; Fried et al., 2018). With the increasing availability of spaceborne SAR sensors such as the S1 constellation, a quasi-continuous observation of glacier front positions became possible.

Process

The glacier front position was delineated using the same geocoded IW SLC γ^0 amplitude images with a pixel spacing of 15×15 m that had previously been used for the extraction of the other parameters. We limited the glacier front position calculation to scenes stemming from a descending orbit (i.e. looking westerly towards the sea), as the radar shadow cast by the glacier front provided higher contrast in comparison to the heightened amplitudes present in scenes from an ascending orbit, especially so in the heavily crevassed frontal area of the glacier tongue. While this selection limited the number of available scenes, there were still more than 450 scenes available for the period of three years stemming from the relative orbits 25, 98, and 127 (see table 5.1), resulting in an estimated glacier front position every 3.2 days on average.

Our approach is an extension of the algorithm laid out by Krieger & Floricioiu (2017) that relied on gradients within the image caused by the differences in backscatter intensity (cf. Fig. 3). We used a Canny edge detection algorithm (Canny, 1986) with a 9×9 Gaussian filter and $\sigma = 1.4$ to calculate the edge magnitude $G(x, y)$ at each pixel location (x, y) after the non-maximum suppression step. In contrast to the method described in Krieger & Floricioiu (2017), we did not use a threshold to make the edge weights binary, but instead normalised the edge magnitudes for each individual scene to $[0, 1]$ using:

$$G_{norm}(x, y) = \left(1 - \frac{G(x, y) - min(G)}{max(G) - min(G)}\right)^k \tag{5.1}$$

The values were (a) inverted in order to be able to run a cost minimization algorithm later and (b) raised to the power of $k = 10$ to increase the penalty for weak edge magnitudes signifying a lack of backscatter gradients within the SAR subset. Further, G_{norm} was set to 0 for a 3×3 sample buffer surrounding the lateral moraines (extracted from a vector data set provided by the Danish Agency for Datasupply and Efficiency, 2022) to allow for an automated selection of the starting and ending positions v_s and v_e. Based on G_{norm}, an adjacency matrix was calculated and G_{norm} used for weighting in this directed graph, applying Dijkstra's algorithm (Dijkstra, 1959) to minimize the path length (i.e. the sum of weights G_{norm} between v_s and v_e). This was done in a first iteration for all candidate SAR subsets, returning the detected glacier front position candidate as a boolean matrix. While the resulting glacier front positions can be used as is, they are prone to outliers caused by strong gradients from heavily crevassed glacier tongues or the ice mélange-plume interface. We therefore applied a novel second iteration, spatiotemporally constraining the search area for the Dijkstra algorithm based on the positions returned from the first iteration. As a constraint, the binary grids containing the glacier front positions

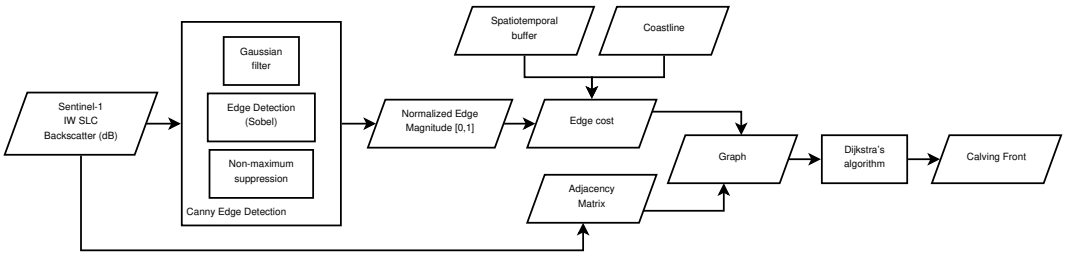

Fig. 3: Methodology for the automated *glacier front position* delineation, relying solely on calibrated Sentinel-1 SAR backscatter and publicly available geodata.

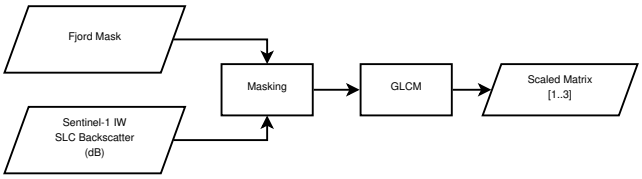

Fig. 4: Methodology for *ice type discrimination* in the fjord, relying solely on calibrated Sentinel-1 SAR backscatter. Areal percentage was calculated using a fjord mask.

from within a 45 day window around a SAR subset were summed up and processed following Eq. (5.1) with $k = 1$, returning edge weights based on the temporal distribution of the glacier front positions, reducing sensitivity to outliers. These edge weights were then used to calculate a spatiotemporally averaged glacier front position using Dijkstra's algorithm. The second iteration follows the same steps as in the first, aside from limiting the search area to within 500 m of the spatiotemporally averaged position by setting all edge weights outside of this area to 1, reducing the number of erroneous solutions.
The width averaged calving front position was calculated using the box method laid out in Moon & Joughin (2008). This method uses a rectangular reference box approximately the width of the glacier tongue (see Fig. 1) to calculate the distance of the front from the arbitrarily chosen reference line upflow from the glacier tongue by dividing the area of the box enclosed by the glacier tongue by the box's width. This width averaged method allows a more robust assessment of changes in glacier front position compared to using a single point along the flow line of the glacier, since it also accounts for uneven changes of the front (Moon & Joughin, 2008). To further eliminate outliers, a subsequent culling step was applied, using the front position and the glacier front's sinuosity derived by dividing the real world length of a line to the direct distance between the line's end points (Leopold et al., 1964). Any glacier fronts deviating more than three local standard deviations from the local median within an eleven-element temporal window for either the glacier's front position or its sinuosity were removed from the set of estimates.

5.2.6 Ice cover and Mélange

The observed changes in glacier dynamics and calving rates are likely to be influenced by processes at the glacier-ocean interface (Bevan et al., 2019; Fried et al., 2018). The presence of sea ice and ice mélange (densely packed calved icebergs in contact with the glacier's terminus) is thought to add a buttressing effect to the glacier, stabilizing its calving front and modulating glacier and terminus dynamics (Amundson et al., 2010; Cassotto et al., 2015; Fried et al., 2018; Reeh et al., 2001).

By using SAR data sets, the extent and type of ice coverage within the fjord can be calculated without the need for *a priori* data, aside from a land/sea mask. Our approach relies on texture analysis of the geocoded γ^0 backscatter images used for the extraction of the other parameters (cf. Fig. 4). A grey-level co-occurrence matrix (Haralick et al., 1973) was calculated for all subsets of each available scene with distance $d = 1$ and angles θ quantised to 45° intervals, symmetric across its diagonal. The input backscatter data was limited to the interval (in dB) $[-20, 5]$ and divided into 3 bins, representing open water, brash ice (small scale drift/pack ice; Singh et al., 2011), and ice mélange. Backscatter lower than -20 dB in the input image was scaled to 1, values higher than 5 dB to 3 in the resulting scaled image. The extent of the ice covered area of the fjord was subsequently calculated based on the sea mask and the scaled image. Pixels in the scaled image with a value of 1 were classified as open water, those with value 2 as brash ice, and those with value 3 as ice mélange.

5.3 Results

The derived SAR-based time series of flow speed, front positions, melt extent and ice cover on the fjord are presented below for all three glaciers. The individual parameters for Eqip Sermia are first examined in detail; correlations and discrepancies between each other are highlighted. For the remaining two glaciers, which are in a contrasting geometric or dynamic setting, the presentation of the results is focused on the differences between the glaciers. In general, the proposed methodologies delivered a nearly continuous time series of all parameters without gaps in the winter-time and a mean temporal resolution within the study area of between 3.2 days for the glacier front position and better than 2.5 days for the remaining parameters. This allows a detailed analysis of changes in glacier dynamics and geometry in relation to variations in external forcings (surface melt, ice mélange) and between the different glaciers.

5.3.1 Eqip Sermia

5.3.1a Glacier Flow Dynamics

The flow speeds (time-averaged over ± 10 days) of Eqip Sermia are shown in Fig. 5 for different positions upstream of the front. Clear seasonal variations are visible. Within 1 km of the calving front (blue and read lines in Fig. 5a), the flow velocities vary seasonally between 4 and 6 m/d. The minimum speed was normally reached at the end of winter (between March in 2017/2018 and April in 2019) and remained at this minimum level for one to two months (2019: one; 2017/2018: two). Subsequently, and concurrent with the onset of surface melt (Fig. 5b), the glacier flow accelerated over a period of about two months, reaching its maximum speed in June or July. From this time onward, the flow velocities gradually and slowly decreased until they reached a minimum speed in early spring, with no detectable influence from the cessation of surface melt in fall. This seasonal velocity pattern was similarly visible up to 3 km upstream from the calving front, but with a strongly subdued seasonal amplitude (red and orange lines in Fig. 5a). For year 2020 the cycle changed. While the minimum velocity was reached in early spring (2020/03/06), the usual one or two month acceleration of the glacier continued on until 2020/09/24, thus for more than half a year, before starting to show slowly

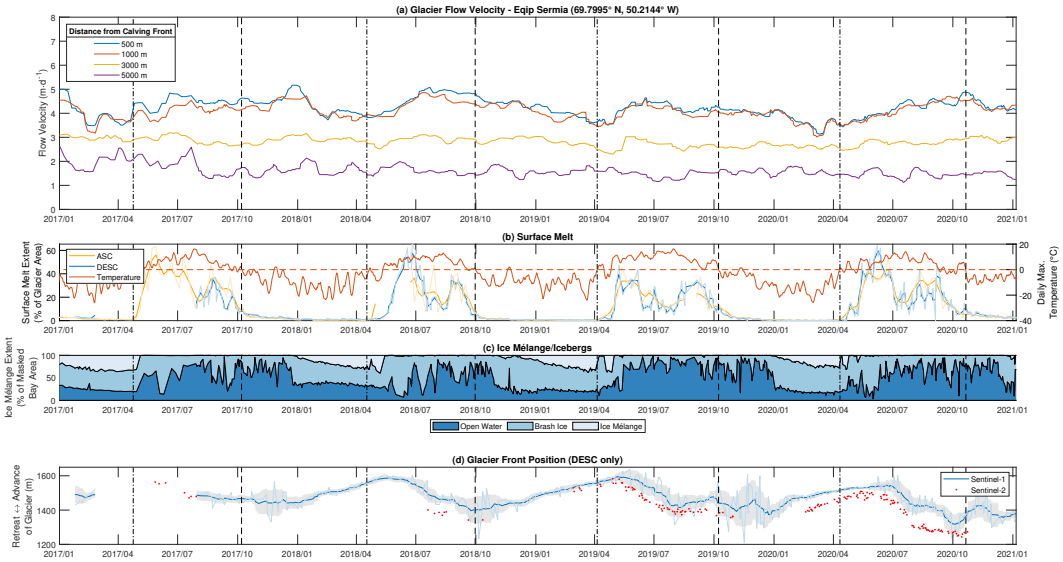

Fig. 5: Parameters retrieved over time period between 2017/01/01 and 2020/12/31 for Eqip Sermia. In (a) the flow speeds at different distances upstream from the terminus are shown (see legend). In (b), the SAR derived melt extents (in percent; blue and orange lines) are shown alongside air temperature (red line) recorded near the terminus (AWS2). (c) shows the evolution of ice composition on the fjord and in (d), the observed front positions from SAR (raw: light blue line; moving average: dark blue line; standard deviation: gray shading) and from S2 (manually mapped) are shown. The vertical dash-dotted lines delineate the beginning, the vertical dashed lines the end of seasonal periods with positive daily maximum temperatures.

decreasing flow velocities. Similar to the years prior, this change in velocity pattern is visible for the data at 3 km upstream from the calving front, albeit subdued. At 5 km upstream from the terminus, no seasonal cycle was detected.

5.3.1b Surface Melt

A clear seasonal pattern in the melt extent is visible (blue line in Fig. 5b) which is seen to have a close relationship to the air temperature record (red line). During the winter months, when maximum daily air temperatures are well below freezing, no melting was detected from the SAR data. As soon as positive air temperatures are reached (normally at the end of April, beginning of May) a melting signal was detected staying until the end of summer when air temperatures went below 0° Celsius. Whereas in the years 2017 and 2018 the melting ceased in early October, in 2019, the melt continued until mid November and never fully ceased until the end of the year 2019. In 2020, the same melt regime was observed, this time even more strongly pronounced. For all four years (2017–2020) and from both orbits (ascending and descending), the peak in surface melt extent was reached within one and a half months after the onset of melt was detected. Daily maximum temperatures consistently remained well above freezing throughout the summer, but in all four years, a local minimum in melt extent was observed around August, before reaching a second melt peak about one month later. Note that the air temperature does not show such a double peak during the summer, suggesting that the shown percentage variations in melt extent should not be interpreted as a direct measure for rates in surface ablation, but rather a means of marking the onset and cessation of the ablation period.

5.3.1c Floating Ice Conditions in Fjord

The abundance and composition of the floating ice in Eqip Sermia's proglacial fjord also followed a clear seasonal pattern. Its pattern appeared to be paced by the occurrence of surface melt (Fig. 5c). With the onset of surface melt, the ice mélange that built up during the winter breaks up, and is replaced by a mixture of brash ice and open water for the remainder of the melting season. During the summer period, the percentages in coverage of brash ice and open water underwent strong fluctuations, likely a result of variations in calving activity, wind intensity and the abundance of melt water plumes at the front. The wind pushes the brash ice in and out of the proglacial area, creating large variations in the extent of open water. Melt water plumes are linked to subglacial discharge, and hence periods of high surface melt (Dowdeswell & Cromack, 1991). They tend to push away any icebergs and brash ice from the calving front and produce there areas of open water. Note that before the onset of ice mélange buildup, a peak in brash ice occurred in all years. At the end of the melting season, and in the absence of proglacial plumes, ice mélange starts to form again, and is building up continuously throughout the winter and spring while air temperatures remain negative. The maximum percentage coverage of ice mélange was very similar for the years 2017–2019, reaching between 36% and 39% of the selected proglacial area (see Fig. 1) and 32% for the year 2020, with the majority of the remaining area being made up of brash ice (that also includes sea ice) and to a lesser extent by areas classified as open water.
Note that the temporal patterns of ice cover were in all years very similar, but the unusually warm period at the end of 2019 and early 2020 not only extended the period of surface melt (see Section 5.3.1b), but also led to an increase in both the duration and extent of open water.

5.3.1d Glacier Front Position

Figure 5d shows the glacier front position estimated using data from descending orbits. The dark blue line depicts the averaged position calculated using a temporal moving average including 11 data points; the bright blue line shows the unaltered values based on the front line delineation described in Section 5.2.5. The gray area shows one standard deviation based on the unaltered values around the smoothed position. The red points show the positions based on a manual delineation using optical S2 imagery, applying the identical box methodology (Moon & Joughin, 2008). Due to S2's requirement for sunlight, validation could not be carried out during polar night. The presence of clouds limited the number of suitable S2 scenes to 175 for the period between 2017/01/01 and 2020/12/31.
Eqip Sermia showed clear seasonal variations in its front position, with an amplitude of about 250 m. A slow and steady advance had set in when surface melting ceased in late autumn, concurrent with the presence of ice mélange in front of the terminus. When daily maximum temperatures rose to above 0°C in the spring, a relatively fast retreat began. The glacier's maximum extent was reached in May in 2018 and 2019 and in June in 2020, but in 2017 no data was available during this time due to changes in the S1 observation scenario. The position of maximum retreat of the calving front was reached in November (2017), September (2018), December (2019) and October (2020). In 2019 and 2020, an unusual pattern of smaller advances and retreats throughout the fall and early winter was observed for the smoothed front position (dark blue line in Fig. 5d). This pattern was consistent with observed variations in the other parameters (velocity, surface melt and ice mélange). In general, the temporal pattern of the front positions and the inflection points

were in good agreement with the validation data from S2 (red dots), although there was a mean and median absolute offset of 68 and 65 m compared to the smoothed glacier front positions (R^2: 0.872; see Table 5.3). During summer periods, whenever a proglacial plume was present (due to substantial melt), the raw front positions (light blue line) showed strong fluctuations that are physically not plausible, as the advance rates would be far beyond the flow speeds observed at the terminus. These fluctuations were most likely an artefact of the front detection algorithm in the specific situation of a substantial melt plume occurring at the calving front (see section 5.2.5).

Tab. 5.3: Differences between S2 and S1 front positions (max. temporal difference between scenes: 6 days, S1 positions smoothed using moving average with span=11)

	Eqip Sermia	Kangilerngata Sermia	Sermeq Kujalleq
Mean (m)	-68.445	-13.542	-61.928
Median (m)	-64.684	-30.261	-64.008
|Mean| (m)	68.448	54.374	74.066
|Median| (m)	64.684	47.469	69.263
Std (m)	32.422	65.178	57.498
R^2 (Ord)	0.872	0.922	0.969
R^2 (Adj)	0.871	0.921	0.969
n	171	175	173

Tab. 5.4: Differences between S2 and raw S1 front positions (max. temporal difference between scenes: 6 days)

	Eqip Sermia	Kangilerngata Sermia	Sermeq Kujalleq
Mean (m)	-68.419	-11.212	-64.538
Median (m)	-67.739	-17.268	-67.344
|Mean| (m)	73.679	52.587	74.816
|Median| (m)	68.923	38.040	69.270
Std (m)	53.140	68.999	54.909
R^2 (Ord)	0.629	0.902	0.966
R^2 (Adj)	0.627	0.901	0.965
n	171	175	173

5.3.2 Sermeq Kujalleq

The northernmost glacier in the region (see Fig. 1), Sermeq Kujalleq, referred to here as Kujalleq in short, showed substantially higher flow speeds than Eqip Sermia, but had a similar seasonal pattern (Fig. 6a). While Eqip Sermia moved at maximum speeds of 5–6 m/d near its calving front, Kujalleq reached 15 m/d to 16.5 m/d. As at Eqip Sermia, the springtime speed up at Kujalleq also coincided with the onset of surface melt, yet the maximum peak was reached about one month later, i.e. between the end of July (2019/2020) and mid September (2018). Again, the subsequent deceleration was rather slow and gradual and continued right into spring for the years 2017, 2018 and 2020, reaching the minimum in flow speed in

April. In the winter of 2019/2020, the deceleration was much less pronounced. Analogous to Eqip Sermia, the flow velocities stayed close to their minimal speed for about two months before accelerating over a period of two (2017/2020) to three (2018/2019) months. As in the case of Eqip Sermia, these seasonal variations in flow speed were clearly visible up to 3 km from the calving front, though with lower amplitude.
The temporal pattern of surface melt extent and the timing of melt onset and cessation was almost identical to that of Eqip Sermia. This is not surprising, given the proximity of these glaciers and that their melt is strongly related to air temperatures.
As was the case for Eqip Sermia, the evolution of ice composition in the proglacial fjord is strongly interlinked with air temperature and thus with the presence or absence of surface melt. Therefore, consistent with the findings from Eqip Sermia, ice mélange started as soon as surface melt ceased, then gradually grew and reached its maximum in April/May covering 28% (2017), 42% (2018), 77% (2019), and 51% (2020) of the fjord mask (see Fig. 1). Again, ice mélange was not present during the months when surface melt was detected. During this period, the proglacial fjord was covered by a mixture of brash ice and open water and again showed strong fluctuations. Similar to the case of Eqip Sermia, a peak in brash ice occured after the end of the melting season, just before the start of the build up of ice mélange.
The position of the glacier front behaved similarly to Eqip Sermia, showing a slow and gradual advance of the glacier front in the presence of ice mélange and a relatively fast retreat after its disappearance, starting with the onset of surface melt. The position of maximum retreat was reached in September (2017/2018), November (2019), and August (2020), the position of maximum advance in April (2018/2020) and May (2019), although throughout the winter of 2019/2020 the advance was much less pronounced than the years before, agreeing with the observations of flow velocity for the same time period. In 2017, there were again no data available during this period, due to changes in the S1 observation scenario. In agreement with the substantially higher percentage of ice mélange extent in 2019, the glacier advanced then more than 300 m further than in 2018. When compared with the positions as delineated from S2, there was a good agreement with regard to the inflection points as well as the absolute positions: a mean absolute difference of 74 m and a median absolute difference of 69 m was observed (R^2: 0.969; see Table 5.3).

5.3.3 Kangilerngata Sermia

Despite its proximity to both Eqip Sermia and Sermeq Kujalleq, Kangilerngata Sermia exhibited considerable differences regarding its inter- and intra-annual glacier flow dynamics as well as its glacier front position. The forcing parameters (melt extent and ice cover on fjord) show however very similar seasonal patterns, as very similar meteorological conditions applied (cf. Fig. 7a).
Kangilerngata Sermia exhibited flow velocities at the glacier terminus similar to those of Eqip Sermia, reaching a yearly maximum of 4.6 m/d in May 2017, 4.3 m/d in July 2018, 5.8 m/d in July 2019. In 2020, the velocity profile was unlike the years before, resulting in a peak velocity of 5.3 m/d already in January. This behaviour as well as the high flow velocities for 2019/2020 was exceptional, since they were likely caused by the partial collapse of the glacier's terminus (see further below). The timing of the velocity peaks for 2017–2019 was in agreement with Eqip Sermia, but preceded Sermeq Kujalleq by up to 45 days. While the seasonal variations in glacier speed were detected only up to a distance of 3 km from the calving front

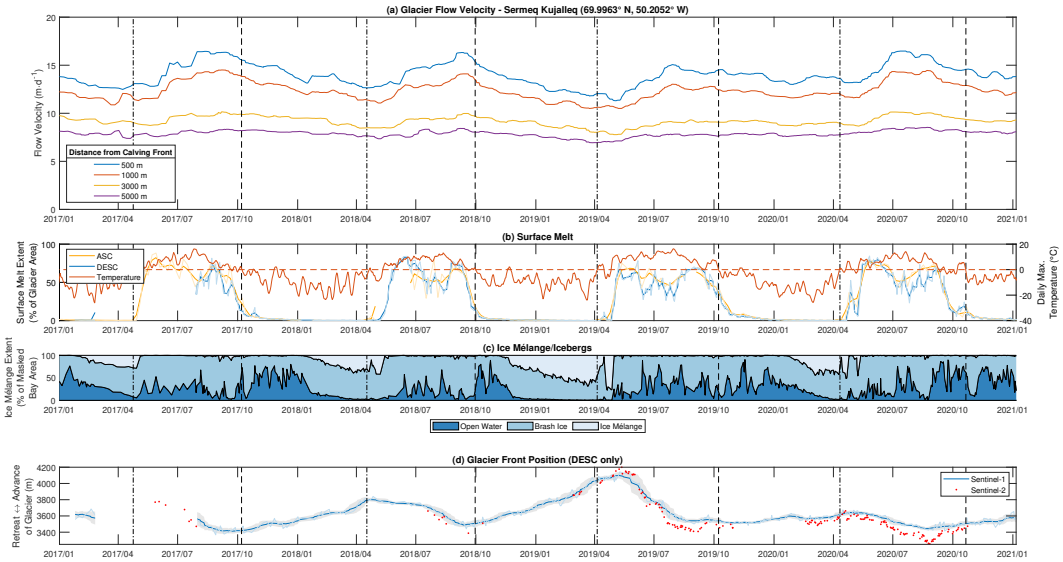

Fig. 6: Extracted parameters for time period between 2017/01/01 and 2020/12/31 for Sermeq Kujalleq. In (a) the flow speeds at different distances upstream from the terminus are shown (see legend). In (b) the SAR derived melt extents (in percent; blue and orange lines) are shown alongside air temperature (red line) recorded near the terminus (AWS2). (c) shows the evolution of ice composition on the fjord and in (d) the observed front positions from SAR (raw: light blue line; moving average: dark blue line; standard deviation: gray shading) and from S2 (manually mapped) are shown. The vertical dash-dotted lines delineate the beginning, the vertical dashed lines the end of seasonal periods with positive daily maximum temperatures.

for the other two glaciers, at Kangilerngata Sermia, they propagated further inland, with a similar seasonal velocity amplitude at 5km as near the front. The decrease in flow speed with upstream distance was at 20% (between front and 5km upstream) much lower than at the other two glaciers (between 40% to 60%).

With regard to the temporal velocity pattern, Kangilerngata Sermia behaved surprisingly different than both Eqip Sermia and Sermeq Kujalleq, which both showed rapid acceleration at the onset of the melting season followed by a slow, constant deceleration during fall and winter (with the exception of Eqip Sermia in 2020). In contrast, Kangilerngata Sermia showed a slow, but continuous acceleration between late summer (end of melting season), when its flow velocity was lowest, to the start of summer, when the peak in flow speed was reached. This long period of acceleration was in the second half of the melting season followed by about two months of rapid deceleration.

The temporal patterns of surface melt extent were very similar to those observed for the other two glaciers, with the same prolongation of the melt period into late fall in 2019 and 2020. As a result of the close proximity of the glaciers and thus little differences in the prevailing climatic conditions, similar temperatures (see red line in Fig. 7b) and by extension similar patterns in surface melt extents can be expected for all three glaciers.

The temporal pattern for ice cover on the fjord was also very similar, resulting in a continuous increase in ice mélange extent throughout the winter months, with ice mélange build up starting in November/December (2017/2018/2020) and reaching its maximum extent in April/May before quickly disappearing with the onset of surface melt. As for Eqip Sermia and Sermeq Kujalleq, there was no ice mélange build-up in fall; it only started in January 2020, likely due to the relatively warm temperatures in conjunction with the prolonged period of surface melt. Also, brash

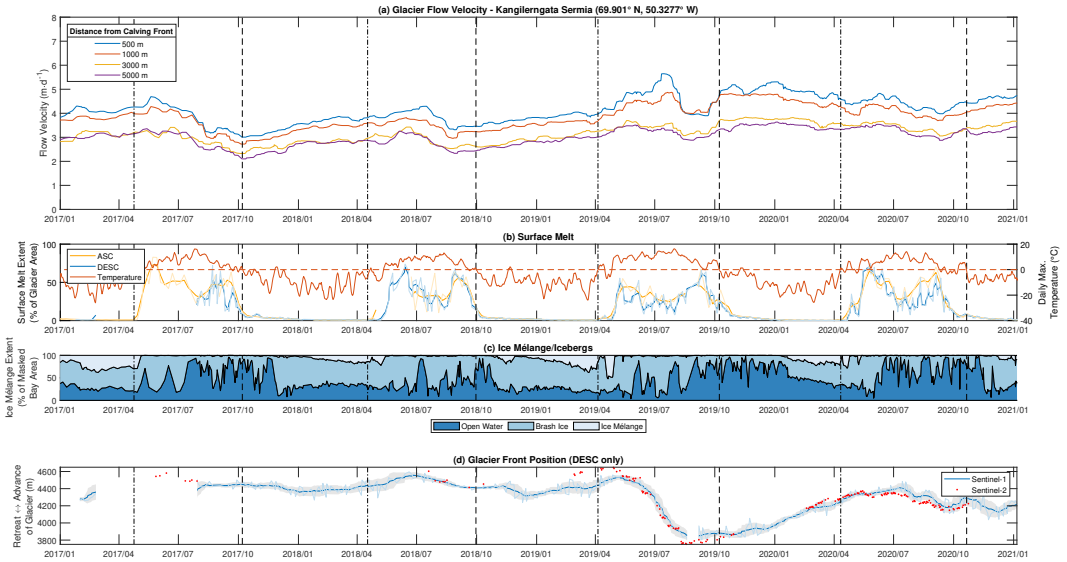

Fig. 7: Extracted parameters for time period between 2017/01/01 and 2020/12/31 for Kangilerngata Sermia. In (a) the flow speeds at different distances upstream from the terminus are shown (see legend). In (b) the SAR derived melt extents (in percent; blue and orange lines) are shown alongside air temperature (red line) recorded near the terminus (AWS2). (c) shows the evolution of ice composition on the fjord and in (d) the observed front positions from SAR (raw: light blue line; moving average: dark blue line; standard deviation: gray shading) and from S2 (manually mapped) are shown. The vertical dash-dotted lines delineate the beginning, the vertical dashed lines the end of seasonal periods with positive daily maximum temperatures.

ice presence followed the pattern observed at the other glaciers, namely fluctuations throughout the melting season and a peak in extent right before the onset of ice mélange formation. Again, this pattern was not as pronounced during the winter of 2019/2020.

As for the glacier flow velocity, the position of the glacier front showed a contrasting behaviour in comparison to Eqip Sermia and Sermeq Kujalleq, with the latter two showing cycles of slow and steady advance and relatively fast retreat. By contrast, Kangilerngata Sermia remained relatively stable within roughly 200 m between January 2017 and May 2019, with slow advances between early winter (Dec/Jan) and July. However, as with the other two glaciers, the onset of advance was observed to be linked to the start of the formation of ice mélange, but the onset of retreat was about 2 months after the ice mélange break-up and onset of surface melt.

In 2019, within one month of the disappearance of the ice mélange in June, the northern part of the glacier front started to retreat dramatically. The retreat extended to the southern part one month later and came to a halt around the middle of August. Averaged over the entire front, the retreat was 700 m over three months, well beyond the magnitude of seasonal front variations. Following the collapse of the glacier front in 2019, Kangilerngata Sermia slowly advanced over the course of the next 10 months, advancing to within 100 m of the glacier front positions of the years before the fast retreat. All three phases, the quasi stable behaviour, the collapse, and the subsequent slow advance of the glacier front, agree well with the manually delineated validation data from the optical S2 data with regard to timing and distance (mean and median absolute differences of 54 m and 47 m, respectively; R^2 of 0.922; see Table 5.3). Note, that the extraordinary retreat episode in 2019 coincided with an additional peak in flow speed at the terminus.

5.4 Discussion

As presented in the previous section, the advent of openly available data from synthetic aperture radar satellite constellations such as the Copernicus programme's S1 platforms offers an unprecedented opportunity for a continual monitoring of polar regions. The methodologies showcased here were specifically chosen to either require no or little *a priori* information, allowing the application of each approach independently across a variety of scenarios. The strengths and weaknesses of these methodologies are presented in the following section. Following that, uncertainties are presented, and the potential of the single-sensor-approach is discussed.

5.4.1 Glacier Flow Dynamics

The main influencing factors for the accuracy of the glacier's flow dynamics are the sampling step size, and the chosen size of the template (Rohner et al., 2019). Given *Eqip Sermia's* calving rate, strong velocity gradients must be expected in the region of interest (Benn et al., 2007; Vieli et al., 2000). To be able to accommodate these steep gradients, a small patch size was chosen, despite the concomitant increase in noisiness of the resulting velocity fields. Furthermore, the small patch size also helps to decrease the area affected by edge effects (i.e. image patches consisting of areas on and off the glacier). In addition to an increase in noisiness caused by small patch sizes, a short temporal baseline between acquisitions might introduce a low signal-to-noise ratio (SNR) in areas with low flow velocities (<2 m/d) (Rohner et al., 2019). However, given the predominance of fast moving, frontal parts of the glacier in the sites studied here, using the S1 standard temporal baseline of 6 days, we were able to generate sufficiently high SNRs.
The use of a short sample interval followed by a downsampling step was shown to be beneficial to capture velocity gradients even close to the glacier's terminus (Rohner et al., 2019), in spite of a higher computational cost. Both, namely the spatial smoothing close to the front, where strong velocity gradients occur, and the edge effects, are commonly shown to be present in the large-scale operational ice velocity products, therefore limiting the utility of such products to users investigating interactions of the glacier's terminus with the proglacial fjord (Rohner et al., 2019).

5.4.2 Surface Melt

Due to a lack of alternative remote sensing data at a comparable spatial resolution (passive microwave brightness temperatures at 25 km and scatterometer backscatter at ∼2–5 km; Howell et al., 2019), we made use of available air temperature information for a plausibility analysis. While the algorithm used to detect the presence of surface melt on the glacier is relatively simple, there is a good agreement with the available air temperature information.
Comparing the plausibility of the results (i.e. positive daily maximum temperatures ($T_{max}D$) and presence of surface melt at more than 5% of a glacier's area; SMA) by means of a confusion matrix showed good agreement, resulting in accuracies of 0.865, 0.866, and 0.860 for Eqip Sermia, Kangilerngata Sermia, and Sermeq Kujalleq respectively. When looking at the Positive and Negative Predictive Values (PPV and NPV, considering the presence of melt as true), the values reach PPV values between 0.811 and 0.846, and NPV values between 0.880 and 0.908.

Despite generally good agreement between the measurements from the SAR scenes and the temperature data, certain limitations applied. First, use of daily maximum temperature is subject to error, as it is generally only reached over the course of the day, and the SAR acquisitions took place at approx. 10:00 UTC or approx. 21:00 UTC. Thus, the meteorological conditions are not necessarily representative, especially during periods with large diurnal fluctuations (spring/autumn). Second, the range of altitudes of the glacier means that different melt regimes can prevail in different parts of the glacier. Thus, the threshold of 5% of the SMA can be exceeded due to locally prevailing temperatures above freezing in the lower-lying part of the glacier, while the upper part of the glacier was not yet experiencing any melting. Third, the necessary use of multiple weather stations due to the limitations laid out in section 5.2.2 required a harmonization of the temperature values. While applying a lapse rate resulted in high R^2 values when comparing the harmonized values between the stations, the lapse rate does not take into account changes in adiabatic effects. In addition, in cases of unavailability of data from weather stations AWS1 and AWS2, gaps were filled based on data from JAR1 or SC. Due to their locations at 962m a.s.l. and 1138 m a.s.l., the measured diurnal temperature variations were expected to be lower in comparison to the weather stations located closer to the glacier's terminus, possibly inflating the false positive/negative values.
An interesting correspondence between the glaciers considered was the regular local minimum in melt area around August described in section 5.3. Due to the agreement of the measurement results between the glaciers and over time, it can be assumed that these occur due to physical conditions and not due to measurement errors. A possible explanation is the slow melting of the glacier's snow cover over the summer. The following local maximum in August, on the other hand, could be due to the end of the polar day, which leads to an increase in the diurnal cycle of temperatures and thus also to renewed nightly snowfall onto the glaciers.

Tab. 5.5: Confusion matrix for each Glacier

		Glacier Surface Melt Area					
		Eqip Sermia		Kangil. Sermia		Sermeq Kujalleq	
		≥5%	<5%	≥5%	<5%	≥5%	<5%
$T_{max}D$	≥0° C	259	44	269	33	271	31
	<0° C	47	324	57	313	63	307

5.4.3 Ice Composition in Fjord

The use of optical images for validating SAR data based mapping of the ice composition in a fjord is limited. For one, the images of the two sensor types are not taken simultaneously, which makes comparisons error-prone given occasional strong changes in the fjord. These strong changes happen mainly due to changes in winds, as explained in section 5.3.1c. Also, between October and February the polar night prevents optical images from being taken, which means that in many cases the growth of the ice mélange cannot be compared against such images. However, comparing the clearing of the ice mélange in the fjords with images from S2, using the approach described in Howat et al. (2010), namely the motion of icebergs at the front and some visible open water as an indicator of ice mélange breakup, the findings between data from the automated derivation and the optical imagery agrees to within a few days (cf. Table 5.6).

Tab. 5.6: Annual day of ice-melange clearing (day of year) and respective differences, as observed in S1 and S2 imagery, for all glacier fjords in the study area.

	Eqip Sermia			Kangilerngata Sermia			Sermeq Kujalleq		
	S1	**S2**	**Diff.**	**S1**	**S2**	**Diff..**	**S1**	**S2**	**Diff.**
2017	125	133	-8 d	125	130	-5 d	125	130	-5 d
2018	134	143	-9 d	134	150	-16 d	134	135	-1 d
2019	121	123	-2 d	121	128	-7 d	122	128	-6 d
2020	134	127	7 d	134	129	5 d	130	135	-5 d
Mean	128.5	131.5	-3 d	128.5	134.25	-5.75 d	127.75	132	-4.25 d
|Mean|			6.5 d			8.25 d			4.25 d

Looking at the annual course of ice composition in the proglacial area off Eqip Sermia and Kangilerngata Sermia, it is noticeable that the values for *open water* are >0% for both glaciers, even in winter. The reason for this is, on the one hand, that both glaciers have crevassing occurring between the compact ice, between which open water is visible. This is due to the shapes of the proglacial fjords, which open up with increasing distance to the glacier tongue and thus allow the crevasses to form. This is not the case at Sermeq Kujalleq, since just north of it, another glacier, Sermeq Avannarleq, is calving, leading to a compressive environment. In addition, the proglacial fjord narrows in front of the two glaciers Sermeq Kujalleq and Sermeq Avannarleq, making crevasse formation difficult. In the case of Kangilerngata Sermia, the island of *Illuluarsuit Nunataat* also acts as a barrier to the outflow of icebergs toward the west, which tends to keep this water area ice-free throughout the year and influences the measured values.
Furthermore, as explained in Section 5.2.6, the approach relies on a texture analysis of the amplitude data. As the transition between brash ice and ice mélange is smooth, binning the SAR data into three bins will result in mis-classifications, since the chosen limits are somewhat arbitrary.
A possible extension of the approach could help minimizing the aforementioned mis-classifications by incorporating knowledge of the glacier flow dynamics in the fjord. In this case, the coherence level of the movements of the sea ice could be used as an indication for ice mélange. However, since we wanted to define the different methods as stand-alone in each case, we refrained from integration at this stage.

5.4.4 Glacier Front Position

We were able to demonstrate our efficient algorithm's ability to automatically detect glacier fronts without an onerous need for prior training. The extracted front positions, when compared against manually detected glacier fronts based on optical satellite images, were in agreement for all three glaciers, despite large differences in the geometric properties of the considered glaciers (steepness and height of the glacier fronts, orientation relative to the satellite orbit). For the calculation, as described in section 5.2.5, we used the box method according to Moon & Joughin (2008), which provides a relative indication of the mean front position regardless of the acquisition method (automated or manual). A disadvantage of this comparative quantity is the lack of a low error absolute reference, i.e. no automatically generated absolute position of the glacier front was available for comparison with other studies or methods.

The differences observed between the manually delineated glacier positions from optical S2 satellite imagery and those from S1 can be attributed to several factors. First, differences in the imaging geometries (30°–45° off-nadir for S1 and nadir for S2) cause differences in the delineation. In the case of S1 acquisitions for glacier fronts with a steepness of $\geq 45°$, only the glacier crest is visible, as the base of the glacier tongue is within the radar shadow. Although an attempt was made to account for this fact in the manual delineation of the glacier front by focusing on the glacier crest in the optical imagery, difficulties in the distinction between the glacier crest and the base of the glacier tongue in optical imagery as well as variations in solar irradiance might have caused inaccuracies.
Second, global warming is causing increased ablation of the glacier tongue, resulting in a lowering. This has been 6 ma^{-1} for Eqip Sermia in recent years (Rohner et al., 2019), thus the glacier front is likely to have subsided by about 40–50 m since the TanDEM-X DEM data was acquired (last image: Jan 2014). These errors in hypsometry lead to an error in the geocoding by incorrectly placing the pixel closer to the near-range edge of the scene (i.e. further East in our case of descending orbits) by about 30–50 m. In addition, a study by Hawker et al. (2019) showed an RMSE of between 2.92 m in flat areas and 6.42 m in areas with a slope $\geq 15°$ when comparing the available TanDEM-X-DEM at 90 m resolution against high resolution LiDAR DEM, possibly further influencing the positional accuracy of the S1 scenes' geocoding.
Third, reliance on differences in backscatter levels caused the susceptibility to strong gradients described in section 5.2.5 that could not be fully mitigated by the introduced outlier detection and culling process, therefore resulting in a tendency to overestimate the advance of the glacier position, especially during the melt season, when there was a plume present in the proglacial fjord.
Fourth, the manual optical sensor-based front position mapping represents a generalization of the front line, since the delineation of each frontal course happened only with a limited number of points (Eqip Sermia: 50.73 m mean distance between two points; Kangilerngata Sermia: 53.17 m; Sermeq Kujalleq: 52.20 m), while the frontal courses were defined by our algorithm using S1 data on a pixel-by-pixel basis.
In addition to the utility of year-round SAR data, the ease of implementation of our approach with no need for *a priori* information (aside from the positions of the lateral moraines, which are, however, freely available from many sources in high quality) is a major advantage. In addition, traceability is fully guaranteed at all times by not relying on machine learning algorithms, nor does it rely on the availability of trained models (as in, e.g., Cheng et al., 2021).
Despite the advantages, our approach also has limitations. In particular, for glaciers such as Eqip Sermia, which is characterized by the presence of a strong plume in summer, the detection of the glacier front at times when such a plume is present was difficult (see section 5.2.5). This negative effect could be mitigated by integrating other data sets, such as glacier velocity information. However, as explained in section 5.4.3, we refrained from linking the separate retrievals at this stage in order to preserve the independence of the individual approaches. Further, the spatial delineation of the possible front courses in the second iteration of the automated method is based on the assumption of a relatively stable glacier position. In the case of a surge or an exceptionally large calving event, this can lead to problems, even if the buffer allows for a change in glacier course of 500 m in 45 days.

5.4.5 Potential

As discussed in section 5.2.1, SAR satellites supply their own illumination source and are therefore able to carry out their measurements without relying on specific meteorological conditions or the availability of sunlight. These characteristics allow a consistent continual observation of a multitude of glacial and glacier-proximal parameters for polar glaciers throughout the year at high temporal resolution.
The four parameters presented in this paper not only were retrieved independently from a single, freely available platform (Sentinel-1), but also did not require any *a priori* data other than air temperature data and basic glacier outlines, both easily retrievable from open sources. The glacial and glacier-proximal parameters were retrieved for three glaciers with different characteristics. The glaciers differed especially regarding advance/retreat behaviour, flow patterns and velocities over a year. Due to the extended polar night, no comparable observations are possible using optical satellite data. Furthermore, we were able to show the feasibility of the chosen methodologies even in the presence of extreme events, such as the rapid retreat of Kangilerngata Sermia in 2019.
The year-round availability of data also enables production of datasets devoid of big data gaps, enabling direct analysis of interactions between different external forcings, such as the presence of melt, and each glacier's response as expressed by its flow velocity. Furthermore, the methodologies are easily implementable and of a generic nature, not relying on specialized hard- and software. The set of consistent time series retrievals of multiple glacier parameters widens the scope of possible systematic analyses along extended coastlines.

5.5 Conclusions

Using S1 SAR amplitude data sets with no or only little *a priori* data, we were able to continuously derive four glacial and glacier-proximal parameters for three ocean terminating outlet glaciers in Western Greenland with differing seasonal behaviors at high spatiotemporal resolution. The derived data enables analysis of the interaction of *flow velocity*, *surface melt*, *glacier front position*, and *presence of ice mélange in the proglacial fjord* on an intra- or inter-annual basis. Using these uninterrupted measurements, we found an apparent relationship between the advance of a glacier's terminus position with the presence or absence of a rigid ice mélange at the glacier-fjord interface. For all three glaciers investigated, and in accordance with other studies (Howat et al., 2010; Joughin et al., 2008; Moon et al., 2015), changes in the ice composition in the proglacial fjord resulted in advancing or retreating behavior of the glaciers' termini. Furthermore, the physically interconnected parameters surface melt and sea ice composition, both primarily controlled by air temperature, were also retrieved in the measurements at a high spatial and temporal resolutions.

As suggested in section 5.4.3, both, derivation of ice composition and glacier front position, could benefit from an incorporation of data from the glacier flow dynamics calculation. In both cases, the coherence level could be used as an indication, either for ice mélange presence or to discriminate between glacier and sea, especially during the presence of a plume in the proglacial fjord.

Bibliography

Amundson, J. M., Fahnestock, M. A., Truffer, M., Brown, J., Lüthi, M. P., & Motyka, R. J. (2010). Ice mélange dynamics and implications for terminus stability, Jakobshavn Isbræ, Greenland. *Journal of Geophysical Research*, *115*(F1), 33729, doi: 10.1029/2009JF001405.

Bauer, A. (1968). *Le glacier de l'Eqe (Eqip Sermia): Mouvement et variations du front (1959). Technical Report 2, Expédition glaciologique internationale au Groenland (EGIG)*. Copenhagen, Denmark: Meddelelser om Grønland.

Benn, D. I., Warren, C. R., & Mottram, R. H. (2007). Calving processes and the dynamics of calving glaciers. *Earth-Science Reviews*, *82*(3-4), 143–179, doi: 10.1016/j.earscirev.2007.02.002.

Bevan, S. L., Luckman, A. J., Benn, D. I., Cowton, T. R., & Todd, J. (2019). Impact of warming shelf waters on ice mélange and terminus retreat at a large SE Greenland glacier. *The Cryosphere*, *13*(9), 2303–2315, doi: 10.5194/tc-13-2303-2019.

Canny, J. (1986). A Computational Approach to Edge Detection. *IEEE Transactions on Pattern Analysis and Machine Intelligence*, *PAMI-8*(6), 679–698, doi: 10.1109/TPAMI.1986.4767851.

Carr, J. R., Stokes, C. R., & Vieli, A. (2017). Threefold increase in marine-terminating outlet glacier retreat rates across the Atlantic Arctic: 1992–2010. *Annals of Glaciology*, *58*(74), 72–91, doi: 10.1017/aog.2017.3.

Cassotto, R., Fahnestock, M. A., Amundson, J. M., Truffer, M., & Joughin, I. (2015). Seasonal and interannual variations in ice melange and its impact on terminus stability, Jakobshavn Isbræ, Greenland. *Journal of Glaciology*, *61*(225), 76–88, doi: 10.3189/2015JoG13J235.

Catania, G. A., Stearns, L. A., Sutherland, D. A., Fried, M. J., Bartholomaus, T. C., Morlighem, M., Shroyer, E., & Nash, J. (2018). Geometric Controls on Tidewater Glacier Retreat in Central Western Greenland. *Journal of Geophysical Research: Earth Surface*, *123*(8), 2024–2038, doi: 10.1029/2017JF004499.

Cheng, D., Hayes, W., Larour, E. Y., Mohajerani, Y., Wood, M., Velicogna, I., & Rignot, E. (2021). Calving Front Machine (CALFIN): glacial termini dataset and automated deep learning extraction method for Greenland, 1972–2019. *The Cryosphere*, *15*(3), 1663–1675, doi: 10.5194/tc-15-1663-2021.

Cowton, T. R., Sole, A. J., Nienow, P. W., Slater, D. A., & Christoffersen, P. (2018). Linear response of east Greenland's tidewater glaciers to ocean/atmosphere

warming. *Proceedings of the National Academy of Sciences of the United States of America*, *115*(31), 7907–7912, doi: 10.1073/pnas.1801769115.

Dabboor, M., Iris, S., & Singhroy, V. (2018). The RADARSAT Constellation Mission in Support of Environmental Applications. *Proceedings*, *2*(7), 323, doi: 10.3390/ecrs-2-05136.

Danish Agency for Datasupply and Efficiency (2022). Grønland 1:250.000 (1990-2000). Retrieved 2022-11-03, from https://dataforsyningen.dk/data/985.

de Quervain, A. & Mercanton, P.-L. (1925). *Résultats scientifiques de l'expédition Suisse au Groenland 1912-1913*. Copenhagen, Denmark: Reitzel.

Dijkstra, E. W. (1959). A note on two problems in connexion with graphs. *Numerische Mathematik*, *1*(1), 269–271, doi: 10.1007/BF01386390.

Dowdeswell, J. A. & Cromack, M. (1991). Behavior of a Glacier-Derived Suspended Sediment Plume in a Small Arctic Inlet. *The Journal of Geology*, *99*(1), 111–123, doi: 10.1086/629477.

Enderlin, E. M., Howat, I. M., Jeong, S., Noh, M. J., van Angelen, J. H., & van den Broeke, M. R. (2014). An improved mass budget for the Greenland ice sheet. *Geophysical Research Letters*, *41*(3), 866–872, doi: 10.1002/2013GL059010.

Fried, M. J., Catania, G. A., Stearns, L. A., Sutherland, D. A., Bartholomaus, T. C., Shroyer, E., & Nash, J. (2018). Reconciling Drivers of Seasonal Terminus Advance and Retreat at 13 Central West Greenland Tidewater Glaciers. *Journal of Geophysical Research: Earth Surface*, *123*(7), 1590–1607, doi: 10.1029/2018JF004628.

Gray, A. L., Short, N. H., Mattar, K. E., & Jezek, K. C. (2001). Velocities and Flux of the Filchner Ice Shelf and its Tributaries Determined from Speckle Tracking Interferometry. *Canadian Journal of Remote Sensing*, *27*(3), 193–206, doi: 10.1080/07038992.2001.10854936.

Haralick, R. M., Shanmugam, K., & Dinstein, I. (1973). Textural Features for Image Classification. *IEEE Transactions on Systems, Man and Cybernetics*, *SMC-3*(6), 610–621.

Hawker, L., Neal, J., & Bates, P. (2019). Accuracy assessment of the TanDEM-X 90 Digital Elevation Model for selected floodplain sites. *Remote Sensing of Environment*, *232*, 111319, doi: 10.1016/j.rse.2019.111319.

Howat, I. M., Box, J. E., Ahn, Y., Herrington, A., & McFadden, E. M. (2010). Seasonal variability in the dynamics of marine-terminating outlet glaciers in Greenland. *Journal of Glaciology*, *56*(198), 601–613, doi: 10.3189/002214310793146232.

Howell, S. E. L., Small, D., Rohner, C., Mahmud, M. S., Yackel, J. J., & Brady, M. (2019). Estimating melt onset over Arctic sea ice from time series multi-sensor Sentinel-1 and RADARSAT-2 backscatter. *Remote Sensing of Environment*, *229*, 48–59, doi: 10.1016/j.rse.2019.04.031.

IPCC (2013). *Climate Change 2013: The Physical Science Basis. Contribution of Working Group I to the Fifth Assessment Report of the Intergovernmental Panel on Climate Change*. Cambridge, United Kingdom and New York, NY, USA: Cambridge University Press.

Joughin, I. (2002). Ice-sheet velocity mapping: a combined interferometric and speckle-tracking approach. *Annals of Glaciology*, *34*(1), 195–201, doi: 10.3189/172756402781817978.

Joughin, I. (2021). MEaSUREs Greenland 6 and 12 day Ice Sheet Velocity Mosaics from SAR, Version 1.

Joughin, I., Howat, I. M., Fahnestock, M. A., Smith, B., Krabill, W., Alley, R. B., Stern, H., & Truffer, M. (2008). Continued evolution of Jakobshavn Isbrae following its rapid speedup. *Journal of Geophysical Research*, *113*(F4), 6487, doi: 10.1029/2008JF001023.

Joughin, I., Smith, B., Howat, I. M., Moon, T., & Scambos, T. A. (2016). A SAR record of early 21st century change in Greenland. *Journal of Glaciology*, *FirstView*, 1–10, doi: 10.1017/jog.2016.10.

Kadded, F. & Moreau, L. (2013). Sur les traces du Paul-Emile Victor, relevés topographiques 3D au Groenland. *Revue XYZ*, *137*(4), 47–56.

Kim, Y., Kimball, J. S., Glassy, J., & Du, J. (2017). An extended global Earth system data record on daily landscape freeze–thaw status determined from satellite passive microwave remote sensing. *Earth System Science Data*, *9*(1), 133–147, doi: 10.5194/essd-9-133-2017.

King, M. D., Howat, I. M., Jeong, S., Noh, M. J., Wouters, B., Noël, B. P. Y., & van den Broeke, M. R. (2018). Seasonal to decadal variability in ice discharge from the Greenland Ice Sheet. *The Cryosphere*, *12*(12), 3813–3825, doi: 10.5194/tc-12-3813-2018.

Kneib-Walter, A., Lüthi, M. P., & Vieli, A. (2019). Calving event size measurements and statistics of Eqip Sermia, Greenland, from terrestrial radar interferometry. *The Cryosphere Discussions*, (pp. 1–23)., doi: 10.5194/tc-2019-102.

Krieger, L. & Floricioiu, D. (2017). Automatic glacier calving front delineation on TerraSAR-X and Sentinel-1 SAR imagery. In IEEE (Ed.), *2017 IEEE International Geoscience and Remote Sensing Symposium (IGARSS)* (pp. 2817–2820).: IEEE.

Lea, J. M., Mair, D. W. F., Nick, F. M., Rea, B. R., van As, D., Morlighem, M., Nienow, P. W., & Weidick, A. (2014). Fluctuations of a Greenlandic tidewater glacier driven by changes in atmospheric forcing: observations and modelling of Kangiata Nunaata Sermia, 1859–present. *The Cryosphere*, *8*(6), 2031–2045, doi: 10.5194/tc-8-2031-2014.

Leopold, L. B., Wolman, M. G., & Miller, J. P. (1964). *Fluvial Processes in Geomorphology*. San Francisco, USA: W.H. Freeman and Co. http://gbv.eblib.com/patron/FullRecord.aspx?p=1894340.

Linlor, W. I. (1980). Permittivity and attenuation of wet snow between 4 and 12 GHz. *Journal of Applied Physics*, *51*(5), 2811, doi: 10.1063/1.327947.

Meier, E., Frei, U., & Nüesch, D. (1993). Precise terrain corrected geocoded images. In G. Schreier (Ed.), *SAR geocoding: data and systems* (pp. 173–185). Karlsruhe: Wichmann.

Moon, T. & Joughin, I. (2008). Changes in ice front position on Greenland's outlet glaciers from 1992 to 2007. *Journal of Geophysical Research*, *113*(F2), F02022, doi: 10.1029/2007JF000927.

Moon, T., Joughin, I., & Smith, B. (2015). Seasonal to multiyear variability of glacier surface velocity, terminus position, and sea ice/ice mélange in northwest Greenland. *Journal of Geophysical Research: Earth Surface*, *120*(5), 818–833, doi: 10.1002/2015JF003494.

Mote, T. L. (2014). MEaSUREs Greenland Surface Melt Daily 25km EASE-Grid 2.0, Version 1. Retrieved 02.06.2017, from http://dx.doi.org/10.5067/MEASURES/CRYOSPHERE/nsidc-0533.001.

Nagler, T., Rott, H., Hetzenecker, M., Wuite, J., & Potin, P. (2015). The Sentinel-1 Mission: New Opportunities for Ice Sheet Observations. *Remote Sensing*, *7*(7), 9371–9389, doi: 10.3390/rs70709371.

Nagler, T., Rott, H., Ripper, E., Bippus, G., & Hetzenecker, M. (2016). Advancements for Snowmelt Monitoring by Means of Sentinel-1 SAR. *Remote Sensing*, *8*(4), 348, doi: 10.3390/rs8040348.

Nick, F. M., Vieli, A., Andersen, M. L., Joughin, I., Payne, A. J., Edwards, T. L., Pattyn, F., & van de Wal, R. S. W. (2013). Future sea-level rise from Greenland's main outlet glaciers in a warming climate. *Nature*, *497*(7448), 235–238, doi: 10.1038/nature12068.

Piesbergen, J., Holecz, F., & Haefner, H. (1995). Snow cover monitoring using multitemporal ERS-1 SAR data. In *1995 International Geoscience and Remote Sensing Symposium, IGARSS '95. Quantitative Remote Sensing for Science and Applications* (pp. 1750–1752).: IEEE.

Reeh, N., Thomsen, H. H., Higgins, A. K., & Weidick, A. (2001). Sea ice and the stability of north and northeast Greenland floating glaciers. *Annals of Glaciology*, *33*, 474–480, doi: 10.3189/172756401781818554.

Rignot, E. & Kanagaratnam, P. (2006). Changes in the velocity structure of the Greenland Ice Sheet. *Science (New York, N.Y.)*, *311*(5763), 986–990, doi: 10.1126/science.1121381.

Rizzoli, P., Martone, M., Gonzalez, C., Wecklich, C., Borla Tridon, D., Bräutigam, B., Bachmann, M., Schulze, D., Fritz, T., Huber, M., Wessel, B., Krieger, G., Zink, M., & Moreira, A. (2017). Generation and performance assessment of the global TanDEM-X digital elevation model. *ISPRS Journal of Photogrammetry and Remote Sensing*, *132*, 119–139, doi: 10.1016/j.isprsjprs.2017.08.008 http://www.sciencedirect.com/science/article/pii/S092427161730093X.

Rohner, C., Small, D., Beutel, J., Henke, D., Lüthi, M. P., & Vieli, A. (2019). Multi-sensor validation of tidewater glacier flow fields derived from synthetic aperture radar (SAR) intensity tracking. *The Cryosphere*, *13*(11), 2953–2975, doi: 10.5194/tc-13-2953-2019.

Schubert, A., Miranda, N., Geudtner, D., & Small, D. (2017). Sentinel-1A/B Combined Product Geolocation Accuracy. *Remote Sensing*, *9*(12), 607, doi: 10.3390/rs9060607.

Shepherd, A. P., Ivins, E. R., A, G., Barletta, V. R., Bentley, M. J., Bettadpur, S., Briggs, K. H., Bromwich, D. H., Forsberg, R., Galin, N., Horwath, M., Jacobs, S., Joughin, I., King, M. A., Lenaerts, J. T. M., Li, J., Ligtenberg, S. R. M., Luckman, A. J., Luthcke, S. B., McMillan, M., Meister, R., Milne, G., Mouginot, J., Muir, A.,

Nicolas, J. P., Paden, J., Payne, A. J., Pritchard, H., Rignot, E., Rott, H., Sørensen, L. S., Scambos, T. A., Scheuchl, B., Schrama, E. J. O., Smith, B., Sundal, A. V., van Angelen, J. H., van de Berg, W. J., van den Broeke, M. R., Vaughan, D. G., Velicogna, I., Wahr, J., Whitehouse, P. L., Wingham, D. J., Yi, D., Young, D., & Zwally, H. J. (2012). A reconciled estimate of ice-sheet mass balance. *Science (New York, N.Y.)*, *338*(6111), 1183–1189, doi: 10.1126/science.1228102.

Singh, V. P., Singh, P., & Haritashya, U. K. (2011). *Encyclopedia of snow, ice and glaciers*. The encyclopedia of earth sciences series. Dordrecht, Netherlands: Springer.

Steffen, K. (2020). Greenland Climate Network (GC-Net) Data: EnviDat. Retrieved 06.03.2021, from https://www.envidat.ch/gcnet/.

Steffen, K., Box, J. E., & Abdalati, W. (1996). Greenland Climate Network: GC-Net. In S. C. Colbeck (Ed.), *Glaciers, Ice Sheets and Volcanoes: A Tribute to Mark F. Meier* (pp. 98–103). Hanover, NH (USA): Cold Regions Research and Engineering Laboratory (CRREL) Special Report 96-27.

Straneo, F., Heimbach, P., Sergienko, O., Hamilton, G., Catania, G. A., Griffies, S., Hallberg, R., Jenkins, A., Joughin, I., Motyka, R. J., Pfeffer, W. T., Price, S. F., Rignot, E., Scambos, T. A., Truffer, M., & Vieli, A. (2013). Challenges to Understanding the Dynamic Response of Greenland's Marine Terminating Glaciers to Oceanic and Atmospheric Forcing. *Bulletin of the American Meteorological Society*, *94*(8), 1131–1144, doi: 10.1175/BAMS-D-12-00100.1.

Strozzi, T., Luckman, A. J., Murray, T., Wegmuller, U., & Werner, C. L. (2002). Glacier motion estimation using SAR offset-tracking procedures. *IEEE Transactions on Geoscience and Remote Sensing*, *40*(11), 2384–2391, doi: 10.1109/TGRS.2002.805079 http://ieeexplore.ieee.org/lpdocs/epic03/wrapper.htm?arnumber=1166597.

Torres, R., Snoeij, P., Geudtner, D., Bibby, D., Davidson, M., Attema, E., Potin, P., Rommen, B., Floury, N., Brown, M., Traver, I. N., Deghaye, P., Duesmann, B., Rosich, B., Miranda, N., Bruno, C., L'Abbate, M., Croci, R., Pietropaolo, A., Huchler, M., & Rostan, F. (2012). GMES Sentinel-1 mission. *Remote Sensing of Environment*, *120*, 9–24, doi: 10.1016/j.rse.2011.05.028.

Vieli, A., Funk, M., & Blatter, H. (2000). Tidewater glaciers: frontal flow acceleration and basal sliding. *Annals of Glaciology*, *31*, 217–221, doi: 10.3189/172756400781820417.

Chapter

6

Synthesis

The publications presented in the previous chapters addressed the research questions formulated in section 1.2. The main findings concerning each of these research questions are discussed in the following sections.

6.1 How can we improve the resolution of steep velocity gradients in the area of a glacier's terminus using SAR intensity tracking, and how can these derived products be used to give better estimates of ice fluxes and the mass budget?

To improve the resolution of steep velocity gradients close to a glacier's terminus, we used SAR amplitude data in conjunction with an adapted speckle tracking methodology presented in Publication 1. As speckle tracking relies on normalized cross-correlation operations, regions close to the glacier's frontal and lateral margins are affected by the template window's overlap with adjacent stable ground. By using an iterative approach starting with smaller template window sizes combined with a short spatial sample interval, we were able to reduce this effect, thereby improving the derivation of offsets (and thus GFD) up to a limit close to the glacier's frontal and lateral margins. We applied this improved methodology with S1 and RS2 data, with the validation showing good agreement in magnitude and spatial patterns with multiple independent ground measurements.

As shown in Publication 1, large-scale operational ice flow velocity products such as the Greenland Ice Sheet CCI Ice Velocity (Nagler et al., 2015) or MEaSUREs (Joughin, 2021) not only lack the temporal resolution (except for selected glaciers) but also underestimate the velocities up to 3 km behind the glacier's terminus by about 10% to 20% (Rohner et al., 2019). As a result of this underestimation in GFD, estimating ice discharge using, e.g., a flux gate approach with operational

products would result in an underestimation of ice flux between 7% and 28% for MEaSUREs and Greenland Ice Sheet CCI, respectively. This underestimation is due to the flux gate approach's use of the surface velocity estimations to approximate horizontal, depth-averaged ice velocity (Osmanoğlu et al., 2013). It is apparent that using an adjusted speckle tracking methodology to derive GFD for small- and medium-sized outlet glaciers instead of large-scale operational products will substantially affect mass loss estimates for the whole GrIS. It is important to note that increased near-terminus ice velocities also lead to higher frontal strain rates, affecting observational constraints for calving models (Choi et al., 2018; King et al., 2018; Morlighem et al., 2017; Nick et al., 2013, 2009; Rohner et al., 2019).

6.2 How can SAR data sets from different sensors and orbital tracks be integrated into a single backscatter composite, and how can a time-series of these composites be used to estimate the timing of melt onset over Arctic (sea) ice?

Due to the inherent limitations of spaceborne microwave sensors, investigators of melt onset in ice and snow have had to choose between either a high *temporal* resolution of e.g. one to two days using PMW or active scatterometer data, or a high *spatial* resolution using SAR sensors. The present-day lack of ARD from SAR has made it difficult to integrate backscatter measurements from different observation geometries, so the temporal resolution has been directly tied to a sensor's repeat-pass interval, resulting in a (relatively) low temporal resolution (Small et al., 2022). With a decadal trend of melt onset for the Arctic of -5.69 days/decade (Bliss & Anderson, 2014), repeat-pass intervals of currently operational SAR constellations would not be able to capture such changes (e.g., S1 6 days (12 days since 23 December 2021), RS2 24 days, RCM 4 days; Dabboor et al., 2018; Short & Gray, 2004; Torres et al., 2012). By using the methodology presented in Publication 2 to produce wide-area, analysis-ready radar backscatter composites, SAR data can provide simultaneously both broad *spatial* coverage and even single-day *temporal* resolution (presently in high latitude regions; Small et al., 2022).

The methodology relies on using the set of local illuminated areas applied previously during each RTC normalisation as weighting factors matched with a set of RTC backscatter estimates (Small, 2012). This weighting operation results in normalized, interoperable backscatter data sets, allowing the combination of different orbital tracks, acquisition modes, resolutions, and sensors operating at the same wavelength into a single 2-D backscatter map (Small et al., 2022). The resulting backscatter map increases the areal coverage and the temporal resolution by including multiple backscatter data sets. In addition, it simultaneously improves the mean spatial resolution and the noise characteristics of the composite backscatter map compared to the individual input data sets (Small et al., 2022).

The applicability of such LRW composites to estimate melt onset over sea ice is presented in Publication 3. Using 1 day, 1–2 day, and 2–4 day composites by combining data sets from S1 constellation and RS2, melt onset estimates from changes in backscatter were calculated for ∼500,000 pixels identified as FYI and ∼250,000 pixels identified as MYI (Howell et al., 2019). The resulting melt onset

detection was in good agreement with data derived from ASCAT and PMW over homogeneous sea ice areas. Simultaneously, melt onset detection was significantly improved in regions with more heterogeneous sea ice and narrow channels (Howell et al., 2019). In addition to their use for melt onset detection over sea ice, LRW composites using data from Envisat ASAR and the S1 constellation have been used successfully in studies mapping the extent of wet snow in mountainous regions and cryospheric applications (Dasser, 2021; Jäger, 2016; Rohner, 2014).

6.3 How can we continuously, automatically, and efficiently derive multiple glacial and glacier-proximal variables from S1 SAR time series, and how do these parameters interact?

As a result of the increasing availability of freely and openly available, but also commercial SAR platforms, the reliable data flow unaffected by weather or the lack of sunlight enables a quasi-continuous derivation of glacial and glacier-proximal parameters at high spatial and temporal resolutions. This unprecedented wealth of data enables integrative, long-term studies investigating the interaction between multiple parameters and over varying time scales that until now have been lacking (Moon et al., 2015). At the same time, the large amount of data also creates the need for algorithms that can derive information and parameters from the data in an automated, reliable manner that is as independent of *a priori* knowledge as possible.

In addition to the methodology described in Publication 1 for extracting GFD from SAR amplitude data, we present an approach based on similar principles as Publication 3 for extracting the glacier area affected by surface melt (SMA). The approach takes advantage of the differences in dielectric properties between frozen and liquid water (Linlor, 1980). Because of the flat topography and a large number of overlapping orbits, a calculation of LRWs did not yield any advantage. However, if the approach were applied at a regional or ice sheet level, using such ARD compositions would be beneficial. The *a priori* data used for the calculation included a glacier mask and weather data, which can be provided with sufficient accuracy from publicly available data sources (e.g. Danish Agency for Datasupply and Efficiency, 2022). Due to the lack of suitable reference data, the method's usability was compared using a plausibility analysis with temperature data. It showed an accuracy of 0.811–0.846 for the glaciers considered (Rohner et al., 2022).

From the same S1 data and using the methodology shown in Publication 4, it is also possible to infer the presence and evolution of ice mélange and brash ice, in contrast to the previous parameter with only the necessity of a mask of the water area within the fjord. Such a water mask can be either extracted from the publicly available geodata already required for the calculation of SMA (e.g. Danish Agency for Datasupply and Efficiency, 2022) or defined manually. The ice composition in the fjord was derived from a texture analysis using a gray-level co-occurrence matrix. As was the case for the last parameter, a comparison with reference data was difficult. Firstly, the ice is subject to substantial, wind-influenced diurnal variation. Secondly, the polar night limits the availability of optical data in the period of maximum ice cover extent (October–February) (Howat et al., 2010). However, cross-

comparisons with studies investigating the clearing of the ice mélange (Howat et al., 2010) showed good agreement with the data derived using our methodology.

The final parameter derived from S1 data is the position of the glacier front. Like the last two parameters, this parameter is based on analyzing amplitude data from single images. However, it is limited to data from a descending orbit due to geometric constraints. The approach adapts the work of Krieger & Floricioiu (2017) and uses image gradients derived from a Canny edge detection algorithm to apply weights to a directed graph. Based on this graph, a cost minimization is then performed using Dijkstra's algorithm (Dijkstra, 1959), which corresponds to the glacier's terminus. A second iteration using the temporally averaged position of the calculated front line to constrain the solution set is run after that before excluding outliers and applying a subsequent culling step on the retrieved glacier positions. The derived terminus positions of the three investigated glaciers were compared with 519 manually delineated glacier fronts using S2 imagery. A mean absolute difference between the positions of 53–75 m was found with R^2 values of 0.629–0.966.

Between these four parameters and in accordance with other studies (Howat et al., 2010; Joughin et al., 2008; Moon et al., 2015), the glacier termini's position changed due to ice composition changes in the proglacial fjords. In agreement with the assumption of a buttressing effect of the ice mélange to the glacier and a stabilizing effect on the glacier front (Amundson et al., 2010; Cassotto et al., 2015; Fried et al., 2018; Reeh et al., 2001), our study also shows an interplay between the presence of ice mélange in the proglacial fjord and the advance of the glacier tongue. Likewise, we measured a retreating tendency in the position of the glacier front almost simultaneously with the disappearance of the ice mélange. Alongside the presence of ice mélange in the proglacial fjord, SMA is also closely related to atmospheric temperatures. The measurements of these two parameters show a clear interconnectedness: the change from temperatures below to temperatures above the freezing point corresponds with the change from a proglacial fjord covered with ice mélange to brash ice or ice-free conditions and the beginning of the melting period of the glacier surface. With the beginning of the period with a detectable SMA, the glacier's speeds also show changes, reaching their peak flow velocities within three months after the beginning of the melting period. Despite ongoing and detectable surface melt, all three glaciers exhibit a slow-down following this flow velocity peak. This slow-down could be explained by the temporal development of an efficient drainage system, a consequential lowering of the basal water pressure, and an increase of basal friction, thereby reducing basal flow speeds (cf. section 1.4.2b; Iken, 1981; van der Veen, 2013).

6.4 Observational Constraints

Despite their proven usability in deriving the glacial and glacier-proximal parameters, the methodologies presented in this dissertation do have their constraints. In the following section, some important limitations are presented.

6.4.1 GFD from SAR

As laid out in Publication 1, there are limits to the accuracy of operational offset tracking using S1 data. Firstly, edge effects caused by overlaps of the templates

with non-moving, unglaciated areas or the proglacial fjord can result in a lack of data or a deterioration in data quality. However, these effects only cover a narrow zone at the glacier's fringes that can be mitigated using the iterative approach presented in Publication 1. Secondly, substantial changes in backscatter due to surface melt can cause a decorrelation, possibly resulting in data voids. Thirdly, detecting small flow velocities can be impaired by a low SNR, causing unreliable and noisy velocity estimates (Rohner et al., 2019). These issues can be solved by doubling the time interval between two images used for the calculations, although one must then accept a poorer temporal resolution.

6.4.2 SMA from SAR

Due to the lack of validation data to use as a reference for the derived values of SMA, the comparison is based on a plausibility analysis using positive daily maximum temperatures ($T_{max}D$). Such a comparison is valid, as SMA is influenced predominantly by the atmospheric conditions. However, as daily maximum temperatures are only reached during the day, they do not necessarily reflect the conditions during the time of acquisition of the SAR image. This is especially relevant for periods with large diurnal fluctuations (Rohner et al., 2022). Furthermore, with glaciers spanning a range of altitudes, a single temperature value can only partially account for the actual atmospheric conditions. Therefore, lower-lying parts of the glacier could experience melting while the upper part is still frozen. Due to the lack of more variated validation data, this could only be circumvented by installing additional weather stations at different altitudes for each glacier.

6.4.3 Presence and development of ice mélange from SAR

The methodologies used to derive the presence and development of ice mélange and brash ice in the proglacial fjords as presented in Publication 4 are based on a texture analysis from amplitude data. Because of the smooth transition between ice mélange and brash ice, classification by texture analysis may be subject to uncertainties and, to a lesser extent, misclassification. Utilizing the coherence data calculated for the GFD approach could provide a more accurate delineation between solid, coherently moving ice mélange and brash ice. However, because we wanted to define the methods as stand-alone, for this study, we chose not to integrate this information.

6.4.4 Terminus position detection from SAR

As described in Publication 4, the methodology relies on gradients in the image caused by differences in backscatter intensity. As a result, we limited our application to imagery from a descending orbit (i.e., looking from East to West), resulting in a strong contrast between the glacier front and the radar shadow cast by it (Rohner et al., 2022). Strong gradients caused by, e.g., a plume in front of the glacier can result in a tendency to overestimate the glacier's advance during these periods. Furthermore, in areas with a glacier front running parallel to the line-of-sight of the SAR satellite, a radar shadow might not be present, thus possibly limiting the reliability of the derived glacier terminus positions.

Chapter

7

Conclusion and Outlook

This chapter summarizes the findings of this thesis and highlights future opportunities for further research that could not be covered during the thesis.

7.1 Conclusions

This dissertation presents a set of methodologies to derive spatially and temporally continuous data for glacial and glacier-proximal parameters from freely and openly accessible S1 SAR data. Using SAR data sets, it is possible to overcome limitations inherent to other data sources such as *in situ* measurements, optical satellite imagery, scatterometers, and passive microwave data. The proposed methodologies were adjusted to allow general applicability over sea ice and tidewater glaciers and minimize the need for *a priori* data while remaining easily implementable, providing traceable results.

Firstly, we were able to prove the validity of an adjusted methodology to derive glacier flow speeds even in the fast-flowing parts close to the glacier's terminus in Publication 1. Therefore, the results of an iterative offset-tracking approach using S1 and RS2 amplitude data sets were compared with flow velocity data from *in situ* measurements stemming from UAV, TRI, and dGPS surveys of *Eqip Sermia*, a medium-sized ocean-terminating outlet glacier located in Western Greenland. In addition, a comparison of the validated flow velocities with operational GFD products from the MEaSUREs (Joughin, 2021) or Greenland Ice Sheet CCI Ice Velocity projects (Nagler et al., 2015) showed substantial underestimation of the ice flow velocity of these ice-sheet wide products by 10%–20% up to 3 km from the glacier's terminus (Rohner et al., 2019). Using the common flux gate approach to estimate ice discharge will result in an underestimation of ice flux by 7%–28% (Rohner et al., 2019). For future projections of changes to runoff and, thus, future trends in global sea level rise, an accurate measurement of ice velocity in the

fast-flowing parts of outlet glaciers is paramount, a requirement that large-scale operational ice velocity products can only partially fulfill.

Another parameter of relevance is melt onset, as this reflects the climatic changes the Arctic is experiencing. Current long-term estimates for melt onset as of 1979 exist from PMW measurements and from scatterometer data starting in the year 2000, offering a daily or bi-daily temporal resolution (Howell et al., 2019). With a spatial resolution of multiple kilometers, their usability for detecting melt onset in narrow channels and regions with a heterogeneous sea ice distribution is limited (Howell et al., 2019). Using the LRW approach presented in Publication 2, the calculation of novel composite images from different sensors, acquisition modes, orbit geometries, and resolutions becomes possible. From our results it was possible to prove the usability of these composites for thematic investigations like the detection of melt onset in such heterogeneous regions at an unprecedented level of detail and in agreement with reference data based on measurements from PMW and scatterometers (cf. Publication 3).

In a manner similar to the measurement of melt onset over sea ice, continuous SMA at high spatial and temporal resolution can be derived from SAR amplitude data by comparing an image's backscatter intensity with a dry reference. Furthermore, we conclude that the measurement of the development and presence of different types of sea ice and the glacier's frontal position is possible using the same S1 SAR amplitude data. The wealth of data can be used to analyze the intricate interaction of parameters on an intra- and interannual time scale. These findings show the buttressing effect of ice mélange in the proglacial fjord, leading to an advance of the glacier's terminus during winter time and a rapid retreat after the disappearance of the stabilizing ice mass. Similarly, the impact of surface melt on the GFD could also be retrieved continuously year-round at a high spatial and temporal resolution. The possibility to retrieve multiple parameters from a single, freely, and openly available SAR data set enables the production of continuous time-series suitable for integrative, long-term studies that until now have been lacking (Moon et al., 2015).

In conclusion, this thesis presents approaches to automatically extract four glacial and glacier-proximal parameters relevant to constrain current calving models better and thus contributes to the improvement of predictions about the future trends in global sea level rise (Amundson et al., 2010; Howat et al., 2010; Moon et al., 2015). Furthermore, despite the developments of the last years in the availability of operational products (e.g. GEUS Dataverse or ITS_LIVE; Andersen et al., 2019; Gardner et al., 2023), the limitations described in sections 1.1 and 1.4.3c regarding the spatial coverage as well as the spatial and/or temporal resolution still remain. Accordingly, for small-scale investigations of the interactions between multiple or the intra- and interannual behavior of individual parameters, own measurements are still necessary. In such cases, the general nature of the methodologies presented in this thesis, as well as the uniform, temporally continuous database, allows measurements to be made at a high spatial and temporal resolution and independently of existing operational products.

7.2 Outlook

The findings portrayed in this thesis enable answering the research questions formulated initially. Nevertheless, new questions and research gaps became apparent

throughout the work. Some new questions and potential future research directions are introduced in the following sections.

- **Integration of other SAR sensors**
  To further improve the spatial and temporal resolution of the parameter time-series, including other SAR satellite platforms would be of interest. Given the recent and planned launches of several public and commercial SAR constellations (e.g., RCM, Capella, ICEYE), an even denser time-series would be possible (at least locally). Further, the stronger attenuation of shorter wavelengths caused by liquid water could prove beneficial to measure SMA.
- **Validation on additional tidewater glaciers**
  While the methodologies presented in this thesis are generic and have been successfully applied to glaciers with differing seasonal patterns, additional validation of the methodologies on other tidewater glaciers would be needed before an operational application.
- **Prolongation of time-series**
  In addition to including current and future satellites to densify the time-series, an extension into the past using data from, e.g., ERS-1/-2 or Envisat ASAR, would be an asset, enabling us to investigate further changes that have occurred over the last 30 years.
- **Extension of ice mélange presence detection algorithm with coherence information from GFD calculation**
  In order to improve the discrimination between brash ice and ice mélange, coherence information from the GFD calculation could be utilized at the expense of independence between the methodologies.

Bibliography

Amundson, J. M., Fahnestock, M. A., Truffer, M., Brown, J., Lüthi, M. P., & Motyka, R. J. (2010). Ice mélange dynamics and implications for terminus stability, Jakobshavn Isbræ, Greenland. *Journal of Geophysical Research*, *115*(F1).

Andersen, J. K., Fausto, R. S., Hansen, K., Box, J. E., Andersen, S. B., Ahlstrøm, A. P., van As, D., Citterio, M., Colgan, W., Karlsson, N. B., Kjeldsen, K. K., Korsgaard, N. J., Larsen, S. H., Mankoff, K. D., Pedersen, A. Ø., Shields, C. L., Solgaard, A., & Vandecrux, B. (2019). Update of annual calving front lines for 47 marine terminating outlet glaciers in Greenland (1999–2018). *Geological Survey of Denmark and Greenland Bulletin*, *43*.

Aschwanden, A., Fahnestock, M. A., Truffer, M., Brinkerhoff, D. J., Hock, R., Khroulev, C., Mottram, R. H., & Khan, S. A. (2019). Contribution of the Greenland Ice Sheet to sea level over the next millennium. *Science advances*, *5*(6).

Belchansky, G. I., Douglas, D. C., Mordvintsev, I. N., & Platonova, N. G. (2004). Estimating the time of melt onset and freeze onset over Arctic sea-ice area using active and passive microwave data. *Remote Sensing of Environment*, *92*(1), 21–39.

Benn, D. I. & Åström, J. A. (2018). Calving glaciers and ice shelves. *Advances in Physics: X*, *3*(1), 1048–1076.

Benn, D. I., Åström, J. A., Zwinger, T., Todd, J., Nick, F. M., Cook, S., Hulton, N. R. J., & Luckman, A. (2017). Melt-under-cutting and buoyancy-driven calving from tidewater glaciers: new insights from discrete element and continuum model simulations. *Journal of Glaciology*, *63*(240), 691–702.

Benn, D. I., Warren, C. R., & Mottram, R. H. (2007). Calving processes and the dynamics of calving glaciers. *Earth-Science Reviews*, *82*, 143–179.

Bernier, M. (1991). *Évaluation des données d'un radar à antenne synthétique (RAS), en bandes C et X, pour la surveillance du couvert de neige.* PhD thesis, Université du Québec, Québec, Canada.

Bliss, A. C. & Anderson, M. R. (2014). Snowmelt onset over Arctic sea ice from passive microwave satellite data: 1979–2012. *The Cryosphere*, *8*(6), 2089–2100.

Bollen, K. E., Enderlin, E. M., & Muhlheim, R. (2022). Dynamic mass loss from Greenland's marine-terminating peripheral glaciers (1985–2018). *Journal of Glaciology*, (pp. 1–11).

Carr, J. R., Stokes, C. R., & Vieli, A. (2017). Threefold increase in marine-terminating outlet glacier retreat rates across the Atlantic Arctic: 1992–2010. *Annals of Glaciology*, *58*(74), 72–91.

Cassotto, R., Fahnestock, M. A., Amundson, J. M., Truffer, M., & Joughin, I. (2015). Seasonal and interannual variations in ice melange and its impact on terminus stability, Jakobshavn Isbræ, Greenland. *Journal of Glaciology*, *61*(225), 76–88.

Catania, G. A., Stearns, L. A., Moon, T. A., Enderlin, E. M., & Jackson, R. H. (2020). Future Evolution of Greenland's Marine–Terminating Outlet Glaciers. *Journal of Geophysical Research*, *125*(2).

Catania, G. A., Stearns, L. A., Sutherland, D. A., Fried, M. J., Bartholomaus, T. C., Morlighem, M., Shroyer, E., & Nash, J. (2018). Geometric Controls on Tidewater Glacier Retreat in Central Western Greenland. *Journal of Geophysical Research: Earth Surface*, *123*(8), 2024–2038.

Cheng, D., Hayes, W., Larour, E., Mohajerani, Y., Wood, M., Velicogna, I., & Rignot, E. (2021). Calving Front Machine (CALFIN): glacial termini dataset and automated deep learning extraction method for Greenland, 1972–2019. *The Cryosphere*, *15*(3), 1663–1675.

Choi, Y., Morlighem, M., Wood, M., & Bondzio, J. H. (2018). Comparison of four calving laws to model Greenland outlet glaciers. *The Cryosphere*, *12*(12), 3735–3746.

Clark, P. U., Shakun, J. D., Marcott, S. A., Mix, A. C., Eby, M., Kulp, S., Levermann, A., Milne, G. A., Pfister, P. L., Santer, B. D., Schrag, D. P., Solomon, S., Stocker, T. F., Strauss, B. H., Weaver, A. J., Winkelmann, R., Archer, D., Bard, E., Goldner, A., Lambeck, K., Pierrehumbert, R. T., & Plattner, G.-K. (2016). Consequences of twenty-first-century policy for multi-millennial climate and sea-level change. *Nature Climate Change*, *6*(4), 360–369.

Cowton, T. R., Sole, A. J., Nienow, P. W., Slater, D. A., & Christoffersen, P. (2018). Linear response of east Greenland's tidewater glaciers to ocean/atmosphere warming. *Proceedings of the National Academy of Sciences of the United States of America*, *115*(31), 7907–7912.

Dabboor, M., Iris, S., & Singhroy, V. (2018). The RADARSAT Constellation Mission in Support of Environmental Applications. *Proceedings*, *2*(7), 323.

Danish Agency for Datasupply and Efficiency (2022). Grønland 1:250.000 (1990-2000). Retrieved 2022-11-03, from https://dataforsyningen.dk/data/985.

Dasser, G. (2021). Analysis of Multi-Track Backscatter Time Series for Cryospheric Applications and their Feasibility for Snow Depth Classification. Master's thesis, University of Zurich, Zurich, Switzerland https://lean-gate.geo.uzh.ch/prod/typo3conf/ext/qfq/Classes/Api/download.php/mastersThesis/734.

Dijkstra, E. W. (1959). A note on two problems in connexion with graphs. *Numerische Mathematik*, *1*(1), 269–271.

Drobot, S. D. & Anderson, M. R. (2001). An improved method for determining snowmelt onset dates over Arctic sea ice using scanning multichannel microwave radiometer and Special Sensor Microwave/Imager data. *Journal of Geophysical Research: Atmospheres*, *106*(D20), 24033–24049.

Enderlin, E. M., Howat, I. M., Jeong, S., Noh, M.-J., van Angelen, J. H., & van den Broeke, M. R. (2014). An improved mass budget for the Greenland ice sheet. *Geophysical Research Letters*, *41*(3), 866–872.

Enderlin, E. M., Howat, I. M., & Vieli, A. (2013a). High sensitivity of tidewater outlet glacier dynamics to shape. *The Cryosphere*, *7*(3), 1007–1015.

Enderlin, E. M., Howat, I. M., & Vieli, A. (2013b). The sensitivity of flowline models of tidewater glaciers to parameter uncertainty. *The Cryosphere*, *7*(5), 1579–1590.

ENVEO (2017). Greenland Calving Front Dataset, 1990 - 2016: v3.0 (Greenland Ice Sheet CCI). Retrieved 2022-09-01, from http://cryoportal.enveo.at.

Fahnestock, M. A., Bindschadler, R. A., Kwok, R., & Jezek, K. C. (1993). Greenland Ice Sheet Surface Properties and Ice Dynamics from ERS-1 SAR Imagery. *Science*, *262*(5139), 1530–1534.

Fried, M. J., Catania, G. A., Stearns, L. A., Sutherland, D. A., Bartholomaus, T. C., Shroyer, E., & Nash, J. (2018). Reconciling Drivers of Seasonal Terminus Advance and Retreat at 13 Central West Greenland Tidewater Glaciers. *Journal of Geophysical Research: Earth Surface*, *123*(7), 1590–1607.

Gardner, A., Fahnestock, M. A., & Scambos, T. A. (2023). MEaSUREs ITS_LIVE Landsat Image-Pair Glacier and Ice Sheet Surface Velocities, Version 1. Retrieved 2023-02-26, from https://doi.org/10.5067/IMR9D3PEI28U.

Gray, A. L., Mattar, K. E., Vachon, P. W., Bindschadler, R. A., Jezek, K. C., Forster, R., & Crawford, J. P. (1998). InSAR results from the RADARSAT Antarctic Mapping Mission data: estimation of glacier motion using a simple registration procedure. In *IGARSS 1998* (pp. 1638–1640).: Institute of Electrical and Electronics.

Gray, A. L., Short, N. H., Mattar, K. E., & Jezek, K. C. (2001). Velocities and Flux of the Filchner Ice Shelf and its Tributaries Determined from Speckle Tracking Interferometry. *Canadian Journal of Remote Sensing*, *27*(3), 193–206.

Holland, D. M., Thomas, R. H., de Young, B., Ribergaard, M. H., & Lyberth, B. (2008). Acceleration of Jakobshavn Isbræ triggered by warm subsurface ocean waters. *Nature Geoscience*, *1*(10), 659–664.

Howat, I. M., Box, J. E., Ahn, Y., Herrington, A., & McFadden, E. M. (2010). Seasonal variability in the dynamics of marine-terminating outlet glaciers in Greenland. *Journal of Glaciology*, *56*(198), 601–613.

Howat, I. M., Joughin, I., Fahnestock, M. A., Smith, B. E., & Scambos, T. A. (2008). Synchronous retreat and acceleration of southeast Greenland outlet glaciers 2000–06: ice dynamics and coupling to climate. *Journal of Glaciology*, *54*(187), 646–660.

Howat, I. M., Joughin, I., & Scambos, T. A. (2007). Rapid changes in ice discharge from Greenland outlet glaciers. *Science*, *315*(5818), 1559–1561.

Howat, I. M., Joughin, I., Tulaczyk, S., & Gogineni, S. (2005). Rapid retreat and acceleration of Helheim Glacier, east Greenland. *Geophysical Research Letters*, *32*(22).

Howell, S. E. L., Small, D., Rohner, C., Mahmud, M. S., Yackel, J. J., & Brady, M. (2019). Estimating melt onset over Arctic sea ice from time series multi-sensor Sentinel-1 and RADARSAT-2 backscatter. *Remote Sensing of Environment*, *229*, 48–59.

Hughes, T. J. (1986). The Jakobshanvs effect. *Geophysical Research Letters*, *13*(1), 46–48.

Iken, A. (1981). The Effect of the Subglacial Water Pressure on the Sliding Velocity of a Glacier in an Idealized Numerical Model. *Journal of Glaciology*, *27*(97), 407–421.

IPCC (2013). *Climate Change 2013: The Physical Science Basis. Contribution of Working Group I to the Fifth Assessment Report of the Intergovernmental Panel on Climate Change*. Cambridge, United Kingdom and New York, USA: Cambridge University Press.

Jäger, D. (2016). Wide-area wet snow mapping of the Alps based on Sentinel-1 multi-track radar backscatter composites. Master's thesis, University of Zurich, Zurich, Switzerland.

Jenkins, A. (2011). Convection-Driven Melting near the Grounding Lines of Ice Shelves and Tidewater Glaciers. *Journal of Physical Oceanography*, *41*(12), 2279–2294.

Jennings, A. E. & Weiner, N. J. (1996). Environmental change in eastern Greenland during the last 1300 years: evidence from foraminifera and lithofacies in Nansen Fjord, 68°N. *The Holocene*, *6*(2), 179–191.

Joughin, I. (2002). Ice-sheet velocity mapping: a combined interferometric and speckle-tracking approach. *Annals of Glaciology*, *34*(1), 195–201.

Joughin, I. (2021). MEaSUREs Greenland 6 and 12 day Ice Sheet Velocity Mosaics from SAR, Version 1. Retrieved 2022-08-17, from https://doi.org/10.5067/6JKYGMOZQFYJ.

Joughin, I., Alley, R. B., & Holland, D. M. (2012a). Ice-sheet response to oceanic forcing. *Science*, *338*(6111), 1172–1176.

Joughin, I., Howat, I. M., Fahnestock, M. A., Smith, B. E., Krabill, W., Alley, R. B., Stern, H., & Truffer, M. (2008). Continued evolution of Jakobshavn Isbrae following its rapid speedup. *Journal of Geophysical Research*, *113*(F4).

Joughin, I., Moon, T. A., Joughin, J., & Black, T. (2015). MEaSUREs Annual Greenland Outlet Glacier Terminus Positions from SAR Mosaics, Version 1. Retrieved 2022-09-01, from https://doi.org/10.5067/DCoMLBOCL3EL.

Joughin, I., Smith, B. E., Howat, I. M., Floricioiu, D., Alley, R. B., Truffer, M., & Fahnestock, M. A. (2012b). Seasonal to decadal scale variations in the surface velocity of Jakobshavn Isbrae, Greenland: Observation and model–based analysis. *Journal of Geophysical Research*, *117*.

Kenneally, J. P. & Hughes, T. J. (2006). Calving giant icebergs: old principles, new applications. *Antarctic Science*, *18*(3), 409–419.

King, M. D., Howat, I. M., Jeong, S., Noh, M.-J., Wouters, B., Noël, B. P. Y., & van den Broeke, M. R. (2018). Seasonal to decadal variability in ice discharge from the Greenland Ice Sheet. *The Cryosphere*, *12*(12), 3813–3825.

Krieger, L. & Floricioiu, D. (2017). Automatic glacier calving front delineation on TerraSAR-X and Sentinel-1 SAR imagery. In IEEE (Ed.), *2017 IEEE International Geoscience and Remote Sensing Symposium (IGARSS)* (pp. 2817–2820).: IEEE.

Krug, J., Weiss, J., Gagliardini, O., & Durand, G. (2014). Combining damage and fracture mechanics to model calving. *The Cryosphere*, *8*(6), 2101–2117.

Kwok, R., Cunningham, G. F., & Nghiem, S. V. (2003). A study of the onset of melt over the Arctic Ocean in RADARSAT synthetic aperture radar data. *Journal of Geophysical Research*, *108*(C11).

Lea, J. M., Mair, D. W. F., Nick, F. M., Rea, B. R., van As, D., Morlighem, M., Nienow, P. W., & Weidick, A. (2014). Fluctuations of a Greenlandic tidewater glacier driven by changes in atmospheric forcing: observations and modelling of Kangiata Nunaata Sermia, 1859–present. *The Cryosphere*, *8*(6), 2031–2045.

Linlor, W. I. (1980). Permittivity and attenuation of wet snow between 4 and 12 GHz. *Journal of Applied Physics*, *51*(5), 2811.

Livingstone, C. E., Singh, K. P., & Gray, A. L. (1987). Seasonal and Regional Variations of Active/Passive Microwave Signatures of Sea Ice. *IEEE Transactions on Geoscience and Remote Sensing*, *GE-25*(2), 159–173.

Luckman, A. & Murray, T. (2005). Seasonal variation in velocity before retreat of Jakobshavn Isbræ, Greenland. *Geophysical Research Letters*, *32*(8).

Mätzler, C. (1987). Applications of the interaction of microwaves with the natural snow cover. *Remote Sensing Reviews*, *2*(2), 259–387.

Meier, M. F. & Post, A. (1987). Fast tidewater glaciers. *Journal of Geophysical Research*, *92*(B9), 9051–9058.

Mengel, M., Levermann, A., Frieler, K., Robinson, A., Marzeion, B., & Winkelmann, R. (2016). Future sea level rise constrained by observations and long-term commitment. *Proceedings of the National Academy of Sciences of the United States of America*, *113*(10), 2597–2602.

Mercenier, R., Lüthi, M. P., & Vieli, A. (2018). Calving relation for tidewater glaciers based on detailed stress field analysis. *The Cryosphere*, *12*(2), 721–739.

Michel, R. & Rignot, E. (1999). Flow of Glaciar Moreno, Argentina, from repeat-pass Shuttle Imaging Radar images: Comparison of the phase correlation method with radar interferometry. *Journal of Glaciology*, *45*(149), 93–100.

Moon, T. A. & Joughin, I. (2008). Changes in ice front position on Greenland's outlet glaciers from 1992 to 2007. *Journal of Geophysical Research*, *113*(F2), F02022.

Moon, T. A., Joughin, I., & Smith, B. E. (2015). Seasonal to multiyear variability of glacier surface velocity, terminus position, and sea ice/ice mélange in northwest Greenland. *Journal of Geophysical Research*, *120*(5), 818–833.

Moon, T. A., Joughin, I., Smith, B. E., & Howat, I. M. (2012). 21st-Century Evolution of Greenland Outlet Glacier Velocities. *Science*, *336*(6081), 576–578.

Morlighem, M., Williams, C. N., Rignot, E., An, L., Arndt, J. E., Bamber, J. L., Catania, G. A., Chauché, N., Dowdeswell, J. A., Dorschel, B., Fenty, I., Hogan, K., Howat, I. M., Hubbard, A. L., Jakobsson, M., Jordan, T. M., Kjeldsen, K. K., Millan,

R., Mayer, L., Mouginot, J., Noël, B. P. Y., O'Cofaigh, C., Palmer, S., Rysgaard, S., Seroussi, H., Siegert, M. J., Slabon, P., Straneo, F., van den Broeke, M. R., Weinrebe, W., Wood, M., & Zinglersen, K. B. (2017). BedMachine v3: Complete Bed Topography and Ocean Bathymetry Mapping of Greenland From Multibeam Echo Sounding Combined With Mass Conservation. *Geophysical Research Letters*, *44*(21), 11051–11061.

Mortin, J., Howell, S. E. L., Wang, L., Derksen, C., Svensson, G., Graversen, R. G., & Schrøder, T. M. (2014). Extending the QuikSCAT record of seasonal melt–freeze transitions over Arctic sea ice using ASCAT. *Remote Sensing of Environment*, *141*, 214–230.

Motyka, R. J., Truffer, M., Fahnestock, M. A., Mortensen, J., Rysgaard, S., & Howat, I. M. (2011). Submarine melting of the 1985 Jakobshavn Isbrae floating tongue and the triggering of the current retreat. *Journal of Geophysical Research*, *116*(F1).

Nagler, T., Rott, H., Hetzenecker, M., Wuite, J., & Potin, P. (2015). The Sentinel-1 Mission: New Opportunities for Ice Sheet Observations. *Remote Sensing*, *7*(7), 9371–9389.

NASA (1986). Report of the EOS Data Panel. Retrieved 2022-08-19, from http://hdl.handle.net/2060/19860021622.

Nick, F. M., Luckman, A., Vieli, A., van der Veen, C. J., van As, D., van de Wal, R. S. W., Pattyn, F., Hubbard, A. L., & Floricioiu, D. (2012). The response of Petermann Glacier, Greenland, to large calving events, and its future stability in the context of atmospheric and oceanic warming. *Journal of Glaciology*, *58*(208), 229–239.

Nick, F. M., Vieli, A., Andersen, M. L., Joughin, I., Payne, A. J., Edwards, T. L., Pattyn, F., & van de Wal, R. S. W. (2013). Future sea-level rise from Greenland's main outlet glaciers in a warming climate. *Nature*, *497*(7448), 235–238.

Nick, F. M., Vieli, A., Howat, I. M., & Joughin, I. (2009). Large-scale changes in Greenland outlet glacier dynamics triggered at the terminus. *Nature Geoscience*, *2*(2), 110–114.

Oerlemans, J. & Nick, F. M. (2005). A minimal model of a tidewater glacier. *Annals of Glaciology*, *42*, 1–6.

Osmanoğlu, B., Braun, M. H., Hock, R., & Navarro, F. J. (2013). Surface velocity and ice discharge of the ice cap on King George Island, Antarctica. *Annals of Glaciology*, *54*(63), 111–119.

Pfeffer, W. T. (2007). A simple mechanism for irreversible tidewater glacier retreat. *Journal of Geophysical Research*, *112*.

Powell, R. D. (1983). Glacial-Marine Sedimentation Processes and Lithofacies of Temperate Tidewater Glaciers, Glacier Bay, Alaska. In B. F. Molnia (Ed.), *Glacial-Marine Sedimentation* (pp. 185–232). Boston, USA: Springer US.

Reeh, N. (1968). On The Calving of Ice From Floating Glaciers and Ice Shelves. *Journal of Glaciology*, *7*(50), 215–232.

Reeh, N., Thomsen, H. H., Higgins, A. K., & Weidick, A. (2001). Sea ice and the stability of north and northeast Greenland floating glaciers. *Annals of Glaciology*, *33*, 474–480.

Richards, J. A. (2009). *Remote Sensing with Imaging Radar*. Berlin, Heidelberg: Springer Berlin Heidelberg.

Rignot, E., Koppes, M., & Velicogna, I. (2010). Rapid submarine melting of the calving faces of West Greenland glaciers. *Nature Geoscience*, *3*(3), 187–191.

Rohner, C. (2014). Relating Snow Wetness Information Gained from the Intercantonal Measurement and Information System Stations in Switzerland to Envisat ASAR Backscatter. Master's thesis, University of Zurich, Zurich, Switzerland.

Rohner, C., Small, D., Beutel, J., Henke, D., Lüthi, M. P., & Vieli, A. (2019). Multisensor validation of tidewater glacier flow fields derived from synthetic aperture radar (SAR) intensity tracking. *The Cryosphere*, *13*(11), 2953–2975.

Rohner, C., Small, D., Henke, D., Lüthi, M. P., & Vieli, A. (2022). Automated derivation of continuous glacial and glacier-proximal variables from Sentinel-1 SAR time series for investigating seasonal variations in tidewater glacier dynamics. *Remote Sensing*.

Sciascia, R., Straneo, F., Cenedese, C., & Heimbach, P. (2013). Seasonal variability of submarine melt rate and circulation in an East Greenland fjord. *Journal of Geophysical Research*, *118*(5), 2492–2506.

Shepherd, A., Ivins, E. R., A, G., Barletta, V. R., Bentley, M. J., Bettadpur, S., Briggs, K. H., Bromwich, D. H., Forsberg, R., Galin, N., Horwath, M., Jacobs, S., Joughin, I., King, M. A., Lenaerts, J. T. M., Li, J., Ligtenberg, S. R. M., Luckman, A., Luthcke, S. B., McMillan, M., Meister, R., Milne, G. A., Mouginot, J., Muir, A., Nicolas, J. P., Paden, J., Payne, A. J., Pritchard, H., Rignot, E., Rott, H., Sørensen, L. S., Scambos, T. A., Scheuchl, B., Schrama, E. J. O., Smith, B. E., Sundal, A. V., van Angelen, J. H., van de Berg, W. J., van den Broeke, M. R., Vaughan, D. G., Velicogna, I., Wahr, J., Whitehouse, P. L., Wingham, D. J., Yi, D., Young, D., & Zwally, H. J. (2012). A reconciled estimate of ice-sheet mass balance. *Science*, *338*(6111), 1183–1189.

Short, N. H. & Gray, A. L. (2004). Potential for RADARSAT-2 interferometry: glacier monitoring using speckle tracking. *Canadian Journal of Remote Sensing*, *30*(3), 504–509.

Slater, D. A., Goldberg, D. N., Nienow, P. W., & Cowton, T. R. (2016). Scalings for Submarine Melting at Tidewater Glaciers from Buoyant Plume Theory. *Journal of Physical Oceanography*, *46*(6), 1839–1855.

Small, D. (2011). Flattening Gamma: Radiometric Terrain Correction for SAR Imagery. *IEEE Transactions on Geoscience and Remote Sensing*, *49*(8), 3081–3093.

Small, D. (2012). SAR backscatter multitemporal compositing via local resolution weighting. In *International Geoscience and Remote Sensing Symposium* (pp. 4521–4524).: IEEE.

Small, D., Rohner, C., Miranda, N., Ruetschi, M., & Schaepman, M. E. (2022). Wide-Area Analysis-Ready Radar Backscatter Composites. *IEEE Transactions on Geoscience and Remote Sensing*, *60*.

Straneo, F., Heimbach, P., Sergienko, O., Hamilton, G., Catania, G. A., Griffies, S., Hallberg, R., Jenkins, A., Joughin, I., Motyka, R. J., Pfeffer, W. T., Price, S. F.,

Rignot, E., Scambos, T. A., Truffer, M., & Vieli, A. (2013). Challenges to Understanding the Dynamic Response of Greenland's Marine Terminating Glaciers to Oceanic and Atmospheric Forcing. *Bulletin of the American Meteorological Society*, *94*(8), 1131–1144.

Strozzi, T., Luckman, A., Murray, T., Wegmuller, U., & Werner, C. L. (2002). Glacier motion estimation using SAR offset-tracking procedures. *IEEE Transactions on Geoscience and Remote Sensing*, *40*(11), 2384–2391.

Torres, R., Snoeij, P., Geudtner, D., Bibby, D., Davidson, M., Attema, E., Potin, P., Rommen, B., Floury, N., Brown, M., Traver, I. N., Deghaye, P., Duesmann, B., Rosich, B., Miranda, N., Bruno, C., L'Abbate, M., Croci, R., Pietropaolo, A., Huchler, M., & Rostan, F. (2012). GMES Sentinel-1 mission. *Remote Sensing of Environment*, *120*, 9–24.

van der Veen, C. J. (1998). Fracture mechanics approach to penetration of surface crevasses on glaciers. *Cold Regions Science and Technology*, *27*(1), 31–47.

van der Veen, C. J. (2002). Calving glaciers. *Progress in Physical Geography: Earth and Environment*, *26*(1), 96–122.

van der Veen, C. J. (2013). *Fundamentals of Glacier Dynamics*. Baton Rouge, USA: Taylor & Francis Group, 2nd ed. edition.

Vieli, A. (2015). Retreat Instability of Tidewater Glaciers and Marine Ice Sheets. In W. Haeberli, C. Whiteman, & J. F. Shroder (Eds.), *Snow and ice-related hazards, risks, and disasters* (pp. 677–712). Amsterdam, Netherlands: Elsevier Science.

Vieli, A., Funk, M., & Blatter, H. (2000). Tidewater glaciers: frontal flow acceleration and basal sliding. *Annals of Glaciology*, *31*, 217–221.

Vieli, A., Funk, M., & Blatter, H. (2001). Flow dynamics of tidewater glaciers: a numerical modelling approach. *Journal of Glaciology*, *47*(159), 595–606.

Vieli, A. & Nick, F. M. (2011). Understanding and Modelling Rapid Dynamic Changes of Tidewater Outlet Glaciers: Issues and Implications. *Surveys in Geophysics*, *32*(4-5), 437–458.

Weertman, J. (1972). General theory of water flow at the base of a glacier or ice sheet. *Reviews of Geophysics*, *10*(1), 287–333.

Woodhouse, I. H. (2006). *Introduction to microwave remote sensing*. Boca Raton, USA: Taylor & Francis.

Publications and Conferences

Publications

Howell, S.E.L., Small, D., **Rohner, C.**, Small, D., Mahmud, M.S., Yackel, J.J., & Brady, M. (2019). Estimating melt onset over Arctic sea ice from time series multi-sensor Sentinel-1 and RADARSAT-2 backscatter. *Remote Sensing of Environment, 229, 48-59.* doi: 10.1016/j.rse.2019.04.031.

Rohner, C., Small, D., Beutel, J., Henke, D., Lüthi, M.P., & Vieli, A. (2019). Multisensor validation of tidewater glacier flow fields derived from synthetic aperture radar (SAR) intensity tracking. *The Cryosphere, 13(11), 2953–2975.* doi: 10.5194/tc-13-2953-2019.

Small, D., **Rohner, C.**, Miranda, N., Rüetschi, M., & Schaepman, M.E. (2022). Wide-area analysis-ready radar backscatter composites. *IEEE Transactions on Geoscience and Remote Sensing, 60, 1–14.* doi: 10.1109/TGRS.2021.3055562.

Rohner, C., Small, D., Henke, D., Lüthi, M.P., & Vieli, A. (in review). Automated derivation of continuous glacial variables from Sentinel-1 SAR time series for investigating seasonal variations in tidewater glacier dynamics. *Remote Sensing.*

Conference Talks

Rohner, C., Small, D., Lüthi, M.P., & Vieli, A. (2017). Variability in Glacier Flow Dynamics of a Greenland Outlet Glacier Using Sentinel-1 SAR Data. Validation with Multiple Ground-based Measurements. *European Association of Remote Sensing Laboratories. Bern, Switzerland. 7–9 February.*

Small, D., **Rohner, C.**, Schubert, A., Howell, S.E.L., Crevier, Y., & Miranda, N. (2017). Hybrid Wide-area Backscatter Maps combining Sentinel-1 and Radarsat-2 Observations. *ESA Polar Science Collocation Meeting. ESA-ESRIN, Frascati, Italy. 28–30 June.*

Rohner, C., Mercenier, R., Vieli, A., Lüthi, M.P., & Small, D. (2018). Variability in Glacier Dynamics of a Greenland Glacier Using Sentinel-1 SAR Data. *Polar 2018. Davos, Switzerland. 19–23 June.*

Small, D., **Rohner, C.**, Vögtli, M., Miranda, N., Howell, S.E.L., & Crevier, Y. (2018). Hybrid Sentinel-1/Radarsat Backscatter Time Series of Arctic Canada. *Polar 2018. Davos, Switzerland. 19–23 June.*

Small, D., **Rohner, C.**, Miranda, N., Howell, S.E.L, Rüetschi, M., & Waser, L.T. (2018). Demonstrations of Wide-area Radar Backscatter Time Series Applications. *BioGeoSAR 2018. Oberpfaffenhofen, Germany. 12–15 November.*

Small, D., **Rohner, C.**, Miranda, N., Howell, S.E.L., & Crevier, Y. (2019). Multi-sensor Wide-area Level-3 Radar Backscatter Time Series. *CEOS WGCV SAR Cal/Val Workshop. ESA-ESRIN, Frascati, Italy, 18–22 November.*

Small, D., **Rohner, C.**, Miranda, N., Howell, S.E.L., Rüetschi, M., & Waser, L.T. (2019): Applications of Seamless Wide-area ARD Backscatter Time Series in Forestry and the Cryosphere. *Living Planet Symposium. Milan, Italy. 13–17 May.*

Conference Posters

Rohner, C., Henke, D., Small, D., Mercenier, R., Lüthi, M.P., & Vieli, A. (2016). Outlet-glacier flow dynamics estimation combining in-situ and spaceborne measurements. *European Geosciences Union General Assembly. Vienna, Austria. 17–22 April.*

Small, D., **Rohner, C.**, Miranda, N., Rüetschi, M., Waser, L.T., Vögtli, M., & Schaepman, M.E. (2018). Level 3 wide-area backscatter time-series for wet-snow mapping and forest classification. *European Geosciences Union General Assembly. Vienna, Austria. 8–13 April.*

Mölg, N., Vieli, A., Ferguson, J., **Rohner, C.**, & Bolch, T. (2018). Evolution of surface topography, debris cover, ice flow, and downwasting features: a holistic reconstruction of a heavily debris-covered Alpine glacier from 1860–2017. *European Geosciences Union General Assembly. Vienna, Austria. 8–13 April.*

Acknowledgements

I would like to thank my supervisors and advisors David Small, Prof. Andreas Vieli, Daniel Henke, and Martin P. Lüthi for their valuable support and inputs, the interesting discussions, the helpful feedback and suggestions on my manuscripts, their guidance and patience throughout the entirety of this PhD.

Furthermore, I would like to thank the additional PhD Committee Members Prof. Michael E. Schaepman and Prof. Alexander Damm for their very good and helpful feedback.

A very special thank you goes out to everyone – family, friends, and colleagues – involved directly or indirectly in the making of this dissertation, without whom it would not have been possible to complete it. Or at least it would have been way less fun.